



NEW QUANTUM CASCADE LASER ARCHITECTURES

II-VI QUANTUM CASCADE EMITTERS,
HIGH k -SPACE LASING,
& SHORT INJECTORS

Kale J. Franz

A DISSERTATION
PRESENTED TO THE FACULTY
OF PRINCETON UNIVERSITY
IN CANDIDACY FOR THE DEGREE
OF DOCTOR OF PHILOSOPHY

RECOMMENDED FOR ACCEPTANCE
BY THE DEPARTMENT OF ELECTRICAL ENGINEERING

Adviser: Claire Gmachl

June 2009

© Copyright by Kale J. Franz, June 2009.
All Rights Reserved

Abstract

Quantum cascade (QC) lasers are today's most capable mid-infrared light sources. With up to watt-level room temperature emission over a broad swath of mid-infrared wavelengths, these tiny semiconductor devices enable a variety of applications and technologies such as ultra-sensitive systems for detecting trace molecules in the vapor phase. The foundation of a QC structure lies in alternating hundreds of wide- and narrow-bandgap semiconductor layers to form a coupled quantum well system. In this way, the laws of quantum mechanics are used to precisely engineer electron transport and create artificial optical transitions. The result is a material with capabilities not found in nature, a truly "designer" material.

As a central theme in this thesis, we stress the remarkable flexibility of the quantum cascade—the ability to highly tailor device structure for creative design concepts. The QC idea, in fact, relies on no particular material system for its implementation. While all QC lasers to date have been fabricated from III–V materials such as InGaAs/AlInAs, I detail our preliminary work on ZnCdSe/ZnCdMgSe—a II–VI materials system—where we have demonstrated electroluminescence.

We then further discuss how the inherent QC flexibility can be exploited for new devices that extend QC performance and capabilities. In this regard, we offer the examples of excited state transitions and short injectors. Excited state transitions are an avenue to enhancing optical gain, which is especially needed for longer-wavelength devices where optical losses hinder performance. Likewise, shortening the QC injector length over a conventional QC structure has powerful implications for threshold current, output power, and wall-plug efficiency. In both cases, novel physical effects are discovered. Pumping electrons into highly excited states led to the discovery of high k -space lasing from highly non-equilibrium electron distributions. Shortening QC injector regions allowed us to observe “classical” superlattice effects such as negative differential resistance and pulse instabilities. While interesting from a scientific perspective, these unique phenomena shed new insight on internal QC laser processes and may themselves lead to further improvements in device performance.

Acknowledgements

One quickly learns in graduate school that progress in research is seldom accomplished alone. The work I present in this thesis is no different, and I am indebted to a great many people for their help, support, friendship, and, patience over the last five years.

My adviser, Professor Claire Gmachl, is most certainly at the top of the list. She is everything you could ever want in a graduate adviser, and a whole lot more. It's taken me the better part of five years to learn that, when we have a disagreement over science, she always ends up being right; the important part was that she let me discover this on my own.

Both Professor Andrew Houck and Professor Gerard Wysocki were kind enough to give up more than one weekend to review this thesis, and I am extremely grateful for their time and valuable input.

One of the greatest advantages of working in Prof. Gmachl's group is the tremendous opportunity provided for collaborative research. I have been fortunate to work with many different groups on several projects, and each of these collaborations has contributed meaningfully to this dissertation.

Before his move to Michigan, Professor Stephen Forrest was kind enough to welcome me into his research group and lab. Using his MBE to grow QC lasers was an invaluable experience. And for their time and patience, I thank Dr. Shashank Agashe, Stephane Kena-Cohen, and especially Kuen-Ting Shiu in teaching me the art of MBE.

My work at Princeton has benefited from several MBE and MOCVD growth collaborators. The II-VI project would have been impossible without the assistance of Professor Maria Tamargo and her group. Professor Aidong Shen, Dr. Hong Lu, and especially William Charles all played significant roles in our progress so far on II-VI QC structures.

I am also deeply indebted to Mary Fong, Jen-Yu Fan, and Xiaojun Wang at AdTech Optics for all of their assistance and support. Not only did they provide excellent QC growth, but they welcomed me as an intern during the summer of 2007. They made it an amazing experience for me, and I'm very appreciative.

Other key collaborators include Professor Fow-Sen Choa and his group at University of Maryland–Baltimore County, Dr. Jerry Meyer and his group at the Naval Research Lab,

and Dr. Fred Towner at Maxion Technologies. I'd also like to thank Dr. Igor Trofimov, always an excellent source of advice for processing and fab techniques and tricks.

I am deeply grateful to Prof. Jacob Khurgin and Dr. Yamac Dikmelik at Johns Hopkins University for a number of extremely fruitful discussions over the last few years. The success of our research team would not be without their valuable membership.

I would also like to thank my fellow members and visitors of the Mid-Infrared Photonics Group at Princeton University: Professor Dan Wasserman, Dr. Jian-Zhang Chen, Dr. Jianxin Chen, Dr. Anna Michel, Dr. Zhijun Liu, Dr. Afusat Dirisu, Fatima Toor, Matthew Escarra, Richard Cendejas, Ekua Bentil, Yu Yao, Peter Liu, Elvis Mujagić, Aleksander Wójcik, Alexander Benz, Abhishek Agrawal, and Tiffany Ko. Working with everyone was a pleasure and I wish you all the best of luck.

Two fellow members of my research group deserve special thanks. Dr. Scott Howard was there from day one when I couldn't tell a lock-in amplifier from a pulse generator, and he has since become a great friend. I also want to thank Dr. Anthony Hoffman, my lab mate, office mate, roommate, and the best of friends. Scott and Anthony, along with Professor Gene Slowinski, all fellow co-founders of Primis Technologies LLC, deserve special recognition for picking up the slack while I've been racing to complete this dissertation.

I also want to acknowledge the support of the National Science Foundation in making my graduate work possible. Both through the NSF Graduate Research Fellowship and NSF's funding of the MIRTHE center, the financial assistance has been invaluable. I am also grateful for the support of the Princeton University Wallace Fellowship during my final year of graduate work.

Finally, I want to thank my family: my mother Marlinda, father Kyle, grandma Jeanne, grandpa Melvin, sister MaKayla, brother-in-law Philip, and nephew Merrick. For all the love and support they've given me, for allowing me to spend five years on the other side of the country to pursue my graduate work, and for all of their inspiration and encouragement along the way, I am eternally grateful.

Table of Contents

Abstract	iii
Acknowledgements	iv
Table of Contents	vi
List of Tables	x
List of Figures	xi
1 Introduction	1
1.1 Engineered Mid-infrared Light Sources: Present and Future	2
1.1.1 Defense countermeasures	3
1.1.2 Open atmosphere data transmission	5
1.1.3 Molecular species detection	6
1.2 Quantum Cascade Lasers	6
1.3 The QC Development Process	9
1.3.1 Design	10
1.3.2 Growth	10
1.3.3 Fabrication	10
1.4 Thesis Overview	11
2 Quantum Cascade Laser Design and Operation Theory	14
2.1 The Schrödinger Equation	14
2.2 Interface Energy Offsets and Bandgaps	17
2.2.1 Materials parameters for ternary alloys	18
2.2.2 Temperature effects on bandgap	20
2.2.3 Strain effects on bandgap and band offset	20
2.3 Effective Mass	23
2.4 Self-consistent Solutions of the Schrödinger and Poisson Equations	25
2.5 Spontaneous Emission Rate and the Optical Dipole Matrix Element	28

Table of Contents

2.6	Stimulated Emission Probability and the Transition Cross Section	32
2.7	LO-phonon Scattering Time	33
2.8	Rate Equations for QC Lasers	35
2.9	Threshold Current & Modal Gain	39
2.10	Slope Efficiency	41
2.11	Output Power and Wall-plug Efficiency	42
2.12	Maximum Current & Differential Resistance	43
2.13	Summary	45
3	ZnCdSe/ZnCdMgSe Quantum Cascade Emitters	46
3.1	Short Wavelength Quantum Cascade Emitters	48
3.2	The ZnCdSe/ZnMgSe Materials System	51
3.3	Epitaxial Growth of ZnCdSe/ZnMgSe Materials	53
3.4	Intersubband Absorption in ZnCdSe/ZnCdMgSe Quantum Wells	55
3.5	A ZnCdSe/ZnCdMgSe Quantum Cascade Structure	56
3.6	Device Fabrication & Processing	58
3.7	Measurements and Data	60
3.7.1	Quantum Cascade Intersubband Absorption	60
3.7.2	Electroluminescence Spectra	61
3.7.3	Light–Current–Voltage Data	63
3.8	Second-Generation Design	64
3.9	Conclusions & Future Directions	66
3.9.1	Summary	66
3.9.2	Future Direction: New II–VI design strategies	67
3.9.3	Future Direction: Strain-compensated growth	71
3.9.4	Future Direction: Fabrication of II–VI QC laser waveguides	71
4	Excited State Quantum Cascade Lasers and High k-Space Lasing	73
4.1	The Long-wavelength Challenge	75
4.2	Excited State Transitions	78
4.3	Excited State QC Laser Design	81
4.4	Device Emission Characteristics	84
4.4.1	Electroluminescence and Identification of the Optical Transitions .	84
4.4.2	Laser Emission	87

Table of Contents

4.4.3	Stacked Transitions	88
4.5	Anti-correlated Light Output Behavior	88
4.6	Lasing High in k -Space	93
4.7	Effects of Non-parabolicity	96
4.8	Rate Equation Modeling	99
4.8.1	A System of Two Coupled Optical Transitions	99
4.8.2	Comparing Threshold Data with Simulation	102
4.8.3	Cavity-length-dependence of Threshold Crossover	104
4.9	Conclusions & Future Directions	105
4.9.1	Summary	105
4.9.2	Future Direction: <i>Intentionally</i> created k -space lasers	107
4.9.3	Future Direction: Further develop the excited state concept	108
4.9.4	Future Direction: Correlated photons	108
5	Short Injector Quantum Cascade Lasers	110
5.1	The Role of the QC Injector	112
5.2	Theoretical Framework	113
5.3	QC Laser with Three Injector Wells	116
5.3.1	Design and Fabrication	116
5.3.2	Results and Discussion	118
5.3.3	Device Performance	123
5.4	QC Laser with Two Injector Wells	128
5.4.1	Design and Fabrication	128
5.4.2	Results and Discussion	128
5.4.3	Device Performance	134
5.5	Conclusions and Future Directions	134
5.5.1	Summary	134
5.5.2	Future Direction: Higher performance QC lasers	138
5.5.3	Future Direction: Improving temperature performance	138
6	Conclusions	140
6.1	Thesis Summary	141
6.1.1	II-VI QC Structures	141
6.1.2	Excited State Quantum Cascade Lasers and High k -Space Lasing . .	142

Table of Contents

6.1.3 Short Injector Quantum Cascade Lasers	143
6.2 Challenges for the Next Decade of Research	144
6.2.1 Tunability	145
6.2.2 Single Mode Emission	145
6.2.3 Wall-plug Efficiency	146
6.2.4 Low Input Power Devices	146
6.2.5 Short Wavelength QC Lasers	147
6.2.6 Long Wavelength QC Lasers	147
6.3 The Feasibility of a Sustainable QC Laser-based Industry	147
Publications	149
Conference Presentations	153
Intellectual Property	158
References	159

List of Tables

2.1	Material parameters: InAs, GaAs, and AlAs	19
2.2	Material bowing parameters: InGaAs and AlInAs	20
3.1	Material parameters: ZnSe, CdSe, and MgSe	53
4.1	Input parameters for the k -space model	100
4.2	LO phonon lifetimes used in the k -space model.	101
4.3	Fitting parameters for the k -space model	102

List of Figures

1.1	The electromagnetic spectrum	3
1.2	Infrared countermeasure flares deployed from an AC-130U gunship	4
1.3	IRCM module	4
1.4	Atmospheric absorption versus wavelength	5
1.5	Spectral absorption signatures for several atmospheric gasses	7
1.6	Basic QC laser band diagram	8
1.7	ErwinJr QC laser design software	9
1.8	QC laser fabrication methods	12
2.1	Example use of the shooting method	17
2.2	Bandgap temperature dependence	21
2.3	Bandgap strain dependence	24
2.4	Sketch of waveguide geometry	35
3.1	Absorption spectra and laser capabilities near the first atmospheric window.	47
3.2	Energy gap vs. lattice constant for III-V and II-VI materials.	49
3.3	Bulk energy band diagrams for InAs, ZnSe, and CdSe	52
3.4	Intersubband absorption of a single quantum structure	55
3.5	First generation $Zn_{0.43}Cd_{0.57}Se/Zn_{0.20}Cd_{0.19}Mg_{0.61}Se$ QC design.	57
3.6	TM absorption spectrum from multi-pass transmission	60
3.7	Polarization-resolved EL spectra	61
3.8	EL spectra at $T = 78$ K	62
3.9	Temperature-dependence of EL spectra	63
3.10	EL structure LIV	64
3.11	Second generation $Zn_{0.43}Cd_{0.57}Se/Zn_{0.20}Cd_{0.19}Mg_{0.61}Se$ QC design.	65
3.12	Superlattice ZnCdSe/ZnCdMgSE QC structure	68
3.13	ZnCdSe/ZnCdMgSE QC structure with fewer layers	69

3.14 Short wavelength ZnCdSe/ZnCdMgSE QC structure	70
3.15 II-VI QC waveguide	72
4.1 Absorption spectra for BTEX molecules	74
4.2 Optical absorption of bulk InGaAs	76
4.3 LO phonon lifetime vs. transition wavelength	77
4.4 Optical dipole matrix elements for a single quantum well.	79
4.5 Energy state mixing in coupled quantum wells.	80
4.6 Excited state QC laser band diagram	82
4.7 SEM of excited state QC stack and waveguide	83
4.8 Excited state structure electroluminescence spectra	85
4.9 Excited state transition identification	86
4.10 EL at high pumping current	87
4.11 Excited state laser spectra	89
4.12 Light output characteristics of a representative laser device	90
4.13 Light-temperature cross-sections	91
4.14 Light-current cross-sections	92
4.15 Threshold temperature-dependence of the transitions	93
4.16 The k -space electron paths	94
4.17 Spectral signature of k -space emission	97
4.18 Model results for transition thresholds	101
4.19 Model results for transition thresholds	104
4.20 Cavity length dependence of transition threshold crossover temperature .	105
5.1 Conventional QC laser structure	113
5.2 Energy band diagrams for the three injector well QC structure	117
5.3 Three injector well EL LIV data	119
5.4 Comparison of EL spectra at pre- and post-NDR operating points	120
5.5 Three injector well LIV	121
5.6 Three injector well LIV near $T_{sink} = 130$ K	122
5.7 Spectra for the 3 injector well laser at $T_{sink} = 79$ K	124
5.8 Spectra for the 3 injector well laser at $T_{sink} = 146$ K	125
5.9 Spectra for the 3 injector well laser at $T_{sink} = 302$ K	126
5.10 Performance data for the three injector well structure	127

List of Figures

5.11 Energy band diagrams for the two injector well QC structure	129
5.12 LIV for a two injector well EL sample	130
5.13 Pulsed LIV data for the two injector well structure (I)	132
5.14 Pulsed LIV data for the two injector well structure (II)	133
5.15 Spectra for the 2 injector well laser at $T_{sink} = 79$ K	135
5.16 Spectra for the 2 injector well laser at $T_{sink} = 301$ K	136
5.17 Performance data for the two injector well structure	137

Chapter 1

Introduction

Never a dull moment. Not in the field of optoelectronics; not since the merging of semiconductors and optics was cemented some half century ago after Chapin and colleagues at Bell Labs made practical use of the photovoltaic effect in a silicon solar cell [1]. And of the many defining moments in optoelectronics research, perhaps paramount of them all was the first observations in 1962 by Hall *et al.* [2] and Holonyak *et al.* [3] of stimulated emission in electrically pumped semiconductors. Since that time, optoelectronic technology has become an integral part of our daily lives. Solar cells may well be on the verge of contributing to the elimination of fossil fuels. Light emitting diodes (LEDs) are rapidly replacing Edison's incandescent bulb. How many liquid crystal display (LCD) devices do you own... too many to count in a single attempt?

Semiconductor laser technology is no different. Without these lasers, our telecommunications pipelines would be vastly less efficient. We would be relying on the same technology that powered Henry's electromagnetic telegraph: electrons traveling through wire (slow) rather than photons traveling through glass (fast!). Today's semiconductor lasers, and indeed to varying degrees most all optoelectronic devices, make use of a fundamental concept dubbed heterostructure engineering. In fact, the heterostructure's ubiquity was recognized by the year 2000 Nobel prize in physics, awarded to Zhores Alferov [4] and Herbert Krömer [5] for their pioneering work. A heterostructure device is composed of layers of different materials, overlayed one after the other. These layers are strategically selected and used to precisely control how electrons—*i.e.* current—pass through a device.

The layers that make up a heterostructure can be made exceedingly thin: thicknesses on the order of a single atomic layer. The ability to form such thin layers make heterostructures one of man's ultimate engineering conquests of quantum mechanics. Just as nature's atom puts electrons into discrete energy orbits, man's quantum-confined heterostructure forces electrons into discrete energy states as they pass through a heterostructure device. By exploiting this ability, we can influence when, where, and how electrons interact with their surroundings. In the seminal work that first recognized this possibility of quantum confinement in heterostructures, Esaki and Tsu in 1970 theorized that a particular heterostructure implementation could result in *negative* resistance at certain applied voltage levels [6]. The following year, Kazaninov and Suris proposed that the man-made energy states of quantum-confined heterostructures could be used as the basic optical transition for a new type of laser [7]. Despite multiple attempts, it took some 25 years to realize such an intersubband heterostructure laser [8], now known as the quantum cascade (QC) laser. The year 2009 marks the 15th anniversary of the first reported QC laser demonstration.

The genius of the heterostructure concept—and the quantum cascade in particular—lies in its innate engineerability. In this thesis, I hope to convey how the QC concept provides vast opportunity for creative new ideas that can expand technological capabilities and improve device performance.

1.1 Engineered Mid-infrared Light Sources: Present and Future

QC lasers are particularly suited for generating light at mid-infrared (mid-IR) wavelengths. Loosely defined, the mid-infrared is the spectral region between 3 and 30 μm in wavelength (10–100 THz in frequency). As illustrated in Fig. 1.1, these boundaries mark convenient transitions between the capabilities of three different technologies that are today's most capable electrically-pumped semiconductor-based laser sources. From the visible region to about 3 μm diode lasers dominate [4] [5]; diode lasers are especially capable at the 0.98 and 1.55 μm “telecom” bands. On the long wavelength side, THz QC lasers are the dominant injection laser technology [9]. Although Pb-salt diode lasers were once the best option for mid-infrared injection sources, QC lasers have emerged as



Figure 1.1: The electromagnetic spectrum. The wavelengths from 0.3 to 300 μm are covered by three semiconductor laser technologies. The mid-infrared, loosely defined as 3 to 30 μm , is the regime of mid-infrared QC lasers. Between the transitions for laser device types—diode-to-mid-IR QC laser and mid-IR QC laser-to-THz QC laser—lie spectral gaps of substantial technical challenge. The first gap, explored in Chapter 3, results from fundamental loss mechanisms in diode lasers and band offset limitations in mid-IR QC lasers. The second gap, explored in Chapter 4, derives fundamentally from the semiconductor restrahlen band in the 30–60 μm region.

far more capable devices. Mid-infrared QC lasers span 2.75 μm [10] to 24 μm [11], with various performance levels in between. In general, room temperature (RT), continuous wave (CW) lasing is now the technological standard from 4–12 μm .

An ability to easily generate mid-infrared light is most certainly of technological importance. Holding a wide swath of the electromagnetic spectrum, mid-infrared light can be exploited for unique applications. While there are numerous applications for mid-infrared light, with more surely on the horizon, here I briefly discuss just three examples: defense countermeasures, open atmosphere data transmission, and molecular species detection.

1.1.1 Defense countermeasures

Deployable flares, such as those being emitted from an AC-130U gunship in Fig. 1.2, are the conventional countermeasure against IR-guided (heat-seeking) missiles. Modern infrared countermeasures (IRCMs), which use directed infrared light sources to “jam” the targeting system on an IR-guided missile—in effect blinding the missile, have qualities that make them far more effective by comparison. The ability to highly tailor the spectral signature and modulation properties of a light source is a key advantage over older flare-based technologies. Modern IRCMs also do not require an aircraft to



Figure 1.2: Infrared countermeasure flares deployed from an AC-130U gunship. An AC-130U gunship jettisons flares over an area near Hurlburt Field, Florida. The flares are a decoy for heat-seeking missiles that may be fired at the aircraft. The aircraft is from the 4th Special Operations Squadron. Courtesy of the U.S. Air Force [12].

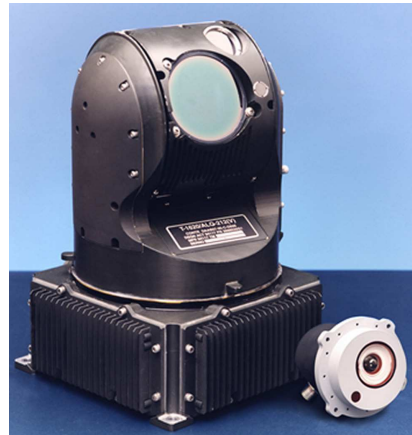


Figure 1.3: IRCM module. An early photo of Lockheed Martin's ATIRCM. Courtesy of BAE Systems press release [13].

undergo “evasive maneuvers” to physically separate itself from dropped flares. As a craft-mountable module, shown in Fig. 1.3, these systems couple threat identification and tracking together with targeting and jamming into a system that does not require expendable components such as flares.

The two modern IRCM programs, Northrup Grumman’s NEMESIS Directional Infrared Countermeasure (DIRCM) and Lockheed Martin’s Advanced Threat Infrared Countermeasures (ATIRCM), both use solid state laser light sources. These are bulky, only operate under pulsed conditions, and have spectral emission characteristics that

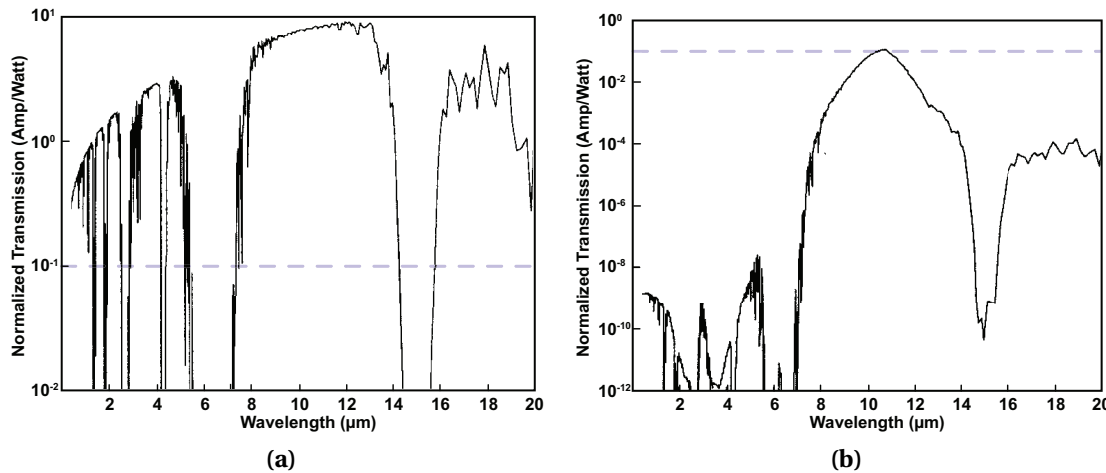


Figure 1.4: Atmospheric absorption versus wavelength. Mid-infrared wavelengths, especially in the second atmospheric window near $10 \mu\text{m}$, are considerably more “clear” during adverse weather. Panel (a) shows transmission for very clear weather (“visibility,” 50 km) while (b) shows transmission for thick fog (“visibility,” 200 m). The dashed line represents normalized transmission at 10^{-1} A/W for comparison. Reprinted from [14] with permission from the Optical Society of America.

are difficult to customize. By comparison, QC lasers are miniature devices, capable of CW operation, and have spectral emission that is highly configurable. Clearly, QC lasers are of interest to replace and improve upon the present-day IRCM light sources.

1.1.2 Open atmosphere data transmission

Methods for transmitting information through the atmosphere, and specifically free space optical communications systems, use laser-based transceivers for line-of-site data transmission. Compared to other communications technologies, free space optical communications combines capabilities of extremely high bandwidth, rapid deployment time, and license- and tariff-free bandwidth allocation. The major weakness of free space optical communications is the threat of sporadic downtime associated with adverse weather conditions such as fog, haze, or rain that prevent the signal (light) from propagating through the atmosphere. The wavelength-dependence of atmospheric absorption for clear and foggy conditions is shown in Fig. 1.4, as calculated by Manor and Arnon [14]. For clear weather, the advanced capabilities of telecom lasers around $1.5 \mu\text{m}$ would certainly suffice. Yet under adverse conditions, as shown in Fig. 1.4b,

transmission near $1.5\text{ }\mu\text{m}$ decreases by approximately 9 orders of magnitude. In comparison, transmission for $10\text{ }\mu\text{m}$ light only decreases by 2 orders of magnitude between the two atmospheric conditions, and the difference between $1.5\text{ }\mu\text{m}$ light on a clear day and $10\text{ }\mu\text{m}$ light on a foggy day is only 1 order of magnitude. The mid-infrared is a most convenient wavelength for applications where atmospheric transmission is important, free space optical communications included.

1.1.3 Molecular species detection

Perhaps the most versatile of the applications for mid-infrared light is its use in the detection of trace molecules. Molecular detection based on sensing the presence of light absorption can be versatile, selective, and sensitive [15]. Individual molecular species have unique energies at which they absorb light, the absorption energies corresponding to vibrational and rotational modes of the molecule. Figure 1.5 shows absorption spectra for several common and important atmospheric gasses. These molecule-specific absorption “fingerprints” can be used to selectively determine the presence of a particular species, including isotropic ratios, by an absorption spectroscopy system. Such a system typically has three components: a light source, a light-matter interaction space, and an optical detector. For gas-phase absorption spectroscopy, the light source wavelength is tuned to correspond to an absorption line of a targeted molecular species, the light is allowed to interact with a gas sample in a cavity such as a Herriot cell, and the remaining light is collected on an optical detector. All else being equal, maximum sensitivity is achieved when the frequency of the light source is selected to be on resonance with the strongest absorption line of the target species. That is, the use of fundamental mode absorption resonances, most typically at mid-infrared wavelengths, will yield the most effective and sensitive detection systems.

1.2 Quantum Cascade Lasers

Understanding the basic operation of a QC laser most easily starts by comparison with the more well-known diode laser. QC lasers and diode lasers share several common elements. Both are semiconductor injection lasers; that is, they employ “top” and “bottom” metal contacts that allow electric current to be pumped through the device.

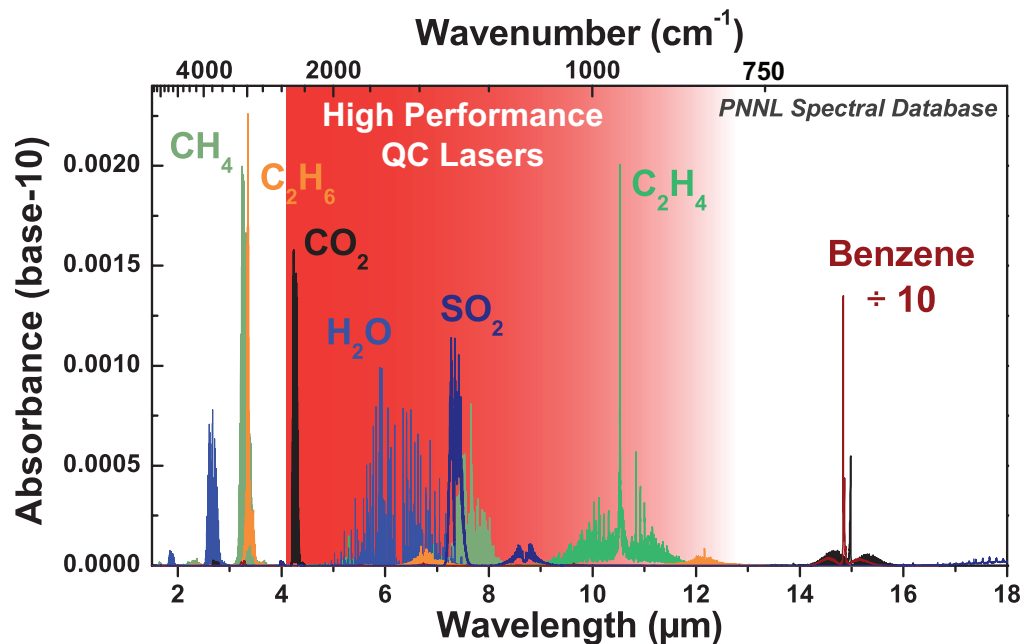


Figure 1.5: Spectral absorption signatures for several atmospheric gasses. Most molecular species have their fundamental resonances at wavelengths beyond 3 μm , out of reach of diode lasers. High performance (RT CW) QC lasers are able to cover a large many of the resonances of interest.

Both laser types make use of similar dielectric waveguide structures, where an optical mode is designed to tightly overlap with a semiconductor region that provides optical gain.

Beyond these characteristics, differences start to emerge. The fundamental mechanics by which diode lasers and QC structures generate light are different. In diode lasers, electrons combine with holes across the fundamental semiconductor bandgap to produce photons at the bandgap energy. Thus a key device property, the emission wavelength, is set by the semiconductor material itself. QC lasers, by contrast, use coupled quantum wells to tailor nearly every aspect of the device properties. Figure 1.6 pictorially shows a QC laser's energy band structure. The positions of each individual energy state are uniquely determined by the selection of well and barrier widths.

A QC laser's design can be divided into two sections: the active regions and the injector regions. QC active regions have at least three important energy "states," which are in fact energy sub-bands. Two states are needed to form the upper and lower energy states of the optical transition. The positions of these states are selected to give

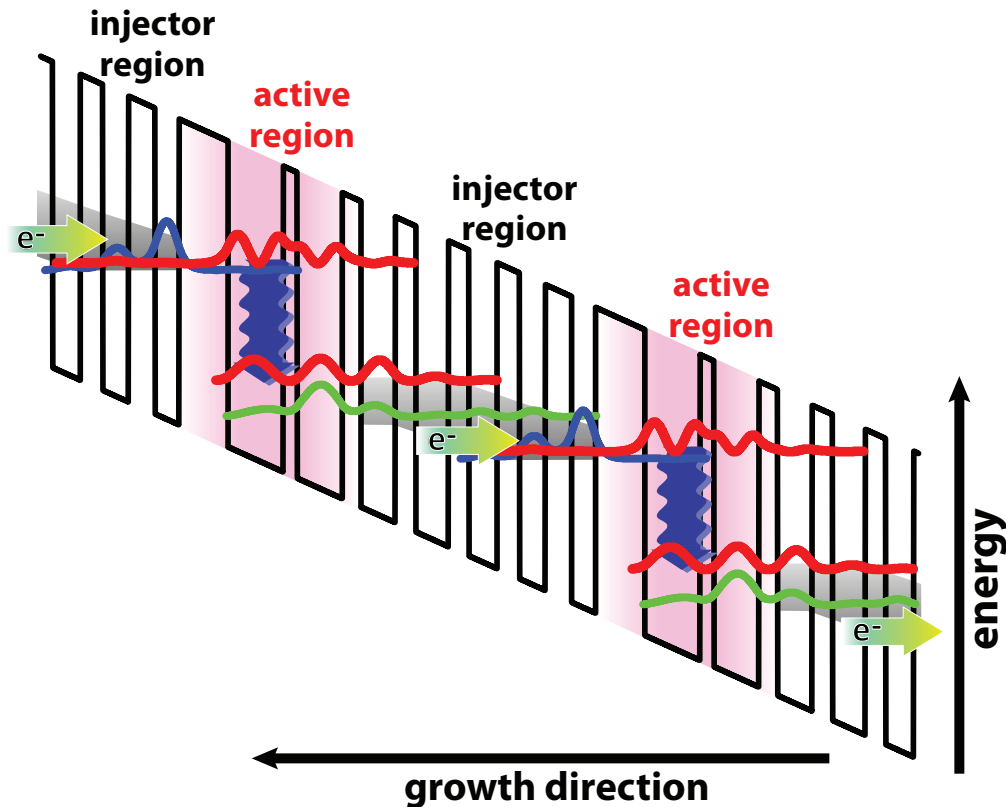


Figure 1.6: Basic QC laser band diagram. The conduction band edge of the alternating wide and narrow bandgap materials is shown, along with the stationary wavefunctions of the quantum wells. QC lasers have an active region, where optical transitions are engineered to occur, and an injector region, which stitches together successively “cascaded” active regions. When a sufficient electric field is applied, indicated in the figure by the constant slope, electrons are able to transit through the entire QC structure.

an energy separation of the desired photon energy, and they are usually designed to have large overlap integrals to yield a large oscillator strength. A third important active region state is placed below the lower laser state; an energy separation of at least one longitudinal optical (LO) phonon is used. LO phonons represent the fastest electron scattering mechanism in semiconductors. This lowest energy state is thus intended to quickly empty the lower energy level, and hence for the first two states provide an in-built population inversion.

The other important QC laser section is the QC injector region. QC injectors do all of the important functions necessary to “stitch together” consecutive active regions. That is, QC injectors impart the ability to take electrons from the lower states in one

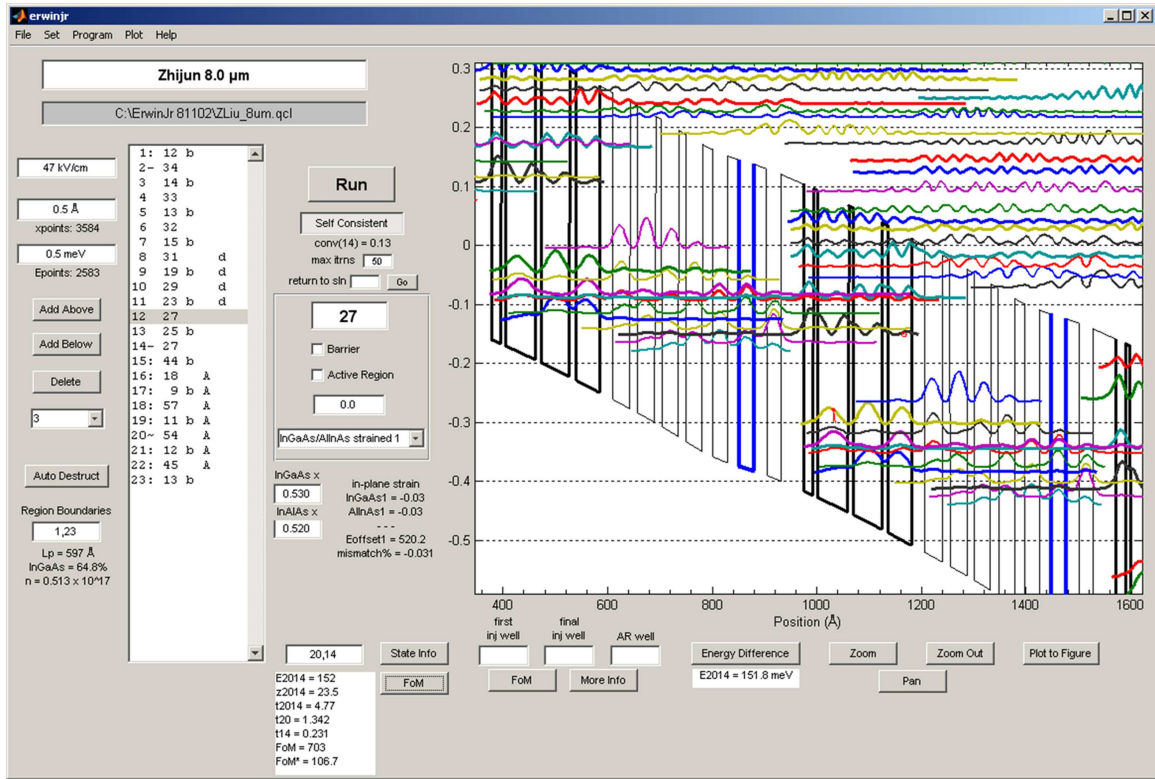


Figure 1.7: ErwinJr QC laser design software. QC laser design has been aided by advances in design tools.

active region and inject them into the upper laser state of the next, down-stream active region. Through this stitching together of multiple active–injector region periods, multiple photons are emitted for each single electron that passes through the structure. A detailed examination of the role of injector regions is given in Chapter 5.

1.3 The QC Development Process

The process of producing QC laser can be divided into three basic steps: design, growth, and fabrication. Each represents a critically important skill set, and high performance QC laser production requires high quality in all three areas.

1.3.1 Design

QC laser design is the first step of laser development. The high degree of flexibility afforded by the QC concept makes design both a creative and challenging process. Successful QC designs have indeed been quite varied in architecture. For example, after years of following the single LO phonon active region convention, Beck *et al.* realized superior performance by using two stacked LO phonon transitions in the active region to empty the lower laser state [16]. A superlattice QC structure, first demonstrated in 1997 [17], creates dense “minibands” of states by using much narrower well and barrier layers as compared to conventional QC structures. Both Raman lasers [18] and Bloch gain [19] have been demonstrated in QC structures. The list of creative design architectures goes on and on. Clearly, the flexibility is advantageous for capitalizing on the discovery of new physical phenomena and for implementing new design strategies.

QC laser design is accomplished using a set of tools that primarily function by solving the Schrödinger equation. Figure 2.1 shows a screen shot of our recently developed software ErwinJr, which can solve for the energy states of complex and large QC structures in a matter of seconds. This ability rapidly speeds the QC design process.

1.3.2 Growth

The epitaxial growth of QC lasers is accomplished either by molecular beam epitaxy (MBE) or metal-organic vapor phase deposition (MOVPE or MOCVD). Both growth methods are highly automated processes, where computers are used to control deposition rates and times. Such automation is absolutely necessary due to the extreme complexity of QC structures. The growth of the hundreds of individual layers required for QC structures by more manual processes (such as liquid phase epitaxy, for example) would simply be prohibitive. Excellent reviews of both growth methods can be found in the *Proceedings of the IEEE*: Ref. [20] for MBE and Ref. [21] for MOVPE.

1.3.3 Fabrication

Methods of QC laser fabrication have become much more advanced since the initial QC laser reported in 1994. The two primary concerns for laser fabrication are creating a low

optical loss waveguide and creating a path for heat to rapidly leave the QC active core. The four basic processing methods used in this thesis are described below.

The most basic processing method is the ridge laser, shown in Fig. 1.8a. The ridge laser is the fastest to process, but also has the least capable heat extraction capabilities. It is best suited for rapid testing of QC laser material, especially applicable when a comparison among the performance of multiple QC structures is needed.

A more advanced processing method is the double trench, as shown in Fig. 1.8b. These laser structures are especially able to capitalize on using thick ($\sim 5 \mu\text{m}$) Au as the top contact, which provides a rapid thermal transport path out of the active region. Double trench lasers have shown the capability of room temperature, continuous wave performance [22].

The most advanced, highest performing, and time-intensive processing method is the buried heterostructure (BH), shown in Fig. 1.8c. These structures were the first to demonstrated room temperature, continuous wave performance [16]. Improved packaging technologies, such as mounting lasers epitaxial-side down on diamond heat sinks [23], have also shown dramatic performance improvements.

The electroluminescence (EL) mesa, as shown in Fig. 1.8d, is another type of QC structure that is most often used for test and analysis purposes. These structures are specifically designed to suppress optical feedback, so that emission is purely from spontaneous emission.

1.4 Thesis Overview

This thesis seeks to demonstrate the power of the quantum cascade as a flexible device technology platform. Never before has a laser system afforded engineers so much control over its fundamental, internal mechanisms. Truly, the QC concept imparts the unprecedented ability to create new device architectures that incorporate new operation concepts. Throughout this thesis, we provide examples of how this flexibility can be exploited to improve device performance and expand device capabilities.

In Chapter 2, we provide a theoretical foundation for basic operation principles of QC lasers. Key tools used in laser design, such as accurate solutions to the Schrödinger equation and the optical dipole matrix element, are explicitly discussed. Derivations

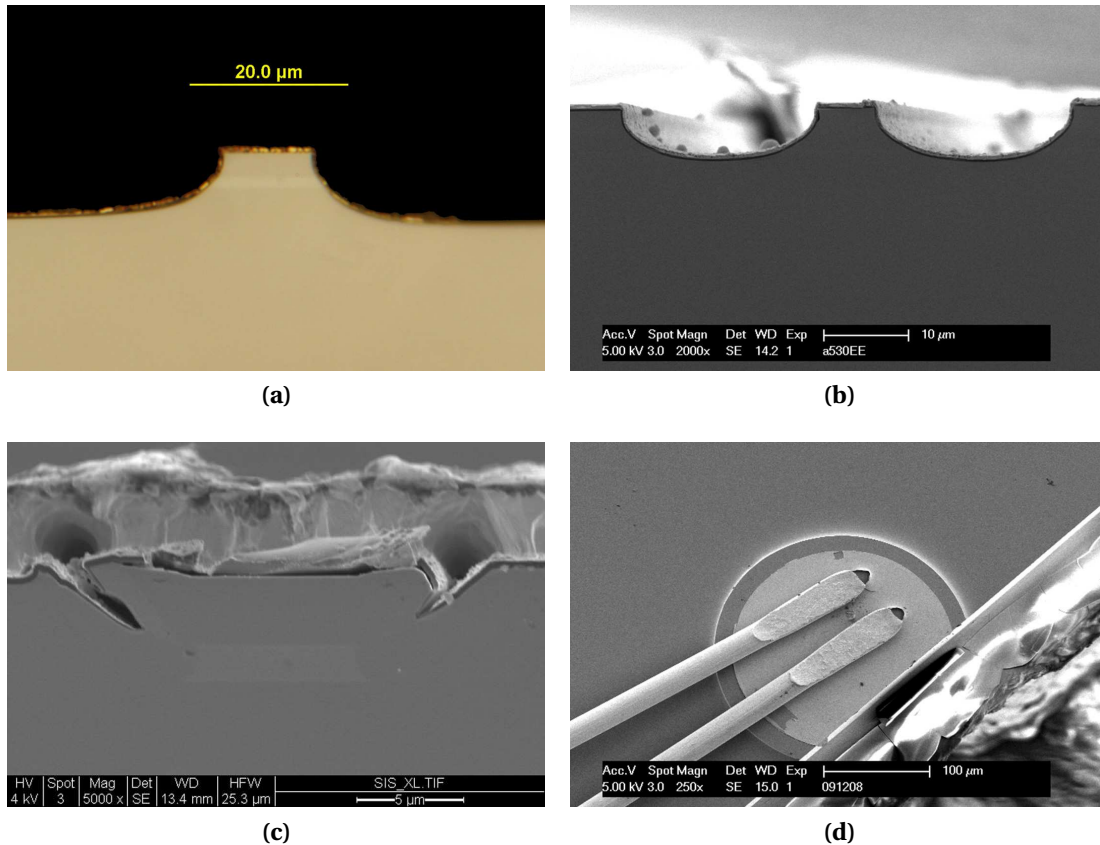


Figure 1.8: QC laser fabrication methods. Ridge lasers, as shown in (a), are the most basic laser type and are the most straight-forward and fast to process. More complex structures, such as the double trench ridge in (b), are more difficult to process but can have improved heat extraction capabilities. Buried heterostructures, shown in (c), are the most advanced and highest performing structures; they are also the most complicated to fabricate, as they require a second InP growth step. Electroluminescence mesas, as shown in (d), are used for QC structure characterization. They have the particular advantage of suppressing optical feedback and therefore suppressing lasing.

for important device performance parameters, such as threshold current and wall-plug efficiency, are given with sufficient detail to clearly understand the origins and contributions of important design parameters.

As an example of the flexibility of the technology platform, Chapter 3 discusses implementing QC structures in an entirely new materials system: ZnCdSe / ZnCdMgSe [24]. This II–VI materials system has some properties that may be advantageous over the currently used III–V materials system, such as larger conduction band offsets,

which ultimately may be useful for developing shorter wavelength QC lasers than those currently available.

In contrast, the motivation for Chapter 4 starts with expanding the capabilities of QC lasers on the long wavelength side. Here, we present a new QC architecture—one which employs optical transitions made completely of quantum well excited states [25]. These excited state structures have the ability to compensate for many of the deleterious factors that make long-wavelength lasing so difficult. Through experimenting with this new structure, we found the unexpected and unique property of lasing high in k -space [26].

Chapter 5 presents a fundamental re-examination of the role of QC injector regions. Since the injector regions are not the source of photons, they can in some ways be viewed as “wasted space.” However, injector regions practically serve several functions that are crucial to high laser performance. Here, we look at minimizing injector length, and we employ QC designs that drastically reduce the overall period length of the structure. Like in the results of Chapter 4, we observe unique and unexpected properties. These observations allow us to draw new insights into and understanding of fundamental QC laser operation mechanisms.

Finally, concluding remarks are given in Chapter 6, along with an outlook for the future of QC technology.

Chapter 2

Quantum Cascade Laser Design and Operation Theory

Because of the inherent flexibility afforded by the QC concept, laser designs are highly customizable. And to optimize a design for any particular goal or set of operating conditions, a basic understanding of the contributions of various laser parameters to performance is key.

In this chapter, I provide the basic tools and derive the fundamental relations important to QC laser design and operation. In sum, it is a QC laser “toolbox” generally applicable to most QC laser design circumstances. Individually, the foundations for most sections of this chapter can be found in the references cited herein. However, no single reference exists that thoroughly covers all the aspects important to QC laser design. This chapter thus compiles knowledge garnered from a number of disparate sources. Furthermore, where I have found no good source for elements I believe to be crucial to QC laser design, I provide a thorough, original discussion.

This theory becomes the foundation for ideas presented in later chapters, and it also provides a basis for new insights and understanding derived from the data presented in the remainder of this thesis.

2.1 The Schrödinger Equation

Fundamental to QC laser design is the ability to accurately calculate the positions of energy states in the quantum-confined dimension. Generally, we are most interested in

the conduction band wavefunctions ψ_c . In the elementary abstraction, we simply solve the time-independent Schrödinger equation

$$-\frac{\hbar^2}{2m^*} \frac{\partial^2}{\partial z^2} \psi_c(z) + qV_c(z)\psi_c(z) = \mathcal{E}_q \psi_c(z) \quad (2.1)$$

where \hbar is Planck's constant, m^* is the conduction band effective mass, z is the dimension of quantum confinement, qV_c is the conduction band potential energy profile, and \mathcal{E}_q is the eigen energy of the quantum state.

Immediately, we encounter a problem. Coupling of the conduction band energy states with the valence bands and other bands makes the solution much more complex than the simple one-band model of Eq. (2.1). However, for our primary interest of bound conduction band solutions, these complex interactions can be reduced to an energy-dependence of the effective conduction band mass [27]. Consequently, as the electron acquires more energy—*i.e.* gets higher up in the band and closer to the vacuum level—the electron gets “heavier.” Also, our QC structure is a system of layered materials, each with a different effective mass from adjacent layers. So, the effective mass is both energy- and position-dependent: $m^*(z, \mathcal{E})$. This results in a small change to the simple Schrödinger equation. When solving the Schrödinger equation, we are taught to match $\psi_c(z)$ and $\frac{\partial}{\partial z}\psi_c(z)$ at the boundaries. Now, with variable effective masses, the solutions of envelope functions [28] are continuous across material interfaces in both $\psi_c(z)$ and $\frac{1}{m^*} \frac{\partial}{\partial z}\psi_c(z)$.

Because of variable effective mass, the classical portrayal of the Schrodinger equation is somewhat different. Given the momentum operator $\mathcal{P}_z = -i\hbar\partial_z$, the kinetic energy operator \mathcal{T} becomes [27]

$$\mathcal{T} = \mathcal{P}_z \frac{1}{2m^*(z, \mathcal{E})} \mathcal{P}_z = -\frac{\hbar^2}{2} \frac{\partial}{\partial z} \frac{1}{m^*(z, \mathcal{E})} \frac{\partial}{\partial z} \quad (2.2)$$

and the Schrödinger equation now becomes

$$-\frac{\hbar^2}{2} \frac{\partial}{\partial z} \frac{1}{m^*(z, \mathcal{E})} \frac{\partial}{\partial z} \psi_c(z) + qV_c(z)\psi_c(z) = \mathcal{E}_q(z)\psi_c(z) \quad (2.3)$$

where $\mathcal{E}_q(z)$ acquires a position-dependence when defined as the energy relative to the conduction band edge and in the presence of an applied electric field E_{field} . Now, to

make Eq. (2.3) discrete, we approximate the derivative as

$$\frac{df}{dz} \approx \frac{\Delta f}{\Delta z} = \frac{f(z + \delta z) - f(z - \delta z)}{2\delta z}. \quad (2.4)$$

The Schrödinger equation above can be discretized by expanding $\mathcal{T}\psi_c(z)$.

$$\frac{1}{m^*(z+\delta z, \mathcal{E})} \frac{\partial \psi(z)}{\partial z} \Big|_{z+\delta z} - \frac{1}{m^*(z-\delta z, \mathcal{E})} \frac{\partial \psi(z)}{\partial z} \Big|_{z-\delta z} = \frac{2}{\hbar^2} [qV_c(z) - \mathcal{E}] \psi_c(z) \quad (2.5)$$

Applying Eq. (2.4) to the above equation, gathering terms in $\psi_c(z)$, and making the transformation $2\delta z \rightarrow \delta z$ gives

$$\begin{aligned} \psi_c(z + \delta z) = & \left\{ \left[\frac{2(\delta z)^2}{\hbar^2} [qV(z)_c - \mathcal{E}] + \frac{1}{m^*(z + \delta z/2, \mathcal{E})} + \frac{1}{m^*(z - \delta z/2, \mathcal{E})} \right] \psi(z) \right. \\ & \left. - \frac{1}{m^*(z - \delta z/2, \mathcal{E})} \psi(z - \delta z) \right\} m^*(z + \delta z/2, \mathcal{E}) \end{aligned} \quad (2.6)$$

The effective mass at the intermediate points $z \pm \delta z/2$ is found by taking the average of the effective mass for the two adjacent points z and $z + \delta z$. By virtue of having coupled quantum well structures with abrupt material interfaces and the presence of varying electric fields, all parameters related to wavefunctions, energies, effective masses, etc. will be implicitly assumed to have position-dependence z , and these references will be hereafter dropped when not explicitly needed.

The shooting method is used to solve for the eigen energies of our system through the application of Eq. (2.6). Specifically, we look for bound solutions of the system confined by the dimensions $z = 0$ and $z = z_{end}$. That is, any energy \mathcal{E} where $\psi(0) = 0$ and $\psi(z_{end}) = 0$. In an elementary implementation of the shooting method, the energy space covered by our potential $V_c(z)$ is initially divided into many discrete steps. Then, Eq. (2.6) is used to propagate through discrete steps in z to find $\psi(z_{end})$ for each initial energy value, where the initial conditions $\psi(0) = 0$ and $\psi(z_{second}) = 1$ are used (z_{second} being the second discrete solve point after $z = 0$). To find the exact energy value of a bound solution, we take advantage of the fact that $\psi(z_{end})$ switches signs at a bound solution. Therefore, when $\psi(z_{end})$ is plotted for all energies over our energy space, noting the location in energy of a sign flip of $\psi(z_{end})$, allows us to iterate in energy around this point

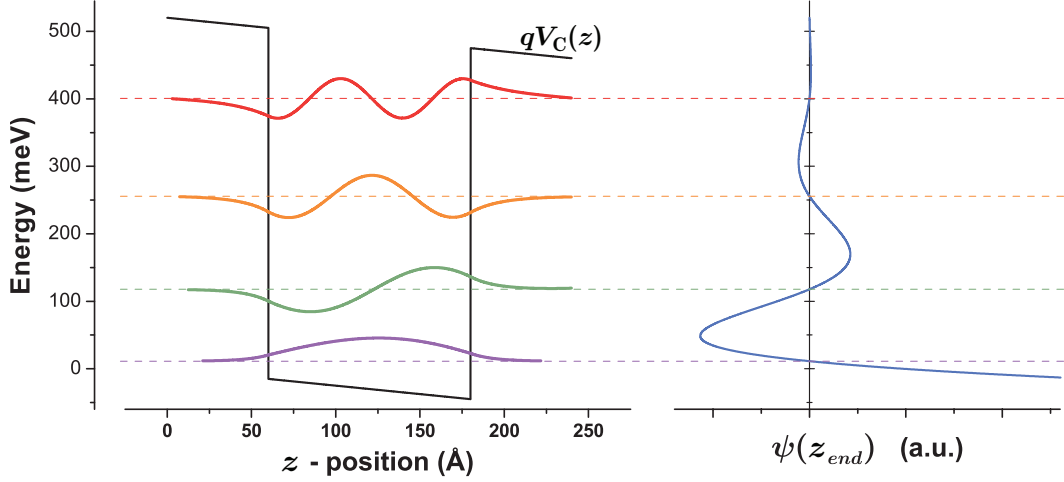


Figure 2.1: Example use of the shooting method. The left panel shows a potential $V(z)$ for an $\text{In}_{0.53}\text{Ga}_{0.47}\text{As} / \text{Al}_{0.48}\text{In}_{0.52}\text{As}$ quantum well with $E_{\text{field}} = 25 \text{ kV/cm}$. Four bound solutions are found by finding the roots of $\psi(z_{\text{end}})$, as shown in the right panel. The wavefunction $\psi(z)$ is plotted for the four bound solutions.

to find the exact value of the bound solution. Figure 2.1 provides an example; here, our potential $V_c(z)$ is for a single quantum well in the $\text{In}_{0.53}\text{Ga}_{0.47}\text{As} / \text{Al}_{0.48}\text{In}_{0.52}\text{As}$ system, with conduction band offset of 520 meV, and an applied electric field $E_{\text{field}} = 25 \text{ kV/cm}$. Four bound solutions are found, and $\psi_t nC(z)$ is plotted for each solution, using the eigen energy as the baseline of the wavefunction.

2.2 Interface Energy Offsets and Bandgaps

To properly use Eq. (2.6) for solving the time-independent Schrödinger equation, we need accurate knowledge of two key parameters: $V_c(z)$ and $m^*(z, \mathcal{E})$. This section is devoted to attaining the band offset values that are so important to coupled quantum well systems such as QC lasers. In the following section, we discuss effective mass in semiconductor systems. This section and the remaining sections in this chapter make heavy use of semiconductor materials parameters; a superb review of important III-V material parameters was published by Vurgaftman *et al.* in 2001 [29], and is summarized in Tables 2.1 and 2.2 for common III-V QC materials.

All QC laser implementations to date have used intersubband transitions in the conduction band. While QC electroluminescence has been shown from valence intersubband transitions [30] [31], we are more keenly interested in the conduction band edge offsets of materials. As it turns out, the valence band offsets have been much more extensively studied [29], owing to the experimental difficulty of measuring conduction band offsets. When considering a valence band offset, the convention is to report the parameter VBO , which is the valence band offset relative to a predetermined reference material where VBO is specified as 0 (*i.e.* $VBO = 0$); Vurgaftman *et al.*, for example, define $VBO(\text{InSb}) = 0$. In this way, the valence band offset for any two arbitrary materials is easily found as the difference in VBO for the two materials of the set. By adding the bandgap of each material to its respective VBO , the conduction band offset for a two material system can likewise be calculated. More concretely, the conduction band edge (at the Γ point) \mathcal{E}_c^Γ can be defined as

$$\mathcal{E}_c^\Gamma = VBO + \mathcal{E}_g^\Gamma + \delta\mathcal{E}_{Varsh} + \delta\mathcal{E}_{\varepsilon c} + \delta\mathcal{E}_{\varepsilon v} \quad (2.7)$$

where \mathcal{E}_g^Γ is the energy gap at the Γ point at temperature $T = 0$ K without strain, $\delta\mathcal{E}_{Varsh}$ is the Varshney correction to the bandgap energy for $T \neq 0$ K, and $\delta\mathcal{E}_{\varepsilon c}$ and $\delta\mathcal{E}_{\varepsilon v}$ are corrections to the conduction and valence band edges due to hydrostatic deformation (*i.e.* strain). Each of these terms is treated in the following sections. With this definition of \mathcal{E}_c^Γ , the conduction band offset at the interface between two materials A and B is $\Delta\mathcal{E}_c^\Gamma = \mathcal{E}_c^\Gamma(A) - \mathcal{E}_c^\Gamma(B)$.

2.2.1 Materials parameters for ternary alloys

Fundamental materials parameters, VBO and \mathcal{E}_g^Γ for example, can be conveniently reported in tabular form for binary semiconductors, as in the review by Vurgaftman *et al.* [29]. Ternary alloys, however, have a degree of freedom in material composition, making tabular recording prohibitive. For any ternary material $A_xB_{1-x}C$, composed proportionally of the two constituent binaries $(AC)_x$ and $(BC)_{1-x}$, a range of values exists over the mole fraction x for any generic material parameter P . Conveniently, we can make use of the composition endpoints $x = 0$ and $x = 1$ to bound the possible values

Table 2.1: Material parameters for the binary alloys InAs, GaAs, and AlAs. Source is [29], unless otherwise indicated. Lattice constants are given for 300 K. The effective mass is given for the bulk band edge, with m_0 the free electron mass.

	InAs	GaAs	AlAs
$a_{\ell c}$ (Å)	6.0583	5.6533	5.6611
c_{11} (GPa)	832.9	1221	1250
c_{12} (GPa)	452.6	566	534
\mathcal{E}_G^Γ (eV)	0.417	1.519	3.099
Δ_{SO} (eV)	0.39	0.341	0.28
VBO (eV)	-0.59	-0.80	-1.33
a_c^Γ (eV)	-5.08	-7.17	-5.64
a_v (eV)	-1.00	-1.16	-2.47
b (eV)	-1.8	-2.0	-2.3
\mathcal{E}_P (eV)	21.5	28.8	21.1
F	-2.90	-1.94	-0.48
m_e^Γ/m_0	0.026	0.067	0.15
α^Γ (meV/K)	0.276	0.5405	0.885
β^Γ (K)	93	204	530
ϵ_s	14.3 ⁽¹⁾	12.90 ⁽¹⁾	10.06 ⁽¹⁾
ϵ_∞	11.6 ⁽¹⁾	10.86 ⁽¹⁾	8.16 ⁽¹⁾
$\hbar\omega_{LO}$	29.93 ⁽¹⁾	35.3 ⁽¹⁾	49.8 ⁽¹⁾

(1) Ref. [32]

of P . Then, P can thus be defined as

$$P(A_x B_{1-x} C) = xP(AC) + (1-x)P(BC) + x(1-x)C_B \quad (2.8)$$

where C_B is the bowing parameter specific to material ABC . Commonly, the bowing parameter is either not well known, or no bowing parameter exists. In the case of $C_B = 0$, the material parameter is just a linear interpolation between the value of the parameter for the two component binaries weighted by x . Bowing parameters common for III–V QC materials are given in Table 2.2.

Table 2.2: Non-zero bowing parameters C_B for the ternary alloys InGaAs and AlInAs. Source is [29].

	InGaAs	AlInAs
\mathcal{E}_G^Γ (eV)	0.477	0.70
Δ_{SO} (eV)	0.15	0.15
VBO (eV)	-0.38	-0.64
\mathcal{E}_P (eV)	-1.48	-4.81
F	1.77	-4.44
m_e^Γ/m_0	0.0091	0.049
a_c^Γ (eV)	2.61	-1.4

2.2.2 Temperature effects on bandgap

The temperature dependence of semiconductor bandgaps is commonly described with the Varshni formula. This is an empirical formula that fits two Varshni parameters— α [$\frac{\text{energy}}{\text{temperature}}$] and β [temperature]—to experimentally obtained values of bandgap with temperature. The Varshni formula gives the temperature T dependence of the bandgap as [33]

$$\mathcal{E}_g(T) = \mathcal{E}_g(T=0) - \frac{\alpha T^2}{T + \beta} \quad (2.9)$$

so that the temperature correction to the conduction band edge is

$$\delta\mathcal{E}_{Varsh} = -\frac{\alpha T^2}{T + \beta}. \quad (2.10)$$

The Varshney corrections for the common QC materials $\text{In}_{0.53}\text{Ga}_{0.47}\text{As}$ and $\text{Al}_{0.48}\text{In}_{0.52}\text{As}$ are plotted in Fig. 2.2.

2.2.3 Strain effects on bandgap and band offset

Strain in epitaxially-grown semiconductors arises when the lattice constant for a particular composition of grown material is different from that of the substrate material. Generally, strain is an undesired condition, as strain buildup will eventually lead to a variety of epitaxial defects. The lattice constant and bandgap are both functions of the

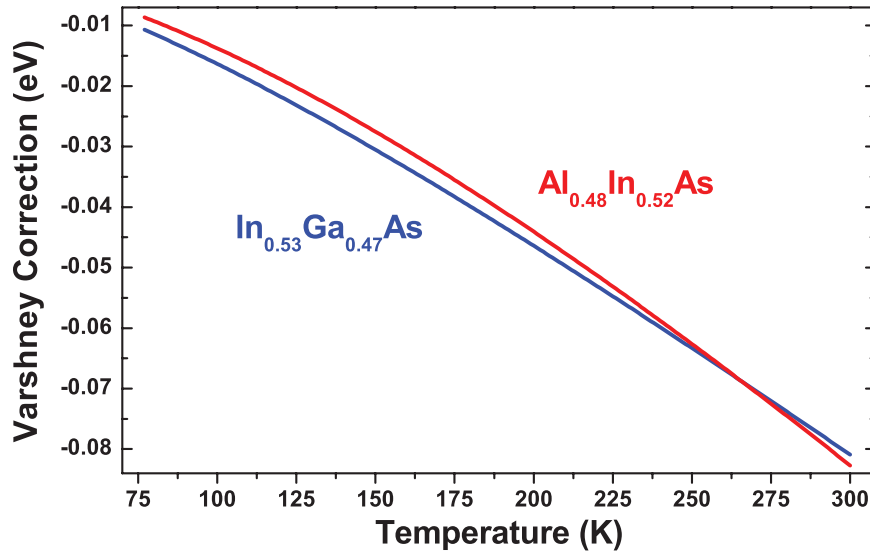


Figure 2.2: Bandgap temperature dependence. The Varshney correction δE_{Varsh} is plotted for the InP-lattice-matched compositions $In_{0.53}Ga_{0.47}As$ and $Al_{0.48}In_{0.52}As$. The effect of increasing temperature is the lowering of the material bandgap.

mole fraction x for any particular ternary material composition; therefore, imposing the condition that all grown materials are lattice-matched to the substrate lattice constant does not generally allow one to adjust mole fraction compositions to alter the material bandgap.*

Since QC lasers operate on intersubband transitions, any optical transition must be confined within the quantum wells of the heterostructure to prevent electrons from escaping. It is thus easy to see that the ability to adjust material compositions to maximize the conduction band offset would be advantageous. This is especially true when seeking high energy, short wavelength photon generation.

The QC concept allows for a clever way to achieve both strain-free bulk material while simultaneously having the ability to adjust material compositions to affect bandgaps. Taking advantage of the alternating layer structure, where a wide bandgap barrier material is interleaved with a narrow bandgap well material, compressive strain can be built into one layer set while tensile strain is built into the other layer set; the result can be an overall strain-balanced heterostructure [34].

* The materials systems GaAs/AlAs and InAs/AlSb represent a special exception where the binary pairs share a nearly identical lattice constant.

Semiconductors with a zinc blende lattice structure (cubic symmetry)—the case for most III–V alloys—acquire biaxial strain when epitaxially grown on a substrate with a different lattice constant. That means, for the three dimensional strain tensor, only the diagonal components ε_{xx} , ε_{yy} , and ε_{zz} are non-zero. Identifying z as the direction of epitaxial growth, values for strain are given by [35]

$$\varepsilon_{xx} = \varepsilon_{yy} = \frac{a_0 - a_{\ell c}}{a_{\ell c}} \quad (2.11a)$$

$$\varepsilon_{zz} = -\frac{2c_{12}}{c_{11}}\varepsilon_{xx} \quad (2.11b)$$

where a_0 is the lattice constant of the substrate, $a_{\ell c}$ is the lattice constant of the epitaxial layer material, and c_{11} and c_{12} are the elastic stiffness constants of the layer material.

The effects of strain on bandgaps are well described by the Pikus–Bir interaction [36] and also by the “model-solid” theory of Van de Walle [37]. Here, the change in band gap due to strain is empirically characterized by the relative change in volume \mathcal{V} due to strain and scaled by a hydrostatic deformation potential a [energy] for both bands. The percent change in volume due to strain is given by

$$\frac{\delta\mathcal{V}}{\mathcal{V}} = \varepsilon_{xx} + \varepsilon_{yy} + \varepsilon_{zz} \quad (2.12)$$

which is the trace of the strain tensor. The change in bandgap due to strain $\delta\mathcal{E}_\varepsilon$ is then

$$\delta\mathcal{E}_\varepsilon = a \frac{\delta\mathcal{V}}{\mathcal{V}} \quad (2.13)$$

and the components of the shift acquired by the conduction and valence bands, $\delta\mathcal{E}_{\varepsilon c}$ and $\delta\mathcal{E}_{\varepsilon v}$ respectively, are

$$\delta\mathcal{E}_{\varepsilon c} = a_c \frac{\delta\mathcal{V}}{\mathcal{V}} \quad (2.14a)$$

$$\delta\mathcal{E}_{\varepsilon v} = a_v \frac{\delta\mathcal{V}}{\mathcal{V}} \quad (2.14b)$$

where a_c and a_v are the conduction and valence band hydrostatic deformation potentials, given that $a = a_c + a_v$. In compound semiconductors, adding hydrostatic pressure (*i.e.* adding compressive strain) results in an increase in band gap. Generally, this means

that compressive strain causes the conduction band edge to move “up” proportionally by $\frac{a_c}{a}$ and the valence band edge to move “down” proportionally by $\frac{a_v}{a}$.

The light hole (LH), heavy hole (HH), and split-off (SO) valence bands have p -state “shape” and therefore lack spherical symmetry, unlike the conduction band (C) with s -state shape. Due to this lack of symmetry, biaxial strain has a shear component that affects the valence bands, and it splits the degeneracy of the heavy hole and light hole bands at the Γ point. Derived from the Pikus–Bir Hamiltonian [36], the energy bandgaps with shear strain and including the spin-orbit interaction are

$$\mathcal{E}_{\text{C-HH}}^{\Gamma} = \mathcal{E}_g^{\Gamma} + \delta\mathcal{E}_{\varepsilon c} + \delta\mathcal{E}_{\varepsilon v} - Q_{\varepsilon} \quad (2.15\text{a})$$

$$\mathcal{E}_{\text{C-LH}}^{\Gamma} = \mathcal{E}_g^{\Gamma} + \delta\mathcal{E}_{\varepsilon c} + \delta\mathcal{E}_{\varepsilon v} + \frac{1}{2} \left(Q_{\varepsilon} - \Delta_{\text{SO}} + \sqrt{\Delta_{\text{SO}}^2 + 2\Delta_{\text{SO}}Q_{\varepsilon} + 9Q_{\varepsilon}^2} \right) \quad (2.15\text{b})$$

$$\mathcal{E}_{\text{C-SO}}^{\Gamma} = \mathcal{E}_g^{\Gamma} + \delta\mathcal{E}_{\varepsilon c} + \delta\mathcal{E}_{\varepsilon v} + \frac{1}{2} \left(Q_{\varepsilon} - \Delta_{\text{SO}} - \sqrt{\Delta_{\text{SO}}^2 + 2\Delta_{\text{SO}}Q_{\varepsilon} + 9Q_{\varepsilon}^2} \right) \quad (2.15\text{c})$$

where Δ_{SO} is the split-off energy without strain and the shear deformation potential b [energy] is included in Q_{ε} , defined as

$$Q_{\varepsilon} = \frac{b}{2} (\varepsilon_{xx} + \varepsilon_{yy} - 2\varepsilon_{zz}) . \quad (2.16)$$

The bandgaps given in Eq. (2.15a) neglect temperature effects, which can be included by adding the $\delta\mathcal{E}_{\text{Varsh}}$ term. A comparison of the effect of strain on $\text{In}_x\text{Ga}_{1-x}\text{As}$ and $\text{Al}_{1-x}\text{In}_x\text{As}$ bandgaps is shown in Fig. 2.3.

2.3 Effective Mass

Just as important as the potential profile to accurate solutions of the Schrödinger equation is the effective mass. Fundamentally, the effective mass of an individual energy band is influenced by the surrounding energy bands. Using $\mathbf{k} \bullet \mathbf{p}$ theory, the conduction band effective mass perpendicular to the plane of epitaxial growth $m^*(z, \mathcal{E}_q)$ can be derived as [27], [29], [38]

$$\frac{1}{m^*(z, \mathcal{E}_q)} = \frac{1}{m_0} \left\{ 1 + 2F + \frac{\mathcal{E}_P}{3} \left[\frac{(\sqrt{2}u - v)^2}{\mathcal{E}_q + \mathcal{E}_{\text{C-LH}}^{\Gamma}} + \frac{(\sqrt{2}v + u)^2}{\mathcal{E}_q + \mathcal{E}_{\text{C-SO}}^{\Gamma}} \right] \right\} \quad (2.17)$$

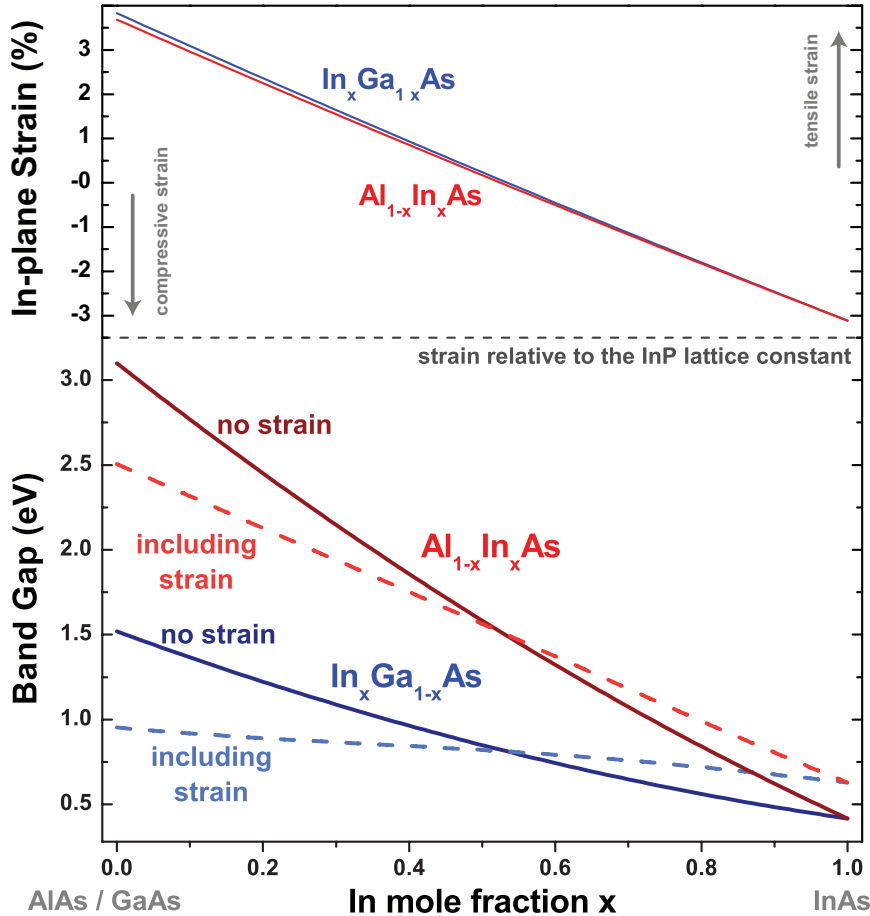


Figure 2.3: Bandgap strain dependence. The top panel shows in-plane strain ε_{xx} relative to the InP lattice constant (at 300 K) for $\text{In}_x\text{Ga}_{1-x}\text{As}$ and $\text{Al}_{1-x}\text{In}_x\text{As}$ of mole fraction x . The bottom panel compares the effect of strain on bandgap for the same materials compositions. Bandgap calculations where strain is ignored—that is, bandgaps only dependent upon material compositions—are shown as solid lines. (Here, $\mathcal{E}_{\text{C-LH}}^{\Gamma}$ and $\mathcal{E}_{\text{C-HH}}^{\Gamma}$ are degenerate when strain is zero.) Calculations for $\mathcal{E}_{\text{C-LH}}^{\Gamma}$ that apply a correction for in-plane strain are shown as dashed lines. The correction $\delta\mathcal{E}_{\text{Varsh}}$ is not included here.

where each of the terms F , \mathcal{E}_P , u , v , \mathcal{E}_q , $\mathcal{E}_{\text{C-LH}}^{\Gamma}$, and $\mathcal{E}_{\text{C-SO}}^{\Gamma}$ have z -dependence. The free electron mass is m_0 , F is the Kane parameter representing the second-order $\mathbf{k} \cdot \mathbf{p}$ perturbation term, \mathcal{E}_P is the energy-unit representation of the momentum matrix element between the s -like conduction bands and p -like valence bands, \mathcal{E}_q is the energy of the quantized energy state above or below the conduction band, and u and

ν represent the degree of mixing between LH and SO states and are give as

$$u = \frac{2\sqrt{2}|Q_\varepsilon|}{C} \quad \text{and} \quad \nu = \frac{(A - B)|Q_\varepsilon|}{CQ_\varepsilon} \quad (2.18)$$

with

$$A = \Delta_{SO} + Q_\varepsilon, \quad B = \sqrt{\Delta_{SO}^2 + 2\Delta_{SO}Q_\varepsilon + 9Q_\varepsilon^2}, \quad \text{and} \quad C = \sqrt{2B(B - A)}. \quad (2.19)$$

In the case of no strain, $u = 1$ and $\nu = 0$. Moreover, for in-plane strain values up to $\sim 2\%$, $u \approx 1$ and $\nu \approx 0$ so

$$\frac{1}{m^*(z, \mathcal{E}_q)} = \frac{1}{m_0} \left\{ 1 + 2F + \frac{\mathcal{E}_P}{3} \left[\frac{2}{\mathcal{E}_q + \mathcal{E}_{C-LH}^\Gamma} + \frac{1}{\mathcal{E}_q + \mathcal{E}_{C-SO}^\Gamma} \right] \right\} \quad (2.20)$$

is a good approximation. Both \mathcal{E}_P and F are well-reviewed for III–V materials by Vurgaftman *et al.* [29], and they are generally considered to be independent of strain and temperature. Using Eq. (2.17) or (2.20), the energy dependence of the effective mass in a quantum well (*i.e.* non-parabolicity) [27], [39] is taken into account by virtue of \mathcal{E}_q . Also, the effects of strain and temperature on effective mass are accounted for by their effects on the bandgaps $\mathcal{E}_{C-LH}^\Gamma$ and $\mathcal{E}_{C-SO}^\Gamma$.

2.4 Self-consistent Solutions of the Schrödinger and Poisson Equations

Knowing the energy gaps and band offsets of our materials system, we can calculate the semiconductor material potential profile $V_{mat}(z)$. However, when semiconductors are doped, the fixed and free charges (ionized impurities and free electrons, respectively) that make up a charge distribution ρ add a perturbation to the potential profile. Given by the Poisson equation, this perturbation V_ρ is

$$\nabla^2 V_\rho = -\frac{\rho}{\epsilon} \quad (2.21)$$

where $\epsilon = \epsilon_r \epsilon_0$ is the material permittivity. The potential $V_\rho(z)$ can otherwise be found through the electric field strength $E(z)$:

$$V_\rho(z) = \int_{-\infty}^z E(z) dz . \quad (2.22)$$

With our system of energy states quantized in one dimension (z), and our wavefunctions $\psi(z)$ numerically solved at discrete points with spacing δz , we can think of the charge density $\rho(z)$ as infinite sheets, with sheet density $\sigma(z)$ and thickness δz (similar to the process outlined by Harrison [28]). The resultant perpendicular electric field to an infinite plane of charge is

$$E = \frac{\sigma}{2\epsilon} \quad (2.23)$$

and we can thus sum the contributions to the aggregate electric field from all of the individual “slices” of δz as

$$E(z) = - \sum_{z'=-\infty}^{z-\delta z} \frac{\sigma(z')}{2\epsilon} + \sum_{z'=z}^{\infty} \frac{\sigma(z')}{2\epsilon} \quad (2.24)$$

which accounts for the sign of the field being dependent on the location of the position z relative to the position of the charge slice z' . The sheet charge density $\sigma(z)$ includes both negative free electron charge and positive ionized impurity charge. For a doping density profile $N_d(z)$ [$\frac{1}{\text{volume}}$], the total free electron sheet density n_s [$\frac{1}{\text{area}}$] will be given by

$$n_s = \int_{-\infty}^{+\infty} N_d(z) dz \quad (2.25)$$

and the fixed charge sheet density is $N_d(z)\delta z$. The net sheet charge density is thus

$$\sigma(z) = q [N_d(z)\delta z - n_s \psi_i^*(z)\psi_i(z)] \quad (2.26)$$

where q is the absolute value of the electron charge ($q = |q|$). It is important to note that Eq. (2.26) holds only if all free electrons are in the quantum state i . If all electrons are not in a single quantum state (*i.e.* $T \neq 0$ K), we can distribute them over the set of relevant states using the Fermi distribution as a weighting function. For the quantum state i at

energy \mathcal{E}_i , the Fermi distribution is

$$f(\mathcal{E}_i) = \frac{1}{e^{\frac{(\mathcal{E}_i - \mathcal{E}_0) - \mathcal{E}_F(T)}{k_B T}} + 1} \quad (2.27)$$

where \mathcal{E}_0 is the energy of the lowest state in the QC period (the injector ground state, for example) and $\mathcal{E}_F(T)$ is the Fermi energy at temperature T given by [40]

$$\mathcal{E}_F(T) = k_B T \ln \left(e^{\frac{\mathcal{E}_F(0)}{k_B T}} - 1 \right) \quad (2.28)$$

and

$$\mathcal{E}_F(0) = n_s \frac{\pi \hbar^2}{m^*}. \quad (2.29)$$

Now, for n_s electrons thermally distributed over quantum states 1 through n , the population in state i can be determined by the weighting coefficient ξ_i such that

$$\xi_i = \frac{f(\mathcal{E}_i)}{\sum_{i=1}^n f(\mathcal{E}_i)} \quad (2.30)$$

and

$$n_i = \xi_i n_s \quad (2.31)$$

so long as we ensure that the individual weighting coefficients sum to one ($\sum_{i=1}^n \xi_i = 1$). Our sheet charge density now becomes

$$\sigma(z) = q \left[N_d(z) \delta z - \sum_{i=1}^n \xi_i n_s \psi_i^*(z) \psi_i(z) \right] \quad (2.32)$$

for the electron-occupied set of quantum states 1 through n .

Following the above procedure to find the charge potential V_ρ , we can apply this correction as a perturbation to the overall potential: $V_c(z) = V_{mat}(z) + V_\rho(z)$. We can then solve our system using Eq. (2.6) and the shooting method described previously with the new composite potential. Certainly, the perturbation from V_ρ changes the solution to the system enough that a new V_ρ can be calculated based on the shifted electron wavefunctions. Thus, an iterative approach is needed, where V_ρ is updated after each iteration until consecutive solutions converge. Ergo, a self-consistent solution.

2.5 Spontaneous Emission Rate and the Optical Dipole Matrix Element

The optical transition rate W_{opt} between two eigen states of a system, such as an upper state ψ_c^u and lower state ψ_c^ℓ , is given by first order perturbation theory (Fermi's golden rule) as [41]

$$W_{opt}^{\vec{k},\vartheta} = \frac{2\pi}{\hbar} |\langle \psi_c^\ell, \mathcal{N}_{\vec{k},\vartheta}^\ell | \mathcal{H}' | \psi_c^u, \mathcal{N}_{\vec{k},\vartheta}^u \rangle|^2 \delta(\mathcal{E}_u - \mathcal{E}_\ell - \mathcal{E}_{\vec{k}}) \quad (2.33)$$

for the optical mode with wavevector \vec{k} and polarization ϑ , where the interaction Hamiltonian \mathcal{H}' is the light-matter perturbation responsible for the transition and the terms $\mathcal{N}_{\vec{k},\vartheta}^u$ and $\mathcal{N}_{\vec{k},\vartheta}^\ell$ represent quantized states (number of photons) of the electromagnetic field. The total Hamiltonian that includes the light-matter interaction for an electron in the conduction band is given as [41]

$$\mathcal{H} = \frac{(\vec{\mathcal{P}} - q\mathbf{A})^2}{2m^*} + qV_c(\vec{r}) \quad (2.34)$$

where $\vec{\mathcal{P}}$ is the momentum operator in three dimensions, \vec{r} is a position vector, and assuming for the moment a constant effective mass m^* . Taking \mathbf{A} to be the vector potential of the optical field in the Coulomb gauge so that $\nabla \cdot \mathbf{A} = 0$, Eq. (2.34) becomes

$$\mathcal{H} = \frac{\vec{\mathcal{P}}^2}{2m^*} - \frac{q}{m^*} (\mathbf{A} \cdot \vec{\mathcal{P}}) + \frac{q^2}{2m^*} A^2 + qV_c(\vec{r}) \quad (2.35)$$

after also using the commutation $[\vec{\mathcal{P}}, \mathbf{A}] = 0$ for the Coulomb gauge [41]. We may assume that the term in A^2 is negligible given sufficiently small optical field intensity and matrix elements of $\vec{\mathcal{P}}$ [42]; that is, we ignore two photon processes [43]. Thus, our interaction Hamiltonian \mathcal{H}' is

$$\mathcal{H}' = -\frac{q}{m^*} (\mathbf{A} \cdot \vec{\mathcal{P}}) \quad (2.36)$$

given that the remainder of Eq. (2.35) is the unperturbed Hamiltonian

$$\mathcal{H}_0 = \frac{\vec{\mathcal{P}}^2}{2m^*} + qV_c(\vec{r}) . \quad (2.37)$$

Applying Eq. (2.36) to Eq. (2.33), the optical transition rate is

$$W_{opt}^{\vec{k},\vartheta} = \frac{2\pi}{\hbar} \frac{q^2}{m^{*2}} |\langle \psi_c^\ell, \mathcal{N}_{\vec{k},\vartheta}^\ell | \mathbf{A} \cdot \vec{\mathcal{P}} | \psi_c^u, \mathcal{N}_{\vec{k},\vartheta}^u \rangle|^2 \delta(\mathcal{E}_u - \mathcal{E}_\ell - \mathcal{E}_{\vec{k}}). \quad (2.38)$$

The operator form of the vector potential \mathbf{A} is derived using a plane wave expansion for a cavity with mode volume $\mathcal{V}_{\vec{k}}$ and permittivity ϵ as [43]

$$\mathbf{A}(\vec{r}) = \sum_{\vec{k},\vartheta} \sqrt{\frac{\hbar}{2\epsilon\omega_{\vec{k}}\mathcal{V}_{\vec{k}}}} [\hat{b}_{\vec{k},\vartheta}^\dagger e^{-i\vec{k}\cdot\vec{r}} + \hat{b}_{\vec{k},\vartheta} e^{i\vec{k}\cdot\vec{r}}] \hat{e}_{\vec{k},\vartheta} \quad (2.39)$$

where $\hat{e}_{\vec{k},\vartheta}$ is the unit vector for the photon mode, $\hat{b}_{\vec{k},\vartheta}^\dagger$ and $\hat{b}_{\vec{k},\vartheta}$ are the photon creation and annihilation operators, and the term $\sqrt{\frac{\hbar}{2\epsilon\omega_{\vec{k}}}}$ provides MKS units. We now invoke the dipole approximation, which treats the photon wavelength as being large compared to the space over which the optical transition occurs [43]. One result of the dipole approximation—with $|\vec{k}| = \frac{2\pi}{\lambda} \approx 10^6 \text{ m}^{-1}$ and the electron confinement space in the QC active region $|\vec{r}| \approx 10^{-8} \text{ m}$ —is that $e^{i\vec{k}\cdot\vec{r}} \approx 1$. Also, using the relation $\mathcal{N}_{\vec{k},\vartheta}^\ell = \mathcal{N}_{\vec{k},\vartheta}^u + 1$ since a photon is created in the transition $|\psi_c^u\rangle \rightarrow |\psi_c^\ell\rangle$,

$$\langle \mathcal{N}_{\vec{k},\vartheta}^u + 1 | \hat{b}_{\vec{k},\vartheta}^\dagger | \mathcal{N}_{\vec{k},\vartheta}^u \rangle = \sqrt{\mathcal{N}_{\vec{k},\vartheta}^u + 1} \langle \mathcal{N}_{\vec{k},\vartheta}^u + 1 | \mathcal{N}_{\vec{k},\vartheta}^u + 1 \rangle = \sqrt{\mathcal{N}_{\vec{k},\vartheta}^u + 1} \quad (2.40a)$$

and

$$\langle \mathcal{N}_{\vec{k},\vartheta}^u + 1 | \hat{b}_{\vec{k},\vartheta} | \mathcal{N}_{\vec{k},\vartheta}^u \rangle = \sqrt{\mathcal{N}_{\vec{k},\vartheta}^u} \langle \mathcal{N}_{\vec{k},\vartheta}^u + 1 | \mathcal{N}_{\vec{k},\vartheta}^u - 1 \rangle = 0. \quad (2.40b)$$

Finally, we can make the approximation that $\vec{\mathcal{P}}$ affects only the electron momentum, which is accurate in our low photon field approximation. In this case, $\mathbf{A} \cdot \vec{\mathcal{P}}$ is separable so that $\langle \psi_c^\ell | \vec{\mathcal{P}} | \psi_c^u \rangle \cdot \langle \mathcal{N}_{\vec{k},\vartheta}^\ell | \mathbf{A} | \mathcal{N}_{\vec{k},\vartheta}^u \rangle$ and Eq. (2.38) becomes

$$W_{opt}^{\vec{k},\vartheta} = \frac{\pi q^2}{\epsilon m^{*2} \mathcal{V}_{\vec{k}}} \frac{(\mathcal{N}_{\vec{k},\vartheta}^u + 1)}{\omega_{\vec{k}}} |\hat{e}_{\vec{k},\vartheta} \cdot \langle \psi_c^\ell | \vec{\mathcal{P}} | \psi_c^u \rangle|^2 \delta(\mathcal{E}_u - \mathcal{E}_\ell - \mathcal{E}_{\vec{k}}) \quad (2.41)$$

for a single optical mode. Now, by applying the commutation relation [41]

$$\vec{\mathcal{P}} = \frac{im^*}{\hbar} [\mathcal{H}_0, \vec{r}] \quad (2.42)$$

we get

$$\langle \psi_c^\ell | \vec{\mathcal{P}} | \psi_c^u \rangle = \frac{im^*}{\hbar} \langle \psi_c^\ell | \mathcal{H}_0 \cdot \vec{r} - \vec{r} \cdot \mathcal{H}_0 | \psi_c^u \rangle = im^* \omega_0 \langle \psi_c^\ell | \vec{r} | \psi_c^u \rangle \quad (2.43)$$

and so

$$W_{opt}^{\vec{k},\vartheta} = \frac{\pi q^2}{\epsilon \mathcal{V}_{\vec{k}}} \left(\mathcal{N}_{\vec{k},\vartheta}^u + 1 \right) \omega_0 |\hat{e}_{\vec{k},\vartheta} \cdot \langle \psi_c^\ell | \vec{r} | \psi_c^u \rangle|^2 \delta(\mathcal{E}_u - \mathcal{E}_\ell - \mathcal{E}_{\vec{k}}). \quad (2.44)$$

From here, we can distinguish two contributions to the optical transition rate: those of stimulated emission $W_{stim}^{\vec{k},\vartheta}$ due to the presence of an inducing field proportional to $\mathcal{N}_{\vec{k},\vartheta}^u$ and spontaneous emission $W_{spon}^{\vec{k},\vartheta}$ due to zero-point field such that

$$W_{opt}^{\vec{k},\vartheta} = W_{stim}^{\vec{k},\vartheta} + W_{spon}^{\vec{k},\vartheta}. \quad (2.45)$$

Since the wavefunctions ψ_c^u and ψ_c^ℓ have quantization only in the z direction, we can further simplify to

$$W_{stim}^{\vec{k},\vartheta} = \frac{\pi q^2}{\hbar \epsilon \mathcal{V}_{\vec{k}}} \omega_0 z_{u\ell}^2 |\hat{e}_{\vec{k},\vartheta} \cdot \hat{z}|^2 \delta(\omega_0 - \omega_{\vec{k}}) \mathcal{N}_{\vec{k},\vartheta}^u \quad (2.46a)$$

$$W_{spon}^{\vec{k},\vartheta} = \frac{\pi q^2}{\hbar \epsilon \mathcal{V}_{\vec{k}}} \omega_0 z_{u\ell}^2 |\hat{e}_{\vec{k},\vartheta} \cdot \hat{z}|^2 \delta(\omega_0 - \omega_{\vec{k}}) \quad (2.46b)$$

where \hat{z} is the unit vector in the z direction, the optical dipole matrix element $z_{u\ell}$ is defined as

$$z_{u\ell} \equiv \langle \psi_c^\ell | z | \psi_c^u \rangle \quad (2.47)$$

and the transformation $\mathcal{E}_u - \mathcal{E}_\ell = \hbar \omega_0$ has been used.

Concentrating now just on the spontaneous emission, the total spontaneous emission rate is realized by summing over all modes in the optical cavity. Equivalently, we can integrate over the product of all possible modes and the density of the cavity photon modes \mathcal{D} .

$$W_{spon} = \sum_{\vec{k},\vartheta} W_{spon}^{\vec{k},\vartheta} = \int \int \int W_{spon}^{\vec{k},\vartheta} \times \mathcal{D}(\omega_{\vec{k}}) d^3 \omega_{\vec{k}} \quad (2.48)$$

For an arbitrarily shaped electromagnetic enclosure where the dimensions are at least a few times the transition wavelength [44], the differential mode density $\mathcal{D}_{3D}(\omega_{\vec{k}})d^3\omega_{\vec{k}}$ is given in spherical coordinates as [45]

$$\mathcal{D}_{3D}(\omega_{\vec{k}})d^3\omega_{\vec{k}} = \frac{d^3\omega_{\vec{k}}}{\frac{8\pi^3}{\mathcal{V}_{\vec{k}}}} = \frac{\mathcal{V}_{\vec{k}}}{8\pi^3} k^2 \sin\theta d\vec{k} d\theta d\phi = \frac{n_{eff}^3}{c_0^3} \frac{\mathcal{V}_{\vec{k}}}{8\pi^3} \omega_{\vec{k}}^2 \sin\theta d\omega_{\vec{k}} d\theta d\phi \quad (2.49)$$

where n_{eff} is the effective refractive index of the mode, c_0 is the speed of light in vacuum, θ is the zenith angle from the positive z -axis, and ϕ is the azimuth angle from the positive x -axis. Combining Eqs. (2.46b) and (2.49) into Eq. (2.48) gives

$$W_{spon} = \frac{q^2 n_{eff}^3 \omega_0}{8\pi^2 \hbar \epsilon c_0^3} z_{u\ell}^2 \int_0^\infty \omega_{\vec{k}}^2 \delta(\omega_0 - \omega_{\vec{k}}) d\omega_{\vec{k}} \int_0^{2\pi} \int_0^\pi |\hat{e}_{\vec{k},\vartheta} \cdot \hat{z}|^2 \sin\theta d\theta d\phi. \quad (2.50)$$

For the two orthogonal polarizations $\hat{e}_{\vec{k},\vartheta=1}$ and $\hat{e}_{\vec{k},\vartheta=2}$, we can choose $\hat{e}_{\vec{k},\vartheta=1}$ to lie in the plane of \hat{z} and k_z so that $|\hat{e}_{\vec{k},\vartheta=2} \cdot \hat{z}|^2 = 0$. Using $|\hat{e}_{\vec{k},\vartheta} \cdot \hat{z}|^2 = \sin^2\theta$ and $\epsilon = n_{eff}^2 \epsilon_0$, the spontaneous emission rate is [42] [43] [44] [46]

$$W_{spon} = \frac{1}{\tau_{spon}} = \frac{q^2 n_{eff} \omega_0^3}{3\pi \hbar \epsilon_0 c_0^3} z_{u\ell}^2 \quad (2.51)$$

where τ_{spon} is the spontaneous emission lifetime.

Normalization of the wavefunctions ψ_c

To this point in our derivation of τ_{spon} , we have assumed an effective mass m^* that is constant with energy. We now appropriately account for the variable effective mass with proper normalization the wavefunctions ψ_c that are used to calculate our optical dipole matrix element $z_{u\ell}$.

In previous sections, our solutions for conduction band eigenstates ψ_c have used the envelope function Hamiltonian in the Kane approximation [47]. In the Kane approximation, the full system Hamiltonian is projected onto the individual subbands (conduction band, light hole band, etc.). If the in-plane electron momentum is assumed to vanish, the total stationary wavefunction is given by the three components ψ_c , ψ_{LH} , and ψ_{SO} , weighted with their corresponding Bloch functions [27]. Consequently, knowledge of

only the conduction component ψ_c is insufficient for the complete physical description of the stationary state, and the stationary state is thus normalized as [27]

$$\langle \psi_c | \psi_c \rangle + \langle \psi_{\text{LH}} | \psi_{\text{LH}} \rangle + \langle \psi_{\text{SO}} | \psi_{\text{SO}} \rangle = 1 \quad (2.52)$$

However, just as our calculation of the energy-dependent effective mass in Eq. (2.17) included the conduction band interaction with the valence bands, we can likewise recast Eq. (2.52) entirely in terms of ψ_c as [27]

$$\langle \psi_c | 1 + \frac{2}{3} \mathcal{P}_z \frac{\mathcal{E}_P}{2m_0 (\mathcal{E}_q + \mathcal{E}_{\text{LH}}^\Gamma)^2} \mathcal{P}_z + \frac{1}{3} \mathcal{P}_z \frac{\mathcal{E}_P}{2m_0 (\mathcal{E}_q + \mathcal{E}_{\text{SO}}^\Gamma)^2} \mathcal{P}_z | \psi_c \rangle = 1. \quad (2.53)$$

Defining the average valence band energy as $\mathcal{E}_v = \frac{2\mathcal{E}_{\text{LH}} + \mathcal{E}_{\text{SO}}}{3}$, we may further simplify Eq. (2.53) and approximate it as [48]

$$\langle \psi_c | 1 + \frac{\mathcal{P}_z^2}{2m^*(\mathcal{E}_q)(\mathcal{E}_q + \mathcal{E}_v)} | \psi_c \rangle = 1 \quad (2.54)$$

or equivalently

$$\langle \psi_c | 1 + \frac{\mathcal{E}_q}{\mathcal{E}_q + \mathcal{E}_v} | \psi_c \rangle = 1. \quad (2.55)$$

2.6 Stimulated Emission Probability and the Transition Cross Section

In the previous section, we derived the probability of stimulated emission for a single optical mode \vec{k} as

$$W_{\text{stim}}^{\vec{k}, \theta} = \frac{\pi q^2}{\hbar e \mathcal{V}_{\vec{k}}} \omega_{\vec{k}} z_{u\ell}^2 |\hat{e}_{\vec{k}, \theta} \cdot \hat{z}|^2 \delta(\omega_0 - \omega_{\vec{k}}) \mathcal{N}_{\vec{k}, \theta}^u \quad (2.56)$$

In general, the transition frequency ω_0 is not a single value, but is instead broadened. We thus substitute $\delta(\omega_0 - \omega_{\vec{k}})$ for the normalized Lorentzian lineshape function $\mathcal{L}(\nu)$ given as

$$\mathcal{L}(\nu) = \frac{\frac{\delta\nu}{2\pi}}{(\nu_0 - \nu)^2 + \left(\frac{\delta\nu}{2}\right)^2} \quad (2.57)$$

and then integrate over ν . Now, the stimulated emission probability becomes [42]

$$W_{stim}^{\vec{k},\vartheta} = \frac{\pi q^2 z_{ul}^2 \mathcal{N}_{\vec{k},\vartheta}}{h \mathcal{V}_{\vec{k}}} \mathcal{L}(\nu) \quad (2.58)$$

We can also now relate the number of mode photons $\mathcal{N}_{\vec{k},\vartheta}$ to a photon mode flux ϕ_{ph} [$\frac{\text{photons}}{\text{area} \times \text{time}}$] using the group velocity v_g where

$$\phi_{ph} = \frac{v_g}{\mathcal{V}_{\vec{k}}} \mathcal{N}_{\vec{k},\vartheta} \quad (2.59)$$

so that [42]

$$W_{stim} = \phi_{ph} \frac{3\lambda_0^2}{8\pi\tau_{spon}} \mathcal{L}(\nu) \quad (2.60)$$

where Eq. (2.51) is used to eliminate z_{ul}^2 . The factor of 3 results from the polarization of the cavity mode [49]. Now, a useful quantity known as the transition cross section $\sigma(\nu)$ [area] and defined as [45]

$$W_{stim} = \phi_{ph} \sigma(\nu) \quad (2.61)$$

is given by

$$\sigma(\nu) = \frac{2\pi^2 q^2 \mathcal{E}_{ph}}{h^2 c \epsilon_0 n_{eff}} z_{ul}^2 \mathcal{L}(\nu) \quad (2.62)$$

and $\sigma(\nu_0) = \sigma_0$ where ν_0 is the lasing frequency at the photon energy \mathcal{E}_{ph} is

$$\sigma_0 = \frac{4\pi q^2}{h c \epsilon_0 n_{eff}} \frac{\mathcal{E}_{ph}}{\delta \mathcal{E}_{ul}} z_{ul}^2. \quad (2.63)$$

2.7 LO-phonon Scattering Time

The fastest scattering process between energy states within the same band of semiconductor quantum wells is the non-radiative longitudinal optical (LO) phonon transition [50]. Because it is the fastest transition process, quantifying the LO phonon lifetime becomes particularly relevant for QC laser design. Charge carrier interaction with the electric polarization produced by the relative displacement of the positive and negative ions of polar semiconductors is referred to as the Fröhlich interaction. The Fröhlich

Hamiltonian \mathcal{H}_F is given as

$$\mathcal{H}_F = \sum_{\mathbf{Q}} \sqrt{\frac{2\pi\hbar\omega_{\text{LO}}q^2}{(\epsilon_{\infty} - \epsilon_s)\mathcal{V}_Q Q^2}} e^{-i\mathbf{Q}\cdot\mathbf{r}} a_{\mathbf{Q}}^{\dagger} \quad (2.64)$$

where $\hbar\omega_{\text{LO}}$ is the LO phonon energy, ϵ_{∞} is the high frequency relative permittivity, ϵ_s is the static relative permittivity, \mathcal{V}_Q is the volume of the system, Q is the magnitude of the phonon wavevector \mathbf{Q} , \mathbf{r} is the position vector, and $a_{\mathbf{Q}}^{\dagger}$ is the creation operator for a phonon in the mode \mathbf{Q} . Using Fermi's golden rule, the LO phonon lifetime $\tau_{u\ell}$ between an initial (upper) state $|u, \mathbf{k}_u\rangle$ and final (lower) state $|\ell, \mathbf{k}_{\ell}\rangle$ with electron wavevector \mathbf{k} at $T = 0$ K is then

$$\frac{1}{\tau_{u\ell}} = \frac{\sqrt{m^*(\mathcal{E}_u)m^*(\mathcal{E}_{\ell})}q^2\omega_{\text{LO}}}{2\hbar^2(\epsilon_{\infty} - \epsilon_s)} \int_0^{2\pi} \frac{\int_{-\infty}^{+\infty} \int_{-\infty}^{+\infty} \psi_c^u(z)\psi_c^{\ell}(z)e^{-Q|z-z'|}\psi_c^u(z')\psi_c^{\ell}(z') dz dz'}{Q} \sin\theta d\theta \quad (2.65)$$

where Q is given by

$$Q = \sqrt{k_u^2 + k_{\ell}^2 - 2k_u k_{\ell} \cos\theta} \quad (2.66)$$

and k_u and k_{ℓ} are related by

$$k_{\ell}^2 = \frac{m^*(\mathcal{E}_{\ell})}{m^*(\mathcal{E}_u)} k_u^2 + \frac{2m^*(\mathcal{E}_{\ell})}{\hbar^2} (\mathcal{E}_{u\ell} - \hbar\omega_{\text{LO}}) . \quad (2.67)$$

If we assume the electron initially starts at wavevector $k_u = 0$, then

$$k_{\ell} = \sqrt{\frac{2m^*(\mathcal{E}_{\ell})}{\hbar^2} (\mathcal{E}_{u\ell} - \hbar\omega_{\text{LO}})} \quad (2.68)$$

and $Q = k_{\ell}$ so Eq. (2.65) simplifies to

$$\frac{1}{\tau_{u\ell}} = \frac{\sqrt{m^*(\mathcal{E}_u)m^*(\mathcal{E}_{\ell})}q^2\omega_{\text{LO}}}{2\hbar^2(\epsilon_{\infty} - \epsilon_s)} \int_{-\infty}^{+\infty} \int_{-\infty}^{+\infty} \frac{\psi_c^u(z)\psi_c^{\ell}(z)e^{-k_{\ell}|z-z'|}\psi_c^u(z')\psi_c^{\ell}(z')}{k_{\ell}} dz dz' . \quad (2.69)$$

The temperature dependence of $\tau_{u\ell}$ is attained by modifying the $T = 0$ K rate using the Bose-Einstein occupation number for phonons of energy $\hbar\omega_{\text{LO}}$. Specifically, taking

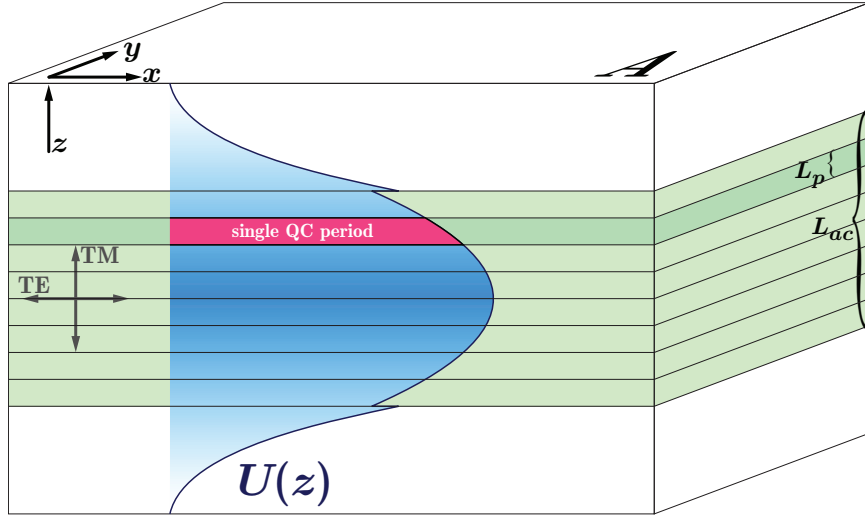


Figure 2.4: Sketch of waveguide geometry. A one dimensional optical mode profile (TM polarization) is shown as $U(z)$. Multiple QC periods with higher refractive index than the surrounding cladding confine the mode, and the reduced field intensity for off-center QC periods is seen. The arrows labeled TM and TE show direction of the electric field vector for the respective polarization.

into account both phonon emission and absorption processes [50],

$$\frac{1}{\tau_{u\ell}(T)} = \frac{1}{\tau_{u\ell}(0)} \left(1 + \frac{2}{e^{\frac{\hbar\omega_{\text{LO}}}{k_B T}} - 1} \right). \quad (2.70)$$

2.8 Rate Equations for QC Lasers

Rate equations are a phenomenological method for describing laser devices from which important performance parameters (*e.g.* output power, wall-plug efficiency, threshold, etc.) can be derived. Before directly discussing rate equations for QC lasers, it is important to recognize some of their unique properties. These properties extend from the fact that QC lasers have multiple active–injector region periods of gain region within the QC core, and each individual period can have its own local properties of photon field intensity and temperature; each period can furthermore have individually-customized emission [51] and doping profiles [52] that can be treated accordingly by the rate equations. In the following discussion, we restrict ourselves to the case where the design

of individual QC periods is identical. In this case, we must concern ourselves only with the local field intensity and the local electron populations for each period.

In semiconductor lasers, field intensities in the gain region are usually treated through the use of confinement factor Γ , which is defined for the 1D case as [53]

$$\Gamma = \frac{\int_{z_0}^{z_0+L_{ac}} n_r(z) U(z) dz}{\int_{-\infty}^{+\infty} n_r(z) U(z) dz} \quad (2.71)$$

where z_0 marks the beginning of the active core, L_{ac} is the thickness of the active core, $n_r(z)$ is the refractive index profile, and $U(z)$ is the dimensionless mode intensity profile normalized such that $\max(U(z)) = 1$. The mode profile $U(z)$ can also be used to identify an “effective mode volume” \mathcal{V}_{ph} , here for the 1D case, such that

$$\mathcal{V}_{ph} = A \int_{-\infty}^{+\infty} U(z) dz \quad (2.72)$$

where A is the device area in the x and y dimensions, and so that the active core volume $\mathcal{V}_{ac} = AL_{ac}$. We now also have a 1D “mode thickness” L_{ph} analogous to the active core thickness L_{ac} given as

$$L_{ph} = \int_{-\infty}^{+\infty} U(z) dz. \quad (2.73)$$

In the typical set of rate equations describing diode lasers, which do not address the QC feature of a multiple gain region stack, it is commonly assumed that the gain profile is a square function over the active region, and so $\Gamma = \frac{L_{ac}}{L_{ph}}$; here, the refractive index profile $n_r(z)$ is also assumed to be constant. We will not make these assumptions in the following rate equation analysis for QC structures. Instead, we will use a “local field coefficient” \bar{U}_i for an individual QC period i given as

$$\bar{U}_i = \frac{\int_{z_i}^{z_i+L_p} n_r(z) U(z) dz}{\int_{z_i}^{z_i+L_p} n_r(z) dz} \quad (2.74)$$

where z_i marks the beginning of the QC period. For a QC structure with N_p identical periods, we have an active-injector period thickness L_p such that $L_{ac} = N_p L_p$ and an active-injector period volume \mathcal{V}_p such that $\mathcal{V}_{ac} = N_p \mathcal{V}_p$. If the active period thickness

L_p is sufficiently thin, $\bar{U}_i \approx U(z_i)$. We can relate \bar{U}_i to Γ by summing \bar{U}_i over all N_p .

$$\Gamma = \frac{L_{ac} \sum_{i=1}^{N_p} \bar{U}_i}{L_{ph}} \quad (2.75)$$

In QC structures, the local electron populations can be individually affected by such things as the local field intensity and the local temperature. Thus, in the following analysis, we will treat the energy state populations of each QC period individually. Describing the change with respect to time in the upper state population $\mathcal{N}_{u,i}$, lower state population $\mathcal{N}_{\ell,i}$, and *total* photon population \mathcal{N}_{ph} of the system gives the system of equations,

$$\mathcal{N}_{u,i} \frac{\text{change}}{\text{w.r.t. time}} = \frac{\text{non-radiative rate in}}{\text{rate out}} - \frac{\text{radiative transition rate}}{\text{rate out}} \quad (2.76a)$$

$$\mathcal{N}_{\ell,i} \frac{\text{change}}{\text{w.r.t. time}} = \frac{\text{non-radiative rate in}}{\text{rate out}} + \frac{\text{radiative transition rate}}{\text{rate out}} \quad (2.76b)$$

$$\mathcal{N}_{ph} \frac{\text{change}}{\text{w.r.t. time}} = \frac{\text{sum over all QC periods}}{\text{(radiative transition rate)}} - \frac{\text{photon loss rate}}{\text{loss rate}} \quad (2.76c)$$

where non-radiative transition rates are given by the population of the state $\mathcal{N}_{x,i}$ divided by the non-radiative lifetime τ_x for the energy state x . Radiative transition rates are given by

$$\text{radiative transition rate} = \left(\frac{\text{population available for stimulated emission}}{\text{population available for absorption}} - 1 \right) \times \frac{\text{probability of stimulated emission}}{\text{local field strength of mode}} \quad (2.77)$$

and

$$\text{probability of stimulated emission} = \frac{\text{photon density}}{\text{photon speed}} \times \frac{\text{transition cross-section}}{\text{local field strength of mode}} \cdot$$

Now, making Eq. (2.76) more explicit, our QC laser rate equations are thus generally expressed as

$$\frac{d\mathcal{N}_{u,i}}{dt} = \eta_{inj} \frac{I}{q} - \frac{\mathcal{N}_{u,i}}{\tau_u} - (\mathcal{N}_{u,i} - \mathcal{N}_{\ell,i}) \frac{\mathcal{N}_{ph}}{\mathcal{V}_{ph}} v_g \sigma_i \bar{U}_i \quad (2.77a)$$

$$\frac{d\mathcal{N}_{\ell,i}}{dt} = \frac{\mathcal{N}_{u,i}}{\tau_{u\ell}} - \frac{\mathcal{N}_{\ell,i}}{\tau_\ell} + (\mathcal{N}_{u,i} - \mathcal{N}_{\ell,i}) \frac{\mathcal{N}_{ph}}{\mathcal{V}_{ph}} v_g \sigma_i \bar{U}_i \quad (2.77b)$$

$$\frac{d\mathcal{N}_{ph}}{dt} = \sum_{i=1}^{N_p} \left[(\mathcal{N}_{u,i} - \mathcal{N}_{\ell,i}) \frac{\mathcal{N}_{ph}}{\mathcal{V}_{ph}} v_g \sigma_i \bar{U}_i \right] - \frac{\mathcal{N}_{ph}}{\tau_{ph}} \quad (2.77c)$$

where $\eta_{inj} \frac{I}{q}$ is the pumping rate for the upper laser state, τ_{ph} is the photon lifetime in the cavity, σ_i is the transition cross-section for the period i , and N_p is the total number of QC periods. The group velocity v_g is approximated by the phase velocity c_0/n_{eff} , which is accurate when dispersion is low. Rate equations are more traditionally represented in terms of population density N [$\frac{1}{\text{volume}}$] rather than the absolute population \mathcal{N} as above, so that we have

$$\frac{dN_{u,i}}{dt} = \eta_{inj} \frac{I}{q\mathcal{V}_p} - \frac{N_{u,i}}{\tau_u} - (N_{u,i} - N_{\ell,i}) N_{ph} v_g \sigma_0 \bar{U}_i \quad (2.78a)$$

$$\frac{dN_{\ell,i}}{dt} = \frac{N_{u,i}}{\tau_{u\ell}} - \frac{N_{\ell,i}}{\tau_\ell} + (N_{u,i} - N_{\ell,i}) N_{ph} v_g \sigma_0 \bar{U}_i \quad (2.78b)$$

$$\frac{dN_{ph}}{dt} = v_g \sigma_0 N_{ph} \frac{\mathcal{V}_{ac}}{\mathcal{V}_{ph}} \sum_{i=1}^{N_p} [(N_{u,i} - N_{\ell,i}) \bar{U}_i] - \frac{N_{ph}}{\tau_{ph}} \quad (2.78c)$$

where electron populations \mathcal{N}_u and \mathcal{N}_ℓ in Eq. (2.77) were divided by the active core gain region volume $\mathcal{V}_{ac} = AL_{ac}$, the photon population \mathcal{N}_{ph} divided by \mathcal{V}_{ph} , and we assume QC periods with identical design, so that $\sigma_i = \sigma_0$. Note that traditionally for diode lasers, $N_p = 1$, $\bar{U}_i = 1$, and $\Gamma = \frac{\mathcal{V}_{ac}}{\mathcal{V}_{ph}}$, so we recover the conventionally-written rate equations [35] [53] in that case.

For QC lasers, it is sometimes convenient to work with energy level populations in terms of sheet density n [$\frac{1}{\text{area}}$] such that $n_i = N_i L_p$. It is also common to work in terms of photon flux photon flux ϕ_{ph} [$\frac{1}{\text{area} \times \text{time}}$] instead of photon density N_{ph} [$\frac{1}{\text{volume}}$], so $N_{ph} = \frac{\phi_{ph}}{v_g}$.

$$\frac{dn_{u,i}}{dt} = \eta_{inj} \frac{J}{q} - \frac{n_{u,i}}{\tau_u} - (n_{u,i} - n_{\ell,i}) \phi_{ph} \sigma_0 \bar{U}_i \quad (2.79a)$$

$$\frac{dn_{\ell,i}}{dt} = \frac{n_{u,i}}{\tau_{u\ell}} - \frac{n_{\ell,i}}{\tau_\ell} + (n_{u,i} - n_{\ell,i}) \phi_{ph} \sigma_0 \bar{U}_i \quad (2.79b)$$

$$\frac{d\phi_{ph}}{dt} = v_g \sigma_0 \phi_{ph} \frac{1}{L_{ph}} \sum_{i=1}^{N_p} [(n_{u,i} - n_{\ell,i}) \bar{U}_i] - \frac{\phi_{ph}}{\tau_{ph}} \quad (2.79c)$$

2.9 Threshold Current & Modal Gain

Using our rate equations in Eq. (2.79), we can solve for threshold current density J_{th} by taking steady state solutions of the rate equations ($\frac{d(\cdot)}{dt} = 0$) and taking $\phi_{ph} = 0$. Applied to Eq. (2.79c), we find

$$\sum_{i=1}^{N_p} [(n_{u,i} - n_{\ell,i})] = \frac{1}{\tau_{ph} v_g \sigma_0 \frac{1}{L_{ph}} \sum_{i=1}^{N_p} \bar{U}_i} \quad (2.80)$$

which can be simplified to

$$n_u - n_\ell = \frac{L_{ac}}{\tau_{ph} v_g \sigma_0 N_p \Gamma} \quad (2.81)$$

if we now make the assumption of identical populations among all QC periods and incorporate Eq. (2.75). Now again taking the steady state solutions and $\phi_{ph} = 0$ for Eqs. (2.79a) and (2.79b), we yield our population inversion in terms of pumping rate and non-radiative lifetimes.

$$n_u - n_\ell = \eta_{inj} \frac{J}{q L_p} \tau_u \left(1 - \frac{\tau_\ell}{\tau_{u\ell}} \right) \quad (2.82)$$

which is our population inversion in terms of pumping rate R_{pump} where

$$R_{pump} = \eta_{inj} \frac{J}{q L_p} \quad (2.83)$$

and the effective upper state non-radiative lifetime τ_{eff} where

$$\tau_{eff} = \tau_u \left(1 - \frac{\tau_\ell}{\tau_{u\ell}} \right). \quad (2.84)$$

Combining Eqs. (2.81) and (2.82), our threshold current density is

$$J_{th} = \frac{qL_{ac}}{\eta_{inj}\tau_{eff}\tau_{ph}v_g\sigma_0N_p\Gamma} \quad (2.85)$$

where a number of substitutions and simplifications will be useful. The photon lifetime τ_{ph} can be given in terms of the mirror loss α_m and waveguide loss α_w [$\frac{1}{\text{length}}$]

$$\frac{1}{\tau_{ph}} = v_g(\alpha_m + \alpha_w) \quad (2.86)$$

or equivalently in terms of total loss α_{tot} where $\alpha_{tot} = \alpha_m + \alpha_w$. We also take $\eta_{inj} = 1$ and apply Eq. (2.63) for σ_0 to arrive at

$$J_{th} = \frac{\alpha_m + \alpha_w}{\frac{4\pi q}{hc_0\epsilon_0 n_{eff}} \frac{\mathcal{E}_{ul}}{\delta\mathcal{E}_{ul}} \frac{1}{L_p} \tau_{eff} z_{ul}^2 \Gamma}. \quad (2.87)$$

Threshold current density is often simplified by incorporating a gain coefficient g [$\frac{\text{length}}{\text{current}}$] given as

$$g = \frac{4\pi q}{hc_0\epsilon_0 n_{eff}} \frac{\mathcal{E}_{ul}}{\delta\mathcal{E}_{ul}} \frac{1}{L_p} \tau_{eff} z_{ul}^2 \quad (2.88)$$

or equivalently

$$g = \sigma_0 \frac{\tau_{eff}}{qL_p} \quad (2.89)$$

so that

$$J_{th} = \frac{\alpha_m + \alpha_w}{g\Gamma}. \quad (2.90)$$

Another common way to represent gain is as modal gain γ [length] defined such that light intensity \mathcal{I} after some distance L is given by

$$\mathcal{I}(L) = \mathcal{I}(0)e^{\gamma\Gamma L} \quad (2.91)$$

which is also equivalent to $\alpha_m + \alpha_w = \gamma\Gamma$ due to gain clamping [45]. Thus, given in terms of the threshold pumping current J_{th} and the transition cross-section σ_0 , modal gain is

$$\gamma = J_{th}g = \frac{J_{th}}{qL_{ac}} N_p \sigma_0 \tau_{eff}. \quad (2.92)$$

2.10 Slope Efficiency

Slope efficiency is the change in output power with current, $\frac{dP}{dI}$. From our rate equations, we have something close to power and current; we have terms of photon flux ϕ_{ph} and current density J . We can therefore solve for $\frac{d\phi_{ph}}{dJ}$ and convert to slope efficiency

$$\text{slope efficiency} = \frac{\text{change in}}{\text{current}} \left(\frac{\text{number of cavity photons}}{\text{pump current}} \right) \times \text{photon energy} \times \text{escape rate}$$

so

$$\frac{dP}{dI} = \frac{d\phi_{ph}}{dJ} \frac{\frac{V_m}{v_g}}{A} \times \mathcal{E}_{ph} \times \frac{1}{\tau_m}. \quad (2.93)$$

where the photon escape rate $\frac{1}{\tau_m}$ is

$$\frac{1}{\tau_m} = v_g \alpha_m. \quad (2.94)$$

To simplify the analysis, we will first look at the case of identical QC periods (*i.e.* all $\bar{U}_i = 1$ and all $n_{u,i}$ and $n_{\ell,i}$ are the same). To solve for $\phi_{ph}(J)$, we can start by solving for the steady state condition of Eq. (2.79c), $\frac{d\phi_{ph}}{dt} = 0$:

$$n_u - n_\ell = \frac{L_{ph}}{\tau_{ph} v_g \sigma_0 N_p}. \quad (2.95)$$

To find a relation for $n_u - n_\ell$, we solve the steady state conditions of Eqs. (2.79a) and (2.79b), and recover for n_u and n_ℓ , respectively,

$$n_u = \eta_{inj} \frac{J}{q} \frac{\frac{1}{\tau_\ell} + \sigma_0 \phi_{ph}}{\frac{1}{\tau_u} \frac{1}{\tau_\ell} + \sigma_0 \phi_{ph} \left(\frac{1}{\tau_u} + \frac{1}{\tau_\ell} - \frac{1}{\tau_{u\ell}} \right)} \quad (2.96a)$$

$$n_\ell = \eta_{inj} \frac{J}{q} \frac{\frac{1}{\tau_{u\ell}} + \sigma_0 \phi_{ph}}{\frac{1}{\tau_u} \frac{1}{\tau_\ell} + \sigma_0 \phi_{ph} \left(\frac{1}{\tau_u} + \frac{1}{\tau_\ell} - \frac{1}{\tau_{u\ell}} \right)} \quad (2.96b)$$

so that combining Eq. (2.96a) and Eq. (2.96b) yields

$$n_u - n_\ell = \eta_{inj} \frac{J}{q} \frac{\tau_u \left(1 - \frac{\tau_\ell}{\tau_{u\ell}} \right)}{1 + \sigma_0 \phi_{ph} \left(\tau_u \left(1 - \frac{\tau_\ell}{\tau_{u\ell}} \right) + \tau_\ell \right)} = \eta_{inj} \frac{J}{q} \frac{\tau_{eff}}{1 + \sigma_0 \phi_{ph} (\tau_{eff} + \tau_\ell)} \quad (2.97)$$

using $\tau_{eff} = \tau_u \left(1 - \frac{\tau_\ell}{\tau_{ue}}\right)$. Combining the results of Eqs. (2.95) and (2.97) gives

$$\phi_{ph} = \eta_{inj} \frac{J \tau_{ph} v_g N_p}{q L_p} \frac{\tau_{eff}}{(\tau_{eff} + \tau_\ell)} - \frac{1}{\sigma_0 (\tau_{eff} + \tau_\ell)} \quad (2.98)$$

and

$$\frac{d\phi_{ph}}{dJ} = \eta_{inj} \frac{v_g N_p \tau_{ph}}{q L_p} \frac{\tau_{eff}}{(\tau_{eff} + \tau_\ell)}. \quad (2.99)$$

Plugging Eq. (2.99) into Eq. (2.93), we get that the slope efficiency is

$$\frac{dP}{dI} = \eta_{inj} N_p \frac{\mathcal{E}_{ph}}{q} \frac{\alpha_m}{\alpha_m + \alpha_w} \frac{\tau_{eff}}{(\tau_{eff} + \tau_\ell)} \quad (2.100)$$

where the cavity escape and photon lifetimes have been converted to the more common mirror and waveguide loss terms. Finally, the inclusion of the local field intensity \bar{U}_i adds a “modal efficiency” factor η_m given by [54]

$$\eta_m = \frac{\left(\sum_{i=1}^{N_p} \bar{U}_i\right)^2}{N_p \sum_{i=1}^{N_p} \bar{U}_i^2} \quad (2.101)$$

and so

$$\frac{dP}{dI} = \eta_{inj} \eta_m N_p \frac{\mathcal{E}_{ph}}{q} \frac{\alpha_m}{\alpha_m + \alpha_w} \frac{\tau_{eff}}{(\tau_{eff} + \tau_\ell)}. \quad (2.102)$$

2.11 Output Power and Wall-plug Efficiency

Having solved for the slope efficiency, a linear relationship for output power results for currents above threshold.

$$P = \frac{dP}{dI} (I - I_{th}) = N_p \frac{\mathcal{E}_{ph}}{q} \frac{\alpha_m}{\alpha_m + \alpha_w} \frac{\tau_{eff}}{(\tau_{eff} + \tau_\ell)} \eta_{inj} \eta_m (I - I_{th}) \quad (2.103)$$

Wall-plug efficiency is simply defined as power out for power in. The input power is simply voltage times current, where the voltage can be broken up into the component terms representing the photon energy drop \mathcal{E}_{ph} , the energy drop Δ_{inj} from the lower laser state of one active region to the upper laser state of the adjacent down-stream active region, and any parasitic series resistance IR_{series} . Thus, input power P_{in} is given

by

$$P_{in} = \left(\frac{N_p}{q} (\mathcal{E}_{ph} + \Delta_{inj}) + IR_{series} \right) I \quad (2.104)$$

and the wall-plug efficiency η_{wp} is

$$\eta_{wp} = \left(\frac{\mathcal{E}_{ph}}{\mathcal{E}_{ph} + \Delta_{inj} + \frac{IR_{series}}{N_p}} \right) \left(\frac{\tau_{eff}}{\tau_{eff} + \tau_\ell} \right) \left(\frac{\alpha_m}{\alpha_m + \alpha_w} \right) \left(\frac{J - J_{th}}{J} \right) \eta_{inj} \eta_m \quad (2.105)$$

expressed as a product of constituent terms, each representing a source of efficiency loss.

2.12 Maximum Current & Differential Resistance

It is often useful to conceptualize transport through a QC structure in terms of total, aggregate transit time τ_{trans} through a single QC period. The velocity of electron flow v_{trans} is thus simply given as,

$$v_{trans} = \frac{L_p}{\tau_{trans}}. \quad (2.106)$$

This transport velocity can be used as a fundamental component of current density J , which also multiplies the electron density participating in transport N_{trans} [$\frac{1}{\text{volume}}$] [55].

$$J = q N_{trans} v_{trans} \quad (2.107)$$

With substitution of Eq. (2.106), Eq. (2.107) becomes

$$J = \frac{q n_{trans}}{\tau_{trans}} \quad (2.108)$$

where $n_{trans} = \frac{N_{trans}}{L_p}$ [$\frac{1}{\text{area}}$] is the sheet density of electrons participating in transport. The total sheet density of electrons present in the system n_s is assumed, for a QC structure, to be the doping density (typically, $n_s \sim 10^{11} \text{ cm}^{-2}$). We can now distinguish between those electrons participating in transport n_{trans} and those doped electrons that are otherwise “trapped” or stationary in the structure $n_{stationary}$, so that

$$n_s = n_{trans} + n_{stationary}. \quad (2.109)$$

When all system electrons are participating in current transport, so that $n_s = n_{trans}$ and $n_{stationary} = 0$, we achieve maximum current density J_{max} .

$$J_{max} = \frac{qn_s}{\tau_{trans}} \quad (2.110)$$

The linear relationship of J_{max} and n_s has been confirmed for QC devices [56] [57].

Since current transport can be conceptually understood through electron transit time, it is also useful to relate device resistance R (more accurately, differential resistance $\frac{dV}{dI}$) in a similar way. Here, we use simple, classical semiconductor device physics (see [55], for example) to first relate conductivity σ as

$$\sigma = q \frac{v_{trans}}{E_{field}} N_{trans} \quad (2.111)$$

where the mobility is given by $\frac{v_{trans}}{E_{field}}$. Now, resistance is simply

$$R = \frac{1}{\sigma} \frac{N_p L_p}{A} \quad (2.112)$$

so combining with Eqs. (2.106) and (2.111),

$$R = \frac{E_{field}}{q N_{trans}} \frac{N_p \tau_{trans}}{A}. \quad (2.113)$$

Taking E_{field} in terms of the applied voltage V_{appl} so that

$$E_{field} = \frac{V_{appl}}{N_p L_p} \quad (2.114)$$

we realize our relation for resistance and transit time.

$$R = \frac{V_{appl}}{q A} \frac{\tau_{trans}}{n_{trans}} \quad (2.115)$$

where $n_{trans} = L_p N_{trans}$. From our relations for J_{max} and R , we can visualize the transit rate $\frac{1}{\tau_{trans}}$ as the size of the “pipe” through which electrons can flow. The bigger the pipe (*i.e.* the shorter τ_{trans}), the more electrons one can send through the structure and therefore the more electrons are available to produce photons.

2.13 Summary

In this chapter, I have provided a comprehensive toolbox of derivations, equations, and relations of fundamental importance to QC laser operation. At times, the ability to understand from basic principles the origin of a laser parameter, threshold current for example, can help to innovate strategies to improve that parameter. This chapter provides such understanding. We have also now established a basis for understanding the new design strategies and interpretation of unique observed data presented in subsequent chapters.

Chapter 3

ZnCdSe/ZnCdMgSe Quantum Cascade Emitters

Among the present-day challenges for light emitters are “gaps” in the spectrum where high quality (room temperature and CW) laser sources are commercially unavailable. Even when considering cutting-edge devices produced by research institutions, key gaps in coverage remain. Of particular immediate interest is the break between the current capabilities of diode lasers and QC lasers—between about 3–4 μm . This technological break inconveniently consumes a large part of the so-called first atmospheric window, the wavelength range from about 3–5 μm where there is minimal atmospheric absorption. Illustrated in Fig. 3.1, this is also the domain of primary ro-vibrational absorption resonances for many important molecular species of academic and industrial interest, especially the C–H stretch.

The gap, however, is closing; three technologies are currently in competition to claim title to this space. Using InGaAsSb wells and AlInGaAsSb quaternary barriers, quantum well diode lasers approaching from the short-wavelength side have reached $\lambda = 3.36 \mu\text{m}$ at 12 °C with 15 mW of CW output power [58]. Because of the small semiconductor band gaps needed to produce these wavelengths, performance here and at longer wavelengths is limited by Auger scattering. From the QC side (the long-wavelength side), a strained InGaAs/AlInAs device producing 143 mW of RT CW power at 3.8 μm has been reported [59]. The short-wavelength challenges for QC sources will be thoroughly discussed later in this chapter. Another technology with potential for covering the 3–4 μm gap is the interband cascade laser (ICL) [60]. Here though, only one RT CW result has been reported [61]—at 3.75 μm . Also, reliability associated with single

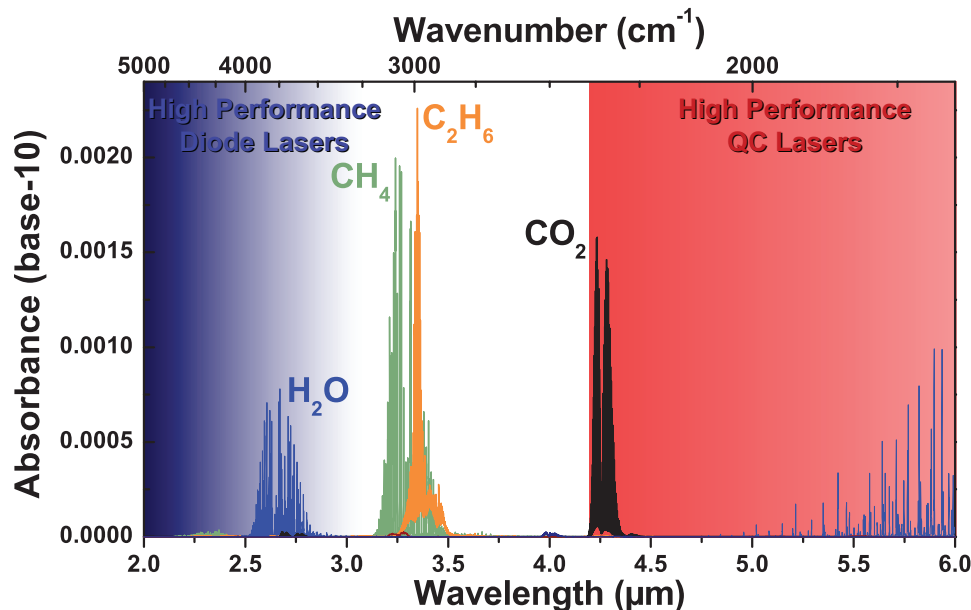


Figure 3.1: Absorption spectra and laser capabilities near the first atmospheric window. Many important molecular species, such as methane and ethane, have ideally strong absorption resonances in the first atmospheric window. Today's commercially available high-performance light sources are unable to cover many of these important wavelengths.

frequency emission from ICL devices has proven a challenge, due to the present inability for distributed feedback device fabrication with an epitaxial overgrowth step [62].

The capabilities of commercially available devices are more limited. Today's high performance off-the-shelf lasers can reach up to about $3.0\text{ }\mu\text{m}$ on the diode side and down to $4.2\text{ }\mu\text{m}$ on the QC laser side of the spectrum. With important and pressing applications, this leaves uncovered more than half of the first-atmospheric window.

In light of the current challenges, the source that will be the commercial choice for the $3\text{--}4\text{ }\mu\text{m}$ gap remains an open question.

In this chapter, we discuss progress toward a new approach to cover the gap. When fundamental limitations exist with the capabilities of any material system, as may be the case with the laser sources just described, new materials must be developed. The QC concept in particular lends itself especially well to new device development. Absent from the prescribed QC emitter construction is the required usage of any individual material system. Rather, there exist four general requirements for any practical QC implementation:

- (1) two materials with sufficient band edge offset to support optical transitions and bandgap to avoid across-gap absorption;
- (2) a method for engineering population inversion between upper and lower energy states of the optical transition;
- (3) at least one of the two materials must be dopable with charge carriers for the intended transport band; and
- (4) the materials must be feasibly fabricated.

Given only these requirements, it is surprising that all QC lasers to date have been implemented in various well-established III-V materials system. Here, we investigate the use of a II-VI materials system, namely ZnCdSe and ZnMgSe, to build QC structures. Advantageously, this semiconductor combination can be fabricated using molecular beam epitaxy technology on a conventional InP substrate. It has a much larger effective conduction band offset than what is found in III-V materials, which allows for higher photon energy conventional short wavelength QC designs. Yet with the many compelling reasons to pursue this research, investigating new materials systems is always a challenge. In this chapter, I describe many of those challenges, and I detail the solutions we have thus far developed.

3.1 Short Wavelength Quantum Cascade Emitters

Pushing the ability of QC lasers to emit at ever shorter wavelengths has long been a research goal of the QC community. On the surface, the fundamental limitation on QC laser short wavelength emission is easy to understand. Rather than “short wavelength,” however, the argument is more aptly recast as “high photon energy” (3 \AA is equivalent to 413 & 310 meV, respectively). As one seeks to design QC lasers with larger and larger photon energies (by making the active region wells more narrow), eventually, one reaches a point where the upper laser state is not sufficiently confined within the well to prevent electron escape. Sufficient upper laser state confinement is even more necessary as one seeks high temperature, CW performance. For such demanding operating conditions, the laser core often heats to ~ 100 K or more above the heat sink temperature, and thermal energy of electrons becomes quite large. Thus, strategies to increase the band offset between the well material and barrier material

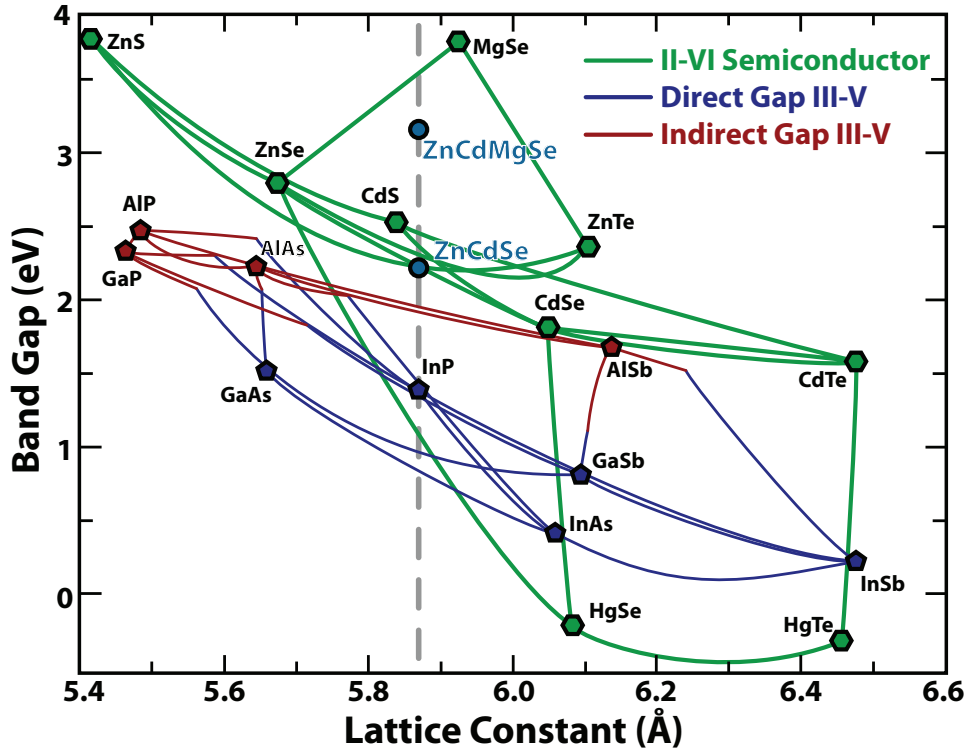


Figure 3.2: Energy gap vs. lattice constant for III-V and II-VI materials. The shortest wavelength QC lasers have been made in III-V systems lattice-matched to InP and InAs. In this work, we investigate QC sources made from ZnCdSe and ZnCdMgSe.

are key to increasing photon energy and improving performance for short wavelength lasers.

The first QC laser, it is interesting to note, operated at a relatively short wavelength of $4.2 \mu\text{m}$ [8]. While this device was implemented in an $\text{In}_{0.53}\text{Ga}_{0.47}\text{As} / \text{Al}_{0.48}\text{In}_{0.52}\text{As}$ materials system (lattice-matched to InP), work has progressed substantially with other materials. For example, “strain compensation” has been used to increase the conduction band offset for the InGaAs/AlInAs materials system. By changing material compositions so that compressive strain is added to InGaAs layers and tensile strain to AlInAs layers, the conduction band offset is increased while maintaining a composition that is overall strain-neutral relative to the InP lattice constant. Faist *et al.* were the first to implement such a structure, and recorded $3.4 \mu\text{m}$ emission up to RT [34]. Today’s highest performing QC lasers are implemented in such a strain-compensated system [63].

Taking this tactic to the extreme, the field has employed AlAs barrier regions with strategic positioning [64] [65] [66] [67] and creative strain compensation strategies [68]. It is at this point we encounter a less obvious constraint to high energy photon generation. When artificially elevating electrons high up in a semiconductor energy band, as we do with short wavelength QC structures, the full band structure of the semiconductor well and barrier material becomes relevant. In particular, satellite valleys exist in the k -space dispersion of the band structure into which electrons can scatter; such intervalley scattering has been shown to be extremely rapid [69] [70]. When electrons scatter to k -space positions away from the Γ point, they are effectively trapped in a position that prevents them from participating in population inversion at the Γ point. For example, in QC structures employing lattice-matched $\text{In}_{0.53}\text{Ga}_{0.47}\text{As}$ as the well material, the energy difference in the conduction band X and Γ local minima $\mathcal{E}_C^X - \mathcal{E}_C^\Gamma = 520$ meV. Since $\Delta\mathcal{E}_C = 520$ meV for the $\text{In}_{0.53}\text{Ga}_{0.47}\text{As} / \text{Al}_{0.48}\text{In}_{0.52}\text{As}$ system, using AlAs blocking layers achieves only small gains in photon energy, and here only with strategic positioning of those blocking layers.

Since different materials in our arsenal have different properties, we can attack the satellite valley problem by optimizing the alloy composition we use. It turns out that between GaAs, AlAs, InAs, and all the ternary compositions between, InAs has the largest Γ -to-satellite valley offset: $\mathcal{E}_C^L - \mathcal{E}_C^\Gamma = 0.716$ eV for InAs [29]. So it comes as no surprise that work in the InAs/AlSb materials system has yielded the shortest wavelength QC lasers to date. At heat sink temperature $T_{sink} = 79$ K, J. Devenson *et al.* recorded $2.75\ \mu\text{m}$ emission ($\mathcal{E}_{ph} = 0.451$ eV) [10]. This result certainly confirms the restriction that satellite-valley scattering places on the QC emission energy. QC laser designers typically consider about half of the conduction band offset $\Delta\mathcal{E}_C$ to be usable for the photon transition, with the remaining offset used for extraneous QC functionality. The Γ point conduction band offset for InAs/AlSb $\Delta\mathcal{E}_C^\Gamma = 2.1$ eV. With the current, hard-fought emission record at $\mathcal{E}_{ph} = 0.451$ eV, the $\mathcal{E}_C^L - \mathcal{E}_C^\Gamma = 0.716$ eV restriction is evident.

The community is investigating other materials systems having large conduction band offsets for short wavelength photon generation. The enormous band gap discontinuities of III–nitrides have not been overlooked [71], and attempts have been made to use these for intersubband devices. GaN-based QC lasers remain elusive, however, primarily due to defects in material quality that lead to problems with vertical transport and current leakage. Still, work is progressing. GaN/AlGaN QC structures

have shown intersubband photoluminescence at $\lambda = 2.13 \mu\text{m}$ [72], and GaN/AlGaN QC photodetectors have been demonstrated with responsitivity near $\lambda \approx 1.7 \mu\text{m}$ [73]. Also, electroluminescence from CdF₂/CaF₂ QC structures grown on Si has also been reported [74].

3.2 The ZnCdSe/ZnMgSe Materials System

Evident in Fig. 3.2, II–VI semiconductors open up a whole new world of possibilities for QC structures. While new to QC lasers, II–VI materials have a substantial history as diode lasers. Through the 1990s and until the successful demonstration of the InGaN blue laser [75], II–VI materials looked especially promising as a blue laser and LED source [76] for consumer products. For these sources, special attention was paid to the ZnCdSe/ZnMgSe system, due to the especially large band gap of MgSe and the ability to grow ZnMgSe lattice-matched to InP [77]. Interest in the material for laser diodes has seen a resurgence, due to its potential [78] to fill the “green gap” where InGaN devices with high In concentration are unable to achieve similar levels of performance [79] as their blue-emitting counterparts. Just as III–V QC laser development was able to capitalize on the substantial infrastructure surrounding telecom laser diodes, QC development in II–VI materials is not without infrastructural backing.

Just as in the blue–green laser diode case, the ZnCdSe/ZnMgSe materials system is appealing for QC structures because of its large band gaps, and—specifically for QC structures—large conduction band offset. With this material system, we enjoy the added benefit that it can be grown lattice-matched on conventional InP substrate with a zinc-blende crystal structure; for Zn_{0.43}Cd_{0.57}Se/Zn_{0.09}Mg_{0.91}Se—the compositions lattice-matched to InP— $\Delta\mathcal{E}_C^\Gamma = 1.2 \text{ eV}$ [82]. In contrast to the large band offset III–V systems, all of the ZnCdSe/ZnMgSe band offset is usable energy space for a QC design. Figure 3.3 compares calculations of full band structures for ZnSe and CdSe (the component materials of the QC wells) with InAs. Here, it is evident that the satellite valleys are much higher in the II–VI material. Indeed, $\mathcal{E}_C^X - \mathcal{E}_C^\Gamma \approx 1.64 \text{ eV}$ and $\mathcal{E}_C^\Gamma - \mathcal{E}_C^X \approx 2.27 \text{ eV}$ for CdSe [81], greater than $\Delta\mathcal{E}_C^\Gamma$ for the ZnCdSe/ZnMgSe system.

When designing QC structures, the values of several materials properties are needed to fully calculate parameters relevant to a QC design. In the next sections, I review these values for ZnSe, CdSe, and MgSe, the three relevant component binary materials in the

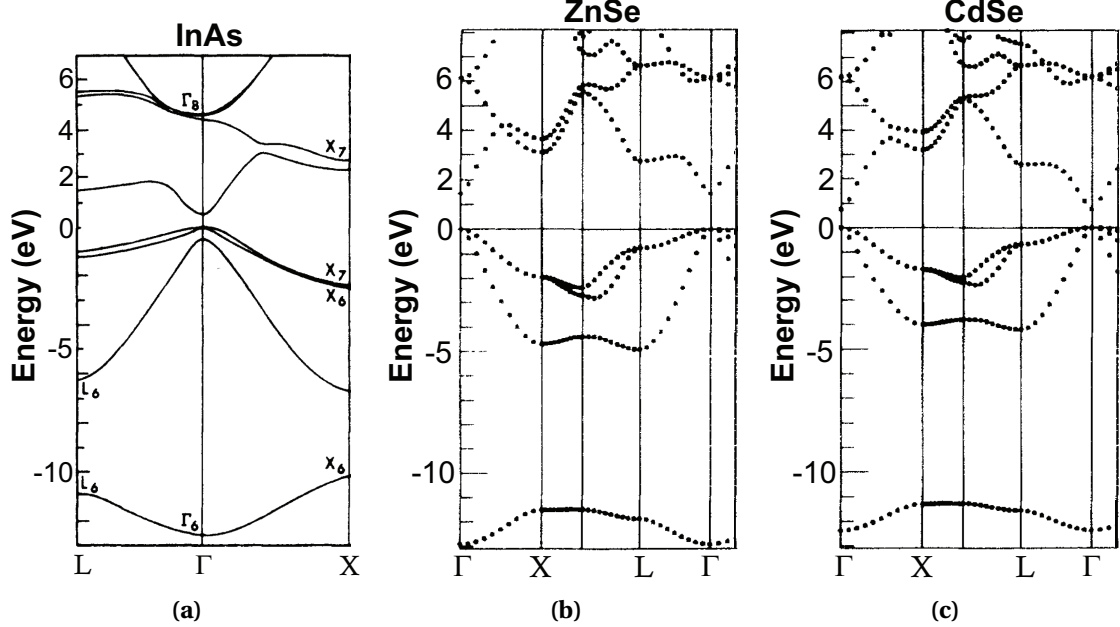


Figure 3.3: Bulk energy band diagrams for InAs, ZnSe, and CdSe. Band diagrams as calculated by the psuedopotential method for (a) InAs [80], (b) ZnSe, and (c) CdSe [81]. The $\mathcal{E}_C^L - \mathcal{E}_C^\Gamma$ offsets for InAs, ZnSe, and CdSe are, respectively, 0.716 [29], 1.29, and 1.88 eV [81]. The $\mathcal{E}_C^X - \mathcal{E}_C^\Gamma$ offsets for InAs, ZnSe, and CdSe are, respectively, 1.016 [29], 1.64, and 2.27 eV [81]. For GaAs, these values are 0.296 and 0.462 eV [29]. Reprinted with permission from the American Physical Society.

present system.* Ternary compounds—such as $Zn_xCd_{1-x}Se$ —are often linearly interpolated based on the relative compositions x and $1 - x$ of each of the two component binaries ZnSe and CdSe. More generally, a bowing parameter C_B is sometimes needed to accurately characterize the material property. For any ternary compound $A_xB_{1-x}C$, a general material property G_{ABC} is given by

$$G_{ABC}(x) = x G_{AC} + (1 - x) G_{BC} + x(1 - x) C_B. \quad (3.1)$$

A quaternary material parameter can be calculated by extending this approach. For an alloy of type $A_xB_yC_{1-x-y}D$, a general property G_{ABCD} is given by

$$G_{ABCD}(x, y) = \frac{y(1 - x - y) G_{ABC}(u) + x(1 - x - y) G_{BCD}(v) + xy G_{ACD}(w)}{xy + y(1 - x - y) + x(1 - x - y)} \quad (3.2)$$

* One should note that the uncertainty in these parameters is much greater than for III–V systems.

Table 3.1: Materials parameters for ZnSe, CdSe, and MgSe. Source is [32], unless otherwise indicated. The effective mass is given for the bulk band edge, with m_0 the free electron mass.

	ZnSe	CdSe	MgSe
$a_{\ell c}$ (Å)	5.6692	6.077	5.91
c_{11} (GPa)	85.7	66.7	75.8
c_{12} (GPa)	50.7	46.3	48.6
\mathcal{E}_G^Γ (eV)	2.721	2.07	4.0
VBO (eV)	0.53 ⁽¹⁾	0.60 ⁽¹⁾	-0.5 ⁽¹⁾
Δ_{SO} (eV)	0.424	0.395	0.4
a_c^Γ (eV)	-4.17	-11.0	—
a_v (eV)	1.65	-8.9	-1.0
b (eV)	-1.8	-0.8	-1.27
m_e^Γ/m_0	0.137	0.119	0.20
α^Γ (meV/K)	5.58	6.96	—
β^Γ (K)	187	281	—
ϵ_s	8.9	9.6	7.8
ϵ_∞	5.9	6.2	3.8
$\hbar\omega_{LO}$	31.2	26.2	42.2

(1) S.-H. Wei and A. Zunger, *Appl. Phys. Lett.* **72**, 2011 (1998).

where $u \equiv 1 - \frac{1}{2}x - y$, and $v \equiv 1 - x - \frac{1}{2}y$, and $w \equiv (1 - x - y)/2$ [29].

3.3 Epitaxial Growth of ZnCdSe/ZnMgSe Materials

The growth of II–VI semiconductors—including ZnCdSe and ZnMgSe—uses the same technological foundation as III–V epitaxial growth. While most II–VI growth is primarily done with molecular beam epitaxy (MBE) [76], metal–organic vapor phase epitaxy (MOVPE) has also been used [83]. The three primary binary III–V substrates—GaAs [84], InP [85], and InAs [86]—have all been used as substrates for II–VI growth, with various II–VI materials that share similar lattice constants. Both ZnCdSe and ZnMgSe have compositions that match the lattice constant of InP, and with their relatively large conduction band offset of 1.2 eV, the system is highly suitable of QC structures.

The first growth of ZnCdSe on an InP [85] substrate had a quite high ($> 10^{10} \text{ cm}^{-2}$) density of stacking faults. One of the most crucial steps in attaining high quality (low defect density) growth of II–VI materials on III–V substrates is achieving a high quality II–VI/III–V interface. II–VI growth on InP is particularly challenging. The standard cleaning method for substrate preparation—an etch such as $\text{H}_2\text{SO}_4:\text{H}_2\text{O}_2:\text{H}_2\text{O}$ (7:1:1)—leaves a protective oxide on the substrate surface. In III–V MBE, the protective oxide is removed in the growth chamber by heating the substrate beyond the oxide desorption temperature. For InP surfaces, however, because the congruent evaporation temperature of InP (360 °C) is less than the oxide desorption temperature (500 °C), an As or P overpressure is used to prevent In droplet formation during the oxide desorption process [20]. Here, now, is the problem for II–VI MBE on InP, because As and P sources are not used in a II–VI MBE chamber. To circumvent this problem, two MBE chambers are used—connected by an ultra-high vacuum (UHV) wafer transfer system. In the first chamber, a III–V MBE chamber, the oxide desorption procedure under As overpressure is done, and then a high quality $\text{In}_{0.53}\text{Ga}_{0.47}\text{As}$ buffer layer is grown. The wafer is transferred under UHV to the second, II–VI MBE chamber, where the II–VI epitaxial growth is then able to proceed. With the growth of an $\text{In}_{0.53}\text{Ga}_{0.47}\text{As}$ buffer layer, in addition to a low temperature (170 °C) ZnCdSe interfacial layer prior to the main II–VI growth at 270 °C, the defect density was reduced to the $10^6\text{--}10^7 \text{ cm}^{-2}$ range [87].

Once a clean InGaAs surface is achieved, a second problem for growing Se-containing II–VI compounds is encountered. At the II–VI/III–V heterointerface, the formation of III–VI compounds (Ga_2Se_3 , for example) are energetically preferred, which themselves form 3D islands rather than a desired 2D growth profile [88]. These 3D islands later result in stacking faults that reduce epitaxial quality. To minimize this interaction, a group II flux (a Zn flux [89] in the case of ZnCdSe growth) can be used as a III–V surface treatment prior to II–VI growth. With this additional Zn irradiation step, etch pit defect densities were reduced to the mid 10^4 cm^{-2} range [89].

For QC barrier layers, while the growth of lattice-matched ZnMgSe [82] or even strained MgSe [90] is possible, the high Mg content can lead to rapid oxidation and degradation of the epitaxial layers. For the purposes of initial research into II–VI QC structures, it is more technologically practicable to used quaternary ZnCdMgSe as the QC barrier layers, so as to reduce this oxidation effect.

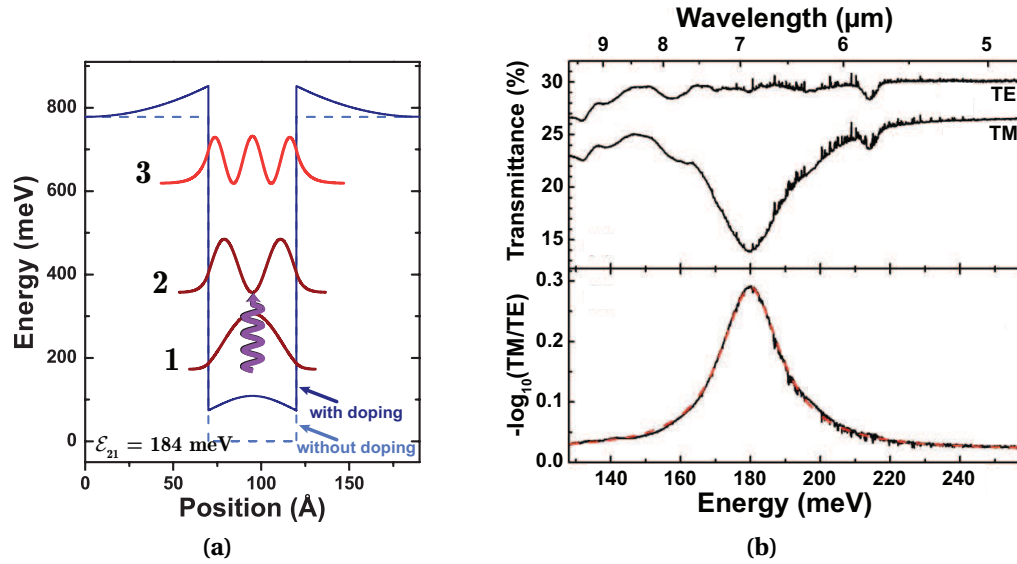


Figure 3.4: Caption. (a) Conduction band diagram for a 50.

3.4 Intersubband Absorption in ZnCdSe/ZnCdMgSe Quantum Wells

As an initial step toward demonstrating ZnCdSe/ZnCdMgSe QC structures, we looked for intersubband absorption in simple single quantum well structures. The transmission properties at mid-infrared wavelengths of a quantum well sample provide useful information for sample characterization. If the structure is n -type doped, electrons will be available for intersubband absorption out of the ground state in the structure where electrons accumulate. In a single quantum well structure, this state is just the quantum well ground state.

We looked at intersubband transitions from 50 Å $\text{Zn}_{0.50}\text{Cd}_{0.50}\text{Se}$ quantum wells surrounded by 140 Å $\text{Zn}_{0.20}\text{Cd}_{0.19}\text{Mg}_{0.61}\text{Se}$ barriers [91] Cl-doped $n = 1 \times 10^{18} \text{ cm}^{-3}$. The sample was grown with 10 quantum well periods. The conduction band energy diagram is shown in Fig. 3.4a, where two quantum well potentials are shown, one that includes the field perturbation from fixed and free charges and one that is only the potential energy of the conduction band edge. The energy states and wavefunctions (moduli squared) shown include the field perturbation from doping.

Transmission data can be taken either in a single-pass configuration, where the wafer is oriented at the Brewster angle relative to the optical axis, or in a multi-pass configuration, where opposing sides of the wafer are polished at a 45° angle. In both cases, the wafer back-side (non-epitaxial side) is also mirror-polished.

Intersubband transitions have transverse magnetic (TM) polarization dependence, since the intersubband energy states result from quantization only in the axis perpendicular to the growth plane. That is, substantially non-zero optical dipole matrix elements only exist for this z direction. The polarization dependence of the absorption is useful for transmission data collection. Since only TM light is absorbed by the quantum wells, transverse electric (TE) light passes through the quantum wells unhindered. Thus, TE transmission provides an effective “background” measurement, where all the properties of detector responsivity, light source spectral intensity, absorption from optical system elements, non-polarization-dependent absorption processes in the semiconductor, etc., are accounted for. Taking the ratio of the TM and TE spectra, the absorption resulting from intersubband transitions is recovered.

The data in Fig. 3.4b, taken with the sample in a multi-pass configuration, show a single absorption centered near 180 meV. This is in very good agreement with the model results shown in Fig. 3.4a, where \mathcal{E}_{21} is calculated at 184 meV. The FWHM of the absorption is 20.8 meV, about 11% of the transition energy, and is an indicator of growth uniformity (InGaAs/AlInAs heterostructures compare at 10%).

3.5 A ZnCdSe/ZnCdMgSe Quantum Cascade Structure

For a first ZnCdSe/ZnCdMgSe QC structure, our strategy was to design a basic, conventional QC active core. A design concept that is well-understood in III-V QC structures could then be used as a basis for our data analysis here. We settled on a simple, two-well active region QC design strategy. Included in our consideration of design elements was a number of trade-offs. The larger band offsets afforded by our new material system can support optical transitions with larger photon energies. But the consequence of larger photon energies is using larger applied electric fields, longer injector regions, or a combination of both. The relation between these design parameters is quite simply

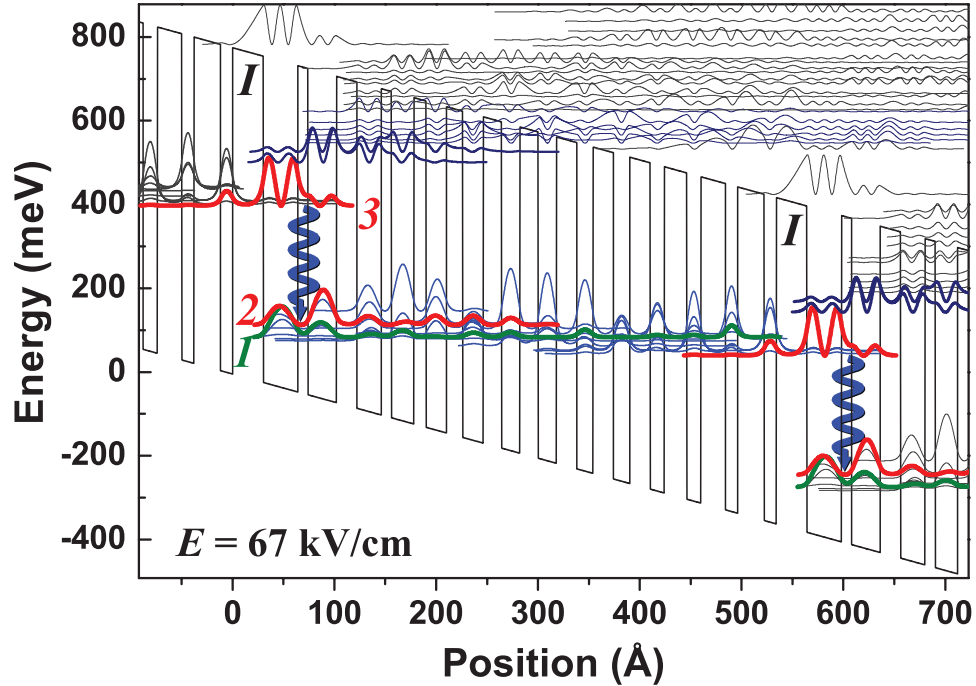


Figure 3.5: First generation $\text{Zn}_{0.43}\text{Cd}_{0.57}\text{Se}/\text{Zn}_{0.20}\text{Cd}_{0.19}\text{Mg}_{0.61}\text{Se}$ QC design. A conventional two-well active region QC structure with $L_p = 534 \text{ \AA}$. The calculated emission wavelength is $4.37 \mu\text{m}$.

given as

$$E_{field} = \frac{\mathcal{E}_{ph} + \Delta_{inj}}{qL_p}. \quad (3.3)$$

Because it was initially unclear how much field the material system could support, we chose a rather low design turn-on field $E_{field} = 67 \text{ kV/cm}$. To keep the QC period length L_p reasonably short, we chose a photon energy of 284 meV ($\lambda = 4.37 \mu\text{m}$); while relatively large compared to the majority of QC devices, this photon energy is far less than the band offset can in principle support.

Our conventional two-well active region QC structure was developed with a $\text{Zn}_{0.43}\text{Cd}_{0.57}\text{Se}$ material composition for the quantum well layers and a $\text{Zn}_{0.20}\text{Cd}_{0.19}\text{Mg}_{0.61}\text{Se}$ material composition for the barrier layers. The Fig. 3.5 conduction band diagram shows the structure at the design field of 67 kV/cm. A single stage of the layer sequence is—in angstroms starting from the injection barrier I , and going from left to right in the direction of electron flow—30 / 34 / 10 / 28 / 20 / 24 / 10 / 22 / 12 / 20 / 16 / 20 / 18 / 18 / 18 / 20 / 16 / 20 / 16 / 20 / 14 / 22 / 14 /

24 / 12 / 26 / 12. Zn_{0.20}Cd_{0.19}Mg_{0.61}Se barriers are in bold and Zn_{0.43}Cd_{0.57}Se wells are in normal font. Underlined layers represent ZnCdSe that is Cl-doped $n = 2 \times 10^{17} \text{ cm}^{-3}$ and ZnCdMgSe doped with the same ZnCl₂ flux as the ZnCdSe layers. We estimate a sheet density per active region-injector period of $n_s = 5.4 \times 10^{11} \text{ cm}^{-2}$. The total QC period length $L_p = 534 \text{ \AA}$, and $\Delta_{inj} = 74 \text{ meV}$ at $E_{field} = 67 \text{ kV/cm}$. We calculate an optical dipole matrix element $z_{u\ell} = 8.7 \text{ \AA}$. In the design, an active region energy state is placed 32 meV below the lower optical transition level, sufficient for longitudinal optical (LO) phonon depopulation of the lower laser state via ZnSe- (31.6 meV) [92] and CdSe-like (26.3 meV) [93] phonons. This configuration results in a calculated upper state lifetime $\tau_u = 0.84 \text{ ps}$, lower state lifetime $\tau_\ell = 0.21 \text{ ps}$, and non-radiative transition time $\tau_{u\ell} = 3.3 \text{ ps}$. Our design calculations included band gaps of 2.08 and 3.03 eV for Zn_{0.43}Cd_{0.57}Se and Zn_{0.20}Cd_{0.19}Mg_{0.61}Se, respectively, with a conduction band offset of 0.78 eV [94]. The corresponding conduction band effective masses are calculated to be 0.128 and 0.181 [94] times the free electron mass, respectively.

3.6 Device Fabrication & Processing

The QC structure was grown by MBE on a low doped ($N < 2 \times 10^{17} \text{ cm}^{-3}$) InP:S substrate. Prior to active core growth, we deposited 0.25 μm of In_{0.53}Ga_{0.47}As (Si-doped $N = 5 \times 10^{17} \text{ cm}^{-3}$) as buffer layer. II-VI growth was preceded by a 40 sec Zn flux treatment and 100 \AA of low temperature (230 °C) ZnCdSe (Cl doped $N = 2 \times 10^{17} \text{ cm}^{-3}$). At the 330 °C growth temperature, another 400 \AA of ZnCdSe (Cl-doped $n = 2 \times 10^{17} \text{ cm}^{-3}$) buffer was deposited. Ten periods of the active region-injector sequence were grown. The structure was capped by 400 \AA ZnCdSe (Cl-doped $n = 2 \times 10^{17} \text{ cm}^{-3}$) and 2000 \AA ZnCdSe (Cl-doped $n = 4 \times 10^{18} \text{ cm}^{-3}$). Digital transition gradings were used between bulk layers and the active core.

Electroluminescence (EL) structures were fabricated in the form of semicircular cleaved mesas. Two different processes were used, both resulting in devices of similar form. The first method began with cleaning the epitaxial surface using acetone, isopropanol, and a 1 min, 100 W O₂ plasma at 100 mTorr. Lithographically-patterned (positive AZ4215E photoresist without image reversal) 400 μm diameter circles were etched into mesa structures using a HBr:HNO₃:H₂O (1:1:10) wet chemical etch solution; a 1 min, 100 W O₂ plasma descum at 100 mTorr immediately preceded the etch. The

etch depth was sufficient to penetrate the epitaxially grown material (about 3 min of etch time). The sample was again cleaned with acetone, isopropanol, and a 1 min, 100 W O₂ plasma at 100 mTorr. A second lithography step (negative AZ4215E photoresist with image reversal) was used to define a lift-off pattern for the top contact metallization, which consisted of 350 μm diameter circles centered on the etched 400 μm diameter mesas. The wafer surface was cleaned and prepared for metalization with a 30 sec, 100 W O₂ plasma descum at 100 mTorr followed by a 45 sec HF:H₂O (1:1) dip to remove surface oxide. These cleaning steps immediately preceded top metal contact deposition. Top contacts consisted of 150 Å Ti followed by 2500 Å Au [95]; Ge/Au back-side InP contacts were also deposited.

A second mesa processing method yielded far more consistent results, especially with regard to repeatable, high quality, ohmic, and mechanically stable top (epitaxial-side) metal contacts. The first processing step was applying the top metal contact, and then the remaining mesa processing steps followed. Processing began with an epitaxial surface cleaning, consisting of acetone, isopropanol, and a 1 min, 100 W O₂ plasma at 100 mTorr. Surface oxides were removed with a 5 min HCl:H₂O (1:1) etch* [95], which immediately preceded application of the epitaxial-side metals. The top contact metal layers were 150 Å Ti followed by 2500 Å and were e-beam evaporated across the entire surface. A first lithography step (positive AZ4215E photoresist without image reversal) consisted of 350 μm diameter circles and was used to define the boundaries of the top metal contacts. An iodine-based Au etch at 25 °C sufficiently removed the unwanted Au after 3 min; the Ti adhesion layer not removed by the Au etch was removed after 15 sec in concentrated HF, effective due to the rapid oxidation of Ti. The sample was again cleaned with acetone, isopropanol, and a 1 min, 100 W O₂ plasma at 100 mTorr. A second lithography step (positive AZ4215E photoresist without image reversal) consisting of 400 μm diameter circles centered over the 350 μm diameter Au circles was used to define the boundaries for the mesa etch. A 1 min, 100 W O₂ plasma descum at 100 mTorr was used to prepare for the mesa etch. Mesas were etched using a HBr:HNO₃:H₂O (1:1:10) solution; the etch depth was sufficient to penetrate the epitaxially grown material (about 3 min of etch time). Finally, the remaining photoresist was stripped with acetone and isopropanol. A back-side Ge/Au contact was also supplied similar to the first method.

* It is worth noting that concentrated HCl etches the II–VI epitaxial layers. HCl that is diluted with equal part H₂O, however, has no appreciable etching of the II–VI epitaxial layer after 5 min, and is thought to be effective at removing surface oxides.

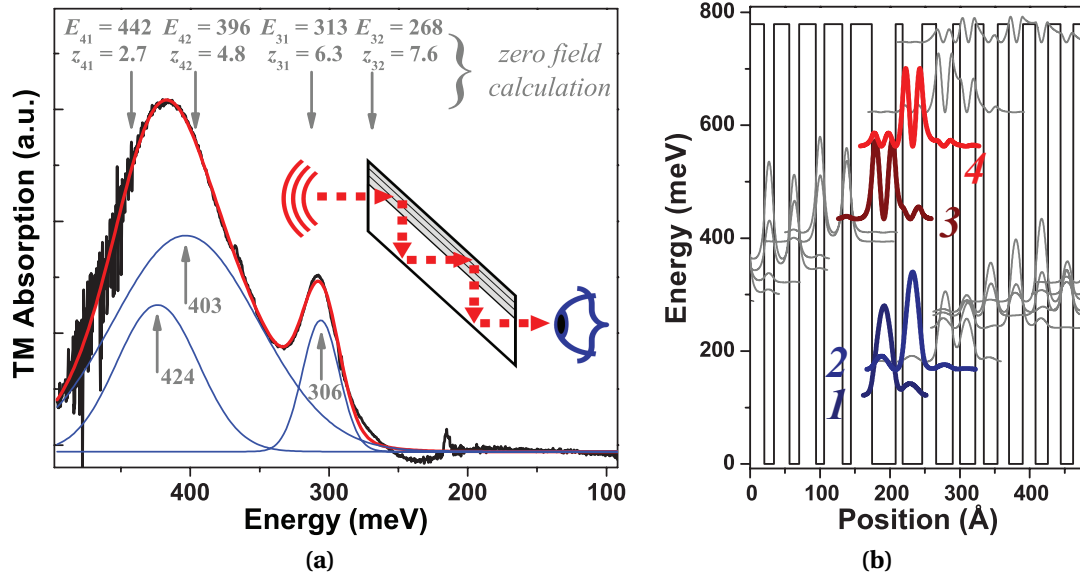


Figure 3.6: TM absorption spectrum from multi-pass transmission. (a) Fitted Gaussians show three resolvable peaks. Optical transition calculations for zero applied field are indicated at the top. The inset shows the multi-pass configuration with broadband light passing through a sample polished to 45° on both ends. (b) The QC conduction band structure at $E_{field} = 0$ kV/cm. Electrons from the doped injector relax to and accumulate in the state labeled 1.

After both processes, the mesas were cleaved into semicircular EL structures and In soldered to Cu heat sinks. The top electrical contacts were wire bonded to contact pads.

3.7 Measurements and Data

3.7.1 Quantum Cascade Intersubband Absorption

We again characterized our QC structure using a multi-pass transmission measurement, schematically depicted in the Fig. 3.6a inset. For a QC structure with zero applied field, as is usually the case for transmission measurements on QC structures, electrons from the doped injector region typically accumulate in the lowest active region state, since the injector region energy states “step down” to the lowest active region state. This can be seen in Fig. 3.6b, which shows our ZnCdSe/ZnCdMgSe QC structure for $E_{field} = 0$ kV/cm.

The absorption spectrum of our structure shows two dominant TM peaks, shown in Fig. 3.6a. For these two peaks, three Gaussian curves—centered at 306, 403, and

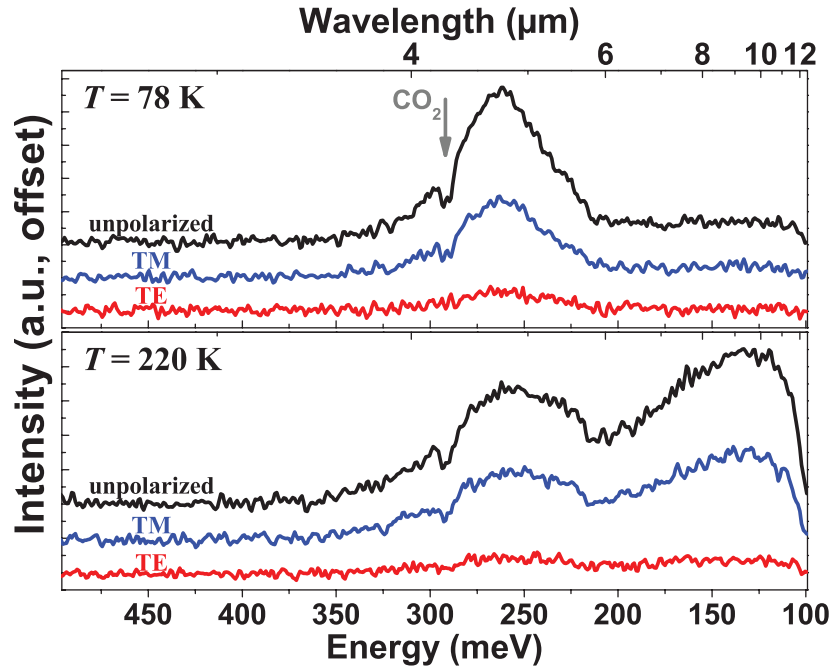


Figure 3.7: Polarization-resolved EL spectra. The data is for a device driven with 9.6 kA/cm^2 at 78 K (top) and 220 K (bottom). The emission is predominantly TM polarized. Additional longer wavelength light is seen at higher heat sink temperatures and currents. Atmospheric CO_2 absorption can be seen near $\lambda = 4.2 \mu\text{m}$. Spectra are not corrected for detector responsivity, which is more sensitive at longer wavelengths.

424 meV—provide an accurate fit. We calculate potential optical transitions for the zero field structure at 268, 313, 396, and 442 meV, as indicated in Fig. 3.6a. These calculations are largely consistent with the observed absorption.

3.7.2 Electroluminescence Spectra

Electroluminescence was collected for a variety of heat sink temperatures and applied current values using a Fourier transform infrared (FTIR) spectrometer in step scan mode and a cooled HgCdTe detector. The applied current pulses were $1 \mu\text{s}$ in duration at 3% duty cycle.

We observed EL centered near $\lambda = 4.8 \mu\text{m}$ (258 meV). Emission polarization characteristics were examined to confirm intersubband light generation. Two exemplary results of polarization-resolved EL spectra are shown in Fig. 3.7 for heat sink temperatures of 78 K and 220 K and a pumping current of 9.6 kA/cm^2 . While a small amount of TE

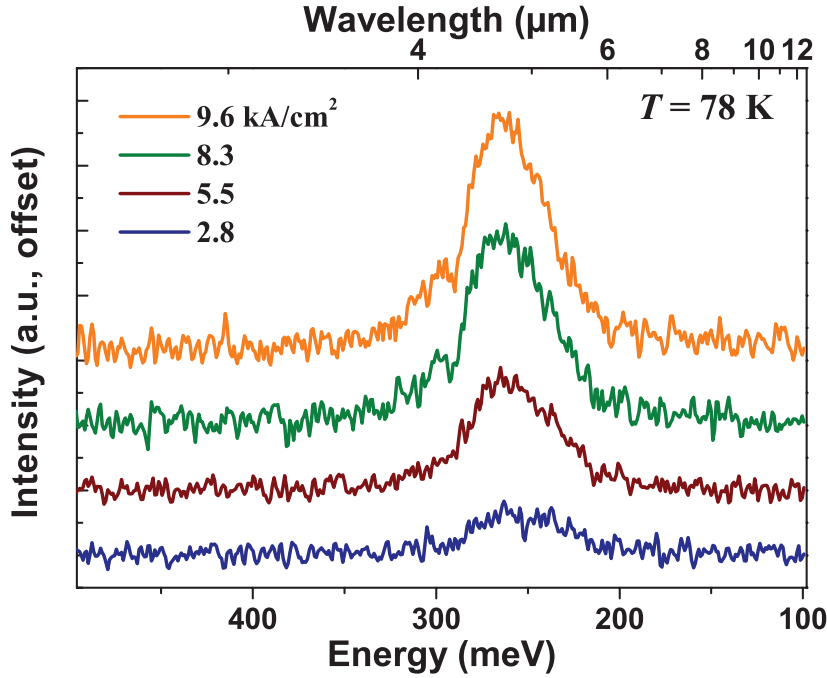


Figure 3.8: EL spectra at $T=78 \text{ K}$. Spectra at various current levels are shown. Emission intensity increases with increasing current. Emission is centered near 4.8 μm .

light is observed, which we attribute to scattering from within the rounded mesa, the EL is predominantly TM polarized.

At low temperatures, the primary emission peak is observed near 4.8 μm . Figure 3.8 shows emission behavior with increasing current for a heat sink temperature of 78 K and no polarizer in the optical path. The 4.8 μm emission peak grows correspondingly with increasing pumping current. At a pumping current density of 2.8 kA/cm^2 , a Gaussian fit gives an EL full-width at half-maximum (FWHM) of 52 meV; at 9.6 kA/cm^2 the FWHM is 47 meV, which is about 20% of the transition energy.

This 4.8 μm light is seen at temperatures ranging from 78 to 300 K. Figure 3.9 shows spectra with increasing temperature for a pumping current density of 9.6 kA/cm^2 . All spectra represent TM polarized light with subtraction of the corresponding unpolarized background. The emission peak centered near 4.8 μm is present over the full temperature range. We also observed the growth of a secondary, temperature-induced, lower energy emission. This broad emission is more intense for both higher currents and higher temperatures. Reported spectra are not corrected for wavelength-dependent variations in detector responsivity; we estimate our detector is 55% more sensitive

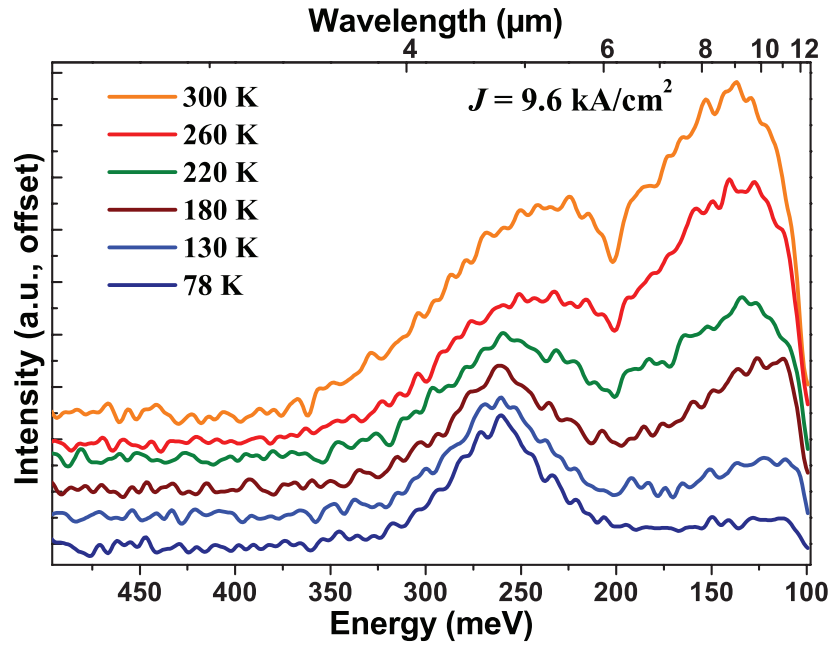


Figure 3.9: Temperature-dependence of EL spectra. EL spectra are at 9.6 kA/cm^2 for heat sink temperatures from 78 to 300 K. Additional longer-wavelength light is seen with increasing temperature. Over the 78 to 300 K temperature range, the $4.8 \mu\text{m}$ peak intensity decreases by 30% and emission width increases by 36%. Spectra are not corrected for variations in detector responsivity, which is more sensitive at longer wavelengths.

for 120 meV photons than for 260 meV photons. While the origin of this low energy emission remains unclear, the $4.8 \mu\text{m}$ emission is dominant and persists through room temperature. This emission has the well-known temperature-dependent behavior: from 78 to 300 K, Gaussian fits that include a rising background show that peak intensity decreases by 30% and emission width increases by 36%.

3.7.3 Light–Current–Voltage Data

Figure 3.10 shows wavelength-integrated light–current–voltage (LIV) measurements for temperatures ranging from 78 to 300 K. The light-current (LI) data represent TM polarized emission. The observed output power grows superlinearly for both increasing current and increasing temperatures. The current-voltage (IV) curves show typical QC behavior, with characteristic current turn-on once sufficient voltage has been applied. Turn-on for 78 K occurs at 5.40 V. At a turn-on field of 64 kV/cm, 3.42 V is dropped over

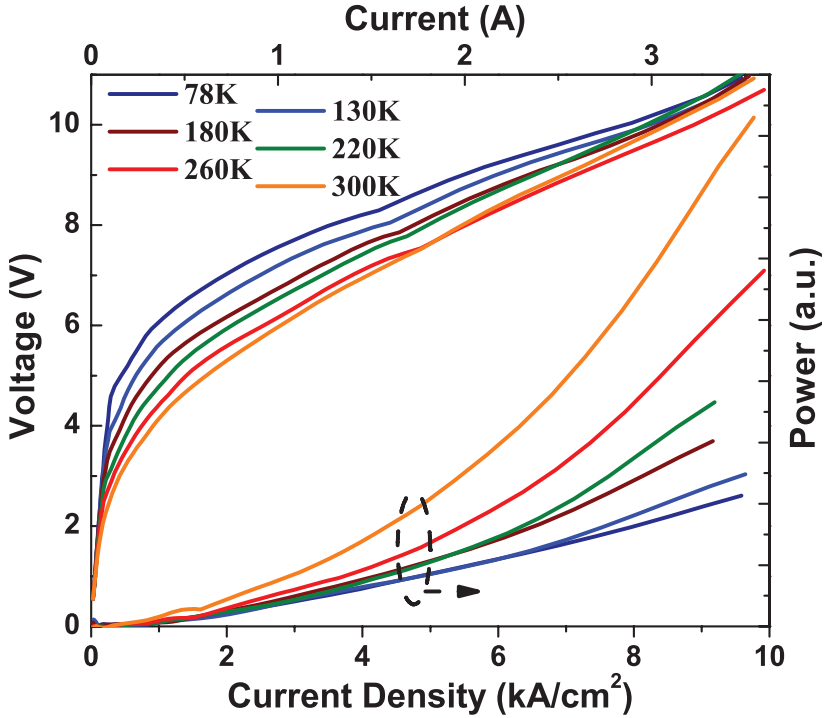


Figure 3.10: EL structure LIV. Spectrally integrated light–current–voltage data from 78 to 300K. The data were collected with 1 μ s pulses at 3% duty cycle. Data are not corrected for detector responsivity.

the active core. We attribute to conduction band offsets at bulk interfaces another 0.35 V. The remaining 1.63 V is likely dropped over the as yet non-ideal top contacts.

3.8 Second-Generation Design

With our initial demonstration of EL, we sought to improve upon the result with an improved QC structure. While we indeed observed some EL, the intensity of the emission was extremely weak. And because of such weak emission, we would not expect to see lasing from the structure, or even the presence of gain. One fundamental problem with the design was an energy spacing between the lowest active region states that is very nearly equal to the LO phonon energy; if the active region barrier ended up being only marginally too large, the LO phonon scattering channel out of the lower laser state would be slowed down considerably and population inversion would be extremely difficult.

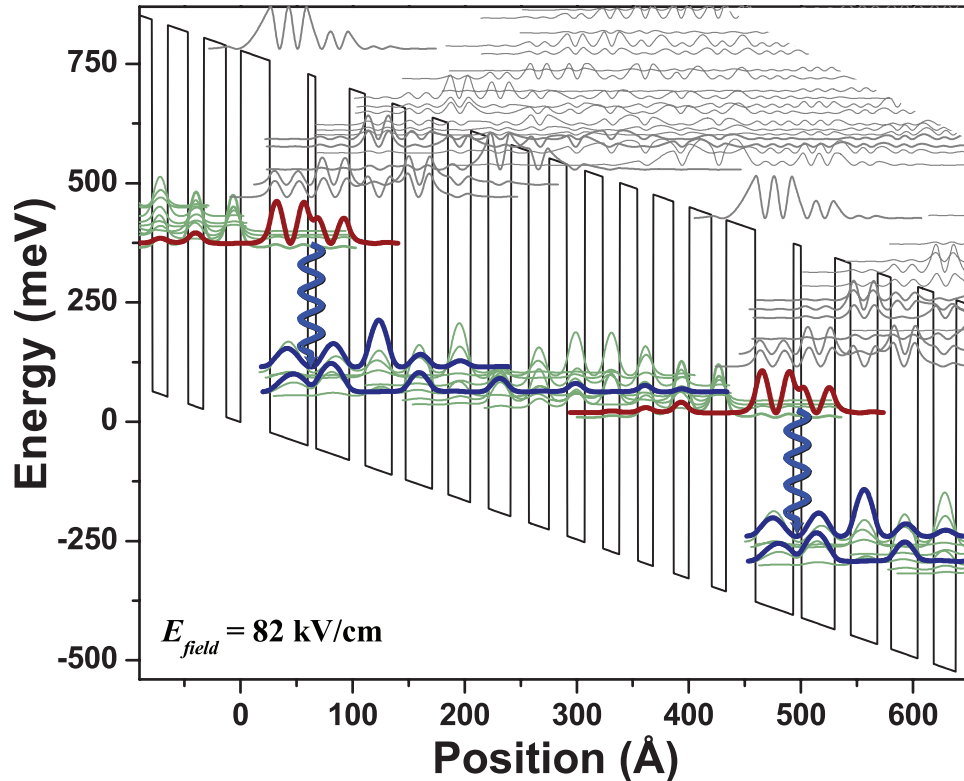


Figure 3.11: Second generation $\text{Zn}_{0.43}\text{Cd}_{0.57}\text{Se}/\text{Zn}_{0.20}\text{Cd}_{0.19}\text{Mg}_{0.61}\text{Se}$ QC design. A conventional two-well active region QC structure with $L_p = 534 \text{ \AA}$, calculated emission is $4.88 \mu\text{m}$.

Another fundamental problem was the “tight” (in energy range) injector that may have limited the amount of current able to be pushed through the device.

In a second generation design, we sought to mitigate these problems. We grew more periods: 25, instead of 10. We also improved the design, which is shown in Fig. 3.11. In this design, the period length has been decreased slightly to $L_p = 432 \text{ \AA}$ and the field increased to $E_{field} = 82 \text{ kV/cm}$. Also, the energy splitting between the lowest to active region states has been increased to 58 meV, to provide room for error in the active region barrier thickness. The layer sequence is, in angstroms starting from the injection barrier, **26 / 34 / 6 / 30 / 14 / 24 / 12 / 24 / 14 / 20 / 16 / 20 / 16 / 18 / 16 / 16 / 16 / 15 / 16 / 14 / 18 / 14 / 20 / 13**. The as-designed photon energy is $\mathcal{E}_{ul} = 254 \text{ meV}$ ($\lambda = 4.88 \mu\text{m}$). $\text{Zn}_{0.20}\text{Cd}_{0.19}\text{Mg}_{0.61}\text{Se}$ barriers are in bold and $\text{Zn}_{0.43}\text{Cd}_{0.57}\text{Se}$ wells are in normal font. Underlined layers represent ZnCdSe that is Cl-doped $n = 3 \times 10^{17} \text{ cm}^{-3}$ and ZnCdMgSe doped with the same ZnCl_2 flux as the ZnCdSe layers.

After growth and processing as previously described, we examined EL spectral data for the device. The spectral emission was remarkably similar to that in Fig. 3.9, with the emission peaks looking nearly identical between the first and second generation devices. The low-energy thermal emission was also both present and similar in the second generation device. This, even though the design wavelengths between the first and second generation devices were nominally different: 4.37 vs. 4.88 μm , respectively. The origins of the similarities remain under investigation, and the finding certainly adds a degree of doubt that the source of the EL is intersubband in nature. Notwithstanding this result, much of the original evidence for the first generation device indeed still points to an intersubband transition as the EL source; the polarized emission, the growing peak intensity with pumping current, and the conventional-looking IV curves, for example, all suggest a functioning QC device.

3.9 Conclusions & Future Directions

3.9.1 Summary

With this work in II–VI heterostructures, we have laid a foundation for a new class of QC lasers. The successful demonstration of a II–VI QC laser would be an important milestone; as the first QC laser outside of a III–V materials system, a II–VI QC laser would truly demonstrate the overtly unencumbered flexibility of the quantum cascade.

In the work presented here, we have shown progress toward demonstrating such II–VI QC lasers. We have developed the capability to design II–VI QC structures, which is able to both accurately reproduce observed data from simple single quantum well samples as well as facilitate II–VI QC design development. A typical first step toward the fabrication of intersubband devices is demonstrating intersubband absorption from simple quantum well structures, which we have done. The processes associated with the fabrication of optoelectronic devices often presents a challenge, and we have developed reliable fabrication methods for our II–VI devices. With regard to QC design, we have developed and grown several structures. From these, we have seen intersubband absorption that is in good agreement with calculated absorption energies. Moreover, we have observed TM-polarized electroluminescence, with emission at a wavelength in good agreement with the design. While recent data brings into question the source of the

EL (whether it is intersubband or of some other origin), the IV curves from these devices are further supporting evidence that we have QC structures with properly functioning electron transport.

3.9.2 Future Direction: New II–VI design strategies

Immediate future work will focus on several new design strategies. The growth of ZnCdSe / ZnCdMgSe structures presents a considerable materials and engineering challenge. II–VI QC growth engineers must be even more skilled and accurate in their calibrations than III–V growth engineers. The larger effective mass of II–VI materials means that equivalent errors in layer thickness between the two systems results in a much more significant variation of the quantum well band structure for the II–VI device; simply put, there is less room for error.

While the demands on the II–VI growth effort are large, QC designers can help the process with designs that are specifically aimed at making the growth engineer’s job easier. Two new design strategies—superlattice QC structures and using less wells in the QC period—may mitigate some of the challenges specifically faced by the II–VI material system.

ZnCdSe/ZnCdMgSe superlattice QC structures

A superlattice QC structure [17] is fundamentally different from other QC structures. In superlattice structures, many more quantum well and barrier layers are used for each QC period, with each layer much narrower by comparison. Superlattice QC structures create a “miniband” of states, in contrast to the more discrete nature of states in conventional QC structures. One marked advantage of superlattice structures, especially for II–VI QC growth, is that the thickness of any individual layer is not nearly as critical.

An example of a superlattice QC structure using $\text{Zn}_{0.43}\text{Cd}_{0.57}\text{Se}$ quantum wells and $\text{Zn}_{0.20}\text{Cd}_{0.19}\text{Mg}_{0.61}\text{Se}$ is shown in Fig. 3.12 for an applied field of 70 kV/cm. In angstroms starting from the injection barrier, the layer sequence is **14** / 29 / **8** / 27 / **8** / 25 / **8** / 23 / **8** / 23 / **8** / 22 / **10** / 20 / **9** / 17 / **9** / 16 / **10** / 15 / **11** / 14 / **11** / 12 / **12** / 12 / **11** / **12** / 10 / **12** / 10 / **12** / 9 / **12** / 8 / **13** / 8 / **13** / 8 / **14** / 7 / **14** / 7, where $\text{Zn}_{0.20}\text{Cd}_{0.19}\text{Mg}_{0.61}\text{Se}$ barriers are in bold font and $\text{Zn}_{0.43}\text{Cd}_{0.57}\text{Se}$ wells are in normal

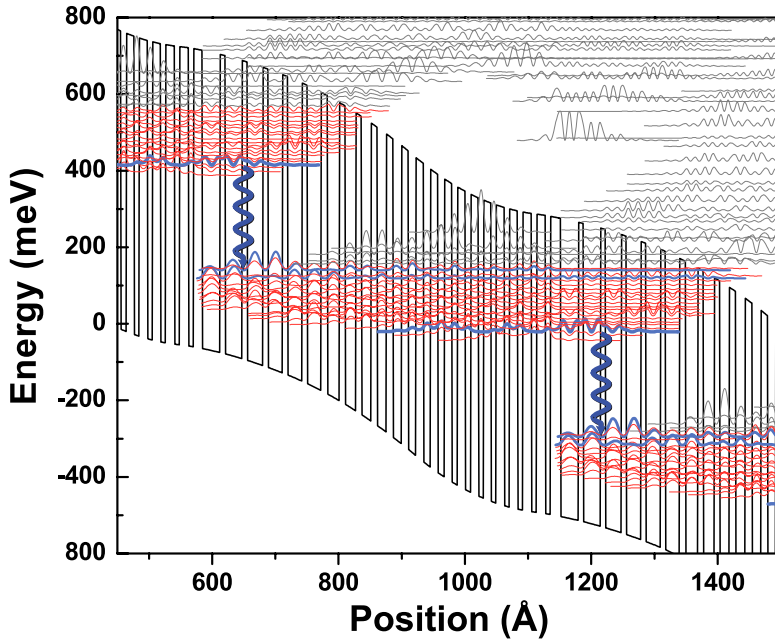


Figure 3.12: Superlattice ZnCdSe/ZnCdMgSE QC structure. Superlattice structures have the advantage that the thickness of any individual layer is not as crucial, which may make the structure easier to grow. This structure, designed in the $Zn_{0.43}Cd_{0.57}Se / Zn_{0.20}Cd_{0.19}Mg_{0.61}Se$ materials system, has a designed photon energy $\mathcal{E}_{ph} = 275$ meV ($\lambda_0 = 4.52 \mu\text{m}$) at an applied field $E_{field} = 70 \text{ kV/cm}$. Band bending of the superlattice structure is seen, resulting from a self-consistent calculation that accounts for energy state positions with the band effects of fixed and free charge.

font. Clearly, this structure contains many more layers than a comparable conventional design, here 44 compared to 28 in Fig. 3.5 which has a similar photon energy. However, the overall period length, 573 Å compared to 534 Å, is not significantly different, so the thickness of the epitaxial growth is about the same.

Fewer layers per QC period

While the superlattice QC structure can make the growth task easier by lessening the importance of individual layer thicknesses, another approach is to decrease the number of layers altogether. By doing this, we can have the same number of photon transitions for a shorter growth time and smaller growth thickness, or equivalently, have more photon transitions for the same epitaxial growth thickness.

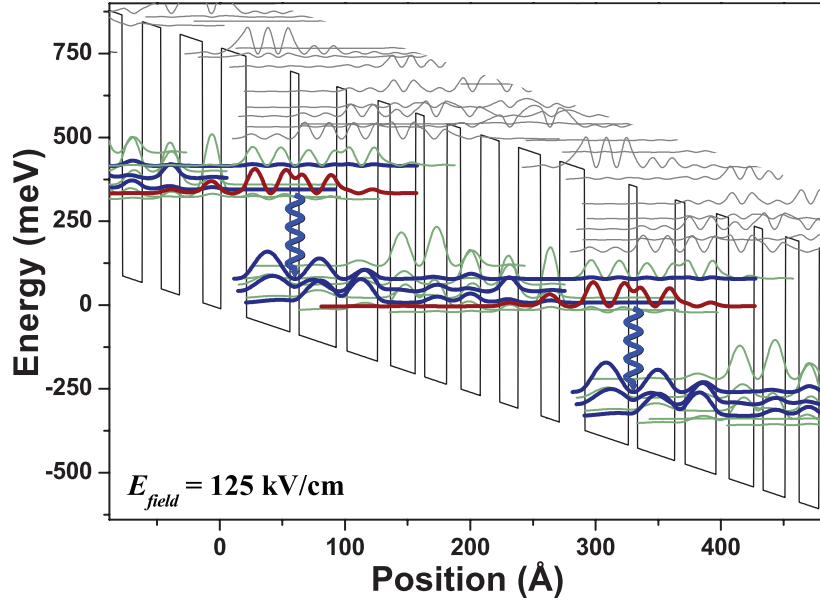


Figure 3.13: ZnCdSe/ZnCdMgSE QC structure with fewer layers. Compared to the first generation design shown in Fig. 3.5 with 28 well and barrier layers, this design has 16 layers for a similar photon energy of $\mathcal{E}_{ph} = 255$ meV ($\lambda_0 = 4.86$ μm). The trade-off is that the field is substantially increased.

The trade-off here, as explained earlier in this chapter, is that a shorter QC period requires a larger applied electric field for any given optical transition energy. However, through the earlier results of this work, we are confident that this II-VI material system can indeed withstand larger fields. As an example, increasing the field to $E_{field} = 125$ kV/cm for a ~ 250 meV photon transition (as in Fig. 3.5), shortens the period length from 534 Å to 270 Å. Specifically, the structure in Fig. 3.13 has a layer sequence, in angstroms starting from the injection barrier, **20** / 35 / 7 / 30 / **8** / 25 / **10** / 20 / 7 / 18 / **11** / 16 / **15** / 15 / **18** / 15, where $\text{Zn}_{0.20}\text{Cd}_{0.19}\text{Mg}_{0.61}\text{Se}$ barriers are in bold font and $\text{Zn}_{0.43}\text{Cd}_{0.57}\text{Se}$ wells are in normal font. With only 16 layers compared to 28 per QC period, growth may be simplified for this structure.

QC structure with larger photon energy

An open question in the work presented is the true origin of the observed EL described in Section 3.7. Due to the similar (but not the same) wavelengths of the first (Fig. 3.5) and second (Fig. 3.11) generation designs, the similarity in emission may be simply

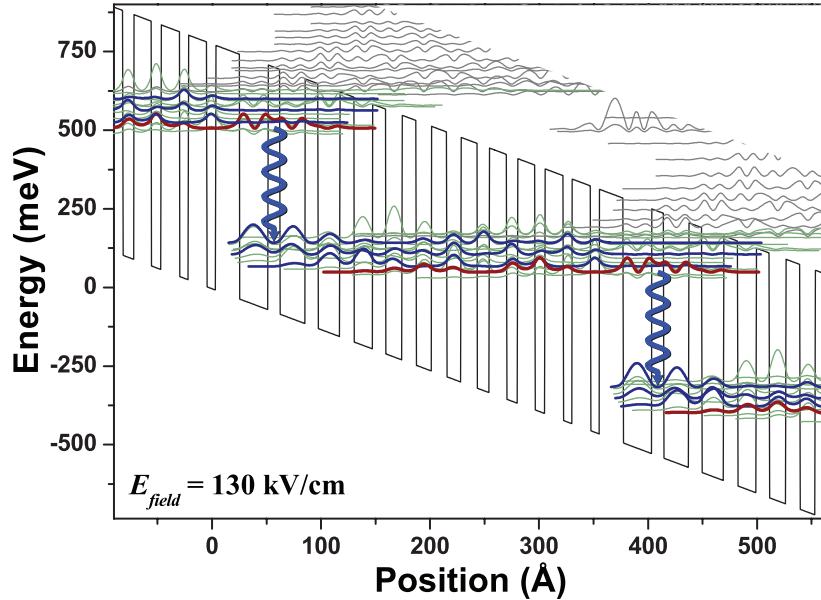


Figure 3.14: Short wavelength ZnCdSe/ZnCdMgSE QC structure. Investigating a higher photon energy QC structure may be beneficial. Here, a $\mathcal{E}_{ph} = 370$ meV ($\lambda_0 = 3.35$ μm) structure achieved using $\text{Zn}_{0.43}\text{Cd}_{0.57}\text{Se}$ quantum wells and $\text{Zn}_{0.20}\text{Cd}_{0.19}\text{Mg}_{0.61}\text{Se}$ barriers.

result from the emission being broad. To test this theory and confirm that we have truly demonstrated intersubband QC EL, a structure that substantially changes the photon energy will be helpful. In a larger photon energy structure, the emission may be easier to observe due to the larger output powers resulting from more energy per photon.

While today's QC designs seek to have ample confinement of the upper laser state within the quantum wells to prevent thermal escape, there have been numerous examples where this is not the case [34], [96]. And indeed, if one is looking for only low temperature emission, having the upper laser state deeply confined in the quantum wells is not necessary. As an example, Fig. 3.14 shows a design for a $\lambda_0 = 3.35$ μm QC structure. The layer sequence, in angstroms from the injection barrier, is **22 / 26 / 11 / 23 / 12 / 20 / 13 / 17 / 12 / 15 / 13 / 14 / 14 / 13 / 15 / 11 / 16 / 10 / 16 / 9 / 17 / 8 / 17 / 8**, with $\text{Zn}_{0.20}\text{Cd}_{0.19}\text{Mg}_{0.61}\text{Se}$ barriers in bold font and $\text{Zn}_{0.43}\text{Cd}_{0.57}\text{Se}$ wells in normal font. Here, even with a substantially larger photon energy ($\mathcal{E}_{ph} = 370$ meV), the QC period length is still kept to a relatively low 352 \AA .

3.9.3 Future Direction: Strain-compensated growth

While increasing the Mg content from the current $x = 61\%$ mole fraction ($\text{Zn}_{0.20}\text{Cd}_{0.19}\text{Mg}_{0.61}\text{Se}$) to the lattice-matched 91% mole fraction (that is, using $\text{Zn}_{0.09}\text{Mg}_{0.91}\text{Se}$) in the barrier layers would support substantially larger photon energies for shorter wavelength generation, another approach might be to incorporate strain. Much as strain compensation has been used for InGaAs / AlInAs structures in III-V QC lasers, we could use a similar concept for ZnCdSe / ZnCdMgSe. The InGaAs and AlInAs materials are well-suited to this scheme, since both have bandgaps that increase with compositions that lead to tensile strain and decrease with compositions that lead to compressive strain. When looking at only ZnCdSe and ZnMgSe materials (not including the quaternary ZnCdMgSe), using strain compensation does not appear possible; like InGaAs and AlInAs, ZnCdSe has a bandgap that decreases with compositions that lead to compressive strain, but ZnMgSe is just the opposite. Therefore, adding tensile strain to one material and compressive strain to the other material in the ZnCdSe/ZnMgSe system will always lead to smaller band offsets. However, with the quaternary ZnCdMgSe, we gain an extra degree of freedom in material composition that again allows strain compensation to be beneficial to increasing the band offset. Thus, strain compensation could be used in the current ternary/quaternary II-VI system without the inclusion of substantially more Mg that in turn leads to growth and reliability challenges from Mg oxidation.

3.9.4 Future Direction: Fabrication of II-VI QC laser waveguides

When it comes to fabricating laser ridges from our II-VI materials grown on InP, we confront a challenge. With a refractive index in the II-VI materials that is substantially lower than that of the III-V materials, creating a waveguide that supports an optical mode with a high gain region confinement factor cannot be done using the traditional methods. In conventional QC lasers grown in InP, the active core has a larger refractive index than the InP cladding, so the mode is easily confined in the active core. Conversely, with II-VI on InP, we have a situation similar to that confronted by InAs/AlSb QC lasers and GaAs/AlGaAs lasers. These devices overcome the challenge by growing thick buffer or superlattice cladding confinement layers, or using in-cladding doping to reduce the refractive index (plasmon-enhanced waveguides).

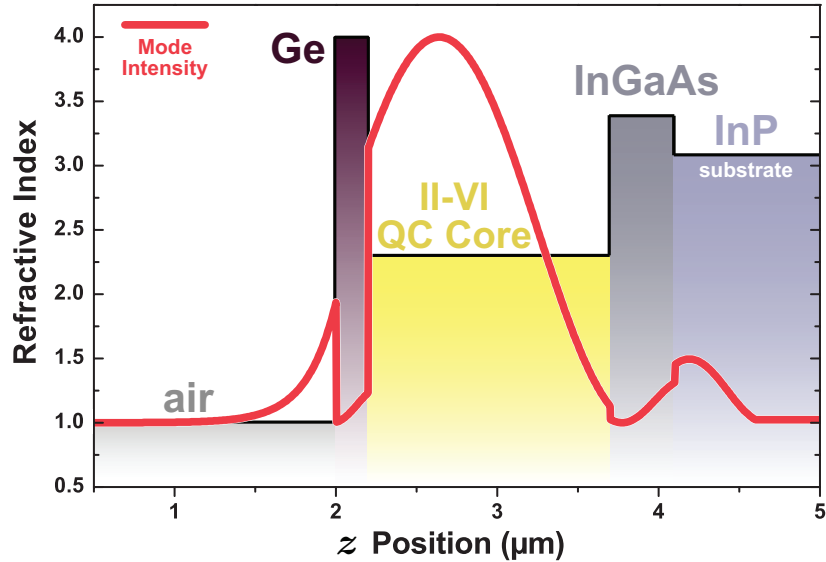


Figure 3.15: II–VI QC waveguide. Because of the low refractive index of II–VI materials relative to InP, making high confinement waveguides for the active II–VI region is difficult. One possible solution is using a Ge top cladding that is deposited during laser ridge fabrication. As shown here for 4.2 μm light, this structure is capable of guiding an optical mode.

Growing optically thick buffer layers of II–VI materials may prove difficult. However, waveguides can still be made. One solution is using a high index $\text{In}_{0.53}\text{Ga}_{0.47}\text{As}$ buffer grown on InP to hold the optical mode; here the II–VI active gain layers would just be off the mode center, and we will have to accept a lower confinement factor. Yet, we may be able to do better. QC lasers using air as waveguide top cladding have been demonstrated by Moreau *et al.* [97], ostensibly in their work for evanescent wave sensing using the optical mode of the laser cavity. Also, as suggested (for example) by Almeida *et al.* [98], modes can be supported in a low index material that is sandwiched between two high index materials, given proper geometries and dimensions for the supported wavelength. For a II–VI QC laser, we can create a high confinement waveguide that symmetrically encompasses the QC active core by using $\text{In}_{0.53}\text{Ga}_{0.47}\text{As}$ as a high index bottom cladding and evaporated Ge as a high index top cladding after initially fabricating the laser ridge with an air top cladding. The mode profile for such a structure is shown in Fig. 3.15.

Chapter 4

Excited State Quantum Cascade Lasers and High k -Space Lasing

The work-horse material system for mid-infrared QC lasers—InGaAs / AlInAs—has a limited range of wavelengths where the fundamental properties of the material system are most amenable to high performance QC designs. The lower end of this “sweet spot” is currently around 4.2 μm , as discussed in Chapter 2. And while the lower limit imposed by material band offsets is relatively abrupt, QC lasers experience gradual but steadily decreasing performance at longer wavelengths. Beyond 12 μm , performance is severely restrained: CW RT QC laser sources beyond 12 μm have not yet been demonstrated.

Indeed, the lack of high performance long-wavelength sources is a problem; a host of pressing applications are in critical need of such technology. For example, the strongest absorption lines for aromatic hydrocarbons are in the 12–16 μm range, as shown in Fig. 4.1 for BTEX (benzene, toluene, ethylbenzene, and xylenes) compounds. The ability to detect benzene, with a fundamental absorption at 14.8 μm , is of particular interest to the petro-chemical refining industry. Another immediate example is uranium hexafluoride (UF_6), a molecule that in its gas phase is a primary precursor in uranium enrichment processes [99]. UF_6 has isotopically-distinct absorption lines near 16 μm [100] [101].

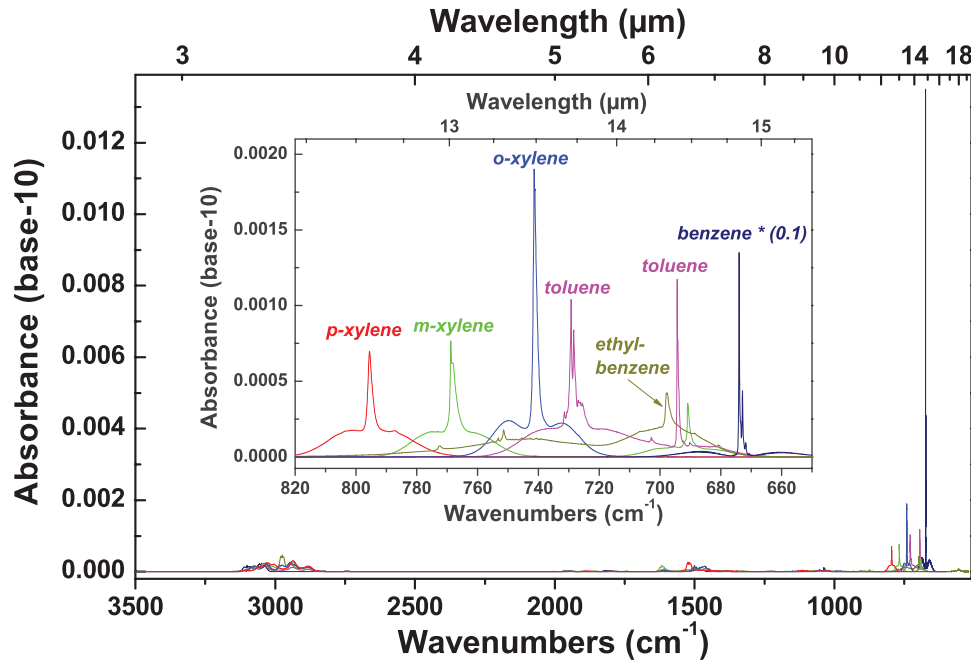


Figure 4.1: Absorption spectra for BTEX molecules. Compared with the fundamental vibrational absorption lines of most molecules, aromatic hydrocarbons have their strongest absorption lines at relatively long wavelengths. Benzene, for example, has an especially strong absorption at 14.8 μm . The absorption lines of BTEX compounds are spectrally distinct, providing an avenue for detection selectivity of these compounds.

The absence of RT CW QC laser sources with emission beyond 12 μm has not been for a lack of trying. Pushing QC capabilities to longer wavelengths began as early as 1998, when C. Gmachl *et al.* reported 13 μm emission from a convention single-phonon, three well active region QC structure [102]. This laser operated up to a pulsed $T_{max} \approx 175$ K. In 1999, A. Tredicucci *et al.* found the QC superlattice architecture well-suited for longer-wavelength emission, with the demonstration of lasing at 17 μm [103]. Superlattice structures later showed emission at 19 μm [104] and then 21.5 and 24 μm [11]. Each of these superlattice demonstrations exhibited a pulsed $T_{max} \approx 140$ K. Without question the best performance demonstrated by a long-wavelength QC laser was by M. Rochat *et al.* at 16 μm [105] [15]. For this “bound-to-continuum” structure, pulsed $T_{max} > 333$ K. Clearly, history has proven longer-wavelength light generation to be a substantial challenge.

In this chapter, I discuss a QC laser design strategy—namely the use of “excited state” optical transitions—intended to boost oscillator strength and thereby overcome many of the aggravating factors preventing high performance lasing at longer wavelengths. While the excited state concept shows promise for such an effect, we discovered that these excited state QC structures are capable of simultaneous dual-wavelength lasing from two different optical transitions within the active region. Furthermore, the secondary emission shows some extra-ordinary properties. The interplay between charge carriers within the active region led to the secondary lasing transition being suppressed until a thermal turn-on; under certain circumstances, performance for the secondary emission actually *improves* with temperature. Ultimately, we found that the secondary emission is lasing only high in k -space: the lasing originates from electrons in a highly non-equilibrium state.

4.1 The Long-wavelength Challenge

The technical hurdles confronted in the pursuit of long-wavelength lasing are perhaps even more daunting than those imposed by material band offsets at the short wavelength limit. Two primary mechanisms—optical loss and decreased upper laser state lifetimes—individually compound in a situation that frustrates QC designs and performance at longer wavelengths.

Optical loss, or waveguide loss α_w , is related to the complex refractive index \tilde{n} as

$$\alpha_w = 2 \frac{2\pi \text{Im}[\tilde{n}]}{\lambda_0}. \quad (4.1)$$

In the long-wave infrared region, \tilde{n} is especially impacted by the presence of free carriers (*i.e.*, electrons). For bulk materials, \tilde{n} can be estimated using the Drude model. Given a plasma frequency ω_p as

$$\omega_p = \sqrt{\frac{4\pi q^2 n_{3D}}{m^* \epsilon_{inf}}} \quad (4.2)$$

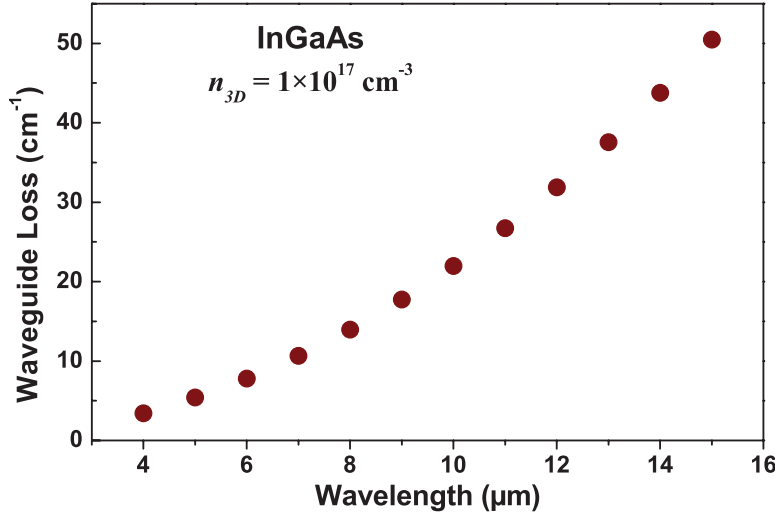


Figure 4.2: Optical absorption of bulk InGaAs. Calculated for $\text{In}_{0.53}\text{Ga}_{0.47}\text{As}$ with a free electron density $n_{3D} = 1.0 \times 10^{17} \text{ cm}^{-3}$. Waveguide loss increases super-linearly with wavelength.

which is dependent on the free electron density n_{3D} and the electron effective mass m^* , the complex refractive index \tilde{n} is

$$\tilde{n} = \sqrt{\epsilon_\infty \left(1 - \frac{\omega_p^2}{\omega^2 + i\frac{\omega}{\tau}} \right)} \quad (4.3)$$

where τ is the mean collision time for free electrons, usually taken as 0.1 ps in III–V semiconductors. A calculation for α_w in bulk $\text{In}_{0.53}\text{Ga}_{0.47}\text{As}$ for a typical doping $n_{3D} = 1 \times 10^{17} \text{ cm}^{-3}$ shows the dramatic increase of waveguide loss with wavelength. As shown in Fig. 4.2, while at $\lambda = 5 \mu\text{m}$ the waveguide loss $\alpha_w \approx 5 \text{ cm}^{-1}$, at $\lambda = 15 \mu\text{m}$, $\alpha_w \approx 50 \text{ cm}^{-1}$!

The ability to attain population inversion also becomes more difficult at longer wavelengths. A fundamental mechanism of most all QC lasers is the use of LO phonon scattering to rapidly depopulate the lower laser state. For a generic three level QC active region, as in Fig. 4.3b, one seeks to position the lowest two energy states one LO phonon energy apart ($\mathcal{E}_{21} \geq \hbar\omega_{LO}$); in InGaAs, $\hbar\omega_{LO} \approx 34 \text{ meV}$ (equivalent to a wavelength of 36 μm). As shown in Fig. 4.3a, the LO phonon scattering time for $\mathcal{E}_{21} = \hbar\omega_{LO}$ is about 0.2 ps. For the optical transition ($|3\rangle \rightarrow |2\rangle$ in Fig. 4.3b), the lifetime due to phonon scattering decreases as the transition energy decreases. However, as \mathcal{E}_{32} approaches \mathcal{E}_{21} ,

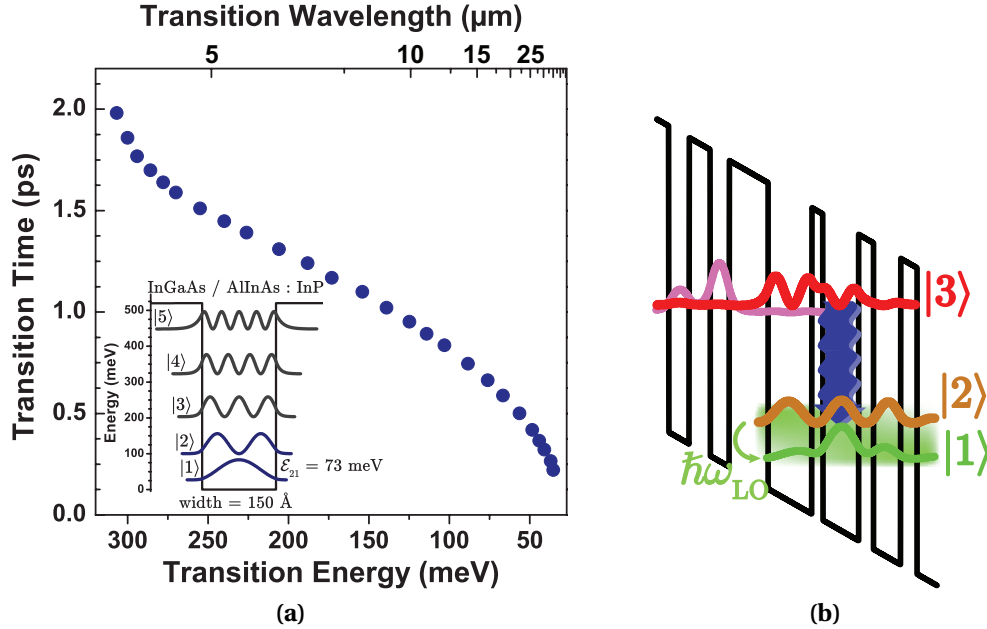


Figure 4.3: LO phonon lifetime vs. transition wavelength. (a) For a single quantum well, the LO phonon scattering time is plotted for decreasing $|2\rangle \rightarrow |1\rangle$ transition energy \mathcal{E}_{21} (increasing transition wavelength). For $\hbar\omega_{LO} < 34$ meV ($\approx 36 \mu\text{m}$), the small transition energy precludes scattering by LO phonons, the fastest scattering process in semiconductors. (b) A schematic representation of a conventional single-phonon active region with optical transition $|3\rangle \rightarrow |2\rangle$ and phonon transition $|2\rangle \rightarrow |1\rangle$.

τ_{32} and τ_2 become similar. With population inversion (and therefore gain) proportional to $\left(1 - \frac{\tau_2}{\tau_{32}}\right)$, maintaining the ability to achieve population is most definitely a concern at longer wavelengths.

The combination of small photon energies, high waveguide losses, and short upper-state lifetimes make long-wavelength QC lasers fundamentally inefficient devices. From Chapter 2, wall-plug efficiency

$$\eta_{WPE} = \left(\frac{\mathcal{E}_{ph}}{\mathcal{E}_{ph} + \Delta_{inj} + \frac{qR_{series}I}{N_p}} \right) \left(\frac{\alpha_m}{\alpha_w + \alpha_m} \right) \left(\frac{\tau_{eff}}{\tau_{eff} + \tau_2} \right) \left(\frac{J}{J - J_{th}} \right) \xi_{inj}. \quad (4.4)$$

The implications of long-wavelength lasing affect nearly every component term that contributes to the overall wall-plug efficiency. The small photon energy \mathcal{E}_{ph} relative to the fixed values of Δ_{inj} and R_{series} substantially reduce voltage efficiency. And while high waveguide losses hurt the out-coupling efficiency, they also decrease current efficiency

by increasing J_{th} . Likewise, the short upper-state lifetimes increase J_{th} and decrease current efficiency, in addition to decreasing transition efficiency term.

4.2 Excited State Transitions

A chief battle long-wavelength lasers must overcome is simply “turning on”—*i.e.*, reaching threshold—at a current density below J_{max} . The challenges posed by long-wavelength lasing are in large part fundamental in nature; the effects of free carrier absorption and phonon lifetimes are built-in properties of the system. However, many design parameters affected by the QC design itself are included in threshold current density:

$$J_{th}(T = 0) = \frac{\alpha_m + \alpha_w}{g\Gamma} \quad (4.5)$$

where

$$g = \frac{4\pi q}{\lambda_0 \epsilon_0 n_{eff}} \frac{1}{\delta\mathcal{E}_{ul}} \frac{\tau_u (1 - \tau_\ell/\tau_{ul}) z_{ul}^2}{L_p}. \quad (4.6)$$

If optical losses and phonon scattering times cannot be directly affected by clever design, another strategy might serve to compensate for these effects by boosting the values of other parameters. For example, the optical dipole matrix element z_{ul} contributes quadratically to the gain. Thus, a modest increase in z_{ul} can have a rather substantial overall impact on lowering J_{th} .

The optical dipole matrix element between two energy states z_{ul} can be simplistically thought of as closely related to the amount of spatial overlap between those states: the more overlap, the larger is z_{ul} . Using the example of a single quantum well, as in Fig. 4.4, it is interesting to observe the relation between various consecutive energy states and z_{ul} . By keeping the transition energy constant—in this case $\mathcal{E}_{ul} = 125$ meV—we obtain a fair comparison of z_{ul} for the ladder of adjacent energy states in the well. Clearly, z_{ul} increases for higher-lying transitions. In this example, $z_{21} = 23.2$ Å and $z_{32} = 30.2$ Å, suggesting a potential increase in gain by a factor of 1.7 (considering the quadratic contribution to optical gain) when using a $|3\rangle \rightarrow |2\rangle$ optical transition rather than a $|2\rangle \rightarrow |1\rangle$ transition.

Further examination of Fig. 4.4a suggests another benefit from using excited state transitions. To keep the transition energy constant while climbing the ladder of

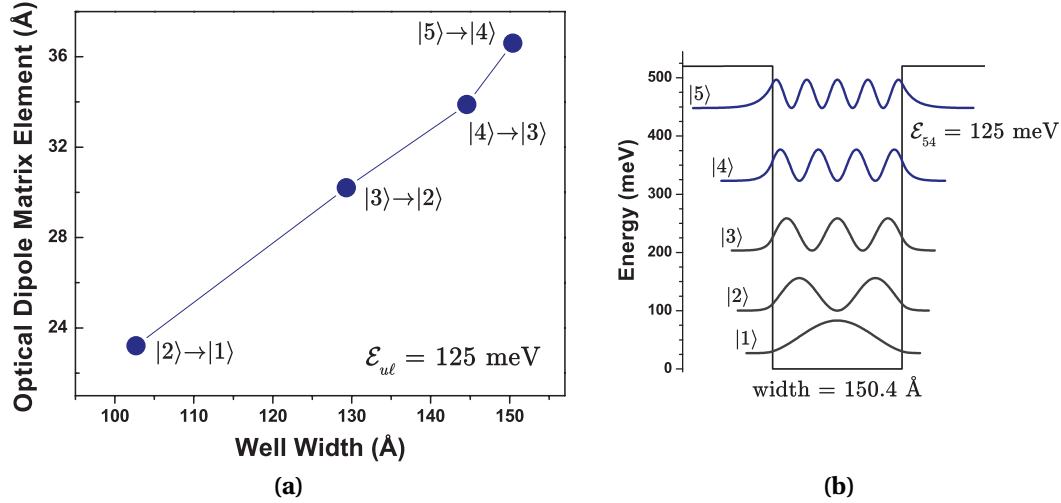


Figure 4.4: Optical dipole matrix elements for a single quantum well. (a) The calculated optical dipole matrix element of the specified transition, where well width has been adjusted to give a transition energy $\mathcal{E}_{ul} = 125 \text{ meV}$. For this constant transition energy, the optical dipole matrix elements and quantum well widths increase for transitions between higher lying adjacent levels. Here we simulate optical transitions in the InGaAs/AlInAs:InP system, which has a conduction band offset of 520 meV. (b) An example configuration for the single quantum well calculation, where the $|5\rangle \rightarrow |4\rangle$ transition energy $\mathcal{E}_{54} = 125 \text{ meV}$ at a well width of 150.4 Å.

transitions between adjacent states, the well itself must be widened. Intuitively, wider wells mean that a relatively smaller portion of the upper laser state wavefunction is perturbed by inhomogeneity at well-barrier interfaces. In most QC lasers, interface roughness-induced broadening is the dominant contributor to the gain spectrum width $\delta\mathcal{E}_{ul}$ [106]. With J_{th} being proportional to $\delta\mathcal{E}_{ul}$, wider QC active region quantum wells can be expected to be a net benefit for laser performance.

By this logic, making use of “excited state” transitions—those made purely from quantum mechanical excited states—is a potential approach for increasing QC laser gain and decreasing threshold current densities. Yet with the multitude of coupled quantum wells that make up a QC laser design, it may not be immediately clear what an excited state QC laser might look like. In the case of the single quantum well in Fig. 4.4, identifying excited states is quite simple: the lowest energy state in the well is the ground state, and each state above the ground state is an excited state. Thus, any transition not between $|2\rangle \rightarrow |1\rangle$ is an excited state transition.

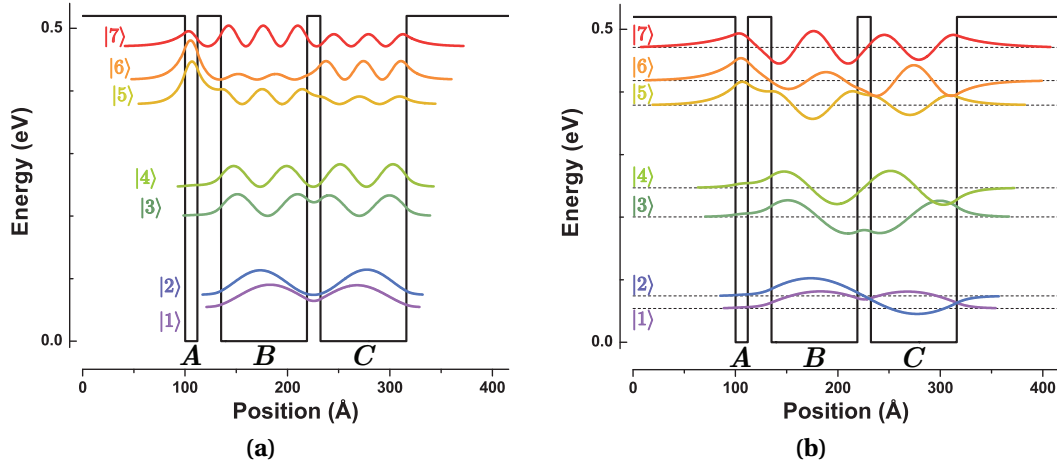


Figure 4.5: Energy state mixing in coupled quantum wells. A pictorial example of energy state mixing calculated for a three coupled quantum well $\text{In}_{0.53}\text{Ga}_{0.47}\text{As} / \text{Al}_{0.48}\text{In}_{0.52}\text{As}$ system. The quantity $\langle\psi(z)|\psi(z)\rangle$ is plotted in (a) and $\psi(z)$ is plotted in (b). States $|1\rangle$ and $|2\rangle$ are ground states, and $|3\rangle$ and $|4\rangle$ are first-excited states. States $|5\rangle$, $|6\rangle$, and $|7\rangle$ are largely second-excited states, with some ground state character in well A.

In the case of coupled quantum wells, what particularly matters for our characterization of excited state transitions is more the “shape” of the energy state, rather than an individual state’s position relative to the other states in the system. A pictorial example may be helpful. In Fig. 4.5, we have three coupled quantum wells; Fig. 4.5a plots our usual $\langle\psi(z)|\psi(z)\rangle$ while Fig. 4.5b plots $\psi(z)$. As in our example of a single quantum well, each of the coupled quantum wells will contribute to the system an energy state that looks quantum mechanically like a ground state; that is, each coupled well contributes to the system one state with a shape having zero nodes within each coupled well. Momentarily ignoring the narrow well A, the states labeled $|1\rangle$ and $|2\rangle$ are the “ground states” for the coupled wells B and C. Likewise, each coupled well will contribute one first-excited state; the states labeled $|3\rangle$ and $|4\rangle$ are “first-excited states” for the coupled wells B and C, since they each have one node within each coupled quantum well. The characterization gets slightly more complicated when narrow wells are placed adjacent to wide wells (as in the case of a QC laser with the conventional narrow injector well adjacent to the first wide active region well). This creates a situation where a ground state “mixes” with an excited state, such as the case for states $|5\rangle$, $|6\rangle$, and $|7\rangle$. Each state in this group has zero nodes in well A, but two nodes in wells B and C; over most of their

probability densities, $|5\rangle$, $|6\rangle$, and $|7\rangle$ are characteristically second-excited states, with some ground state shape in well A.

Using this convention, most all QC lasers to date have used a first-excited state and ground state, respectively, for the upper and lower states of the laser transition. For example, the now classic double-phonon design * [16] uses three wide active region wells, thus yielding three ground states $|3\rangle$, $|2\rangle$, and $|1\rangle$ —with \mathcal{E}_{32} and \mathcal{E}_{21} roughly the energy of one LO phonon. The upper laser state, conventionally labeled $|4\rangle$, is a first-excited state, making the laser transition $|4\rangle \rightarrow |3\rangle$ a first-excited state to ground state transition. There are, however, a few examples in the literature of QC lasers that have used optical transitions composed completely from excited states. In an attempt to achieve a “cascaded” QC laser—that is, a QC active region with sequentially stacked optical transitions that would be a scheme for correlated photon generation [107]—J. Faist *et al.* injected electrons into state $|3\rangle$ of a single quantum well active region. In this work, they observed lasing from $|3\rangle \rightarrow |2\rangle$, an excited state transition similar to $|3\rangle \rightarrow |2\rangle$ in Fig. 4.4b. Notably, they were unable to achieve lasing from $|2\rangle \rightarrow |1\rangle$. More examples exist for THz QC lasers—lasers where $\hbar\omega_{ph} < \hbar\omega_{LO}$. In a THz QC structure, G. Scalari *et al.* also observed stacked transitions; in this case different applied electric field values resulted in switching emission between $|3\rangle \rightarrow |2\rangle$ and $|4\rangle \rightarrow |3\rangle$, yielding field-selectable output at either $\mathcal{E}_{32} = 5.75$ meV (1.39 THz) or $\mathcal{E}_{43} = 9.5$ meV (2.3 THz) [108].

4.3 Excited State QC Laser Design

We have implemented an excited state QC laser design in a two-well active region configuration using $In_{0.53}Ga_{0.47}As$ wells and $Al_{0.48}In_{0.52}As$ barriers. The conduction band energy diagram is shown in Fig. 4.6. Rather than injecting electrons into state $|3\rangle$ as in a conventional two-well (single-phonon) QC laser, our injector region is specifically designed on the downstream side to inject electrons into state $|5\rangle$. Our optical transition is thus designed to be between states $|5\rangle$ and $|4\rangle$; because $|5\rangle$ is a second-excited state and $|4\rangle$ is a first-excited state, the transition $|5\rangle \rightarrow |4\rangle$ is an excited state transition. The design energy $\mathcal{E}_{54} = 128$ meV ($\lambda = 9.68$ μm). The injector region is also designed with relatively narrow barriers on the upstream side; these narrow barriers result in a large

* For an example conventional double phonon band structure, see Fig. 5.1.

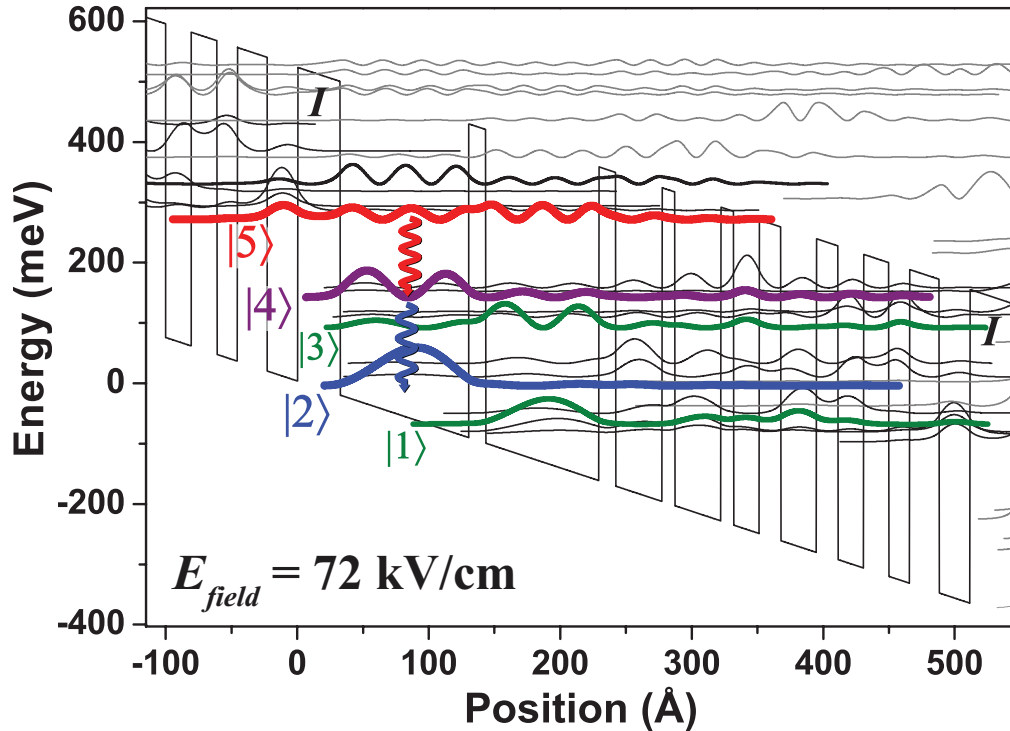


Figure 4.6: Excited state QC laser band diagram. Optical transitions are observed between states $|5\rangle \rightarrow |4\rangle$ and $|4\rangle \rightarrow |2\rangle$.

splitting of the injector states, intended to efficiently empty out the active region states $|4\rangle$ through $|1\rangle$.

The laser was grown using gas-source molecular beam epitaxy on a low-doped ($n_{3D} < 2 \times 10^{17} \text{ cm}^{-3}$) InP:S substrate. The active core consisted of 40 active-injector region periods, and the design included $0.55 \mu\text{m}$ of $\text{In}_{0.53}\text{Ga}_{0.47}\text{As}$ (Si-doped $n_{3D} = 5 \times 10^{16} \text{ cm}^{-3}$) for the cladding regions above and below the QC stack. A $0.9 \mu\text{m}$ InP ($n_{3D} = 5 \times 10^{16} \text{ cm}^{-3}$) buffer layer was grown before the bottom $\text{In}_{0.53}\text{Ga}_{0.47}\text{As}$ cladding. After the top $\text{In}_{0.53}\text{Ga}_{0.47}\text{As}$ cladding, additional cladding layers of $3.9 \mu\text{m}$ InP ($n_{3D} = 5 \times 10^{16} \text{ cm}^{-3}$) and $1.1 \mu\text{m}$ InP ($n_{3D} = 6.7 \times 10^{18} \text{ cm}^{-3}$) were grown, before capping the growth with $0.06 \mu\text{m}$ of $\text{In}_{0.53}\text{Ga}_{0.47}\text{As}$ ($n_{3D} = 2 \times 10^{19} \text{ cm}^{-3}$).

The as-grown structure, plotted in the Fig. 4.6 conduction band diagram is, in angstroms from the injection barrier, **32.3 / 97.7 / 12.9 / 86.0 / 12.9 / 35.2 / 9.7 / 35.2 / 9.7 / 19.5 / 16.1 / 27.4 / 16.1 / 19.5 / 19.4 / 15.6 / 22.6 / 23.5**. Here, $\text{Al}_{0.48}\text{In}_{0.52}\text{As}$ layers are in

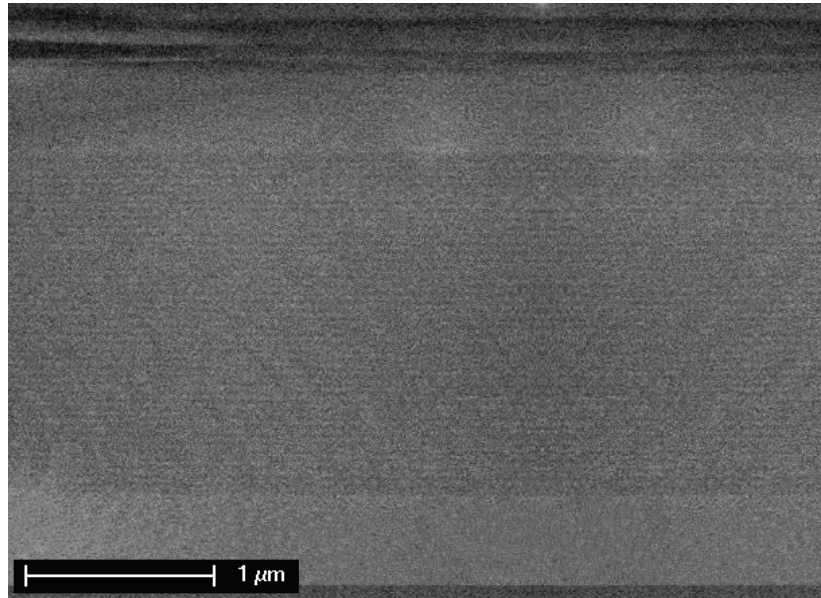


Figure 4.7: SEM of excited state QC stack and waveguide. From bottom to top, color separations are seen representing the InP substrate, In_{0.53}Ga_{0.47}As bottom cladding, 40 period QC stack, In_{0.53}Ga_{0.47}As top cladding, and InP top cladding.

bold type, In_{0.53}Ga_{0.47}As layers are in plain type, and layers Si-doped $n_{3D} = 2 \times 10^{16} \text{ cm}^{-3}$ are underlined; the structure has an active core sheet density $n_s = 1.6 \times 10^{11} \text{ cm}^{-2}$.

Following growth, we post-calibrated our structure by measuring active region and cladding layer thicknesses with high magnification scanning electron microscope (SEM) images, such as in Fig. 4.7. Here, we are able to see each individual QC period in the active core, along with the In_{0.53}Ga_{0.47}As cladding layers, giving us an accurate measurement of the actual period thicknesses. In_{0.53}Ga_{0.47}As cladding thicknesses showed the In_{0.53}Ga_{0.47}As growth rate was slow by a factor of 0.96 from the original calibration; the active core thickness showed the Al_{0.48}In_{0.52}As growth rate was slow by a factor of 0.80 from the original calibration.

To confirm accuracy of our post-calibrated structure, we analyzed the wafer with high resolution double crystal X-ray diffraction. X-ray data show the primary InP reflection along with five satellite peaks that correspond to the QC core periodicity. Analysis of the satellite peak positions shows a QC period length of 489.2 Å with lattice mismatch of 0.04%. Our post-growth SEM-based characterization resulted in a period length of 511.3 Å. In comparing these two numbers, it is important to note that X-ray

data was taken for a sample from the wafer edge, which generally has thinner layer thicknesses than the “prime real estate” of the wafer center. The data set as a whole is consistent, since such a narrowing in layer thickness from center to edge is standard in MBE-grown material.

Lasers were processed as deep-etched ridge waveguides with stripe widths ranging from 9 to 15 μm by conventional photolithography and wet chemical etching, and were electrically insulated by 0.3 μm thick SiN_x . After evaporation of a Ti/Au (30 nm / 300 nm) top contact, the sample was thinned to $\sim 200 \mu\text{m}$ and a back Ge/Au (30 nm / 300 nm) contact was deposited. Laser bars were cleaved, mounted epitaxial-side up on Cu heat sinks with In solder, and wire bonded. Electroluminescence (semi-circular cleaved-mesa) devices were also fabricated.

4.4 Device Emission Characteristics

4.4.1 Electroluminescence and Identification of the Optical Transitions

Emission spectra for EL mesa structures were collected using an FTIR spectrometer in step scan mode. Electroluminescence data are summarized in Fig. 4.8 for heat sink temperatures T_{sink} at 80, 120, and 160 K. The data clearly show two distinct emission peaks, one near $\lambda \approx 8 \mu\text{m}$ and one near $\lambda \approx 10 \mu\text{m}$. At higher injection currents, higher photon energy emission is observed near $\lambda \approx 6.5 \mu\text{m}$. The two primary emission peaks have features largely independent of each other. As both injection current and temperature increase, the $\sim 8 \mu\text{m}$ emission gets stronger in relation to the $\sim 10 \mu\text{m}$ emission. Fitting Lorentzian line shapes to the individual peaks helps further quantify distinguishing characteristics. As electric field changes, a clear Stark tuning is present for both emission peaks; however, the peaks tune in opposite directions. As indicated in Fig. 4.8 for $T_{sink} = 80 \text{ K}$ and explicitly plotted in Fig. 4.9, the $\sim 10 \mu\text{m}$ emission blue-shifts from 118 to 134 meV over an increasing applied field range of 15 kV/cm, while the $\sim 8 \mu\text{m}$ emission red-shifts from 156 to 152 meV over the same field range. Such field-dependent behavior suggests that the $\sim 10 \mu\text{m}$ emission results from a transition that is rather diagonal in nature, while the $\sim 8 \mu\text{m}$ emission is from a transition that is more vertical. The spectral widths of each peak additionally support diagonal and

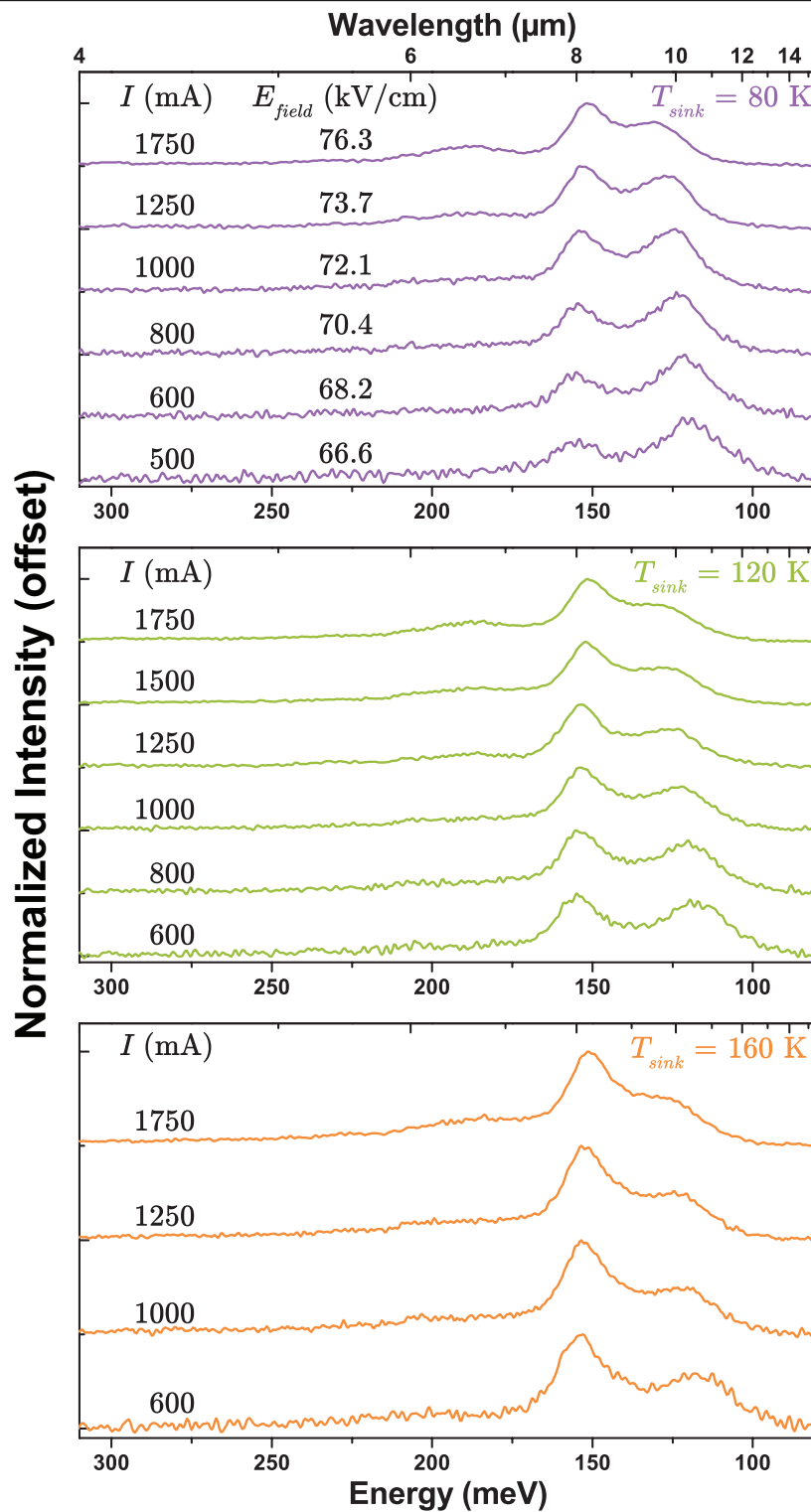


Figure 4.8: Excited state structure electroluminescence spectra. Electroluminescence spectra from a 0.027 mm^2 semi-circular mesa. Data were taken with current pulse width $t_{\text{pulse}} = 100 \text{ ns}$ at an 80 kHz repetition rate.

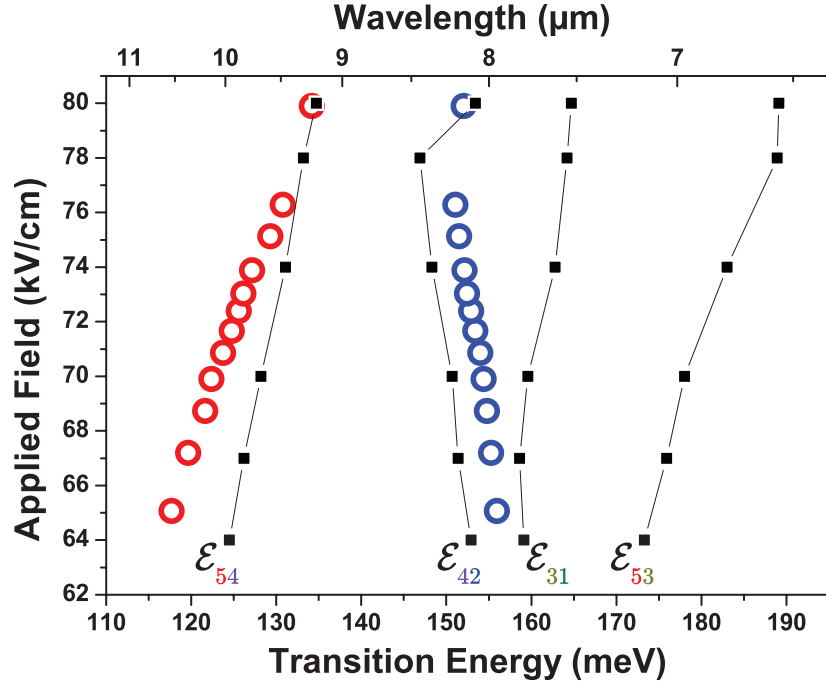


Figure 4.9: Excited state transition identification. Measured and calculated values of the optical transition energies in EL as a function of the electric field. Hollow circles represent the center points of multi-Lorentzian fits to the EL data as displayed in Fig. 4.8 for $T_{sink} = 80$ K. Solid squares show the calculated transition energies.

vertical origins for the ~ 10 and ~ 8 μm peaks. At $E_{field} = 72$ kV/cm, the $\sim 10 \mu\text{m}$ emission ($\hbar\omega_{ph} = 125.6$ meV) has a FWHM $\delta\mathcal{E}_{ul} = 18.7$ meV ($\frac{\delta\mathcal{E}_{ul}}{\hbar\omega_{ph}} = 14.9\%$) and the $\sim 8 \mu\text{m}$ emission ($\hbar\omega_{ph} = 152.9$ meV) has $\delta\mathcal{E}_{ul} = 16.2$ meV ($\frac{\delta\mathcal{E}_{ul}}{\hbar\omega_{ph}} = 10.6\%$). Because diagonal transitions are more heavily influenced by interface roughness, such transitions are expected to be spectrally broader [109].

We identified the origin of the two transitions within the active region structure using the properties and behavior of the EL emission. We calculated the energies and field-dependent behavior of all possible optical transitions within the structure, and in Fig. 4.9, we show this data for the transitions $|5\rangle \rightarrow |4\rangle$, $|4\rangle \rightarrow |2\rangle$, $|3\rangle \rightarrow |1\rangle$, and $|5\rangle \rightarrow |3\rangle$. As expected, our designed excited state $|5\rangle \rightarrow |4\rangle$ transition is the source of the $10 \mu\text{m}$ light. Because both the field-dependent behavior and energies of the $|5\rangle \rightarrow |3\rangle$ and $|3\rangle \rightarrow |1\rangle$ transitions differ from the EL and laser spectra, we rule out these two transitions as the source of the $\sim 8 \mu\text{m}$ light. We thus identify the source of the $\sim 8 \mu\text{m}$ light to be the

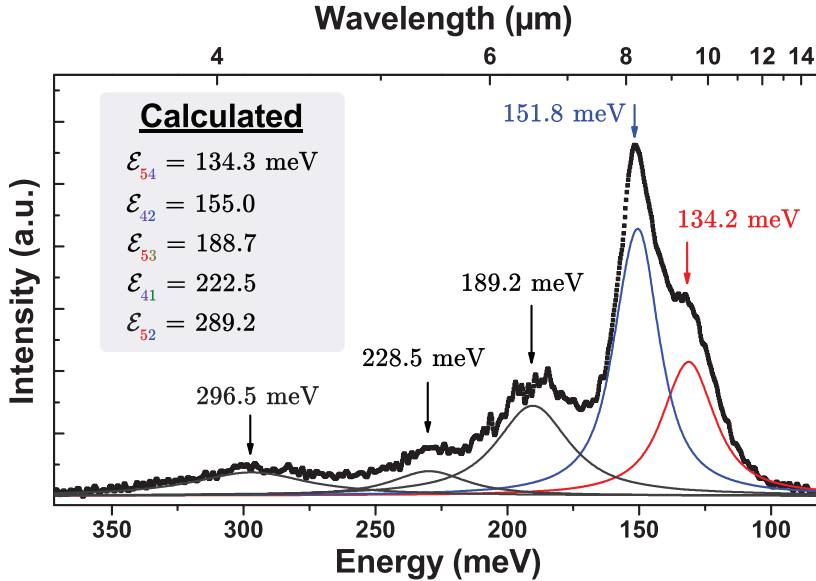


Figure 4.10: EL at high pumping current. At $T_{sink} = 80$ K and for $t_{pulse} = 100$ ns, the EL spectra at 2.5 A for a 0.027 mm^2 device is fitted with five Lorentzian peaks. The spectrum is shown without correction for detector responsivity. Calculated transition energies are given for an electric field $E_{field} = 80$ kV/cm and are in excellent agreement with the data.

$|4\rangle \rightarrow |2\rangle$ transition; the unique field tuning behavior and the match in emission energy between observed and calculated data are in good agreement.

As further verification of the accuracy of our calculations, we examined EL at high pumping current (2.5 A, 80 kV/cm). Here, we observe five EL peaks, as shown with fitted Lorentzians in Fig. 4.10. We find excellent agreement between these peak positions and the calculated energies for the $|5\rangle \rightarrow |4\rangle$, $|5\rangle \rightarrow |3\rangle$, $|5\rangle \rightarrow |2\rangle$, $|4\rangle \rightarrow |2\rangle$, and $|4\rangle \rightarrow |1\rangle$ transitions. We note that transitions from state $|3\rangle$ are absent ($\mathcal{E}_{32} = 100.6$ meV and $\mathcal{E}_{31} = 163.4$ meV). This is most likely due to a lack of electrons available to populate state $|3\rangle$ as an optical transition upper state.

4.4.2 Laser Emission

We observe lasing from both transitions associated with the primary EL peaks $|5\rangle \rightarrow |4\rangle$ and $|4\rangle \rightarrow |2\rangle$. As with EL emission behavior, the two laser lines have distinctive and separate behavior. Fig. 4.11 shows laser emission at $T_{sink} = 80$ K for a range of injection currents and pulse widths. Noting that FTIR spectra are time-integrated, the

emission changes from strongly favoring the $|5\rangle\rightarrow|4\rangle$ transition to strongly favoring the $|4\rangle\rightarrow|2\rangle$ transition by changing the current pulse width t_{pulse} from 10 to 100 ns. That is, for $t_{pulse} = 10$ ns, the $|4\rangle\rightarrow|2\rangle$ transition does not lase for $I \leq 1.7$ A; for $t_{pulse} = 100$ ns, the $|4\rangle\rightarrow|2\rangle$ threshold appears to be less than that of $|5\rangle\rightarrow|4\rangle$. Simultaneous lasing of both the $|5\rangle\rightarrow|4\rangle$ and $|4\rangle\rightarrow|2\rangle$ transition is seen for much of the parameter space.

4.4.3 Stacked Transitions

Knowing our laser transitions are $|5\rangle\rightarrow|4\rangle$ and $|4\rangle\rightarrow|2\rangle$, a re-examination of the band structure in Fig. 4.6 illustrates how these transitions are energetically “stacked.” Indeed, with simultaneous lasing of both transitions, this appears to be the “cascaded” transition setup sought by C. Sirtori *et al.* [109] for producing correlated photons. Besides the production of correlated photons, such stacked transitions could be useful for ultra-low noise spectroscopy applications, where the system noise of a secondary laser line is used to subtract out noise sources present in the laser line of primary interest. Such an ability would result from the carrier populations of the two transitions being inherently linked.

While these applications certainly make the energy configuration represented in the Fig. 4.6 band diagram highly interesting, the spectral data presented so far point to a problem with the interpretation. In a relative sense, both EL and laser spectra show that when one transition becomes stronger, the other becomes weaker. In the simple stacked transition picture, one would intuitively think that if one transition gets stronger, the other transition would also get simultaneously stronger; more carriers for one transition should yield carriers for the other. In contrast to such output power behavior that is correlated, we observe just the opposite: anti-correlated behavior in output power.

4.5 Anti-correlated Light Output Behavior

Knowing that the two laser lines in the structure are substantially separated in wavelength, short-pass ($\lambda_{pass} < 8.70$ μm) and long-pass ($\lambda_{pass} > 8.65$ μm) filters were used to more thoroughly examine light vs. current (LI) characteristics of the laser devices. In the LI data, the distinctive behavior of each transition becomes even more apparent, with light output and thresholds showing evident differences with remarkable temperature dependencies.

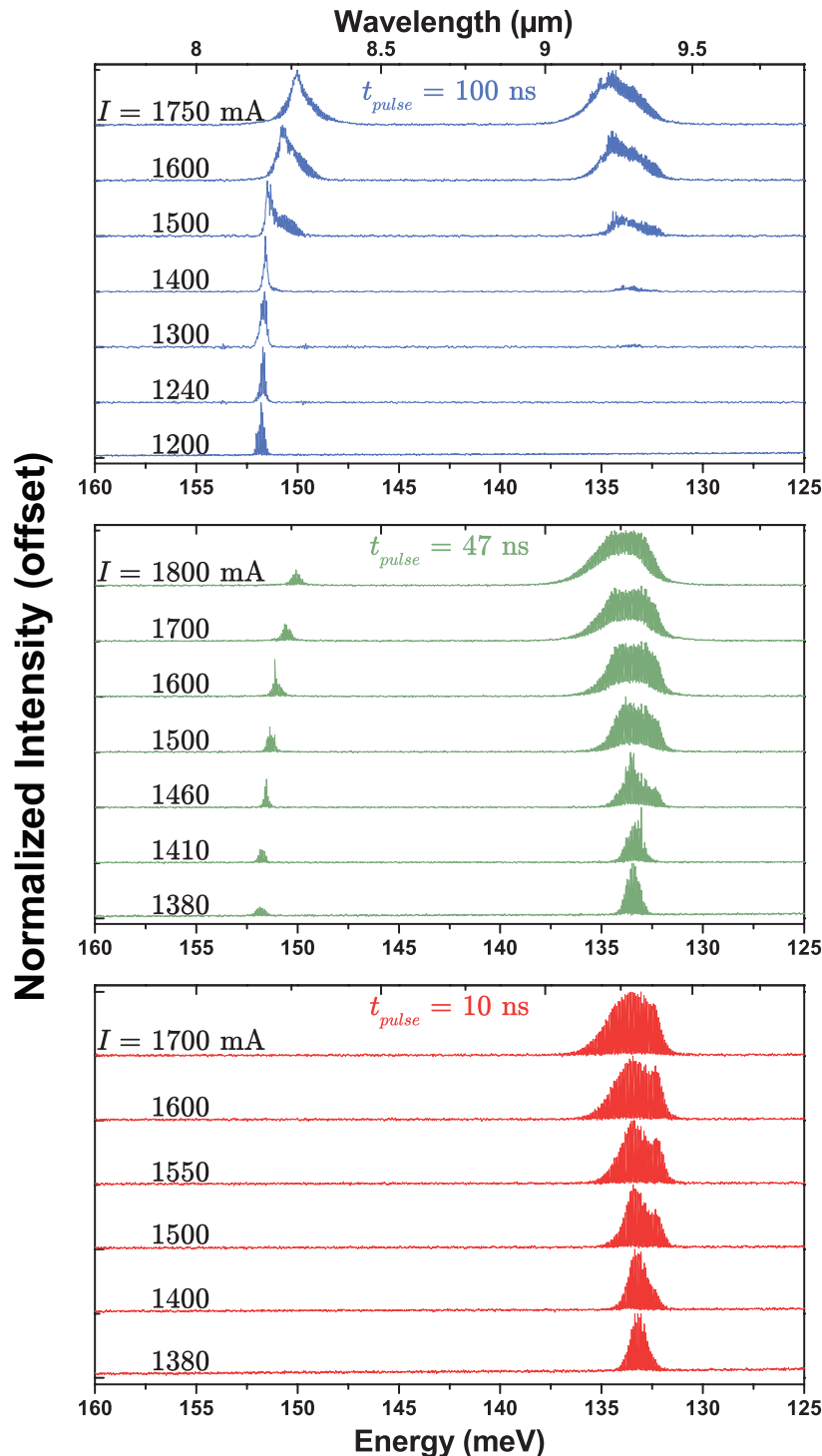


Figure 4.11: Excited state laser spectra. Pulsed lasing spectra for a $2.5 \text{ mm} \times 10 \text{ } \mu\text{m}$ laser ridge at a heat sink temperature $T_{sink} = 80$ K. Current pulse widths t_{pulse} were 10, 47, and 100 ns at an 80 kHz repetition rate.

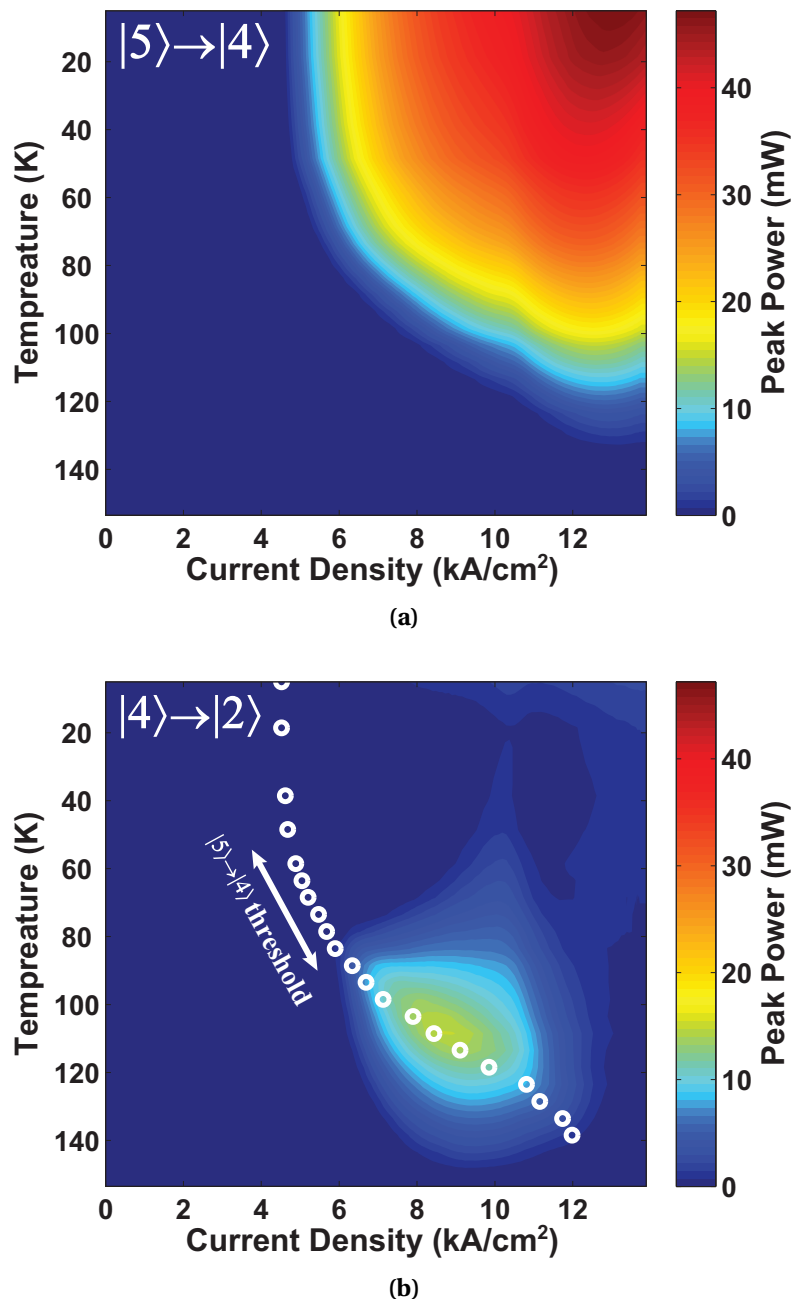


Figure 4.12: Light output characteristics of a representative laser device. Light output versus current density and heat sink temperature of a $1.48 \text{ mm} \times 12.1 \mu\text{m}$ laser for the (a) $|5\rangle \rightarrow |4\rangle$ and (b) $|4\rangle \rightarrow |2\rangle$ transitions. Data shown for the $|5\rangle \rightarrow |4\rangle$ transition are consistent with standard QCL laser behavior. In contrast, the $|4\rangle \rightarrow |2\rangle$ transition operates poorly at the lowest heat sink temperatures; the transition instead has a thermally induced peak performance near 115 K. With the $|5\rangle \rightarrow |4\rangle$ transition threshold (white circles) overlaid on (b), it can be seen that the $|4\rangle \rightarrow |2\rangle$ roll-off is coincident with $|5\rangle \rightarrow |4\rangle$ turn-on.

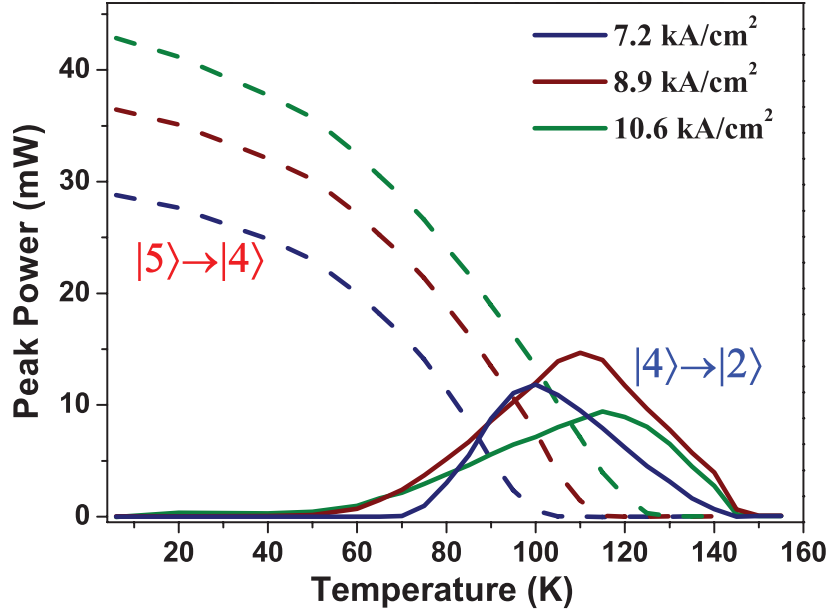


Figure 4.13: Light-temperature cross-sections. Spectrally resolved light output for three fixed pumping current densities with increasing temperature. The $|5\rangle\rightarrow|4\rangle$ transition is shown with dashed lines and the $|4\rangle\rightarrow|2\rangle$ transition is shown with solid lines. The $|4\rangle\rightarrow|2\rangle$ transition output is affected by the $|5\rangle\rightarrow|4\rangle$ transition output power.

Light from the $|5\rangle\rightarrow|4\rangle$ transition shows a behavior typical of a QC laser intersubband optical transition and is rather unremarkable. As indicated in Figs. 4.12a and 4.13, the highest output power and lowest threshold currents are achieved at the lowest temperatures. With increasing temperature, shorter non-radiative transition times, thermal population of the lower laser state, thermionic emission from the upper laser state, and decreased upper laser level injection efficiency make obtaining population inversion more difficult. Consequently stronger pumping is required to achieve laser action, until a temperature is reached where the laser is unable to achieve threshold, in this case near $T_{sink} = 125$ K [110].

The lower $|4\rangle\rightarrow|2\rangle$ transition deviates from the familiar QC behavior significantly. Most strikingly, the transition lases more effectively at elevated temperatures (near $T_{sink} = 100$ K), while performance is substantially diminished at lower temperatures. As shown in Figs. 4.12b and 4.13 for a $1.48\text{ mm} \times 12.1\text{ }\mu\text{m}$ device, lasing onset is induced near 60 K. Peak output power with constant current density *increases* with temperature up to 115 K, while threshold current simultaneously *decreases*. For temperatures above

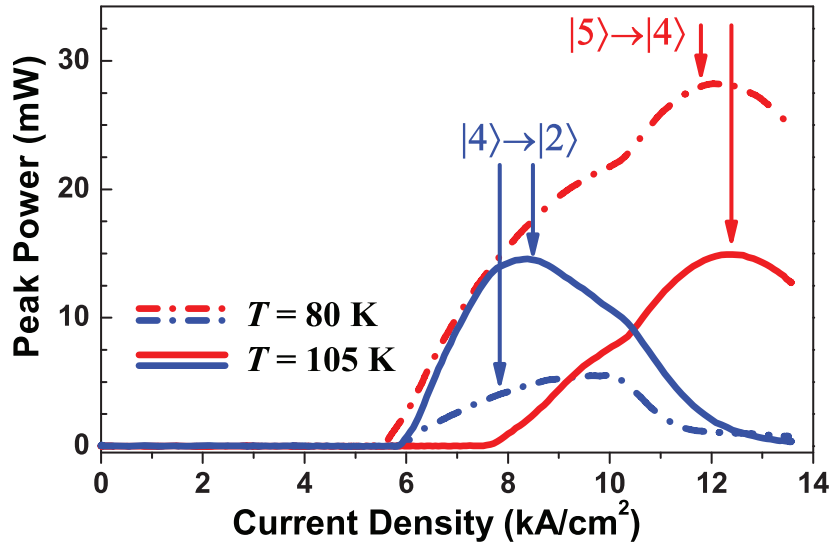


Figure 4.14: Light-current cross-sections. For each optical transition, light-current curves are shown at 80 and 105 K. A crossover in laser thresholds occurs at 85 K, where the $|4\rangle \rightarrow |2\rangle$ transition achieves a lower threshold than the $|5\rangle \rightarrow |4\rangle$ transition. At 105 K, transition $|4\rangle \rightarrow |2\rangle$ has the lower threshold; here, the $|5\rangle \rightarrow |4\rangle$ transition threshold marks the beginning of the $|4\rangle \rightarrow |2\rangle$ power roll-off.

115 K, a more typical thermal roll-over in power is observed. The light-current curves in Fig. 4.14 reveal more: a threshold ‘‘crossover’’ is observed at 85 K, above which point the $|4\rangle \rightarrow |2\rangle$ transition develops a lower threshold than the $|5\rangle \rightarrow |4\rangle$ transition. At temperatures below this crossover, if the $|4\rangle \rightarrow |2\rangle$ transition is lasing, the $|5\rangle \rightarrow |4\rangle$ transition is also lasing. After the crossover and for low pumping rates, a regime exists where only the lower $|4\rangle \rightarrow |2\rangle$ transition lasers. However, as soon as the upper $|5\rangle \rightarrow |4\rangle$ transition reaches threshold, an abrupt drop in $|4\rangle \rightarrow |2\rangle$ output power is observed. This anti-correlation in output power between the two transitions persists even above threshold. The Fig. 4.15 plot of thresholds shows that after crossover, the $|4\rangle \rightarrow |2\rangle$ transition threshold takes on a more typical QC laser behavior, having a characteristic temperature $T_0 \approx 220\text{ K}$; before crossover, however, the transition has a *negative* characteristic temperature $T_0 \approx -66\text{ K}$! The sharp ‘‘kink’’ in the $|4\rangle \rightarrow |2\rangle$ transition threshold at the crossover point along with the anti-correlated output power behavior are indicative of a strong interaction between the carrier populations of the two laser transitions.

For a thorough study of the structure, along with preliminary characterization of multiple (~ 30) laser devices, we performed full, detailed, temperature-dependent

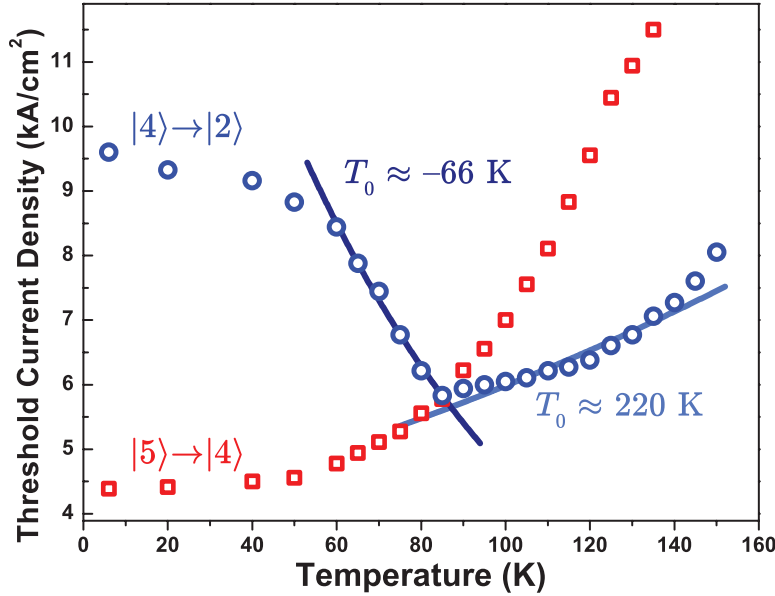


Figure 4.15: Threshold temperature-dependence of the transitions. Red symbols indicate observed threshold current densities for the $|5\rangle\rightarrow|4\rangle$ transition and blue symbols the $|4\rangle\rightarrow|2\rangle$ transition. A crossover in thresholds is seen near 85 K. Before this crossover, the $|4\rangle\rightarrow|2\rangle$ transition threshold decreases with increasing temperature, giving a negative characteristic temperature ($T_0 \approx -66$ K). After the crossover, the $|4\rangle\rightarrow|2\rangle$ transition has a more conventional $T_0 \approx 220$ K.

characterizations on six different lasers from different parts of the wafer. Cavity lengths were 1.38, 1.48, 1.50, 1.63, 1.93, and 2.28 mm. All data sets showed device characteristics similar to the data presented in Figs. 4.12–4.15. All devices showed anti-correlated behavior between two competing optical transitions lasing near $\lambda \approx 9.5$ μm and 8.2 μm . Also, a stronger $|5\rangle\rightarrow|4\rangle$ transition always led to a weaker $|4\rangle\rightarrow|2\rangle$ transition.

4.6 Lasing High in k -Space

The simple stacked transition representation suggested by Fig. 4.6 cannot account for the observed anti-correlated behavior in output power. As earlier mentioned, such a stacked transition scheme would more directly lead to correlated—rather than anti-correlated—behavior in output power. Our typical representation of the energy band configuration, such as in Fig. 4.6, hides many characteristics of the system. Specifically, the system only has energy state quantization in one dimension, the direction of

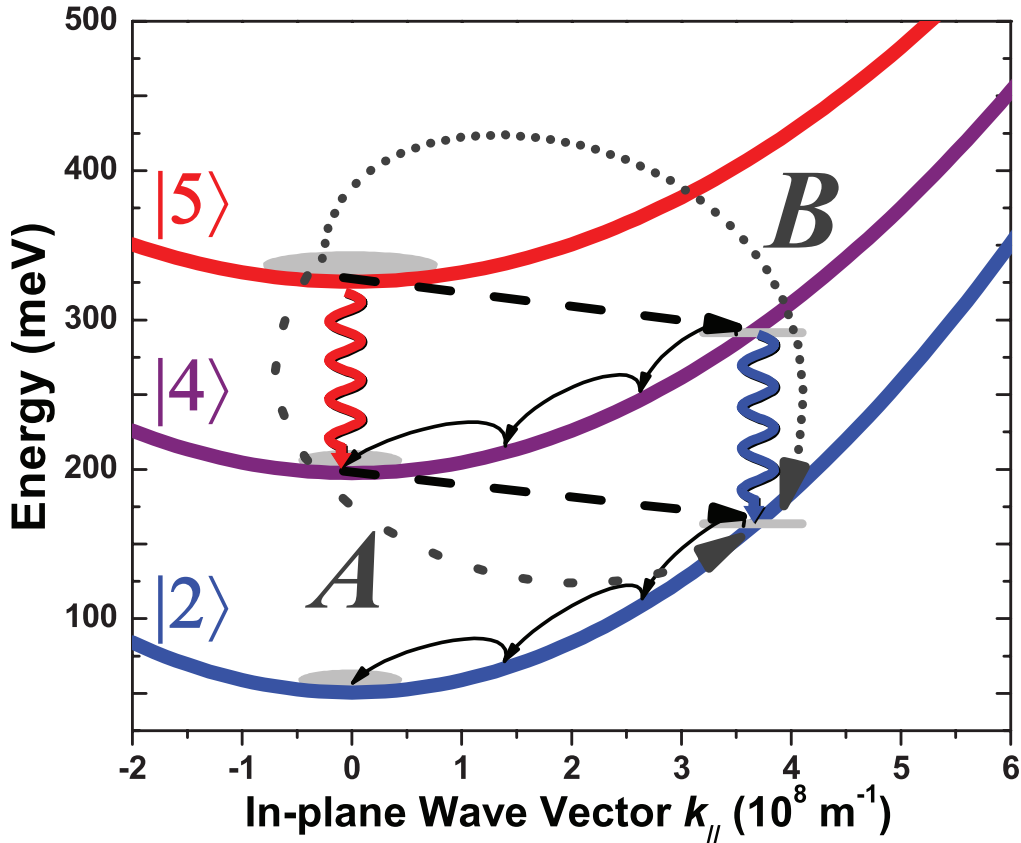


Figure 4.16: The k -space electron paths. The in-plane k -space dispersion k_{\parallel} of the subbands $|5\rangle$, $|4\rangle$, and $|2\rangle$ is shown. Electrons being injected into state $|5\rangle$ can follow either path A (the $|5\rangle \rightarrow |4\rangle$ optical transition) or path B (the $|4\rangle \rightarrow |2\rangle$ optical transition preceded by LO phonon scattering). Path A is typical for a QC laser transition, and path B represents the high k -space transition. Optical transitions are indicated by wavy arrows, intersubband phonon transitions are shown with dashed-line arrows, intrasubband scattering is shown with curved arrows, and paths A and B are shown with dotted arrows. Local k -space minima (*i.e.*, “electron pools”) are shown as gray areas.

epitaxial growth. In the other two (“in-plane”) dimensions, electrons are free to take on a much broader range of momentum (and therefore energy) values. This in-plane freedom of motion creates an energy dispersion of the individual subbands of roughly parabolic form. Generally, any consideration of such dispersion is neglected in our energy band diagrams, since only the energy values at the energy band minima—the Γ point ($k = 0$)—are indicated by the plot. In most cases, the simple picture is

good enough, since most opto-electronic devices operate using electrons in a quasi-equilibrium state, or in a state where electrons are able to “pool” for a long time relative to other relevant system times.

The data presented in the previous sections require that we envision a mode of operation whereby a second optical transition is in competition with a first transition for charge carriers. In a QC structure such as ours, we arrive at the model schematically depicted in Fig. 4.16: the secondary laser transition is a vertical transition between subbands, positioned high in k -space. Given the three identified energy subbands $|5\rangle$, $|4\rangle$, and $|2\rangle$, several different electron transport paths are possible; two are labeled *A* and *B*. Path *A* is characteristic for a QC laser optical transition, where electrons undergo a radiative transition followed by LO phonon scattering. When the $|5\rangle \rightarrow |4\rangle$ transition is lasing, large cavity photon densities at the $|5\rangle \rightarrow |4\rangle$ transition energy and strong stimulated emission ensure that this is the dominant electron path. However, at elevated temperatures, path *B* becomes available with increased LO phonon scattering out of state $|5\rangle$, populating state $|4\rangle$ high in k -space. In the situation where path *A* is “off” because threshold has not yet been reached for the $|5\rangle \rightarrow |4\rangle$ transition, carriers are provided so that lasing can occur at high k -space for the $|4\rangle \rightarrow |2\rangle$ transition. If at any time path *A* turns on, path *B* and therefore $|4\rangle \rightarrow |2\rangle$ population inversion is suppressed because

- (i) fewer electrons are available to populate the upper state of the high k -space $|4\rangle \rightarrow |2\rangle$ optical transition and
- (ii) electrons are injected into the lower state of the high k -space $|4\rangle \rightarrow |2\rangle$ transition.

Moreover, if transport through path *A* is slowed due to a weakening $|5\rangle \rightarrow |4\rangle$ laser transition, path *B* will concurrently see an enhancement of available electrons able to contribute to $|4\rangle \rightarrow |2\rangle$ lasing. This effect accounts for the dramatic decrease in $|4\rangle \rightarrow |2\rangle$ threshold from 55 to 85 K. The observed anti-correlated behavior of the two transitions is thus sustained. It is worth noting that this anti-correlated transport picture implies that the $|4\rangle \rightarrow |2\rangle$ transition has only “local” population inversion; that is, population inversion does not exist globally over the entire subbands $|4\rangle$ and $|2\rangle$. This is not the first time local population inversion has been reported. J. Faist *et al.* reported such local inversion in 1996 [111]. However, their report detailed local inversion at $k = 0$. In contrast, our structure does not attain inversion at $k = 0$ at all, and instead only reaches a local population inversion at high k -space values.

The energy subband dispersion $\mathcal{E}_n(k_{\parallel})$ plotted in Fig. 4.16 for subbands n incorporates the energy dependence of the effective mass. We define $\mathcal{E}_n(k_{\parallel})$ relative to the conduction band edge as $\mathcal{E}_n(0)$ (the subband energy at $k = 0$) plus a dispersion term $\delta\mathcal{E}_n(k_{\parallel})$,

$$\mathcal{E}_n(k_{\parallel}) = \mathcal{E}_n(0) + \delta\mathcal{E}_n(k_{\parallel}) \quad (4.7)$$

and

$$\delta\mathcal{E}_n(k_{\parallel}) = \frac{\hbar^2 k_{\parallel}^2}{2m^*(\mathcal{E}_n(k_{\parallel}))} = \frac{\hbar^2 k_{\parallel}^2}{2\left(1 + \frac{\mathcal{E}_n(0) + \delta\mathcal{E}_n(k_{\parallel})}{\mathcal{E}_G^\Gamma}\right)m_e^*} \quad (4.8)$$

using here the empirical approach of Nelson *et al.* [39] where $m^*(\mathcal{E}) = \left(1 + \frac{\mathcal{E}}{\mathcal{E}_G^\Gamma}\right)m_e^*$. In the calculation for Fig. 4.16, we use a Γ -point bandgap $\mathcal{E}_G^\Gamma = 0.784$ eV (which corresponds to a non-parabolicity parameter $\gamma = \frac{\hbar^2}{2m_e^*\mathcal{E}_G^\Gamma} = 1.13 \times 10^{-14} \text{ cm}^2$ [27]) and assume the band-edge effective mass to be that of the $\text{In}_{0.53}\text{Ga}_{0.47}\text{As}$ well ($m_e^* = 0.043m_e$).

Making the assumption that $\hbar\omega_{LO} = 34$ meV, electrons scattering out of state $|5\rangle$ (at $k = 0$) into state $|4\rangle$ via LO phonons acquire a k -space value $k_{\parallel} = 3.6 \times 10^8 \text{ m}^{-1}$. We therefore infer that the observed high k -space lasing occurs near $k_{\parallel} = 3.6 \times 10^8 \text{ m}^{-1}$, which is further supported by evidence described in the next section. It is worthwhile to note that at $k_{\parallel} = 3.6 \times 10^8 \text{ m}^{-1}$, $\delta\mathcal{E}_4(k_{\parallel}) \approx 90$ meV, giving about three LO phonon intrasubband scattering events before the electron reaches the quasi-equilibrium point at $k = 0$. Likewise, $\delta\mathcal{E}_2(3.6 \times 10^8 \text{ m}^{-1}) \approx 113$ meV, again giving roughly three LO phonon events before the a high k -space electron reaches the quasi-equilibrium point in subband $|2\rangle$.

This energy-dependence of the effective mass results in “non-parabolicity” of the energy subbands, a diversion of the energy subband from the truly parabolic shape proportional to k_{\parallel}^2 when effective mass has no energy dependence. In our particular device, this non-parabolicity effect results in some highly interesting consequences.

4.7 Effects of Non-parabolicity

Of particular interest for such a high k -space transition is the effect of energy subband non-parabolicity [112]. At the Brillouin zone center $k = 0$, energy subbands have a substantially parabolic form. However, non-parabolicity implies that, with both

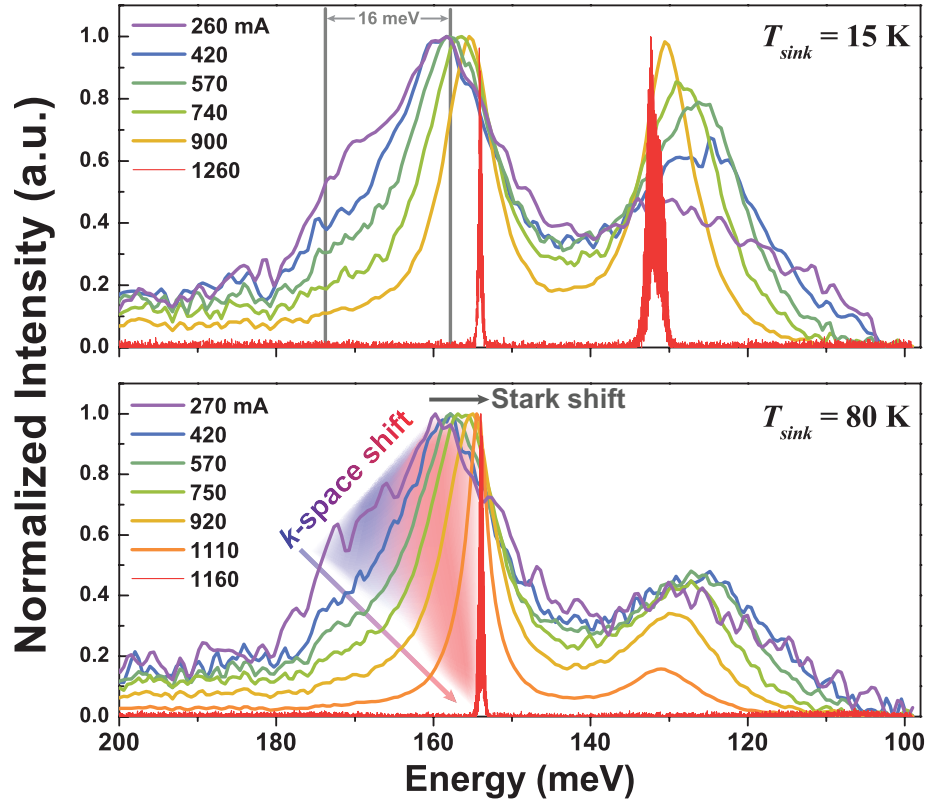


Figure 4.17: Spectral signature of k -space emission. Spectral behavior of a $1.93 \text{ mm} \times 9.4 \mu\text{m}$ laser at 15 and 80 K, with the $|4\rangle \rightarrow |2\rangle$ transition emission centered around 160 meV. Resulting from subband non-parabolicity, high k -space emission has less photon energy than emission from $k = 0$. For the $|4\rangle \rightarrow |2\rangle$ transition, the broad emission with pronounced asymmetry at low injection currents is indicative of optical emission originating from a distribution of k values. As the injection current increases, the transition preferentially emits photons at the low-energy edge of the distribution—that is, from high in k -space.

increasing k and increasing subband energy above the band edge, the subbands flatten [27]. This non-parabolicity has spectral consequences: for a transition between two subbands, the transition energy decreases as the transition occurs at higher k values. For the $|4\rangle \rightarrow |2\rangle$ transition in our structure, we calculate that photons generated at $k_{||} = 3.6 \times 10^8 \text{ m}^{-1}$ will have 16.1 meV less energy than photons generated at $k = 0$. Sub-threshold spectral data, as shown in Fig. 4.17 for a $1.93 \text{ mm} \times 9.4 \mu\text{m}$ laser, reveal such a k -space spectral signature. For the $|4\rangle \rightarrow |2\rangle$ emission around 160 meV, we observe two effects that contribute to a spectral red-shift. Over a range of injection currents that spans deeply sub-threshold to just above threshold, Stark tuning shifts the peak

emission by ~ 5.5 meV. More interestingly, at low injection currents, the $|4\rangle \rightarrow |2\rangle$ emission exhibits pronounced asymmetry. At the lowest injection currents, the spectral width is quite broad: about 16 meV. As injection current is increased, the higher energy side of the emission collapses; the transition strongly favors emission on the side of low energy. Also, as injection current is increased, the emission asymmetry gives way to a more typical Lorentzian-shaped emission. Thus, for a laser device where cavity effects strongly influence emission behavior, these spectral features are consistent with laser emission originating high in k -space.

Non-parabolic energy subbands lead to two interesting and favorable consequences for an electrically-pumped high k -space laser transition. Firstly, threshold currents are reduced due to a decrease in the primary source of optical absorption loss—that is, intersubband absorption at the lasing energy from the electron pool at $k = 0$. With a high k -space transition between non-parabolic energy subbands, the optical emission process is decoupled from the normally concurrent reverse process of optical absorption. Secondly, the presence of non-parabolicity helps achieve a more favorable lifetime profile for the $|4\rangle \rightarrow |2\rangle$ transition. Because of non-parabolicity, the energy conversion of an LO phonon requires the exchange of a larger k values for higher energy subbands, which in turn reduces the scattering rate [113] [114] [115] as $1/k^2$ [28] [116]. The influences of these effects are reflected in the results of our rate equation model. As detailed in the next section, to reconcile calculated temperature-dependent thresholds with observed data, the optical absorption loss associated with the $|4\rangle \rightarrow |2\rangle$ laser energy was decreased by about a factor of 10.

Prior work on the theory of QC laser gain spectra [117] hinted at the feasibility of such an electrically-pumped high k -space laser transition. Here, Gorfinkel *et al.* predicted the existence of local high k -space population inversion resulting purely from the presence of energy subband non-parabolicity. Because higher-energy subbands are “flatter,” the assumption of thermally-distributed k -space energy dispersion implies that an inverted population profile can exist at high k -space values even if the higher energy subband contains less total carriers than the lower subband. In the work presented in this chapter, rather than relying on a thermal distribution of electrons around $k = 0$ to populate a high k -space energy band, our excited state QC design directly injects non-quasi-equilibrium high k -space electrons.

4.8 Rate Equation Modeling

4.8.1 A System of Two Coupled Optical Transitions

To further confirm the plausibility of our k -space interpretation, we modeled our laser with a common rate equation methodology. Our rate equation model includes electron populations for six energy “levels”: four for each of the active region energy levels $|5\rangle$, $|4\rangle$, $|3\rangle$, and $|2\rangle$ in Fig. 4.6, and two high k -space regions for subbands $|4\rangle$ and $|2\rangle$. The model also includes stimulated emission terms and photon fluxes for the transitions $|5\rangle \rightarrow |4\rangle$ and $|4\rangle \rightarrow |2\rangle$. The temperature dependence of energy state lifetimes [118], injection efficiency, thermal backfilling of energy states [118], and thermionic emission [55] were all included. Using the symbolic math toolbox in Matlab, we solved the system of rate equations under steady state conditions ($\frac{d(\cdot)}{dt} = 0$).

$$\begin{aligned}
 \frac{dn_5}{dt} &= \eta_{inj} \frac{J}{q} - n_5 \left(\frac{1}{\tau_{54}} + \frac{1}{\tau_{53}} + \frac{1}{\tau_{52}} + \frac{1}{\tau_{51}} \right) - \frac{n_5}{\tau_{therm}} - S_{54}g_{54}(n_5 - n_4) \\
 \frac{dn_{4k}}{dt} &= (1 - \eta_{inj}) \frac{J}{q} + \frac{n_5}{\tau_5} - \frac{n_{4k}}{\tau_{4k}} - S_{42}g_{42}(n_{4k} - n_{2k}) \\
 \frac{dn_4}{dt} &= \frac{n_{4k}}{\tau_{4k}} - n_4 \left(\frac{1}{\tau_{43}} + \frac{1}{\tau_{42}} + \frac{1}{\tau_{41}} \right) + S_{54}g_{54}(n_5 - n_4) \\
 \frac{dn_3}{dt} &= \frac{n_5}{\tau_{53}} + \frac{n_4}{\tau_{43}} - n_3 \left(\frac{1}{\tau_{32}} + \frac{1}{\tau_{31}} \right) \\
 \frac{dn_{2k}}{dt} &= \frac{n_5}{\tau_{52}} + \frac{n_4}{\tau_{42}} + \frac{n_3}{\tau_{32}} - \frac{n_{2k}}{\tau_{2k}} + S_{42}g_{42}(n_{4k} - n_{2k}) \\
 \frac{dn_2}{dt} &= \frac{n_{2k}}{\tau_{2k}} - \frac{n_2}{\tau_{21}} + \frac{n_{inj} e^{-\frac{\Delta_{inj} + \epsilon_{21}}{kT}}}{\tau_{21}} \\
 \frac{dS_{54}}{dt} &= \left(N_p g_{54}(n_5 - n_4) - \frac{1}{\tau_{ph1}} \right) S_{54} \\
 \frac{dS_{42}}{dt} &= \left(N_p g_{42}(n_{4k} - n_{2k}) - \frac{1}{\tau_{ph2}} \right) S_{42}
 \end{aligned} \tag{4.9}$$

The temperature-dependence of all energy state lifetimes $\tau_{u\ell}$ was included with the standard relation derived from by the Bose–Einstein occupation of LO phonons.

$$\frac{1}{\tau_{u\ell}(T)} = \frac{1}{\tau_{u\ell}(0)} \left(1 + \frac{2}{e^{\frac{\hbar\omega_{LO}}{k_B T}} - 1} \right) \tag{4.10}$$

Table 4.1: Parameters used in the k -space laser rate equation model.

R	0.27	L_p	511 Å
width	12 μm	N_p	40
L	1.5 mm	Δ_{inj}	27.3 meV
$\hbar\omega_{LO}$	34 meV	n_{inj}	$1.6 \times 10^{11} \text{ cm}^{-3}$
\mathcal{E}_{21}	67.4 meV	\mathcal{E}_{3c}	60 meV
w	197 Å	m^*	$0.043m_e$
Γ_{54}	0.60	Γ_{42}	0.67
α_{w54}	7.4 cm^{-1}	α_{w42}	5.2 cm^{-1}
\mathcal{E}_{54}	128 meV	\mathcal{E}_{42}	151 meV
z_{54}	23 Å	z_{42}	13 Å
$\delta\mathcal{E}_{54}$	24 meV	$\delta\mathcal{E}_{42}$	15 meV

The injection efficiency η_{inj} into the upper laser state $|5\rangle$ (and into the k -space state $|4\rangle$) [119] was treated in a similar manner.

$$\eta_{inj}(T) = \eta_{inj}(0) \left[1 - \left(1 + \frac{2}{e^{\frac{\hbar\omega_{LO}}{k_B T}} - 1} \right) \right] \quad (4.11)$$

Thermionic emission out of the upper laser state $|5\rangle$ was included using the method of S. Sze [55].

$$\tau_{therm}(T) = w \sqrt{\frac{2\pi m^*}{k_B T}} e^{\frac{\mathcal{E}_{3c}}{k_B T}} \quad (4.12)$$

The gain coefficient $g_{u\ell}$ for the transition $|u\rangle \rightarrow |\ell\rangle$ is given by

$$g_{u\ell} = \frac{c\Gamma_{u\ell}}{N_p n_{eff}} \frac{2q^2 \mathcal{E}_{u\ell} z_{u\ell}^2}{hce_0 n_{eff} \delta\mathcal{E}_{u\ell} L_p} \quad (4.13)$$

and the photon lifetime with the cavity for the transition $|u\rangle \rightarrow |\ell\rangle$ is

$$\tau_{ph,u\ell} = \frac{n_{eff}}{c \left(-\frac{1}{L} \ln(R) + \alpha_{w,u\ell} \right)}. \quad (4.14)$$

The parameters used for the calculation are given in Tables 4.1 and 4.2.

Table 4.2: Calculated LO phonon lifetimes at $T = 0$ K used in the k -space laser rate equation model.

		upper state u			
		5	4	3	2
lower state ℓ	4	4.0			
	3	4.2	1.2		
	2	7.0	1.9	3.0	
	1	9.3	10.6	3.5	7.2

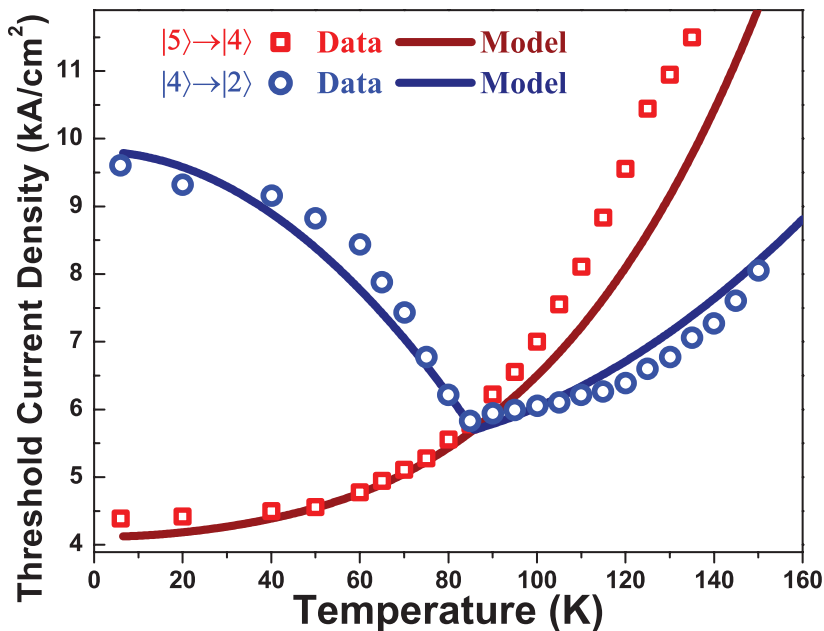


Figure 4.18: Model results for transition thresholds. Observed and modeled temperature-dependent threshold current densities for the two optical transitions. Red symbols indicate thresholds for the $|5\rangle \rightarrow |4\rangle$ transition and blue symbols the $|4\rangle \rightarrow |2\rangle$ transition. A crossover in thresholds is seen near 85 K. Before this crossover, the $|4\rangle \rightarrow |2\rangle$ transition threshold decreases with increasing temperature. A sharp kink is observed in the $|4\rangle \rightarrow |2\rangle$ threshold when it becomes lower than that of the transition $|5\rangle \rightarrow |4\rangle$. These features are reproducible with a conventional QC rate equation model with temperature-dependent parameters, the results of which are indicated by solid lines.

Table 4.3: Fitting parameters used to match the k -space rate equation model to observed data.

	scaling value	final value
α_{w54}	4.6	34 cm^{-1}
α_{w42}	0.1	0.52 cm^{-1}
η_{inj}		0.88

4.8.2 Comparing Threshold Data with Simulation

Threshold current densities provide direct means for comparing observed data with the model results. In using our rate equation model to find threshold current densities, we look for roots of the expression $S_{ul}(J)$ as a function of temperature; that is, when $S_{ul}(J) = 0$, we have a threshold condition. Figure 4.18 shows a comparison of observed data (open symbols) and calculated thresholds (solid lines). Using three fitting parameters, our rate equation model is able to provide an excellent reproduction of our observed data. The three fitting parameters used each control primarily one “feature” of the plotted data. First, by scaling the $|5\rangle \rightarrow |4\rangle$ waveguide loss α_{w54} , we match the observed and calculated values of threshold current density for transition $|5\rangle \rightarrow |4\rangle$ over the full temperature range. Second, by scaling the $|4\rangle \rightarrow |2\rangle$ waveguide loss α_{w42} , we match the observed and calculated values of threshold for $|4\rangle \rightarrow |2\rangle$ for $T > 85 \text{ K}$. This is the temperature range where transition $|4\rangle \rightarrow |2\rangle$ behaves like a conventional QC transition, and where transport through the transition $|5\rangle \rightarrow |4\rangle$ lasing channel is not available since $|5\rangle \rightarrow |4\rangle$ has yet to reach threshold. Our final fitting parameter is the injection efficiency η_{inj} into state $|5\rangle$ and the k -space state $|4\rangle$. Decreasing η_{inj} has the effect of increasing the separation in thresholds for the two transitions for $T < 85 \text{ K}$.

To achieve the fit between observed and calculated data shown in Fig. 4.18, α_{w54} was scaled by a factor of 4.6, α_{w42} was scaled by a factor of 0.1, and η_{inj} was set to 0.88. The large scaling factor for the transition $|5\rangle \rightarrow |4\rangle$ loss is not surprising, since free carrier loss calculated by the Drude model usually results in an under-estimate [120]. The extremely small scaling factor for the transition $|4\rangle \rightarrow |2\rangle$ loss needed to reconcile observed and calculated thresholds reflects the effects of k -space non-parabolicity described in Section 4.7.

We were particularly keen on confirming that a k -space transition model could reproduce three key features observed in the threshold behavior of the $|5\rangle \rightarrow |4\rangle$ and $|4\rangle \rightarrow |2\rangle$ transitions; those were

- (i) the unconventional threshold behavior of the $|4\rangle \rightarrow |2\rangle$ laser transition that decreases then increases with temperature;
- (ii) the crossing of the $|5\rangle \rightarrow |4\rangle$ and $|4\rangle \rightarrow |2\rangle$ laser thresholds; and
- (iii) the sharp kink in the temperature-dependent evolution of the $|4\rangle \rightarrow |2\rangle$ transition threshold at the crossover point.

As clearly seen in Fig. 4.18, the k -space rate equation model is able to accurately reproduce these key features.

A more thorough understanding of the model details may be useful in understanding the origin of the rapid decrease in transition $|4\rangle \rightarrow |2\rangle$ threshold in the 50–85 K temperature range and the sharp kink in the $|4\rangle \rightarrow |2\rangle$ transition at the crossover point. Since our system of equations represents two coupled optical transitions, each $S_{u\ell}(J)$ has four possible solutions, but real roots for only two. Each solution represents a different physical state of the system:

- (i) a solution for when both transitions are lasing (a real root for both S_{54} and S_{42});
- (ii) a solution for when transition $|5\rangle \rightarrow |4\rangle$ is lasing and transition $|4\rangle \rightarrow |2\rangle$ is not (a real root for only S_{54});
- (iii) a solution for when transition $|4\rangle \rightarrow |2\rangle$ is lasing and transition $|5\rangle \rightarrow |4\rangle$ is not (a real root for only S_{42});
- (iv) a solution for when neither transition is lasing (no real roots).

These solutions “cross” in temperature when transition $|5\rangle \rightarrow |4\rangle$ and transition $|4\rangle \rightarrow |2\rangle$ have the same threshold. Furthermore, each solution is only meaningful for a limited set of conditions. For example, at $T = 40$ K, we see four plotted values in Fig. 4.19, two for each optical transition. Of the two values that correspond to threshold for the $|5\rangle \rightarrow |4\rangle$ transition (red lines *a* and *d*), one value corresponds to when $|5\rangle \rightarrow |4\rangle$ is on and $|4\rangle \rightarrow |2\rangle$ is off, and the other corresponds to when both $|5\rangle \rightarrow |4\rangle$ and $|4\rangle \rightarrow |2\rangle$ are on. Since the values for the $|4\rangle \rightarrow |2\rangle$ transition (blue lines *b* and *c*) are both larger than the values for the $|5\rangle \rightarrow |4\rangle$ transition, the $|5\rangle \rightarrow |4\rangle$ threshold is less than the $|4\rangle \rightarrow |2\rangle$ threshold. Thus, the physically meaningful solutions at $T = 40$ K are represented by lines *a* and *c*.

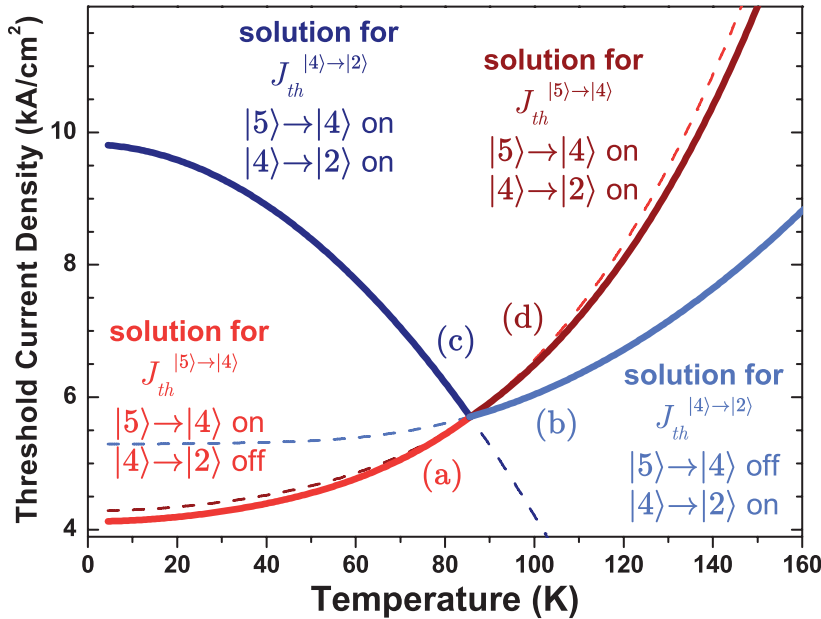


Figure 4.19: Model results for transition thresholds. Modeled temperature-dependent threshold current densities for the two optical transitions. Four solutions exist for each $S_{ul}(T)$; only two are physically meaningful. The physically meaningful solutions correspond to (i) when a single transition reaches threshold and (ii) when both transitions have reached threshold. The physically meaningful portions of the solutions are plotted in bold lines.

With this understanding of the rate equation model, it is now easier to identify the origin of some of the unique threshold behavior features. While an increased LO phonon transition rate partially contributes to the rapid improvement in the $|4\rangle\rightarrow|2\rangle$ threshold around 55–85 K, the improvement is more aptly recast as a degradation in the $|5\rangle\rightarrow|4\rangle$ threshold, reflecting the fact that, when transition $|5\rangle\rightarrow|4\rangle$ is lasing, the $|4\rangle\rightarrow|2\rangle$ path is carrier-starved. The kink at the threshold crossover results from a transition between two different operating regimes of the laser: the regime where $|5\rangle\rightarrow|4\rangle$ has a lower threshold and the regime where $|4\rangle\rightarrow|2\rangle$ has a lower threshold.

4.8.3 Cavity-length-dependence of Threshold Crossover

The extremely low loss associated with the $|4\rangle\rightarrow|2\rangle$ transition results in a marked length-dependence of the two transition thresholds. As in a typical QC laser, the $|5\rangle\rightarrow|4\rangle$ loss is dominated by waveguide loss for most cavity lengths; mirror loss and waveguide loss are comparable for only very short cavity lengths ($L \leq 1$ mm). In contrast, the

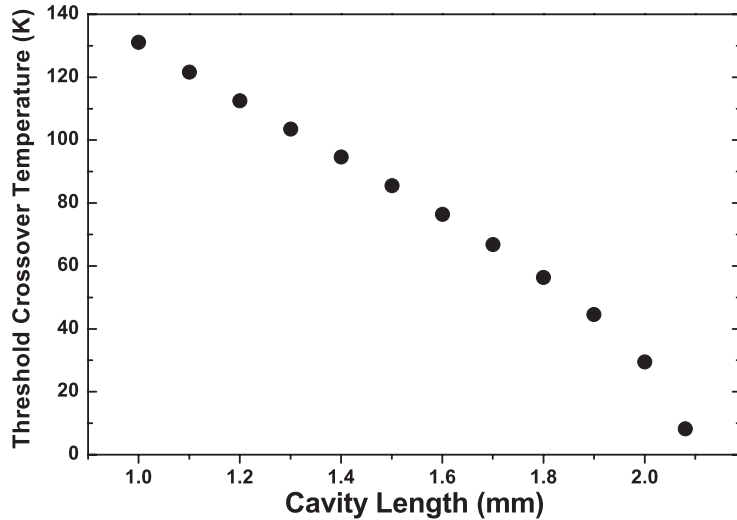


Figure 4.20: Cavity length dependence of transition threshold crossover temperature. Resulting from the extremely low optical loss of the $|4\rangle \rightarrow |2\rangle$ transition, the temperature at which the two transition thresholds cross is highly dependent on cavity length. Here, the rate equation model results are shown. Laser data confirm this behavior.

$|4\rangle \rightarrow |2\rangle$ k -space transition total loss is dominated by mirror loss for even very large cavity lengths. Thus, since $\alpha_m = -\frac{1}{L} \ln(R)$, thresholds current densities decrease substantially faster with cavity length for transition $|4\rangle \rightarrow |2\rangle$ than they do for transition $|5\rangle \rightarrow |4\rangle$. The result is especially noticeable in temperature at which the threshold crossover occurs. Figure 4.20 plots calculated threshold crossover vs. cavity length, and we can see that, because the net gain increases with increasing cavity length for $|4\rangle \rightarrow |2\rangle$, the crossover temperature decreases with increasing cavity length.

4.9 Conclusions & Future Directions

4.9.1 Summary

The work presented in this chapter began with the investigation of a novel QC architecture: the use of an excited state lasing transition. Because of the extreme flexibility afforded by the general QC concept, unique designs that radically depart from the conventional QC configuration are relatively simple to implement. However, it is this exact same flexibility to innovate that led us to the primary result of this work so far. By

injecting into an excited state optical transition, other lower-lying transitions also with large oscillator strengths were present in the active region; indeed, we confirmed lasing from such a lower-lying transition. Because of the unique configuration of our particular laser design, population inversion was not achieved at the Γ point in the band structure for the lower transition. But, because electrons were injected via LO phonon scattering into a high k -space position, local population inversion high in k -space resulted in high k -space laser action. While both transitions lase simultaneously under certain conditions, the high k -space transition is anti-correlated with the primary, excited state laser transition. A rate equation model based on incorporating a high k -space optical transition reproduces the characteristic features of the observed temperature-dependent emission behavior.

To be sure, the demonstration of high k -space lasing represents a departure from the conventional approaches to semiconductor lasers. In semiconductor lasers, because of charge carriers' propensity for extremely fast momentum relaxation [121] [113], they accumulate at band extrema—*i.e.*, near $k = 0$ in direct-gap semiconductors. Conventional wisdom thus holds that the “interesting” device-level physics happens at these band extrema, including population inversion for lasing. This behavior is universal among diode lasers [4] [5], interband quantum well lasers [122], and QC lasers.

The history of QC lasers is decorated with unique methods for obtaining laser action. Laser transitions with one state being a virtual state have been demonstrated both through Bloch gain [19] [67] and stimulated Raman scattering [18]. In every semiconductor injection mechanism to date though, inversion is achieved from electron populations in quasi-equilibrium and thermally distributed around the Γ -point. Our finding of k -space injection via LO phonons adds yet another fundamentally unique mechanism to the list of QC-based innovations.

In studying high k -space laser transitions, one cannot help but draw a parallel to the hot-hole (p-Ge) laser [123] [124]. Here, a combination of large crossed electric and magnetic fields preferentially populates the light hole band of a bulk semiconductor by trapping electrons in cyclotron orbits at high k -space, while the applied electric field sweeps holes out of the heavy hole band through streaming motion [125]. Once these streaming holes in the heavy hole band reach the energy of an optical phonon, a scattering path opens where they can then repopulate the light hole band. In the

work presented here, instead of using externally applied electric and magnetic fields, we employ the optical phonons, a process intrinsic to the material.

4.9.2 Future Direction: *Intentionally created k -space lasers*

The possibility of designing intersubband devices that make more cognizant use of full k -space population distributions provides a variety of intriguing advantages and possible applications. The decoupling in energy of the optical emission and reabsorption processes is one point on which high k -space transitions are fundamentally superior to Γ -point transitions. It is certainly possible that high k -space transitions will one day lead to higher performing QC lasers. But other means may exist to capitalize on the high k -space concept.

In addition to the decoupling of emission and absorption, another interesting result of the built-in non-parabolicity is the range over which the transition “tunes” as it moves in k -space. If one can make a global population inversion for subbands that are pumped at high k -space, an additional method for creating tunable QC lasers could be realized. Today’s most tunable QC sources rely on broadening the gain spectrum by a number of means: rough interfaces [106], bound-to-continuum designs [126], diagonal transitions [127], etc. Placed in an external cavity setup [128] or a DFB array [129], these methods can yield tunability in the range of 100 cm^{-1} . In comparison, the non-optimized k -space transition in our laser had a tuning range in k -space of about 16 meV , or 130 cm^{-1} . Coupling a high k -space transition with other broadening mechanisms could ultimately yield much better spectral coverage out of a single laser device.

Extension of the k -space concept need not be strictly limited to QC lasers. Our demonstration of the usefulness of electrons in highly non-equilibrium states could be useful in other semiconductor and opto-electronic devices and systems. For example, in indirect bandgap semiconductors such as silicon, achieving laser action through the traditional across-gap mechanism has proven elusive. The ability to use non-equilibrium electrons, *e.g.* populating a “state” at the Γ -point, could expose new possible routes to achieving lasing in these systems.

Before exploring the strategic use of high k -space transitions, one must confront and resolve a primary challenge: how best to populate the high k -space state? We have demonstrated that the momentum transfer associated with LO phonons can

accomplish the task; Yamanishi *et al.* have demonstrated a similar upper laser state population mechanism [130]. However, using the electron-LO phonon process may ultimately prove to be a transport bottleneck that limits performance [127]. Another possibility might be taking advantage of the (normally) parasitic satellite k -space valleys. Given sufficient electron energy above the band edge, electron-electron scattering between valleys is extremely rapid. Innovation on this front will be necessary to realize a practical high k -space device.

4.9.3 Future Direction: Further develop the excited state concept

The work on QC lasers specifically designed to maximize the large oscillator strengths accompanying excited state transitions is ongoing. Whether this design strategy will ultimately be useful for long-wavelength lasing remains to be proven. As demonstrated throughout the chapter, achieving high performance at long-wavelengths is hindered by multiple challenges. While the excited state strategy addresses some of these challenges by compensating for large optical losses with larger oscillator strengths, the strategy itself introduces some new challenges. For example, excited state transitions can make achieving population inversion even more difficult. When more lower states are added below the optical transition, as in excited state structures, the ratio $\left(1 - \frac{\tau_\ell}{\tau_{u\ell}}\right)$ becomes smaller. A carefully balanced design will ultimately yield the best trade-off between this effect of decreased lifetimes and maximizing oscillator strength.

Another primary challenge for the excited state strategy that must be overcome is the huge energy drop between optical transitions, the effective Δ_{inj} . While such a large Δ_{inj} can aggravate the problem of resonant absorption in the injector region, it also leads to a significant reduction in wall-plug efficiency. Careful design can minimize injector region resonant absorption. A potential fix for the hit to wall-plug efficiency might be engineering two optical transitions of the same energy in the active region. By creating a “double photon” structure, energy that would normally be surrendered to the lattice can be used to create more photons.

4.9.4 Future Direction: Correlated photons

In this chapter, we have shown that simultaneous lasing is in principle possible from stacked transitions. In the QC design and devices presented here, the lower optical

transition did not achieve population inversion at the Γ point due to a lack of states into which electrons could scatter. However, more careful design that specifically seeks to empty out the lowest active region state could create an active region with stacked transitions that both attain population inversion at the Γ point. In this case, simultaneous lasing could lead to the generation of correlated photons.

One primary challenge of generating correlated photons by this strategy will be to maximize the transport path where electrons make two successive Γ -point optical transitions. Another transport path, where electrons scatter to the middle state of the stacked transitions via LO phonons, should be minimized.

Chapter 5

Short Injector Quantum Cascade Lasers

For QC lasers, the ultimate measure of performance is wall-plug efficiency: quite simply, power out for power in. And up to only a few years ago, even the best lasers reported in the literature had abysmal wall-plug efficiencies—at most, in the range of a few percent. Improvement in wall-plug efficiencies will make more applications more accessible; across the board, regardless of the application specifics, more efficient lasers will enhance QC technology’s utility. For example, more efficient lasers ultimately mean lasers that are capable of higher output power. High power lasers are certainly of paramount interest for infrared-based defense countermeasures, but high power is also needed for such things as lidar, which has a diverse array of applications. For applications where Watt-level output power is not needed—several methods of trace gas sensing, for example—low input power is often a requirement.

Certainly, the QC field has devoted considerable effort to improving laser performance; along with our understanding of the physical mechanisms at work in QC lasers, performance has improved substantially. Of chief concern in the initial QC work was achieving population inversion; to realize the first QC laser [8], Faist *et al.* sought to maximize population inversion by using spatially-delocalized upper and lower energy states for the laser transition. Dubbed a “diagonal transition” design, the consequence of such spatial separation—reduced oscillator strength [131]—was soon realized. As a result, “vertical transitions,” those where the energy states share the same physical space, were investigated [132], and performance improvements were realized [133]. Later, the importance of resonant tunneling through the injector barrier was identified

[134], and the active region was modified to include a narrow, first active region well to enhance coupling [135]. The result was a “hybrid” active region design that had the appearance of a somewhat diagonal yet somewhat vertical optical transition. Further performance improvements were again realized [136] from this insight.

The so-called “double-phonon” structure, a 2001 design advance [137], led to the first CW room temperature QC laser [16]. Here, a structural modification is again made to the QC active region. The double-phonon active region is composed of at least three wide quantum wells, where each of the three active region quantum ground states are spaced sequentially one longitudinal optical (LO) phonon energy apart; this allows enhanced relaxation out of the lower laser state [16]. The extra energy drop imparted by the secondary LO phonon transition also mitigates lower laser level thermal backfilling [110].

More recent performance advances have primarily been demonstrated through improved understanding and implementation of thermal management strategies; QC stacks in a buried heterostructure waveguide mounted epitaxial-side down on diamond submounts have surpassed watt-level power in continuous wave mode at room temperature [138]. While impressive, these lasers are implemented with designs that are simply derivatives of the double-phonon QC strategy. Since 2001, no significant performance improvement has been realized by implementing a fundamentally superior QC design.

While much attention has been paid to improving QC performance by modifications to the *active region* structure, in this chapter, I focus on a re-examination of the role of *injector regions* in QC laser performance. Injectors play numerous roles important to QC laser operation; they are not themselves, however, the source of photons. For reasons later detailed, it is theoretically advantageous to minimize the amount of space occupied by injector regions. We have therefore studied QC structures composed of only two and three injector wells; conventional QC structures at similar photons energies use seven or more injector wells. While we recover performance comparable with today’s best lasers, we observe several unique effects in QC lasers—such as negative differential resistance (NDR) and distinctive laser turn-off mechanisms—that ultimately help us better understand fundamental QC mechanisms.

5.1 The Role of the QC Injector

Since injector regions themselves are not the source of photon generation, prior work in the field has examined the possibility of eliminating injector regions altogether. In these “injectorless” QC structures, active regions are successively stitched together without the aid of injector region energy states. The first such device was the work of M.C. Wanke *et al.*, where a chirped superlattice design emitting at 11 μm lased up to 195 K [139]. More recently, A. Friedrich, S. Katz, *et al.* have removed the injector wells from the more conventional single- and double-phonon active region structures [66] [140]. These injectorless QC lasers have shown low threshold current densities and pulsed lasing at room temperature over a range of mid-infrared wavelengths. And while not purely injectorless, it is worth noting that today’s best performing THz QC lasers [141] [142] have significantly shorter injector regions (one or two wells) than the first THz QC lasers [143]. Also, while reductions in injector length have been sought, so has a reduction in the average energy drop across the injector—energy that does not get converted into photons—through a QC design that employed a heterogenous injector strategy [52].

Notwithstanding these attempts at eliminating injector regions, QC injectors do serve a multitude of important functions. Indeed the absence of these features may well have limited the performance of previous injectorless designs. Among the key functions of QC injector regions are

- efficient injection of electrons into the upper laser state;
- isolation of the upper laser state from the continuum;
- Bragg reflection of the upper laser state, preventing electron escape by tunneling;
- facilitation of electrons in “relaxing” out of the active region;
- spatial and energetic separation of the lower laser state from the downstream electron pool;
- providing space over which electrons can gain energy relative to the conduction band edge; and
- providing a convenient space for doping to reduce impurity scattering.

High performance conventional designs, such as the one in Fig. 5.1, are able to perform all of these functions. Conventional injector regions, however, consume a substantial portion of the total active core space. The QC period length L_p for the Fig. 5.1 structure is 504 Å; fully 335 Å, 66%, is injector region.

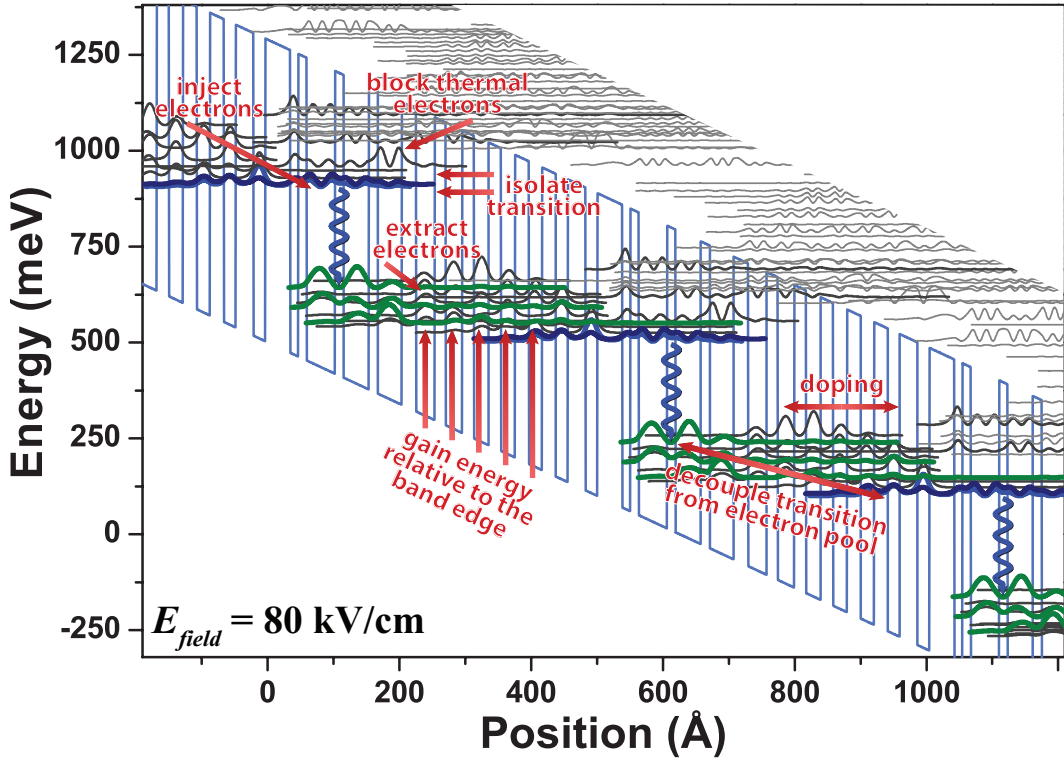


Figure 5.1: Conventional QC laser structure. Several of the important functions of injector regions are indicated. This design, dating to 2004 [144], has shown the highest performance to-date from a QC laser [23]. It has a QC period length of $L_p = 504 \text{ \AA}$, with 7 total injector wells. The design energy is $\mathcal{E}_{ph} = 265 \text{ meV}$ ($\lambda_0 = 4.68 \mu\text{m}$).

5.2 Theoretical Framework

The motivation for minimizing injector region length is compelling. Key among the performance parameters of high quality lasers are small threshold current densities, large slope efficiencies, and large wall-plug efficiencies. In examining the relations for each of these performance parameters, we see that injector length plays a key role. For example, the low temperature threshold current density is given by

$$J_{th} = \delta_{ul} \frac{\epsilon_0 \lambda_0 n_{eff}}{4\pi q} \frac{\alpha_m + \alpha_w}{\tau_{eff} z_{ul}^2} \frac{d_{ac}}{\Gamma N_p} . \quad (5.1)$$

We can see from this relation for J_{th} that, for any fixed value of L_{ac}/Γ (*i.e.* fixed active core thickness and waveguide configuration), lower thresholds are achieved when more

QC periods N_p are “squeezed” into the QC stack. Ideally then, one should shorten the overall QC period length. But the length of the QC active region is somewhat fixed for any given emission wavelength and active region design strategy. The only practical place to decrease the QC period length is the injector region.

As injector lengths are shortened and more QC periods are added to the active core, we can likewise expect an increase in total output power P .

$$P = N_p \frac{\mathcal{E}_{ph}}{q} \eta_{inj} \eta_m \frac{\tau_{eff}}{\tau_{eff} + \tau_\ell} \frac{\alpha_m}{\alpha_m + \alpha_w} (J - J_{th}) A \quad (5.2)$$

The “modal efficiency” η_m is defined as [54]

$$\eta_m = \frac{\left(\sum_i^{N_p} \Gamma_i \right)^2}{N_p \sum_i^{N_p} \Gamma_i^2} \quad (5.3)$$

which weights the reduction of photon generation caused by (vertical) spatial hole burning. The individual, per-period confinement factor Γ_i is effectively the “local field coefficient” $f^2(z)$, where $f(z)$ is the electric field profile of the optical mode in the growth direction z normalized such that $\max(f(z)) = 1$. Two direct effects of shortened injector regions on P become clear. We have already demonstrated that shortened injectors reduce J_{th} , which is accompanied by a commensurate increase in P for any $J > J_{th}$. We also see a linear increase in P as we fit more QC periods N_p into the same mode profile (*i.e.*, as η_m remains constant).

The wall-plug efficiency η_{wp} is yet another performance metric that should be improved by shortened injectors. The wall-plug efficiency can be expressed as a product of constituent terms, as

$$\eta_{wp} = \frac{\mathcal{E}_{ph}}{\mathcal{E}_{ph} + \Delta_{inj} + \frac{IR_{series}}{N_p}} \frac{\tau_{eff}}{\tau_{eff} + \tau_\ell} \frac{\alpha_m}{\alpha_m + \alpha_w} \frac{(J - J_{th})}{J} \eta_{inj} \eta_m \quad (5.4)$$

where IR_{series} is the voltage drop across the device not attributable to the active core. Insofar as there is some series resistance R_{series} for the device (from top and bottom contacts, for example), increasing N_p will decrease the net parasitic effect on η_{wp} . As in output power, increasing N_p also increases “current efficiency” for $J > J_{th}$.

As a final point, a reduction in the individual QC period length $L_p = \frac{L_{ac}}{N_p}$ could ultimately lead to the ability to produce more total output power. With maximum output power $P_{max} \propto J_{max} - J_{th}$, a large “dynamic range” in operating current is desirable. The maximum current density J_{max} a QC laser can carry before a turn-off condition is reached can be found as [134] [56]

$$J_{max} = \frac{qn_{trans}}{\tau_{trans}} \quad (5.5)$$

where τ_{trans} is the total time needed for an electron to traverse one QC period and n_{trans} is the sheet density of electrons that participate in transport across the period. The total number of electrons present in the system n_s should equal $n_{trans} + n_{stationary}$, with n_s being the doping sheet density and $n_{stationary}$ being the sheet density of conduction band electrons that do not contribute to current transport. The transit time τ_{trans} can be simplistically thought of as comprising the active region transit time and the injector region transit time τ_{inj} . One might intuitively reason that, with shorter injector regions, τ_{inj} decreases, therefore increasing J_{max} . Expressed in another way, τ_{trans} relates to the differential resistance over the active core (injectors and active regions) R_{ac} as

$$R_{ac} = \frac{1}{A} \frac{V_{appl}}{qn_{trans}} \tau_{trans} \quad (5.6)$$

where V_{appl} is the applied voltage. A shorter τ_{trans} and therefore lower differential resistance means the upper laser state and injector ground state can remain in resonance over a larger range in current, increasing J_{max} and P_{max} .

When designing short injector QC lasers, one becomes particularly aware of the operating field E_{field} . In a QC structure, E_{field} is simply expressed as

$$E_{field} = \frac{\mathcal{E}_{ph} + \Delta_{inj}}{qL_p} \quad (5.7)$$

Thus, for a fixed emission wavelength and optimally designed Δ_{inj} , E_{field} and QC period length L_p are inversely proportional. The consequential higher operating field for shortened injector regions often results in more difficulty in designing confinement for the upper laser state—which can be counteracted by use of high band-offset strained materials—and sometimes leads to laser reliability problems.

5.3 QC Laser with Three Injector Wells

5.3.1 Design and Fabrication

We designed a QC laser consisting of six quantum wells per QC period—shown in the Fig. 5.2 conduction band diagram—with emission energy $\mathcal{E}_{ph} = 239$ meV ($\lambda_0 = 5.19 \mu\text{m}$) and energy defect $\Delta_{inj} = 116$ meV. With three active region wells and three injector wells, the total period length $L_p = 307 \text{ \AA}$, in contrast to $L_p > 500 \text{ \AA}$ for the best conventional QC structures [145]. The combination of energies and period length result in a turn-on field $E_{field} = 114 \text{ kV/cm}$. The layer sequence is, in angstroms starting from the injection barrier, **32** / 52 / **10.5** / 43 / **8.5** / 36 / **16** / 27 / **16.5** / 26 / **18** / 21.5, where $\text{Al}_{0.710}\text{In}_{0.290}\text{As}$ layers are in bold type, $\text{In}_{0.638}\text{Ga}_{0.362}\text{As}$ layers are in plain type, and layers Si-doped $n = 1.0 \times 10^{17} \text{ cm}^{-3}$ are underlined; the structure has an active core sheet density $n_s = 1.1 \times 10^{11} \text{ cm}^{-2}$ per period. At 125 kV/cm, where the upper and lower laser states are somewhat isolated, we calculate $\tau_u = 1.4 \text{ ps}$, $\tau_\ell = 0.5 \text{ ps}$, $\tau_{u\ell} = 5.6 \text{ ps}$, and $z_{u\ell} = 20.6 \text{ \AA}$, for a Figure of Merit $FoM = \tau_{eff} z_{u\ell}^2 = 544 \text{ ps \AA}^2$ and $FoM^* = \tau_{eff} z_{u\ell}^2 \mathcal{E}_{ph} = 130 \text{ ps \AA}^2 \text{ eV}$.

The laser was grown using metal-organic vapor phase epitaxy (MOVPE) on a low doped ($n < 2 \times 10^{17} \text{ cm}^{-3}$) InP substrate. The QC active–injector sequence was repeated 50 times. The QC active core was surrounded on each side by $0.12 \mu\text{m} \text{ In}_{0.53}\text{Ga}_{0.47}\text{As}$ Si-doped $n = 0.5 \times 10^{17} \text{ cm}^{-3}$ to enhance gain region confinement factor. Following the $\text{In}_{0.53}\text{Ga}_{0.47}\text{As}$ confinement layer, the top cladding consisted of $2.5 \mu\text{m} \text{ InP}$ Si-doped $n = 0.5 \times 10^{17} \text{ cm}^{-3}$, $0.7 \mu\text{m} \text{ InP}$ Si-doped $n = 80 \times 10^{17} \text{ cm}^{-3}$, $0.1 \mu\text{m} \text{ InP}$ Si-doped $n = 200 \times 10^{17} \text{ cm}^{-3}$, and finally $0.06 \mu\text{m} \text{ In}_{0.53}\text{Ga}_{0.47}\text{As}$ Si-doped $n = 500 \times 10^{17} \text{ cm}^{-3}$. Standard quantum well gradings between bulk $\text{In}_{0.53}\text{Ga}_{0.47}\text{As}$ and InP regions were used to assist electron transport across the bulk interfaces. For transitions from InP to $\text{In}_{0.53}\text{Ga}_{0.47}\text{As}$, the grading layer sequence (in angstroms) was 25 / **25** / 30 / **20** / 35 / **15** / 40 / **10** / 45 / **5**, where $\text{Al}_{0.48}\text{In}_{0.52}\text{As}$ layers are in bold type and $\text{In}_{0.53}\text{Ga}_{0.47}\text{As}$ layers are in plain type.

Ridge lasers with thin Au top contacts were fabricated using standard processes [25]; buried heterostructure (BH) devices with InP overgrowth were likewise fabricated. We also fabricated and tested electroluminescence (EL) mesas [25] designed to suppress optical feedback in order to study spontaneous emission properties of the structure.

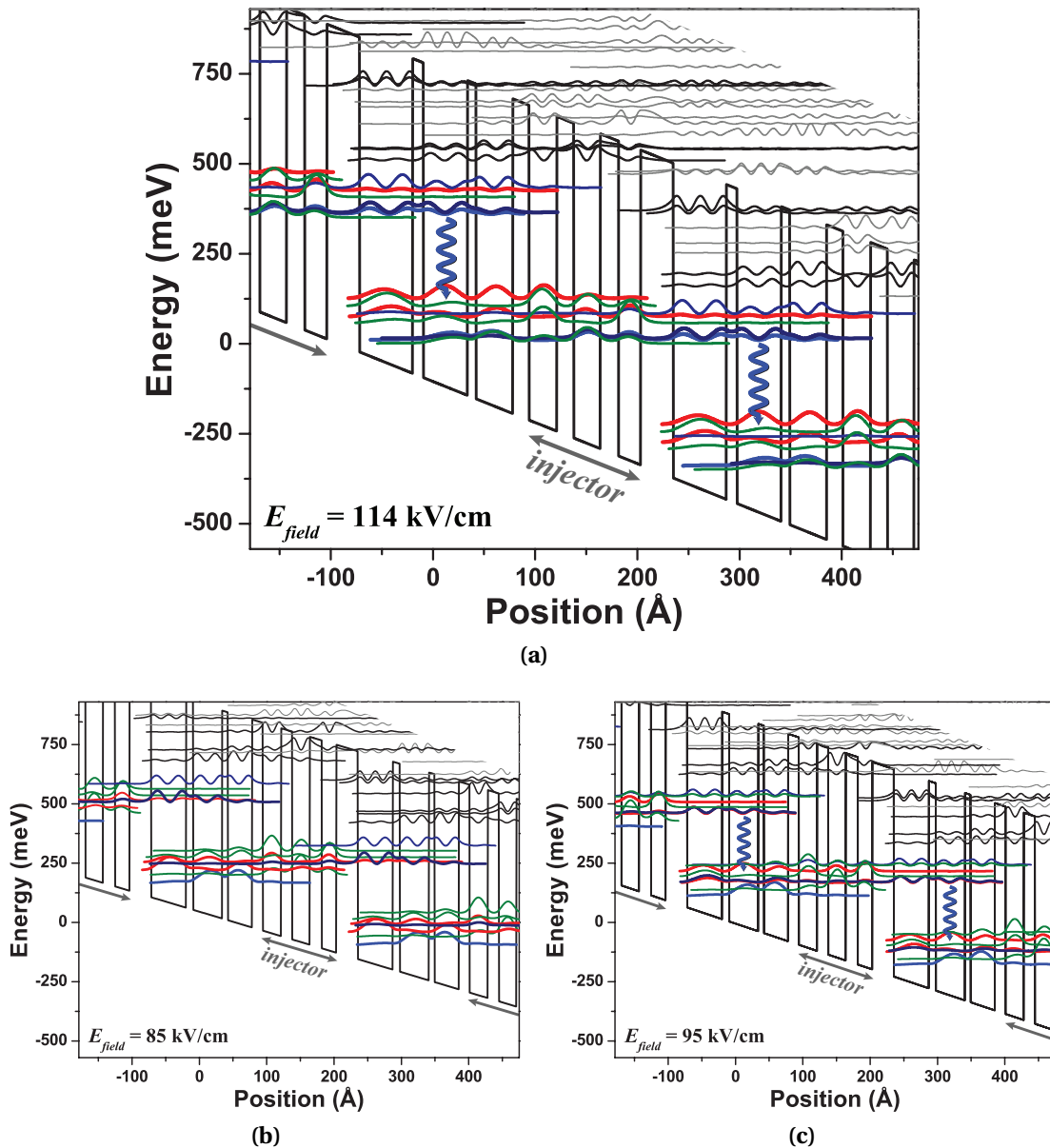


Figure 5.2: Energy band diagrams for the three injector well QC structure. The as-designed turn-on field is 114 kV/cm, shown here in (a). According to EL data, current transport begins at a field of 85 kV/cm, shown in (b). Electron transport leading to negative differential resistance is also observed starting at 95 kV/cm, shown in (c). At 95 kV/cm the second energy level of one active region is in resonance with the down-stream upper laser state at this field.

5.3.2 Results and Discussion

We examined the light–current–voltage (LIV) properties of both EL mesas and ridge lasers. We observe a pronounced negative differential resistance (NDR) feature in all devices. In EL mesas at a heat sink temperature $T_{sink} = 80$ K and current densities near 0.3 kA/cm 2 , we see a rapid 1.7 V (11 kV/cm) “jump,” as shown in Fig. 5.3a. The voltage increase is accompanied by a reduction in current density of 0.13 kA/cm 2 . After the NDR feature, the differential resistance dV/dI decreases by a factor of 2. We also observe in the light–current (LI) data that, after the NDR feature, the radiative efficiency dP/dI increases by a factor of 3. We furthermore see from Fig. 5.3b that the NDR persists through room temperature.

The NDR can be understood in that the two operating states—before the NDR feature and after—represent two different energy band configurations. At $T_{sink} = 80$ K, the difference in turn-on of the two current paths is 2.9 V (19 kV/cm). Associating the current path in operation after the NDR feature with the band alignment at the design field of 114 kV/cm, the first current path operates with turn-on at 95 kV/cm. The energy diagram at 95 kV/cm, plotted in Fig. 5.2c, elucidates a process of electron transport across the injector region after just a single phonon transition from the lower laser state. In this case, $\Delta_{inj} = 49$ meV, rather than the 116 meV at 114 kV/cm.

Interestingly, this is strong evidence of current flow and light generation with the lowest state of one active region significantly below the upper laser state of the next down-stream active region. At the lower field of 95 kV/cm in Fig. 5.2c, most of the dopant electrons n_s are “trapped” in the lowest active region state (*i.e.* $n_{stationary} \approx n_s$). In contrast, at $E_{field} = 114$ kV/cm, $n_{trans} \approx n_s$. The NDR can thus be interpreted as the existence of two different values of J_{max} : one for the 95 kV/cm band alignment, and a second, larger J_{max} for the 114 kV/cm band alignment.

EL spectra collected at pre- and post-NDR points, as in Fig. 5.4, are absent any discernable spectral changes between the two operating points. We thus conclude that the upper and lower energy states of the optical transition remain the same between the two operating points. The field re-alignment changes only the configuration of the injector states relative to the active region states.

The data become all the more interesting for laser devices, *i.e.* with the inclusion of stimulated emission in the overall device behavior. Figure 5.5a shows that no NDR

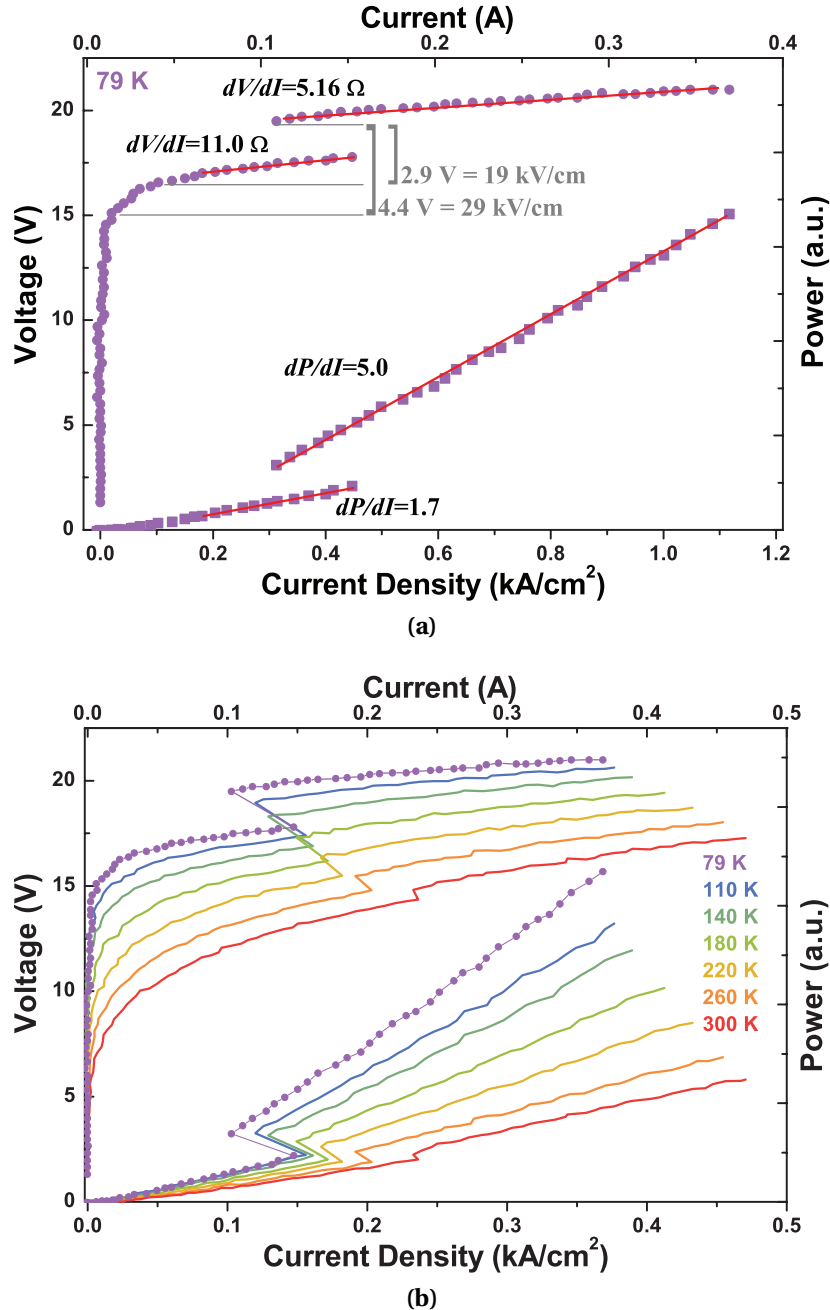


Figure 5.3: Pulsed LIV data of electroluminescence mesas for the three injector well QC structure. The area of the tested device is 0.033 mm^2 . Pronounced negative differential resistance is seen at low temperature (a) and persists through room temperature (b).

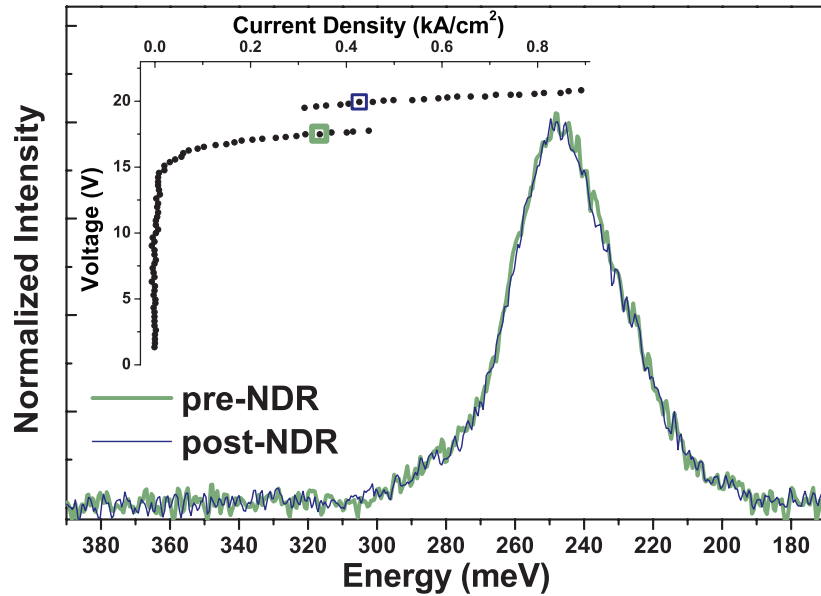


Figure 5.4: Comparison of EL spectra at pre- and post-NDR operating points. The pre-NDR point, light-colored bold line, is at $J = 0.34 \text{ kA/cm}^2$ and $V = 17.5 \text{ V}$. The post-NDR point, dark-colored narrow line, is at $J = 0.43 \text{ kA/cm}^2$ and $V = 19.9 \text{ V}$. We observe no spectral distinction between the two operating points. The spectral resolution of the data is 1 meV.

is observed in the current–voltage (IV) data at 80 K. Rather, the NDR only appears at temperatures near and above 140 K. Figure 5.5b shows the onset of NDR behavior with greater temperature resolution. Here, we see the NDR feature appear at 130 K, the first temperature where threshold current density is greater than the current density at which the NDR occurs ($J_{th} > J_{NDR}$). Apparently, it is the presence of cavity photons (stimulated emission) that prevents the observation of NDR and locks the laser into the pre-NDR band configuration for $T_{sink} < 130 \text{ K}$. Also of note is that the laser exhibits two thresholds for $T_{sink} = 130 \text{ K}$ and slightly above. The two thresholds directly result from the NDR—that is, the decrease in pumping current as the energy level configuration re-aligns at the higher field.

Perhaps even more surprising, for T_{sink} corresponding to $J_{th} > J_{NDR}$, increasing cavity photon density actively “pulls down” the operating voltage. Effectively, the internal electric field decreases, returning the band configuration to the pre-NDR state. This, in fact, is a second form of NDR, where voltage decreases with increasing current, rather than the more typically thought-of NDR where current decreases with increasing

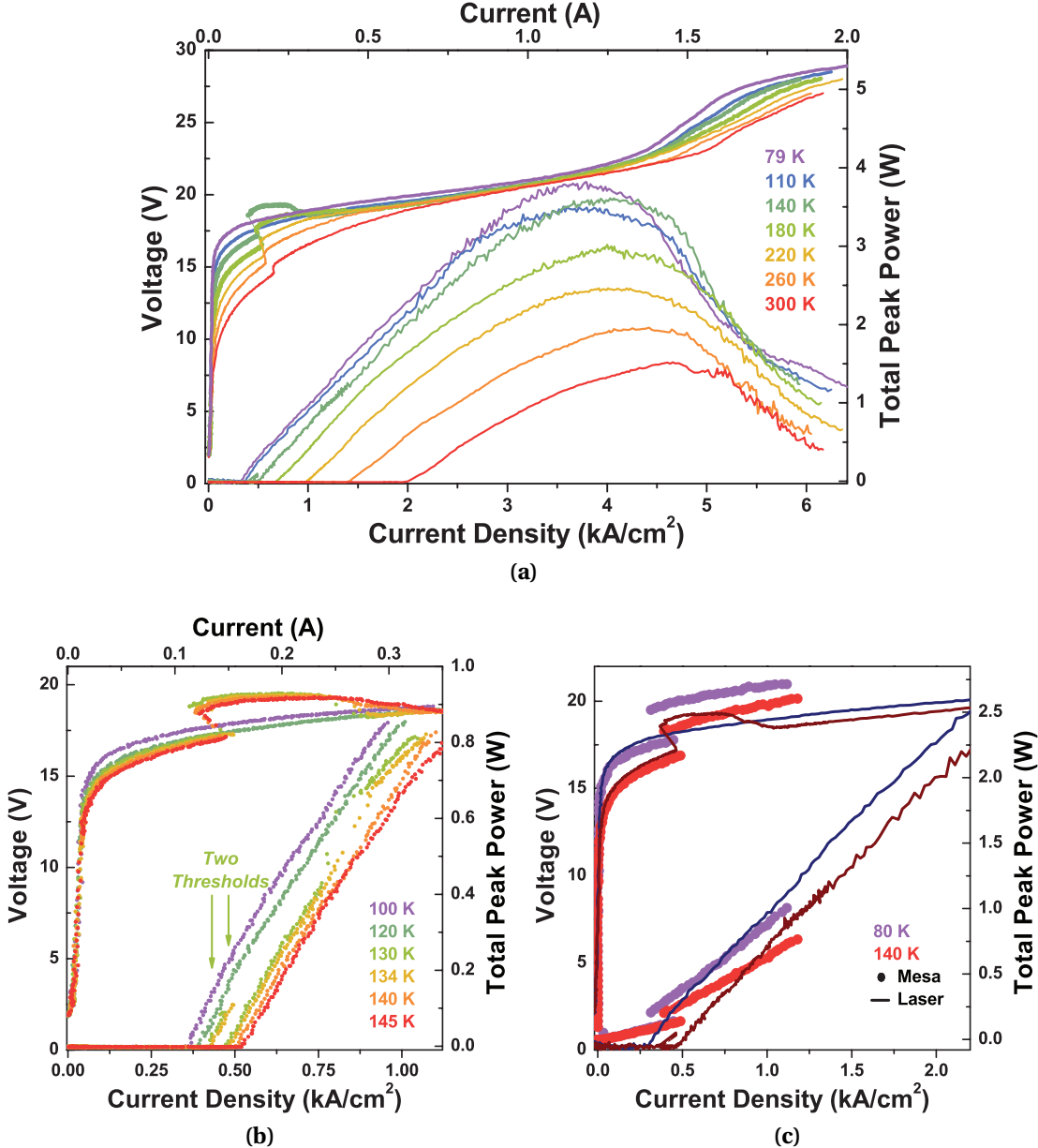


Figure 5.5: Three injector well LIV. A representative ridge laser device, $10.4 \mu\text{m} \times 3 \text{ mm}$. As seen in (a), negative differential resistance (NDR) is observed, but only at elevated temperatures. From (b), we see that the NDR appears only for $J_{th} > J_{NDR}$, i.e. here for $T_{sink} \geq 130 \text{ K}$. Because of the NDR, we observe two thresholds for $T_{sink} = 130 \text{ K}$ and slightly above. The comparison of LIV data from this laser device and EL data from Fig. 5.3b, as in (c), shows the effect of cavity photon density on the current–voltage behavior.

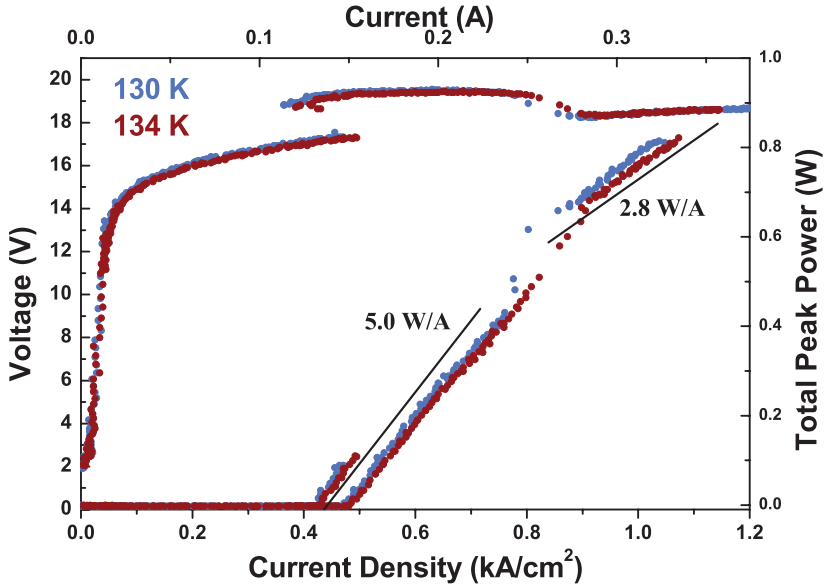


Figure 5.6: Three injector well LIV near $T_{sink}=130$ K. Different slope efficiencies are observed before and after the band configuration that results from the presence of stimulated emission. No observable change in slope efficiency is observed before and after the NDR point.

voltage. The feature can plainly be seen in Fig. 5.5c, where we compare LIV data from mesa and laser devices at $T_{sink} = 80$ K and 140 K.

The behavior of these two NDR features can be explained by considering contributions to the total per period transport rate $\frac{1}{\tau_{trans}}$. We can simplify the total carrier transit time through a QC period τ_{trans} as being the sum of active region and injector region transit times due to non-radiative processes such as phonon scattering—respectively τ_{act} and τ_{inj} —and including a term τ_{stim} that accounts for photon-assisted transport due to stimulated emission. The stimulated emission term effectively decreases the active region transit time.

$$\tau_{trans} = (\tau_{act}^{-1} + \tau_{stim}^{-1})^{-1} + \tau_{inj} \quad (5.8)$$

Here, τ_{act} and τ_{stim} are grouped in recognition that active region transport may be either by stimulated emission and/or non-radiative scattering. To explain the first NDR feature, where the temperature dependence of J_{th} affects the presence of this NDR, we return to our consideration of J_{max} . Stimulated emission significantly extends J_{max} , especially if the total non-radiative transport time is dominated by τ_{act} (due to the long lifetime of the upper laser state) in the absence of stimulated emission. Thus, for

temperatures below 130 K where no NDR is observed, $J_{max}(E_{field} = 95 \text{ kV/cm})$ includes stimulated emission and is therefore large. For temperatures at and above 130 K where we see NDR, $J_{max}(E_{field} = 95 \text{ kV/cm})$ is smaller since $J_{th} < J_{max}$.

To explain the second NDR feature, where voltage decreases with increasing current for $T_{sink} \geq 130 \text{ K}$, we again look to the effect of stimulated emission on $\frac{1}{\tau_{trans}}$ and J_{max} . Specifically, this behavior can be understood with the insight that J_{max} changes with the presence of stimulated emission, and the assumption that, faced with two transport options, the device will naturally operate in the configuration that minimizes τ_{trans} . For $T_{sink} \geq 130 \text{ K}$, $J_{max}(E_{field} = 114 \text{ kV/cm}) > J_{th}$, but, due to the presence of stimulated emission, $J_{max}(E_{field} = 95 \text{ kV/cm})$ is also greater than J_{th} once lasing has been established. Now, with two available transport paths, the laser selects the path that minimizes transport time. Thus, the presence of stimulated emission causes the laser to revert back to the lower field configuration.

After the second NDR feature, we observe a marked decrease in slope efficiency. In Fig. 5.6, we see that the slope efficiency for the low field band configuration (Fig. 5.2c) is nearly half that of the high field configuration (Fig. 5.2a): 2.8 vs. 5.0 W/A, respectively. This discrepancy is at least consistent with the factor of 3 observed in the EL case (Fig. 5.3). Although the exact origin is unclear, we can narrow the source of the difference down to either injection efficiency into the upper laser state or the laser transition efficiency, since $\frac{dP}{dI} \propto \eta_{inj} \frac{\tau_{eff}}{\tau_{eff} + \tau_\ell}$, and no other terms in $\frac{dP}{dI}$ change with a change in band structure configuration alone.

5.3.3 Device Performance

Figures 5.7, 5.8, and 5.9 show laser spectra at $T_{sink} = 79, 146$, and 302 K , respectively. Shown with each set of data is an LIV plot, with each LIV point corresponding to a spectral measurement. The NDR feature is clearly seen in the $T_{sink} = 146 \text{ K}$ LIV data, but no discernable spectral feature can be distinctly correlated with the NDR. As shown in Fig. 5.10a, a standard red-shift is seen with increasing temperature: $\lambda_0 \approx 5.1 \mu\text{m}$ for $T_{sink} = 79 \text{ K}$ and $\lambda_0 \approx 5.4 \mu\text{m}$ at room temperature.

For the ridge laser device described by the Fig. 5.5 data, pulsed total output power peaks at 3.8 W at 80 K, while room temperature output power is 1.5 W. Threshold current density is 313 A/cm^2 at 80 K, and reaches 2.0 kA/cm^2 at room temperature. Figure 5.10b

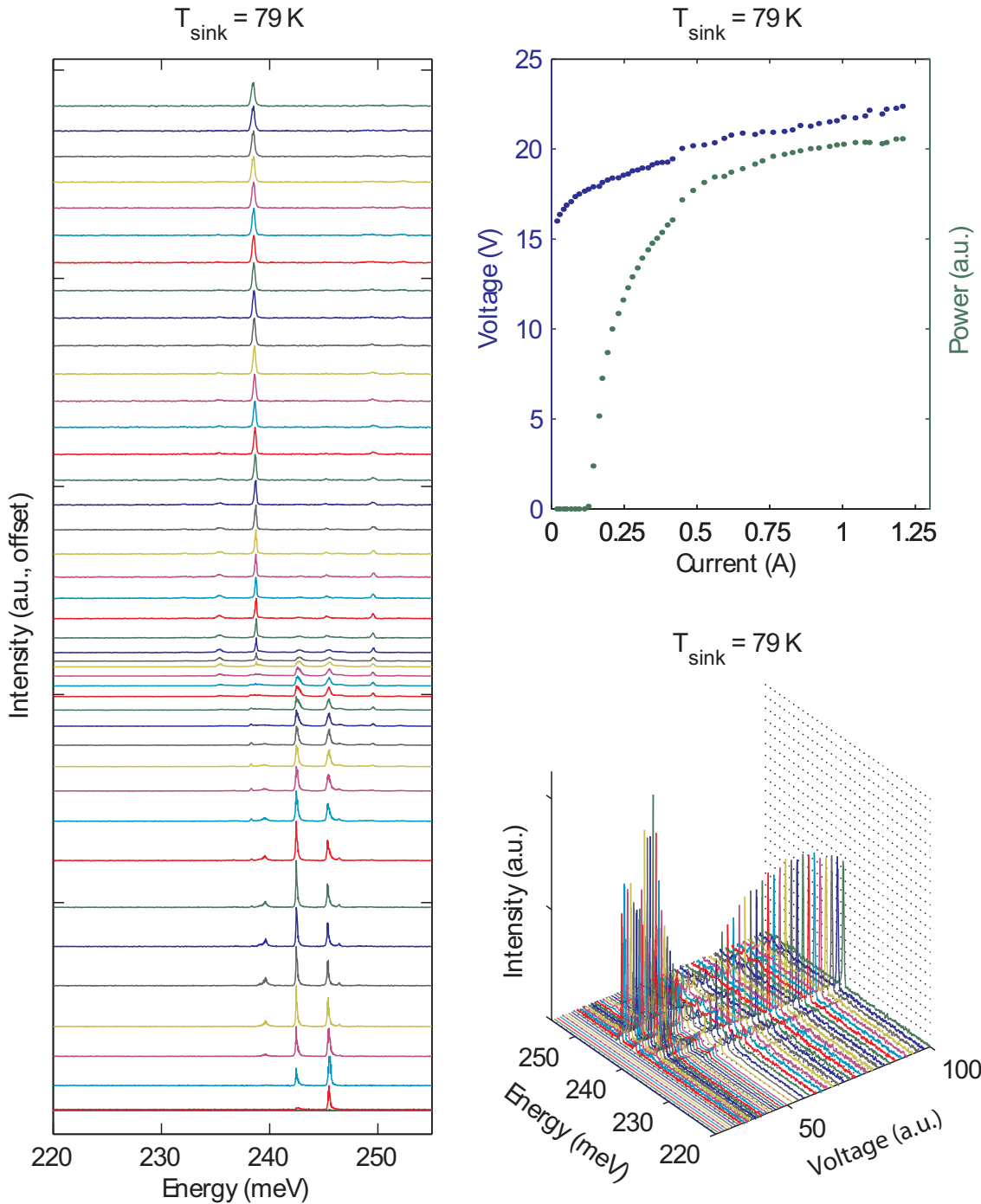


Figure 5.7: Spectra for the 3 injector well laser at $T_{\text{sink}} = 79 \text{ K}$. The device size was $10.4 \mu\text{m} \times 3 \text{ mm}$ pulsed at 80 kHz with a 100 ns current pulse. Each point in the LIV (top-right) has one corresponding spectra in the left and bottom-right plots.

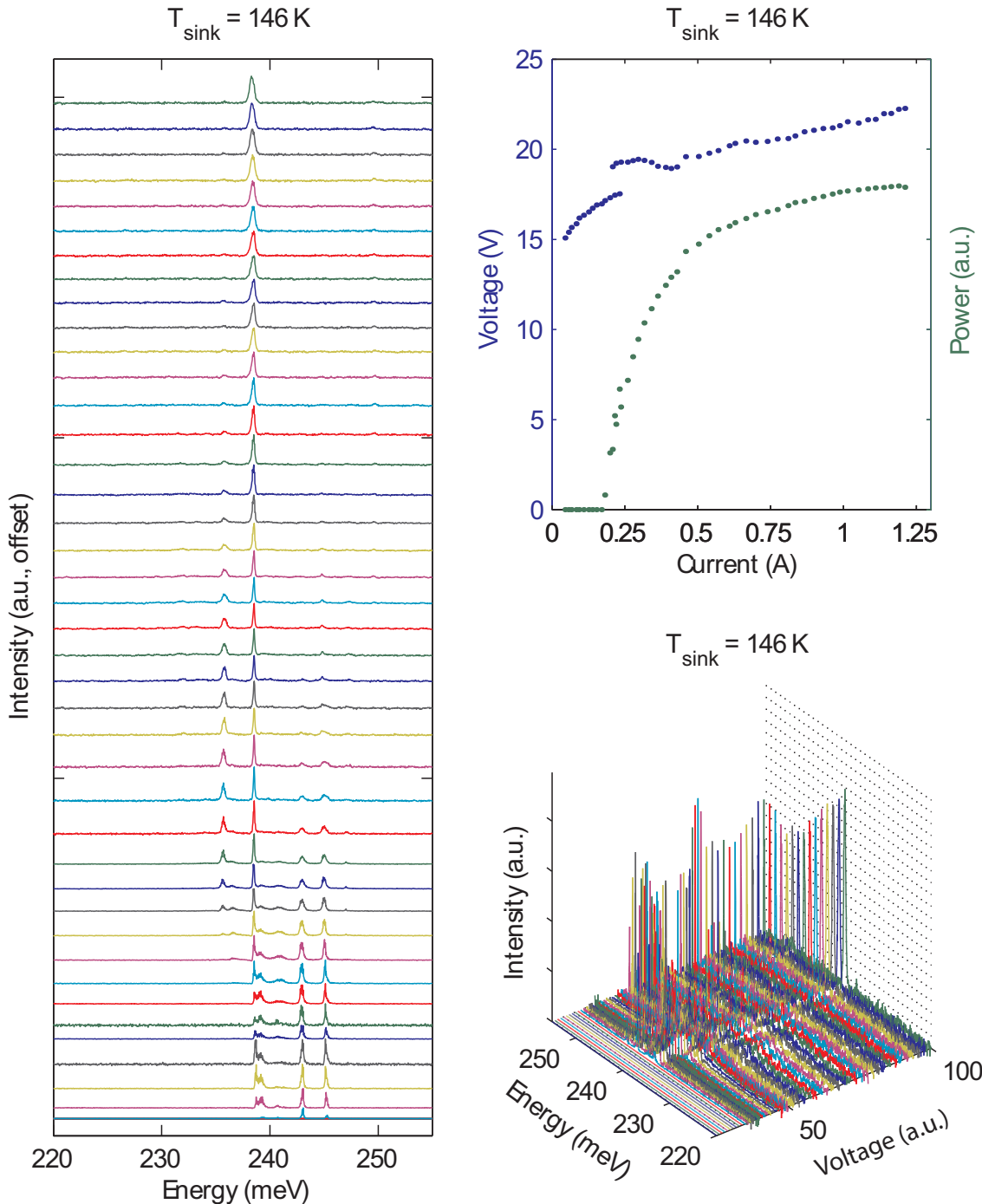


Figure 5.8: Spectra for the 3 injector well laser at $T_{\text{sink}} = 146 \text{ K}$. The device size was $10.4 \mu\text{m} \times 3 \text{ mm}$ pulsed at 80 kHz with a 100 ns current pulse. Each point in the LIV (top-right) has one corresponding spectra in the left and bottom-right plots.

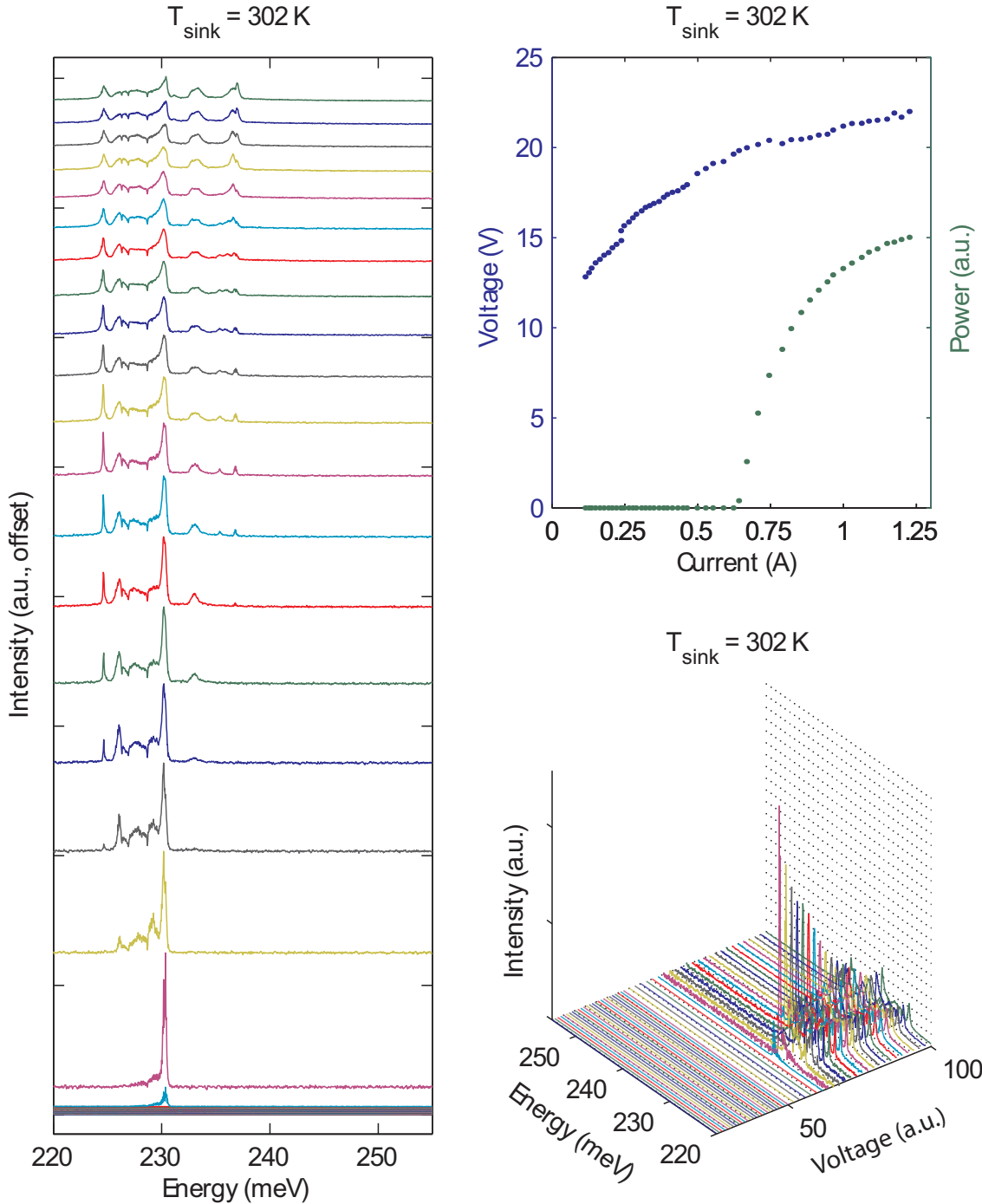


Figure 5.9: Spectra for the 3 injector well laser at $T_{\text{sink}} = 302 \text{ K}$. The device size was $10.4 \mu\text{m} \times 3 \text{ mm}$ pulsed at 80 kHz with a 100 ns current pulse. Each point in the LIV (top-right) has one corresponding spectra in the left and bottom-right plots.

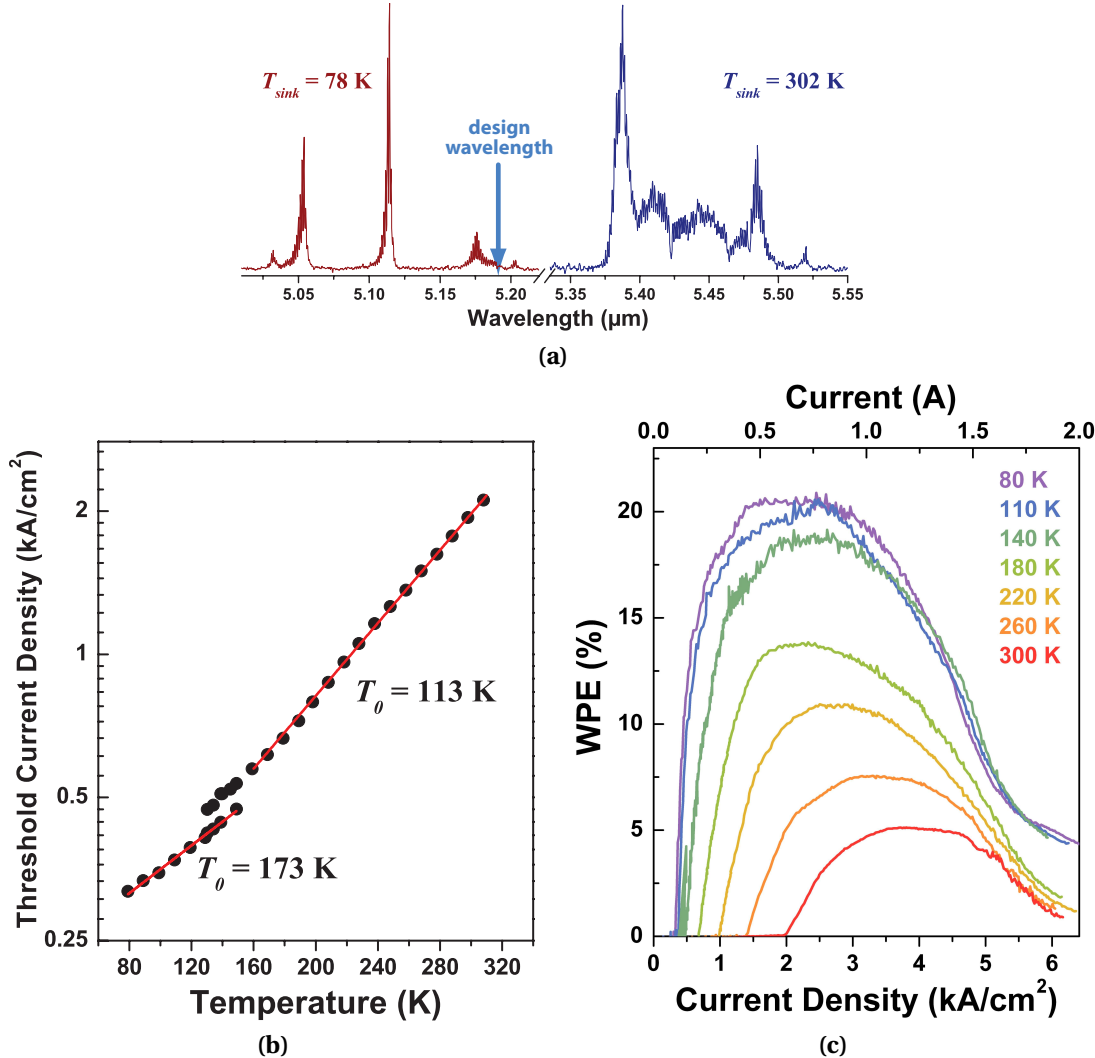


Figure 5.10: Performance data for the three injector well structure. (a) Representative normalized spectra of the three injector well structure for $T_{sink} = 78 \text{ K}$ and 302 K near threshold. Characteristic temperature T_0 (b) and pulsed wall-plug efficiency (c) for a $10.4 \mu\text{m} \times 3 \text{ mm}$ ridge laser device.

explains this result, with the rather low characteristic temperature $T_0 = 113 \text{ K}$ for T_{sink} where $J_{th} > J_{NDR}$. However, for T_{sink} where $J_{th} < J_{NDR}$, T_0 is much higher at 173 K. Wall-plug efficiency—as shown in Fig. 5.10c—peaks at 20.5% for $T_{sink} = 80 \text{ K}$ and 5.1% at 300 K.

5.4 QC Laser with Two Injector Wells

5.4.1 Design and Fabrication

To further test such short injector structures, we designed a second laser with only two injector wells and three active region wells. Besides the removal of one injector well, the two laser designs are otherwise similar. The emission energy was designed to be $\mathcal{E}_{ph} = 241$ meV ($\lambda_0 = 5.14$ μm) and energy defect designed to be $\Delta_{inj} = 107$ meV. The total QC period length $L_p = 274.5$ Å, for a design field $E_{field} = 128$ kV/cm. As shown in the Fig. 5.11 conduction band diagram, the layer sequence is, in angstroms starting from the injection barrier, **35** / 53 / **10.5** / 43 / **8.5** / 35 / **21** / 28.5 / **15.5** / 24.5, where $\text{Al}_{0.710}\text{In}_{0.290}\text{As}$ layers are in bold type, $\text{In}_{0.638}\text{Ga}_{0.362}\text{As}$ layers are in plain type, and layers Si-doped $n = 1.4 \times 10^{17}$ cm $^{-3}$ are underlined; the structure has an active core sheet density $n_s = 0.96 \times 10^{11}$ cm $^{-2}$. At 132 kV/cm, with the upper laser state somewhat isolated from the injector region states, we calculate $\tau_u = 1.41$ ps, $\tau_\ell = 0.23$ ps, $\tau_{u\ell} = 4.55$ ps, and $z_{u\ell} = 20.1$ Å, for a Figure of Merit $FoM = 542$ ps Å 2 and $FoM^* = 131$ ps Å 2 eV.

The laser was grown by MOVPE with a waveguide structure identical to that described in the previous section. Fabrication and processing were also similar.

5.4.2 Results and Discussion

Similar to the three well injector design reported in the previous section, LIV data for this design also show NDR, as seen in Fig. 5.12 for an EL mesa; in this case though, it is much less pronounced. Following the analysis of the previous section, the NDR appears 3.6 V (26 kV/cm) below the designed turn-on voltage. In this design, we calculate that the upper laser state and the second active region state of the up-stream active region mix at $E_{field} = 103$ kV/cm; here, the difference between the field at which these states align and the designed turn-on field—25 kV/cm—is in excellent agreement with the data. However, the states mix to a much less extent, which is consistent with the lower current change associated with the NDR feature.

The two injector well design shows other characteristic features in the LIV data. For example, in Fig. 5.13 we see two physically separate mechanisms that limit light output. For an applied 20 V, we see an increase in differential resistance; the feature is roughly

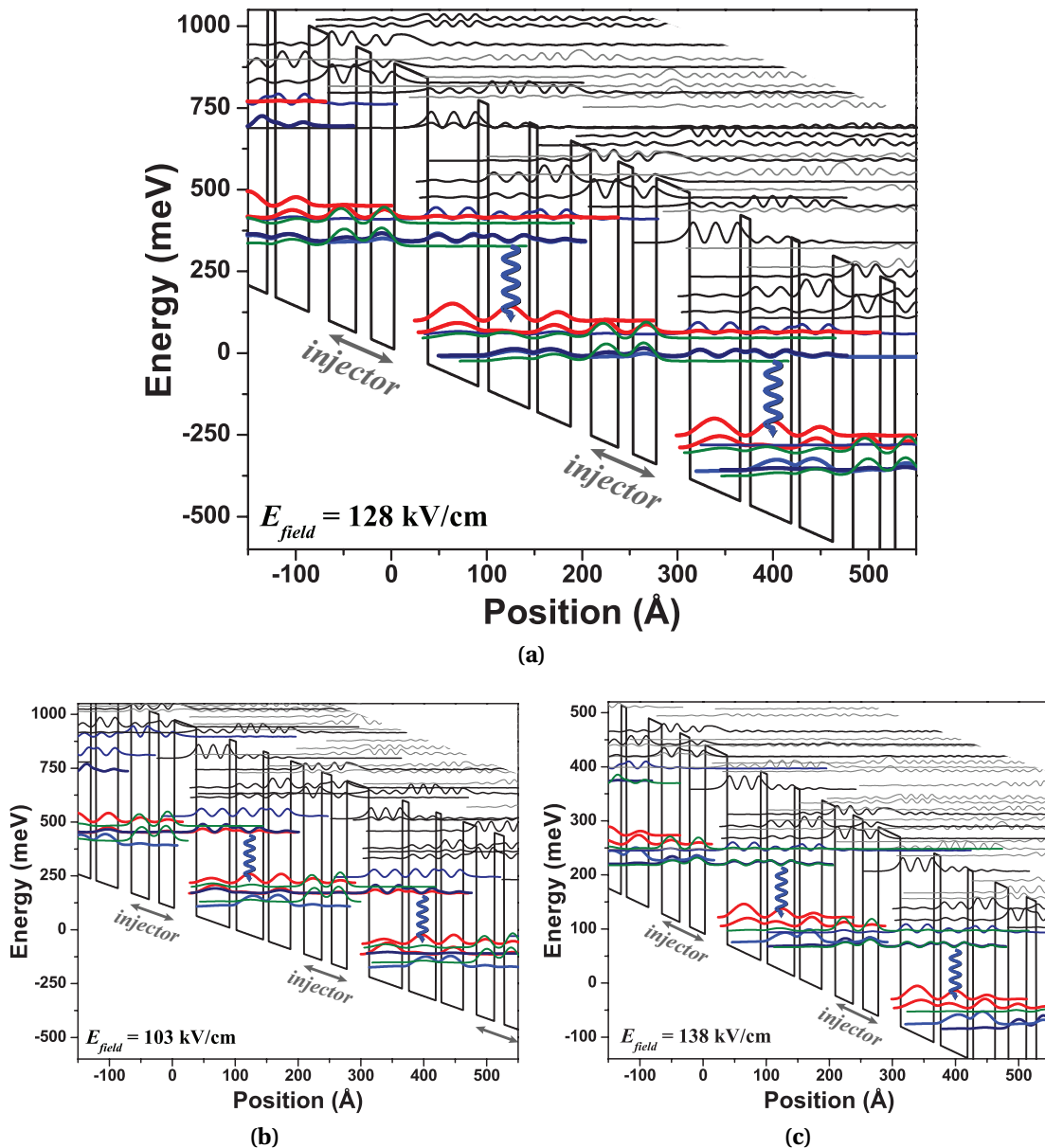


Figure 5.11: QC structure with two injector wells and three active region wells. The designed turn-on field is 128 kV/cm, shown here in (a). NDR is observed in this structure at $E_{field} = 103$ kV/cm, shown in (b). Also, an increase in differential resistance is seen in device data consistent with a re-configuration of the band alignment where the upper laser state is in resonance with the injector ground state, as in (c), near $E_{field} = 138$ kV/cm.

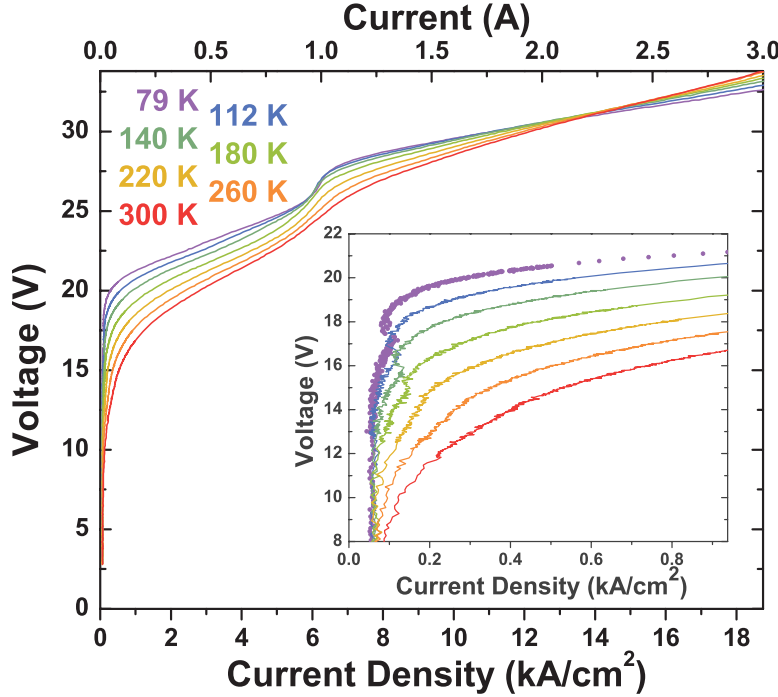


Figure 5.12: LIV for a two injector well EL sample. NDR is also seen in the two injector well design, but it is much less pronounced than in the three injector well design. Here, we see small NDR for a 0.016 mm^2 EL mesa.

independent of temperature, and it corresponds to a drop in slope efficiency. A second increase in differential resistance is observed, this time at a constant current density of about 7 kA/cm^2 (independent of temperature). Again, this feature generally corresponds to a decrease in output power. That the first effect appears with constant applied field and the second appears with constant current density is telling of the physical origins. The constant-current feature is the “turn-off” most commonly seen in QC lasers, where a maximum current density is reached based on the intrinsic transit times and the finite amount of doping n_s of the QC structure [56].

The constant-voltage turn-off feature in Fig. 5.13 is not as commonly observed. One explanation for this feature arises from examining the injector region configuration relative to the active region at different fields. At $T_{sink} = 79 \text{ K}$, the difference between the turn-on voltage of the device and this constant-voltage turn-off is about 2.1 V (15 kV/cm). Our laser was intentionally designed for the lowest state of one active region to be in resonance with the upper laser state of the adjacent down-stream active region

at threshold, providing efficient transport between active regions and thus decreasing τ_{inj} . In this design, these levels are in full resonance when $E_{field} = 128 \text{ kV/cm}$. However, because of the spatial separation of these two states, they remain strongly coupled over only a small field range. At $E_{field} = 128 \text{ kV/cm}$, the lowest injector state is below these two aligned states; increasing the field to 138 kV/cm puts the lowest injector state and the upper laser state in full resonance. This secondary field alignment and electron path is conceivably slower, as electrons have to travel through an additional state, increasing the differential resistance. The increase in differential resistance observed at constant applied field with variations in temperature may thus arise from these two injector region alignments. The successful operation of both these band alignments is further evidence that electrons can directly tunnel from one active region to the next—in effect, ballistic transport—in these short injector structures.

Yet another interesting feature is seen in the Fig. 5.13 LIV characteristics. Rather than peak output at the lowest temperatures, these lasers have peak output at elevated temperatures (180 K in this device), while highly unstable pulse behavior at lower temperatures limits average output power. The time evolution of the light pulse over the 100 ns period also indicates highly irregular behavior, with pulse-to-pulse variations on the order of 100 mW at low temperatures. These pulse instabilities are damped with increasing temperature, and they disappear around 140 K .

In QC structures, electric field profiles are largely assumed to be homogenous when the doping density is low, or periodic but stable when the doping density is higher. However, charge instabilities have long been known to exist in superlattice structures [146]. Intuitively, charge instabilities can result when local disruptions of the charge density locally perturb the field, leading to electric field domains. The highly nonlinear event of lasing onset is expected to exacerbate this instability, and in these minimalized QC structures, these instabilities are now more apparent.

Both of the previous features—constant-voltage turn-off and pulse instabilities—result from the highly discrete nature of the individual quantum states in our structure. In actuality, we have composed a QC structure out of only six relevant states: a ground state for each of the five quantum wells in the QC period and one quantum well first-excited state that is the upper laser state. Having only six states spread across $\Delta_{inj} = 107 \text{ meV}$ is unusual for QC structures; a comparable conventional design with a four well active region and seven injector wells would have 12 states spread across the same

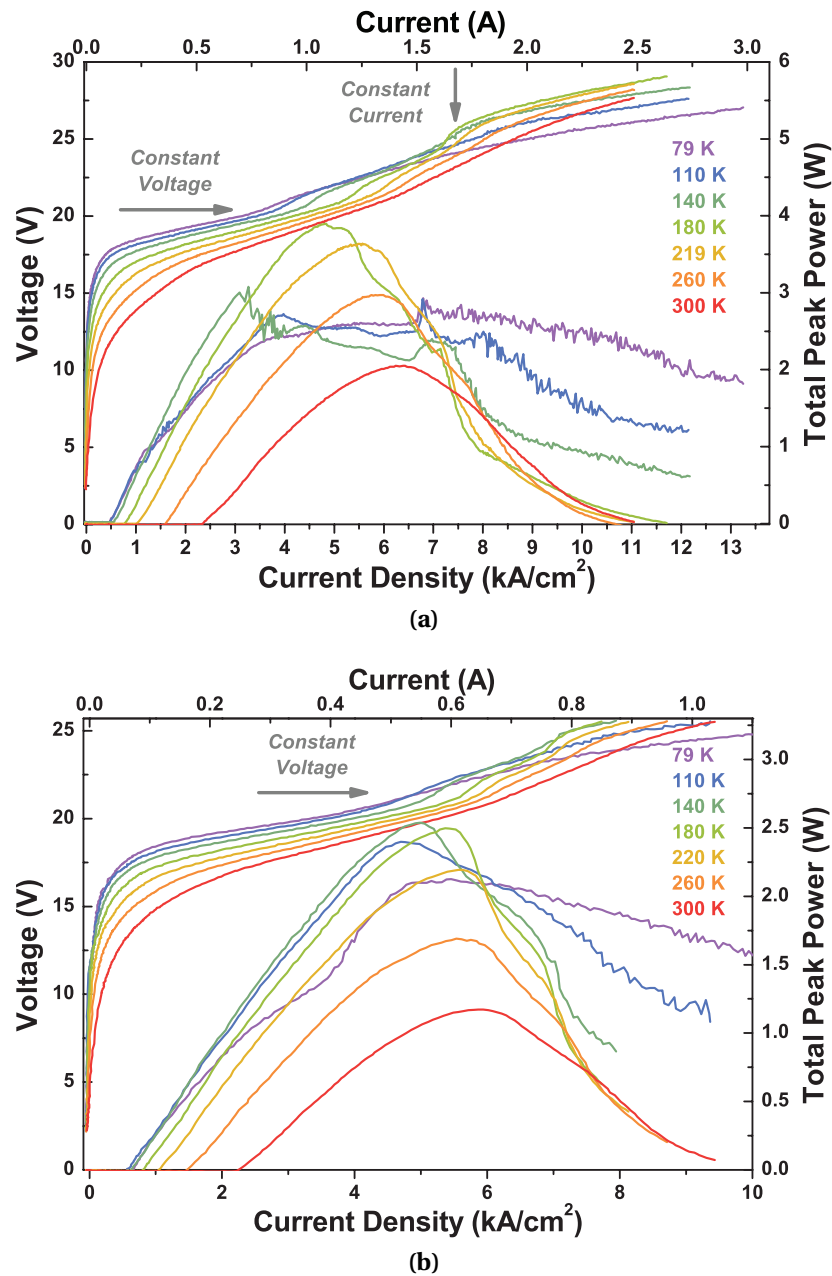


Figure 5.13: Pulsed LIV data for the two injector well structure (I). Panel (a) is for a $7.5 \mu\text{m} \times 3 \text{ mm}$ BH laser and (b) is for a $5.5 \mu\text{m} \times 2 \text{ mm}$ BH laser. Two “turn-off” features are seen, one occurring with constant voltage and one with constant current. Pulse instabilities are also evident at lower temperatures. Because of these instabilities, output power is highest at elevated temperatures.

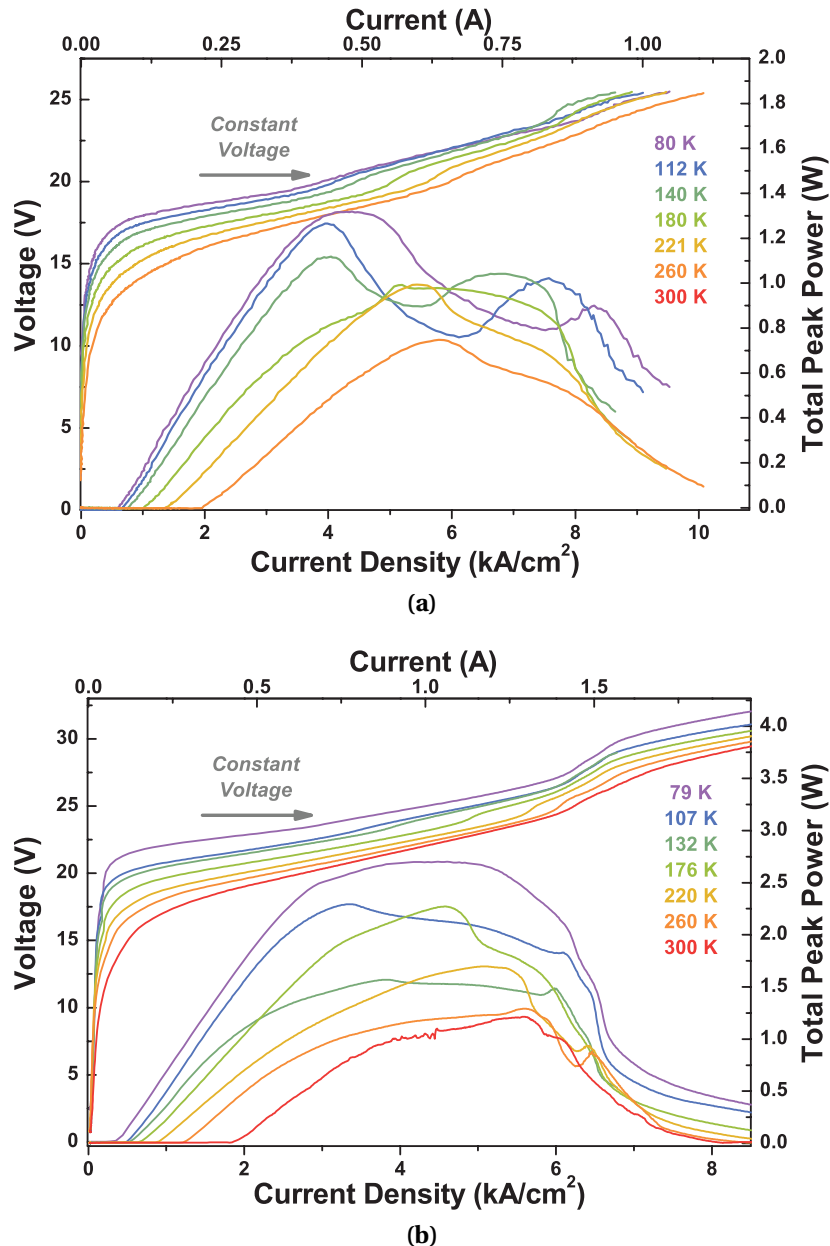


Figure 5.14: Pulsed LIV data for the two injector well structure (II). Panel (a) is for a $5.5 \mu\text{m} \times 2 \text{ mm}$ BH laser and (b) is for a $13 \mu\text{m} \times 3 \text{ mm}$ ridge laser. Again, two “turn-off” features are evident, one occurring with constant voltage and one with constant current.

Δ_{inj} . In this situation, we see the effect of the highly discrete injector region states; the positioning of individual states matters more than ever.

5.4.3 Device Performance

Figures 5.15 and 5.16 show laser spectra at $T_{sink} = 79$ and 301 K, respectively. Shown with each set of data is an LIV plot, with each LIV point corresponding to a spectral measurement. As shown in Fig. 5.17a, a standard red-shift is seen with increasing temperature: $\lambda_0 \approx 5.0 \mu\text{m}$ for $T_{sink} = 79$ K and at $\lambda_0 \approx 5.2 \mu\text{m}$ at room temperature.

Even with all of the unique features of the present device, performance is comparable to the field's best designs. For the BH laser device described by the Figs. 5.13a and 5.17 data, pulsed total output power peaks at 3.9 W at 180 K, while room temperature output power is 1.4 W. Low temperature output power in these devices is severely limited by the pulse instabilities previously discussed. Threshold current density is 460 A/cm² at 80 K, and reaches 2.3 kA/cm² at room temperature. Figure 5.17b shows threshold behavior similar to the three injector well design. As in the three injector well device, the T_0 approaching room temperature is relatively low at 113 K; the low temperature $T_0 = 305$ K. Wall-plug efficiency—as shown in Fig. 5.17c—peaks at 23.0% for $T_{sink} = 140$ K and 7.6% at 300 K. Again, wall-plug efficiency at low temperatures is limited by pulse instabilities.

5.5 Conclusions and Future Directions

5.5.1 Summary

In this chapter, I have presented our study on short injector region QC lasers, taking the approach of shrinking the conventional (approximately) seven well injector region to only two or three wells. Making the active core gain region “more dense” with optical transitions by shortening the QC period length in principle leads to improvement in performance metrics associated with output power and efficiency. That performance should be improved for shorter QC period lengths should come as no surprise. And recognizing the cascading effect of QC lasers, the field has a history of maximizing (and optimizing) the number of stacked QC periods [147].

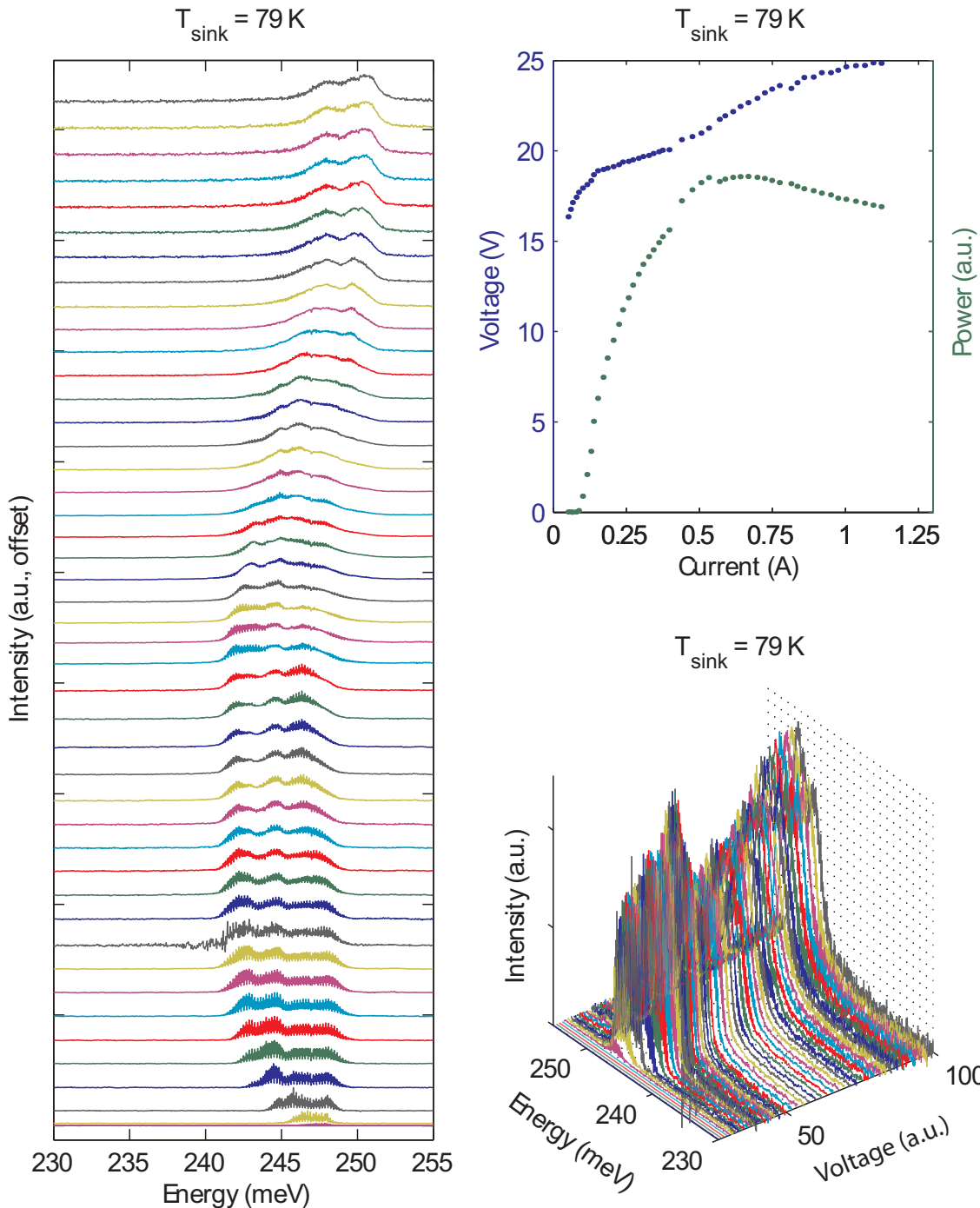


Figure 5.15: Spectra for the 2 injector well laser at $T_{\text{sink}} = 79 \text{ K}$. The device size was $5.5 \mu\text{m} \times 2 \text{ mm}$ pulsed at 80 kHz with a 100 ns current pulse, and corresponds to the LIV data in Fig. 5.13b. Each point in the LIV (top-right) has one corresponding spectra in the left and bottom-right plots.

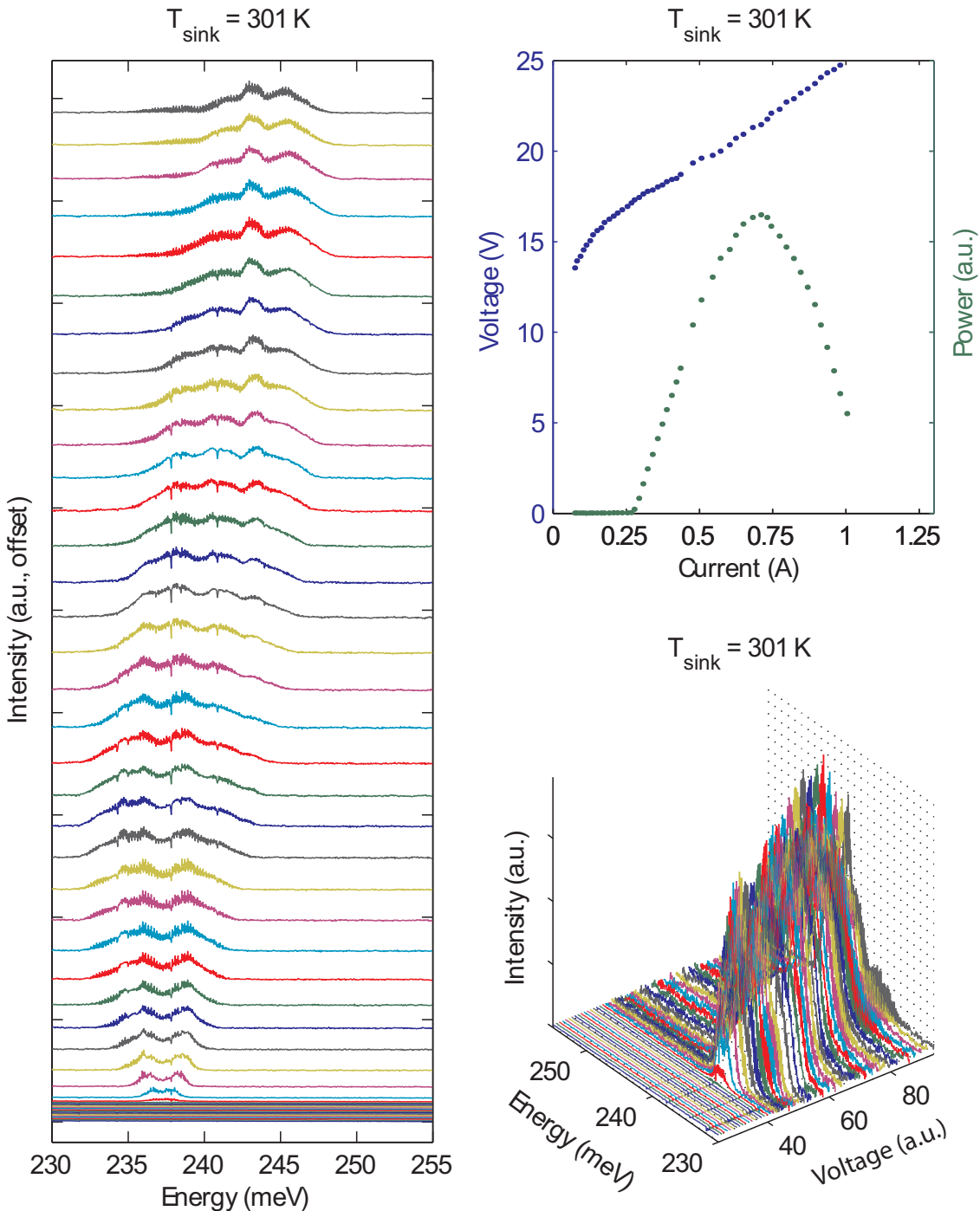


Figure 5.16: Spectra for the 2 injector well laser at $T_{\text{sink}} = 301 \text{ K}$. The device size was $5.5 \mu\text{m} \times 2 \text{ mm}$ pulsed at 80 kHz with a 100 ns current pulse, and corresponds to the LIV data in Fig. 5.13b. Each point in the LIV (top-right) has one corresponding spectra in the left and bottom-right plots.

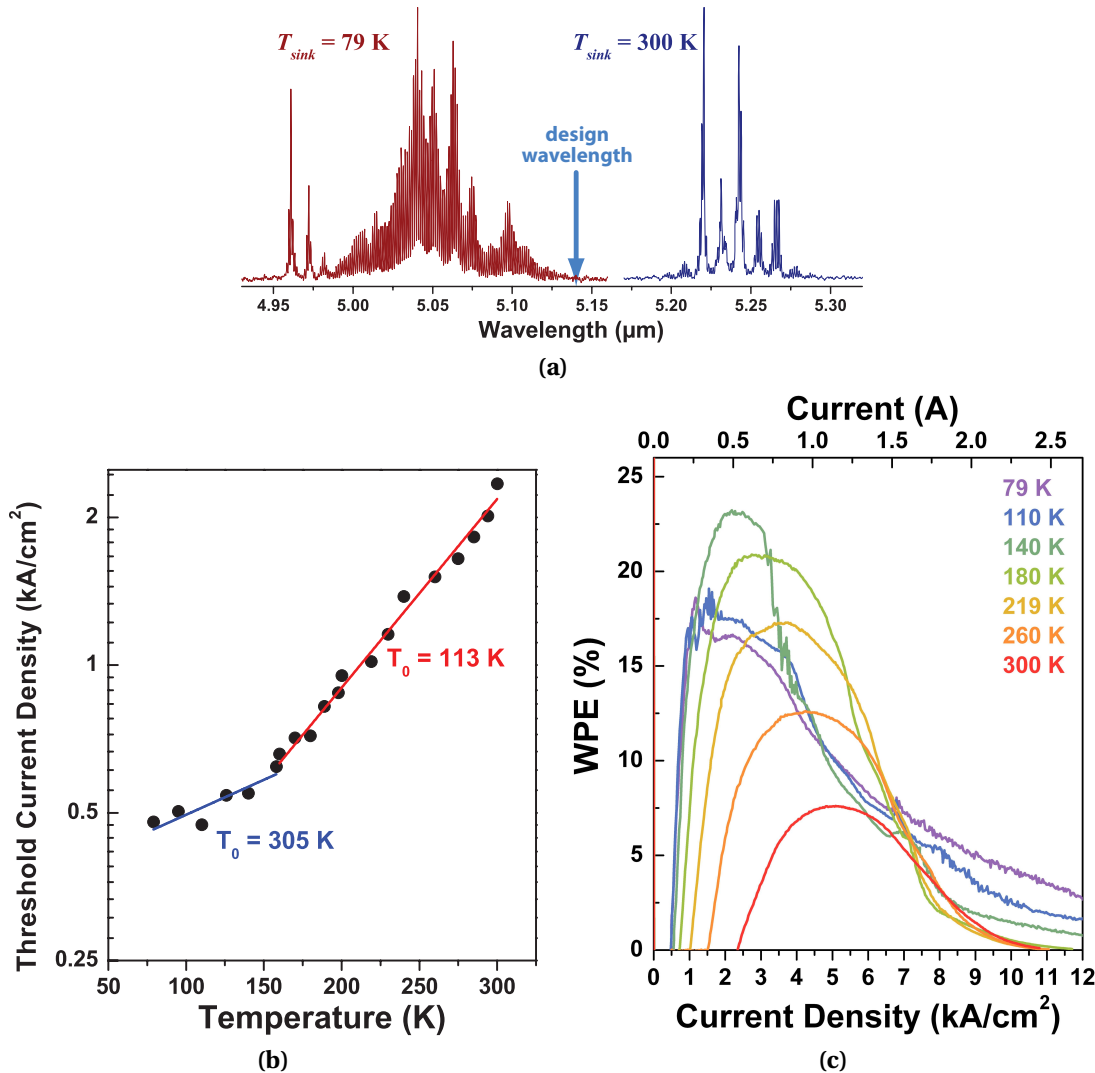


Figure 5.17: Performance data for the three injector well structure. (a) Representative normalized spectra of the two injector well structure for $T_{sink} = 79\text{ K}$ and 300 K near threshold. Characteristic temperature T_0 (b) and pulsed wall-plug efficiency (c) for the two injector well $7.5\text{ }\mu\text{m} \times 3\text{ mm}$ BH laser device that corresponds to the Fig. 5.13a LIV data.

Through this study of short injectors, we have observed a host of unique effects in QC lasers. Pronounced NDR is observed, where the presence of stimulated emission impacts the operating configuration of the laser band structure. Turn-off mechanisms—increases in differential resistance—are observed at constant voltages with temperature, in addition to the more conventional turn-off features observed at constant current. These effects can be attributed to two distinctive characteristics of the short injector

designs presented here: enhanced “coupling” of neighboring active regions due to the close proximity afforded by the extremely abbreviated injector regions; and the highly discreet nature of the injector region energy states.

The observation of these new phenomena provide additional insight into the mechanisms of QC laser operation. These effects are particularly relevant when designing QC lasers having minimalized injector regions. Much of what we have observed confirms that such abbreviated QC structures behave in many ways similar to the classical superlattice. For example, the highly discrete nature of individual states becomes particularly relevant, as well as the need to damp pulse instabilities [148] associated with shifting charge distributions. The pronounced NDR of the three injector well laser and its successful operation at a lowered field demonstrates the effect of stimulated emission on electron distributions and energy state lifetimes. It brings into question the field’s perception that electrons always pool in the lowest energy state, and that states must be aligned in a downward order before sufficient transport occurs for laser action.

Even with these effects, we have shown data comparable with state-of-the-art designs. We expect future improvement for designs making cognizant use of these discoveries.

5.5.2 Future Direction: Higher performance QC lasers

Notwithstanding the many of unique features discussed in this chapter—some of which may have limited performance in these first-generation short injector devices—optimizing length and other structural elements in injector regions holds great potential for improving QC wall-plug efficiency and overall performance. As of this writing, we have achieved 46.6% wall-plug efficiency from a $\lambda_0 = 4.6 \mu\text{m}$ QC laser that incorporates a short injector ($L_p = 346 \text{ \AA}$) with further improvement of injector region structure [149]. While this record efficiency is for $T_{sink} = 80 \text{ K}$, the result is a discontinuity in the incremental performance improvements of the last several years. Performance is rapidly improving, and shortened injectors are playing a key role.

5.5.3 Future Direction: Improving temperature performance

The two short injector designs herein presented, along with other short injector structures not yet reported, have shown consistently low characteristic temperatures:

$T_0 \leq 120$ K. Ultimately, such low T_0 will prove untenable for the commercially practicable case of room temperature high performance lasers. The systematic nature of these low T_0 s may ultimately a clue to the origin of the problem. While we commonly refer to threshold current densities J_{th} , we rarely consider threshold voltage V_{th} . Systematic examinations of V_{th} reveal that this value is remarkably constant with temperature. This isn't surprising: in a QCL, a sufficient voltage must be applied to achieve the desired—designed—band alignment. As the temperature increases in a laser core, the thermal distribution of electrons increases and the energy levels broaden. This commonly results in the “softening” of the initial IV turn-on with temperature. The slower the turn-on, the more current must be pumped through the laser to reach V_{th} .

It is possible that short injector regions are making this effect worse. Where a conventional, long injector region provides a sizeable barrier over which thermal electrons must “jump” before they can contribute to such a “thermal current,” a short injector imparts an ostensibly smaller barrier. That is, as the injector region is shortened, energy states in adjacent active regions more readily mix, increasing the tunneling probability—and therefore thermal transport rate—between. Thus, the very same mechanisms that at low temperature make short injectors so compelling create an additional hurdle at higher temperatures.

With an understanding of the source of the problem, solutions can be devised. Ideally, what is needed is a way to block electron transport until V_{th} is reached. Indeed, we may have demonstrated just such a mechanism in this chapter. We showed that transit times are sufficiently fast for short injector structures that a significant amount of injected current is supported without the aid of doped carriers. Specifically, the three well injector structure exhibited current transport at a field where the free electrons contributed from doping were still trapped in the active region ground state. Capitalizing on this effect could be the key to realizing the promise of short injector structures.

Chapter 6

Conclusions

In this thesis, we have demonstrated how QC lasers can be remarkably amenable to new laser design strategies. It's true: QC lasers have a level of engineerability unlike any other laser system known. The gain media for gas and solid state lasers, for example, have properties that are almost exclusively determined by nature. And even in semiconductor diode lasers, but for the inclusion of strained wells in 1988 [150], the same basic quantum confined double heterostructure first envisioned in 1974 [151] and demonstrated in 1975 [152] is still today's state-of-the-art gain medium. The tremendous improvement in diode laser performance since that time is substantially a result of better growth and fabrication techniques.

Seeking to exploit the inherent flexibility in QC structures, we have in this dissertation presented our work with new QC design strategies. Specifically, we looked at excited state QC lasers for the application of long wavelength emission and at shortened injector regions for improving laser performance. While work progressed toward our initial application goals, we also discovered several new phenomena that may one day be further exploited for better performance and innovative applications.

We discussed the generality of the QC concept; that is, QC structures are not limited to any single material system. While all QC lasers to date have been implemented in III-V materials, this need not, and someday will not, be the case. Here, we discussed our work towards implementing QC structures in II-VI materials. In the future, intersubband devices such as QC lasers may be made from even more exotic structures, such as from alternating layers of semiconductor and oxide materials [153].

In the following sections, we summarize the key results of this thesis; we also discuss my perspective on the future of the mid-infrared QC laser field.

6.1 Thesis Summary

In Chapter 1, we outlined several applications for mid-infrared light. These included both currently in-use applications, such as a variety of trace gas sensing applications, and also promising applications for the future, such as defense countermeasures. After a basic introduction to QC laser operating principles, we discussed some of the current capabilities and limitations facing state-of-the-art QC lasers. Finally, we gave an overview of the QC laser development process, discussing the basic inputs to design, growth, and processing.

Chapter 2 of this thesis was used to present a “toolbox” for designing QC lasers. Included were details necessary for solving QC band structures. Then, parameters that are of interest for QC laser quantum design, such as the optical dipole matrix element and LO phonon scattering time, were discussed. Finally, the fundamental relations that govern performance metrics, threshold current, output power, and slope efficiency were derived from first principles.

6.1.1 II-VI QC Structures

As mentioned in Chapter 1, a current challenge faced by QC lasers is performance that cuts off sharply at wavelengths below $4\text{ }\mu\text{m}$ for high performance InGaAs/AlInAs structures. Yet, with highly important molecular resonances in the $3\text{--}4\text{ }\mu\text{m}$ range—such as the C-H stretch—along with the presence of a key infrared countermeasure band, high performance light sources at wavelengths below $4\text{ }\mu\text{m}$ would be of commercial interest. Chapter 3 thus discusses our work with II-VI QC structures, a materials system that is not plagued by the limitations of conduction band offset and intervalley scattering present in III-V materials. After reviewing the state-of-the-art in alternative QC materials systems such as those incorporating Sb, we discuss the materials properties and epitaxial growth of ZnCdSe / ZnCdMgSe structures grown on InP. We also gave an in-depth discussion of fabrication and processing techniques related ZnCdSe / ZnCdMgSe on InP, which in some areas we found to be different than the standard processing steps

used for III-V InGaAs/AlInAs structures. Our preliminary work looked to confirm the presence of intersubband transitions in ZnCdSe / ZnCdMgSe quantum well structures, which we observed as resonant TM absorption at the ground state energy transition of the as-grown single quantum well. With this result, we were able to proceed in the design of a ZnCdSe / ZnCdMgSe QC structure. A first generation design took the conventional, well-understood strategy of a two-well active region QC structure. We confirmed intersubband absorption in the fabricated structure that was a good match to calculated absorption energies. With electrical pumping, we saw TM-polarized EL at 80 K that was centered near 4.8 μm , in good agreement with the design wavelength of 4.4 μm . This 4.8 μm emission was observed to persist through room temperature. Along with the 4.8 μm light, we observed longer wavelength light that grew in intensity with temperature. The IV characteristics of the first generation structure confirmed electron transport behavior as expected from a QC device.

Second generation devices with a theoretically improved design and a slightly different design wavelength (4.8 μm) were also grown and tested. These devices showed extraordinarily similar emission energies as the first generation devices, despite the nominally different design wavelengths. While contributing doubt to the origin of the initial EL observation, the majority of the data is nevertheless largely consistent the EL originating from an intersubband optical transition.

Concluding remarks in the chapter shared a number of ideas for future directions for II-VI QC research. These included multiple new design strategies to compensate for the high degree of MBE growth difficulty, the inclusion of strain compensation to increase the material band offset, and a method for overcoming challenges associated with laser waveguides in ZnCdSe/ZnCdMgSe on InP structures.

6.1.2 Excited State Quantum Cascade Lasers and High k -Space Lasing

Achieving high performance at longer wavelengths—beyond about 12 μm —is perhaps even more difficult than lasing below 4 μm . In Chapter 4, we proposed a new QC design strategy that can increase the optical dipole matrix element: excited state transitions. By increasing the optical dipole matrix element, we can reduce the extremely high thresholds that pose such a challenge to long wavelength devices. After the design and fabrication of an excited state QC laser design, we observed unexpected dual

wavelength emission from the devices. We determined that the emission originated from energetically stacked transitions within the QC active region.

Further study of the temperature dependence of the individual LI curves for the two transitions showed remarkably unusual behavior. Rather than output power for the two transitions being positively correlated—as would intuitively be expected for stacked transitions—we observed just the opposite. This anti-correlation in output power suggested carrier populations that were strongly linked. We rationalized that the second, lower optical transition in the active region was positioned high in k -space. A new discovery in QC lasers to be sure, our excited state structure made this observation possible because of the method by which we populated a highly excited state in the active region, resulting in multiple transitions with large oscillator strength in each active region. Since non-radiative LO phonon scattering populates an energy subband high in k -space, our excited state structure was able to make use of these high k -space electrons in a lasing transition. We confirmed the feasibility of our explanation through a rate equation model that included stimulated emission terms for two optical transitions (one at high k -space) and all applicable temperature-dependencies. Our model was accurately fit to observed threshold data. We moreover confirmed k -space lasing through the observation of a spectral red-shift in the k -space emission that is due to energy state non-parabolicity.

Concluding remarks in the chapter discussed a number of applications for high k -space lasing. These included making use of k -space transitions for lowering threshold currents and for improving QC laser tunability. Also, we discussed the possibility of excited state structures that produce stacked optical transitions being used for correlated photon pair generation, so long as both transitions are made able to lase at the Γ point.

6.1.3 Short Injector Quantum Cascade Lasers

In Chapter 5, we explored in-depth the role of the QC injector region. While injectors are not the source of photon generation, they perform many other functions vital to healthy QC laser performance. So while we cannot eliminate injector regions altogether, we examine the possibility of minimizing the space they take up. In theory, optimizing (that is, minimizing) injector length should lead to lower threshold currents, higher slope

efficiencies, higher wall-plug efficiencies, lower differential resistance, and ultimately higher output power.

We designed and analyzed two short injector structures containing three active region quantum wells and either two or three injector region quantum wells. In these structures, the total QC period length was reduced by nearly a factor of two over a conventional QC structure of a similar emission wavelength. We observed many unique properties in the LI and IV data for each device that we attribute (i) to the enhanced coupling between adjacent active regions due to the shortened injector length and (ii) to the highly discrete nature of the injector energy states resulting from so few quantum wells per QC period. The first of these observed behaviors was pronounced negative differential resistance in the three injector well structure; the NDR showed a complex and rich interaction with the presence of stimulated emission. Here, we concluded that two primary current transport paths (field alignments) are naturally supported by the structure, and that the laser dynamically chooses which to operate in based on the per period transit time. Furthermore, we found this transit time to be highly dynamic, and dependent upon the cavity photon density in the presence of stimulated emission.

While the two injector well structure showed some of these same NDR features, the NDR was not nearly as pronounced here. The two injector well structure featured its own unique behavior, with a distinctive turn-off feature that happened at a constant applied voltage with temperature. This was in addition to the customary turn-off feature that happens at a constant current with temperature—that is, the standard J_{max} . We attributed the presence of this constant voltage turn-off to the highly discrete nature of the injector region states.

To conclude the chapter, we discussed a present limitation of short injector structures: consistently low T_0 leading to substantially degraded performance near room temperature. We proposed an alternative way to interpret threshold—a threshold voltage rather than threshold current—which may provide insight into how to ultimately improve laser performance at elevated temperatures.

6.2 Challenges for the Next Decade of Research

The future development of mid-infrared QC lasers holds only the utmost of promise. Performance and capabilities have seen rapid improvement and expansion in just the

last few years alone. Continued development and progress seems at this point to be unbounded: with an understanding of the root cause of present challenges, the remarkably flexible QC concept will undoubtedly allow for the engineering of new QC architectures that mitigate or eliminate the problem's root cause.

There are several challenges that at present dominate the QC landscape. These challenges present rich opportunities for impactful research. Here, I name these challenges explicitly, and I give forward-looking predictions and personal opinions regarding the field's prospects.

6.2.1 Tunability

The ability to tune the emission wavelength over a substantially broad range will be useful for versatile trace gas sensing systems. Currently, the internal tuning mechanisms available to a QC laser are limited to changing the device temperature. This of course can be complemented with the external tuning mechanism of an external cavity [128]. Both have limitations: temperature tuning is slow, and external cavities are still limited by the internal width of the QC gain spectrum. This thesis has suggested one new mechanism for internally augmenting the tunability—high k -space transitions—and research into the ability to voltage-tune a QC structure also appears promising [127].

The Challenge Can we make a single structure that can tune across the second atmospheric window? The first? Both?

6.2.2 Single Mode Emission

While tunability is important, gas-phase laser spectroscopy relies on laser emission at a single spectral mode. Traditionally, this has been accomplished through distributed feedback [154] or distributed Bragg reflector [155] structures. Yet these methods for single mode emission impose structures that are mechanically hard-written into the laser itself. Certainly, these methods are prohibitive to the possibility of internal, dynamic tunability mechanisms. Coupling *both* tunability and single mode emission is a tall order indeed.

The Challenge Can we develop methods for single mode emission internal to the QC laser that also accommodate internal tunability?

6.2.3 Wall-plug Efficiency

QC laser wall-plug efficiency has made extraordinary progress over the last few years. However, research here has focused only on a narrow wavelength band. And the DARPA-imposed “top of the mountain,” 50% at RT CW, has yet to be reached. Furthermore, the record numbers reported in the literature are commonly thought of as “hero” results, where a single device may possess such high performance, but the median capability of all similarly produced devices is considerably lower.

Improving the efficiency of QC lasers would significantly expand the number of problems for which QC lasers are a solution. Efficiency goals will not be reached with today’s conventional thinking. Unconventional ideas—those that capitalize upon and exploit the innate engineerability of the quantum cascade—will be required. To be sure, unconventional thinking is risky, and ideas most often fail to yield the intended result. But sometimes they succeed.

The Challenge Can RT CW lasers operating with 50% WPE be made over a large swath of wavelengths? And can they be manufactured reproducibly?

6.2.4 Low Input Power Devices

One almost completely unexplored area in the QC landscape is low input power devices [156] [157]. Most spectroscopy systems—representing the vast majority of present-day uses for QC lasers in terms of number of applications—do not need a lot of optical power. Usually, 10–100 mW is plenty. There is great opportunity for optimizing laser design and performance to *minimize input power*.

Using the typical 5 mW green laser pointer as a basis for comparison, a 10 W QC laser is exceedingly bright, and it would be overkill for many applications. Furthermore, high output power necessitates high input power: a system surrounding a 5% efficient laser operating with 20 W of input power must dissipate 19 W of heat! A 5 mW QC laser with the same 5% efficiency, by comparison, would need only 0.1 W of input power and thus would be accompanied by substantially reduced thermal dissipation requirements.

The Challenge Can we meet the 50% WPE challenge with devices geared toward low input power rather than high output power?

6.2.5 Short Wavelength QC Lasers

The 3–4 μm gap in semiconductor laser capability remains a challenge. With further research, strained InGaAs / AlInAs QC lasers will easily reach 3.7 μm CW RT emission; innovative design concepts may put 3.5 μm within reach. Emission down to 3.3 μm for this material system poses a considerable challenge.

Because of issues of intervalley transfer in the QC well material, Sb will never be of practical use for QC lasers grown on InP substrates. However, InAs / AlSb should be able cover the 3–3.5 μm span nicely—with RT CW performance—given further research. The challenges with InAs substrates are of now sizable; improvement will be needed on all QC frontiers: QC design, waveguide design, growth, fabrication, and heat sinking/mounting technology. In a practical sense, diode lasers may more effectively cover the 3–3.5 μm gap for low power applications. The high power 3–3.5 μm applications, however, will necessarily have to be covered by QC lasers.

The Challenge Can QC lasers fully cover the 3–4 μm gap with RT CW performance? Can the industry-preferred InGaAs / AlInAs structures reach 3.3 μm ?

6.2.6 Long Wavelength QC Lasers

RT CW emission at long wavelengths is among the most daunting challenges faced by QC lasers today. Indeed, achieving a 20 μm CW RT laser (that is, lasing at all, at any efficiency) is probably a bigger challenge than a 4.5 μm laser at 50% CW RT. Despite the challenge, expanding capabilities to longer wavelengths is important. The potential applications, especially out to about 20 μm , could be highly rewarding. Progress on this front will be realized only through further innovation in design strategy.

The Challenge Can QC lasers be made to operate RT CW at a wavelength of 20 μm ?

6.3 The Feasibility of a Sustainable QC Laser-based Industry

I wish to close by sharing some thoughts about the potential degree to which QC lasers will have a real-world impact.

Without question, I am an enthusiastic believer that QC technology is in store for a brilliant future.

Over the last two years, I have had the privilege of founding and working with Primis Technologies LLC, a startup company with the mission of commercializing mid-infrared technologies. When colleagues and I embarked on this journey, I knew earning a Ph.D. while simultaneously running a company would be a challenge. Yet ambition got the better of me, and doing both was the only option. Priorities as they are, research took first seat. To this point, Primis has been much more of a side project than it deserved. Still, I would not want to give up the experience. And my position of straddling industry and academia has given me a unique perspective.

I find the mid-infrared industry, at present, to be lacking in its ability to innovate. Applications drive the ultimate impact of any technology. Mid-infrared technology is in need of demonstrably successful applications—that is, successful in the private sector. The industry right now is far too reliant on the “obvious” and “easy” applications, those of military or homeland security scope where government is the ultimate end user and consumer. Innovation is needed to develop new ideas and new applications that will be of interest and importance to private—at least, non-government—consumers. There are problems out there waiting to be solved. Just one example: in a world of limited raw inputs, especially in a market like the first half of 2008 where the costs of raw inputs were at historic levels, marked improvements in efficient use of inputs will (i) prove profitable and (ii) ultimately enhance the sustainability of the human condition. Innovative and creative uses of mid-infrared technology can without doubt improve raw input efficiency in commercially-relevant areas.

That said, perhaps all that’s needed is time. With the relative size of the industry compared to the shear number of potential applications, competition should not be a concern. As the industry has yet to secure legitimacy, and since mid-infrared technology has yet to broadly prove itself, the industry as a whole will reap substantial benefit from the success of any individual participant. The more participants there are, the faster this will happen. Truly, problems exist that are uniquely suited to solutions making use of mid-infrared light. Let’s find them; let’s solve them. Those solutions in hand, a healthy mid-infrared industry will inevitably emerge.

Publications

K. J. Franz, K.-T. Shiu, S. R. Forrest, and C. Gmachl, “A dual-wavelength quantum cascade laser with two optical transitions in each active region,” *Proc. IPRM* **18**, 26 (2006).

H. Lu, A. Shen, W. Charles, I. Yokomizo, M. C. Tarmargo, **K. J. Franz**, C. Gmachl, and M. Munoz, “Optical characterization of intersubband transitions in $Zn_xCd_{1-x}Se / Zn_{x'}Cd_{y'}Mg_{1-x'-y'}Se$ multiple quantum well structures by contact-less electroreflectance,” *Appl. Phys. Lett.* **89**, 241921 (2006).

S. Zhang, X. Zhou, A. Shen, W. Wang, R. Alfano, H. Lu, W. O. Charles, I. Yokomizo, M. C. Tamargo, **K. J. Franz**, and C. Gmachl, “Optical Properties of Heavily Doped n-type CdSe Quantum Dots for Intersubband Device Applications,” *Proc. MRS* **959E**, 0959-M06-05 (2006).

A. Shen, H. Lu, M. C. Tamargo, W. Charles, I. Yokomizo, **K. J. Franz**, C. Gmachl, S. K. Zhang, X. Zhou, R. R. Alfano, and H. C. Liu, “Intersubband absorption in CdSe/ZnCdMgSe self-assembled quantum dot multi-layers,” *Appl. Phys. Lett.* **90**, 071910 (2007).

K. J. Franz, D. Wasserman, A. J. Hoffman, D.C. Jangraw, K.-T. Shiu, S. R. Forest, and C. Gmachl, “Evidence of cascaded emission in a dual-wavelength Quantum Cascade laser,” *Appl. Phys. Lett.* **90**, 091104 (2007).

A. Shen, H. Lu, M. C. Tamargo, W. Charles, I. Yokomizo, C. Y. Song, H. C. Liu, S. K. Zhang, X. Zhou, R. R. Alfano, **K. J. Franz**, and C. Gmachl, “Intersubband transitions in molecular-beam-epitaxy-grown wide band gap II-VI semiconductors,” *J. Vac. Sci. Tech. B* **25**, 995 (2007).

- H. Lu, A. Shen, M. C. Tamargo, W. Charles, I. Yokomizo, M. Munoz, Y. Gong, G. F. Neumark, **K. J. Franz**, C. Gmachl, C. Y. Song, and H.C. Liu, “Study of intersubband transitions of $Zn_xCd_{1-x}Se/Zn_xCd_yMg_{1-x-y}Se$ multiple quantum wells grown by molecular beam epitaxy for midinfrared device applications,” *J. Vac. Sci. Tech. B* **25**, 1103 (2007).
- A. J. Hoffman, L. Alekseyev, S. S. Howard, **K. J. Franz**, D. Wasserman, V. A. Podolskiy, E. E. Narimanov, D. L. Sivco, and C. Gmachl, “Negative refraction in semiconductor metamaterials,” *Nature Materials* **6**, 946 (2007).
- A. J. Hoffman, S. Schartner, S. S. Howard, **K. J. Franz**, F. Towner, and C. Gmachl, “Low voltage-defect quantum cascade laser with heterogeneous injector regions,” *Opt. Express* **15**, 15818 (2007).
- K. J. Franz**, W. O. Charles, A. Shen, A. J. Hoffman, M. C. Tamargo, and C. Gmachl, “ZnCdSe/ZnCdMgSe Quantum Cascade Electroluminescence,” *Appl. Phys. Lett.* **92**, 121105 (2008).
- W. O. Charles, A. Shen, **K. J. Franz**, C. Gmachl, Q. Zhang, Y. Gong, G. F. Neumark, and M. C. Tamargo, “Growth and Characterization of $Zn_xCd_{1-x}Se / Zn_{x'}Cd_yMg_{1-x'-y'}Se$ Asymmetric Coupled Quantum Well Structures for Quantum Cascade Laser Applications,” *J. Vac. Sci. Tech. B* **26**, 1171 (2008).
- A. Shen, W. O. Charles, B. S. Li, **K. J. Franz**, C. Gmachl, Q. Zhang, and M. C. Tamargo, “Wide Band Gap II-VI Selenides for Short Wavelength Intersubband Devices,” *J. Cryst. Growth*, doi:10.1016/j.jcrysgro.2008.10.102.
- W. O. Charles, **K. J. Franz**, A. Shen, A. Zhang, B. Li, Y. Gong, G. F. Neumark, C. Gmachl, and M. C. Tamargo, “Molecular Beam Epitaxy Growth of $Zn_xCd_{1-x}Se / Zn_{x'}Cd_{y'}Mg_{1-x'-y'}Se$ —InP Quantum Cascade Structures,” *J. Cryst. Growth* **310**, 5380 (2008).

S. S. Howard, D. P. Howard, **K. J. Franz**, A. J. Hoffman, D. L. Sivco, and C. Gmachl, “The effect of injector barrier thickness and doping level on current transport and optical transition width in a $\lambda \sim 8 \mu\text{m}$ QC structure,” *Appl. Phys. Lett.* **93**, 191107 (2008).

K. J. Franz, S. Menzel, A. J. Hoffman, D. Wasserman, J. W. Cockburn, and C. Gmachl, “High k -space lasing in a dual wavelength quantum cascade laser,” *Nature Photonics* **3**, 50 (2008).

Y. Yao, **K. J. Franz**, Z. Liu, A. J. Hoffman, and C. F. Gmachl, “Voltage tuning of gain spectra in quantum cascade lasers,” *Proc. SPIE* **7230**, 723012 (2009).

A. J. Hoffman, P. X. Braun, M. D. Escarra, **K. J. Franz**, X. Wang, and C. Gmachl, “Lasing-induced reduction of core heating in high wall plug efficiency quantum cascade lasers,” *Appl. Phys. Lett.* **94**, 041101 (2009).

J. B. Khurjin, Y. Dikmelik, P. Q. Liu, A. J. Hoffman, M. D. Escarra, **K. J. Franz**, and C. F. Gmachl, “Role of interface roughness in the transport and lasing characteristics of quantum-cascade lasers,” *Appl. Phys. Lett.* **94**, 091101 (2009).

C. R. Young, R. Cendejas, S. S. Howard, W. Sanchez-Vaynshteyn, A. J. Hoffman, **K. J. Franz**, Y. Yao, B. Mizaikoff, X. Wang, J.-Y. Fan, and C. Gmachl, “Wavelength selection for quantum cascade lasers by cavity length,” *Appl. Phys. Lett.* **94**, 091109 (2009).

Y. Yao, Z. J. Liu, A. J. Hoffman, **K. J. Franz**, and C. F. Gmachl, “Voltage Tunability of Quantum Cascade Lasers,” *IEEE J. Quantum Electron.*, accepted.

A. J. Hoffman, L. Alekseyev, A. Sridhar, P. X. Braun, S. S. Howard, **K. J. Franz**, D. Wasserman, V. A. Podolskiy, E. E. Narimanov, D. L. Sivco, and C. Gmachl, “Mid-infrared Semiconductor Optical Metamaterials,” *J. Appl. Phys.*, accepted.

K. J. Franz, M. D. Escarra, A. J. Hoffman, P. Q. Liu, J. J. J. Rafty, S. S. Howard, Y. Dikmelik, J. B. Khurjin, X. Wang, J.-Y. Fan, C. Gmachl, “Short Injector Quantum Cascade Lasers,” *IEEE J. Quantum Electron.*, submitted.

Publications

M. D. Escarra, A. J. Hoffman, **K. J. Franz**, S. S. Howard, R. Cendejas, X. Wang, J.-Y. Fan, and C. Gmachl, “Voltage defect in quantum cascade lasers of less than one longitudinal optical phonon energy,” *Appl. Phys. Lett.*, submitted.

Y. Yao, **K. J. Franz**, X. Wang, J.-Y. Fan, and C. Gmachl, “Widely voltage tunable gain spectra of quantum cascade lasers,” *Appl. Phys. Lett.*, submitted.

P. Q. Liu, A. J. Hoffman, M. D. Escarra, **K. J. Franz**, J. B. Khurgin, Y. Dikmelik, X. Wang, J.-Y. Fan, and C. Gmachl, “Highly Power-Efficient Mid-Infrared Lasers,” *Science*, submitted.

Conference Presentations

K. J. Franz, K.-T. Shiu, S. R. Forrest, and C. Gmachl, “A dual-wavelength quantum cascade laser with two optical transitions in each active region,” *IPRM Princeton*, NJ, May 2006. **Best Student Paper Award**

K. J. Franz, K.-T. Shiu, S. R. Forrest, and C. Gmachl, “Excited state and dual-wavelength quantum cascade lasers,” *CLEO Semiconductor Laser Workshop* Long Beach, CA, June 2006.

A. Shen, H. Lu, M. C. Tamargo, W. Charles, I. Yokomizo, C. Y. Song, H. C. Liu, S. K. Zhang, X. Zhou, R. R. Alfano, **K. J. Franz**, and C. Gmachl, “Intersubband Transitions in MBE-grown Wide Bandgap II-VI Semiconductors,” *NAMBE* Durham, NC, Oct 2006.

S. Zhang, X. Zhou, A. Shen, W. Wang, R. Alfano, H. Lu, W. O. Charles, I. Yokomizo, M. C. Tamargo, **K. J. Franz**, and C. Gmachl, “Optical Properties of Heavily Doped n-type CdSe Quantum Dots for Intersubband Device Applications,” *MRS Fall Meeting* Boston, MA, Nov 2006.

K. J. Franz, K.-T. Shiu, S. R. Forrest, and C. Gmachl, “Monolithic Mid-Infrared Integration of a Quantum Cascade Laser and a Passive Semiconductor Waveguide,” *APS March Meeting* Denver, CO, Mar 2007.

K. J. Franz, D. Wasserman, A. J. Hoffman, K.-T. Shiu, S. R. Forrest, and C. Gmachl, “Cascaded Emission in a Dual-Wavelength Quantum Cascade Laser,” *PRISM/PCCM/MIRTHE Industry Day* Princeton, NJ, Mar 2007.

K. J. Franz, D. Wasserman, A. J. Hoffman, K.-T. Shiu, S. R. Forrest, and C. Gmachl, “Cascaded Emission in a Dual-Wavelength Quantum Cascade Laser,” *CLEO Baltimore*, MD, May 2007.

S. S. Howard, A. J. Hoffman, **K. J. Franz**, T. Ko, and C. Gmachl, “Current Injection Transition Broadening in Quantum Cascade Lasers,” *ITQW Ambleside*, Cumbria, U.K., Sept 2007.

K. J. Franz, S. Menzel, A. J. Hoffman, D. Wasserman, K.-T. Shiu, S. R. Forrest, and C. Gmachl, “Excited State Optical Transitions in Quantum Cascade Lasers for Low Thresholds and Multi-Wavelength Emission,” *ITQW Ambleside*, Cumbria, U.K., Sept 2007.

W. O. Charles, A. Shen, **K. J. Franz**, C. Gmachl, Q. Zhang, Y. Gong, G. F. Neumark, and M. C. Tamargo, “Asymmetric Coupled Quantum Well Structure for Quantum Cascade Laser Applications,” *NAMBE* Albuquerque, NM, Sept 2007.

A. J. Hoffman, S. Schartner, S. S. Howard, **K. J. Franz**, F. Towner, and C. Gmachl, “Low-Voltage Defect Quantum Cascade Laser with Heterogeneous Injector Regions,” *IEEE LEOS Annual Meeting* Lake Buena Vista, FL, Oct 2007.

S. S. Howard, A. J. Hoffman, **K. J. Franz**, D. P. Howard, T. Ko, D. L. Sivco, and C. F. Gmachl, “Effect of Injection Barrier Thickness and Doping on Transport and Gain in a $\lambda = 8.2 \mu\text{m}$ Quantum Cascade Laser,” *IEEE LEOS Annual Meeting* Lake Buena Vista, FL, Oct 2007.

K. J. Franz, A. J. Hoffman, S. S. Howard, Z. J. Liu, S. Menzel, S. Schartner, D. Wasserman, and C. Gmachl, “Mid-Infrared Quantum Cascade Lasers,” *Mauterndorf Winterschool* Bad Hofgastein, Austria, Feb 2008.

K. J. Franz, S. Menzel, A. J. Hoffman, D. Wasserman, J. W. Cockburn, and C. Gmachl, “High k -Space Lasing in a Dual Optical Transition Quantum Cascade Laser,” *Mauterndorf Winterschool* Bad Hofgastein, Austria, Feb 2008. poster presentation

K. J. Franz, S. Menzel, A. J. Hoffman, D. Wasserman, J. W. Cockburn, and C. Gmachl, “Excited State Quantum Cascade Lasers and Lasing in k -Space,” *PRISM/PCCM/MIRTHE Industry Day* Princeton, NJ, Mar 2008.

M. D. Escarra, A. J. Hoffman, S. S. Howard, **K. J. Franz**, A. Sridhar, and C. Gmachl, “High Efficiency Quantum Cascade Lasers,” *APS March Meeting* New Orleans, LA, Mar 2008.

W. O. Charles, **K. J. Franz**, A. Shen, M. C. Tamargo, and C. Gmachl, “Growth and properties of wide band gap II-VI multi-quantum well structures for mid-infrared quantum cascade lasers,” *APS March Meeting* New Orleans, LA, Mar 2008.

M. A. Talukder, F.-S. Choa, C. R. Menyuk, **K. J. Franz**, S. S. Howard, C. F. Gmachl “Novel Heat Removal Waveguide Structure for High Performance Quantum Cascade Lasers,” *CLEO* San Jose, CA, May 2008. poster presentation

A. J. Hoffman, S. Schartner, S. S. Howard, **K. J. Franz**, F. Towner, and C. Gmachl, “Low Voltage Defect Heterogeneous Quantum Cascade Laser,” *CLEO* San Jose, CA, May 2008.

S. Menzel, **K. J. Franz**, D. Wasserman, A. J. Hoffman, J. W. Cockburn, and C. F. Gmachl, “Laser Action at High k -Space Values in Anti-Correlated Multi-Wavelength Quantum Cascade Lasers,” *CLEO* San Jose, CA, May 2008.

K. J. Franz, W. O. Charles, A. Shen, A. J. Hoffman, M. C. Tamargo, and C. Gmachl, “Intersubband Electroluminescence from a ZnCdSe/ZnCdMgSe Quantum Cascade Structure,” *CLEO* San Jose, CA, May 2008.

Y. Dikmelik, J. B. Khurjin, A. J. Hoffman, S. S. Howard, **K. J. Franz**, and C. F. Gmachl, “Excited-State Absorption in High-Power Mid-Infrared Quantum Cascade Lasers,” *CLEO* San Jose, CA, May 2008. poster presentation

K. J. Franz, W. O. Charles, A. Shen, A. J. Hoffman, M. C. Tamargo, and C. Gmachl, “Electroluminescence from a ZnCdSe/ZnCdMgSe Quantum Cascade Structure,” *ICPS* Rio de Janeiro, Brazil, July 2008. poster presentation

K. J. Franz, S. Menzel, D. Wasserman, A. J. Hoffman, J. W. Cockburn, and C. Gmachl, “High k -Space Lasing in Excited State Quantum Cascade Lasers,” *ICPS* Rio de Janeiro, Brazil, July 2008.

A. Shen, W. O. Charles, B. S. Li, **K. J. Franz**, C. Gmachl, Q. Zhang, and M. C. Tamargo, "Wide Band Gap II–Selenides for Short Wavelength Intersubband Devices," *MBE2008* Vancouver, Canada, Aug 2008.

A. J. Hoffman, M. D. Escarra, S. S. Howard, **K. J. Franz**, X. Wang, J.-Y. Fan, and C. Gmachl, "Strategies for Improved Wall-plug Efficiency in Quantum Cascade Lasers," *MIOMD IX* Freiburg, Germany, Sept 2008.

K. J. Franz, W. O. Charles, A. Shen, A. J. Hoffman, M. C. Tamargo, and C. Gmachl, "Quantum Cascade Electroluminescence from a ZnCdSe/ZnCdMgSe on InP Structure," *MIOMD IX* Freiburg, Germany, Sept 2008.

Y. Yao, Z. Liu, A. J. Hoffman, **K. J. Franz**, and C. F. Gmachl, "Voltage tunability of quantum cascade lasers," *IQCLSW* Monte Verita, Switzerland, Sept 2008.

Y. Dikmelik, J. B. Khurjin, A. J. Hoffman, S. S. Howard, **K. J. Franz**, and C. F. Gmachl, "Excited-State Absorption in High-Power Mid-Infrared Quantum Cascade Lasers," *IQCLSW* Monte Verita, Switzerland, Sept 2008. poster presentation

M. D. Escarra, A. J. Hoffman, S. S. Howard, **K. J. Franz**, X. Wang, M. Fong, and C. F. Gmachl, "Improved Voltage Efficiency in Quantum Cascade Lasers," *IQCLSW* Monte Verita, Switzerland, Sept 2008. poster presentation

W. O. Charles, **K. J. Franz**, A. Shen, Q. Zhang, C. Gmachl, and M. C. Tamargo, "Growth and Characterization of $Zn_xCd_{1-x}Se / Zn_{x'}Cd_{y'}Mg_{1-x'-y'}Se$ Quantum Cascade Emitters," *IQCLSW* Monte Verita, Switzerland, Sept 2008.

K. J. Franz, P. Q. Liu, A. J. Hoffman, S. S. Howard, M. D. Escarra, Y. Dikmelik, J. B. Khurjin, X. Wang, J.-Y. Fan, and C. Gmachl, "Short Injector Regions for Improved Quantum Cascade Laser Performance," *IQCLSW* Monte Verita, Switzerland, Sept 2008. **Invited**

Y. Yao, **K. J. Franz**, Z. Liu, A. J. Hoffman, and C. F. Gmachl, "Voltage tuning of gain spectra in quantum cascade lasers," *Photonics West* San Jose, CA, Feb 2009.

Y. Dikmelik, J. B. Khurgin, M. D. Escarra, P. Q. Liu, A. J. Hoffman, **K. J. Franz**, C. F. Gmachl, J.-Y. Fan, and W. Wang “Intersubband Absorption Loss in High-Performance Mid-Infrared Quantum Cascade Lasers,” *CLEO* Baltimore, MD, June 2009. poster presentation

M. D. Escarra, A. J. Hoffman, **K. J. Franz**. S. S. Howard, X. Wang, J.-Y. Fan, and C. Gmachl, “Ultra-Low Voltage Defect Quantum Cascade Lasers,” *CLEO* Baltimore, MD, June 2009.

A. J. Hoffman, P. X. Braun, M. D. Escarra, S. S. Howard, **K. J. Franz**, X. Wang, J.-Y. Fan, C. Gmachl, “Instantaneous Power and Threshold in Continuous Wave Quantum Cascade Lasers,” *CLEO* Baltimore, MD, June 2009.

P. Q. Liu, A. J. Hoffman, M. D. Escarra, **K. J. Franz**, J. B. Khurgin, Y. Dikmelik, X. Wang, J.-Y. Fan, and C. F. Gmachl, “Quantum Cascade Lasers with Ultra-Strong Coupling Injection,” *CLEO* Baltimore, MD, June 2009.

K. J. Franz, J. J. J. Raftery, P. Q. Liu, A. J. Hoffman, M. D. Escarra, S. S. Howard, Y. Dikmelik, J. B. Khurgin, X. Wang, J.-Y. Fan, and C. Gmachl, “Negative Differential Resistance and Pulse Instabilities in Minimalized Quantum Cascade Laser Structures,” *CLEO* Baltimore, MD, June 2009.

Y. Yao, **K. J. Franz**, X. Wang, J.-Y. Fan, and C. F. Gmachl, “Widely Voltage Tunable Quantum Cascade Lasers,” *CLEO* Baltimore, MD, June 2009.

C. Young, R. Cendejas, S. S. Howard, W. Sanchez-Vaynshteyn, A. J. Hoffman, **K. J. Franz**, Y. Yao, G. Mizaikoff, X. Wang, J.-Y. Fan, and C. F. Gmachl, “Enhancing Wavelength Selection for Quantum Cascade Laser Based Chemical Sensors by Cavity Length Variation,” *CLEO* Baltimore, MD, June 2009. poster presentation

J. B. Khurgin, Y. Dikmelik, P. Q. Liu, A. J. Hoffman, M. D. Escarra, **K. J. Franz**, and C. F. Gmachl, “Role of Interface Roughness in the Transport and Lasing Characteristics of Quantum-Cascade Lasers,” *CLEO* Baltimore, MD, June 2009.

Intellectual Property

Claire Gmachl and Kale J. Franz, “Excited State Quantum Cascade Photon Source,” United States, filed 4 May 2007.

Kale J. Franz and Claire Gmachl, “Mid-Infrared Photonic Integration,” United States, provisional patent application.

Kale J. Franz, Claire Gmachl, Anthony J. Hoffman, and Scott S. Howard, “Heterogeneous Quantum Cascade Lasers with Low Voltage Defect,” United States, provisional patent application.

References

- [1] D. M. Chapin, C. S. Fuller, and G. L. Pearson, “A New Silicon p-n Junction Photocell for Converting Solar Radiation into Electrical Power,” *J. Appl. Phys.* **25**, 676 (1954).
doi:[10.1063/1.1721711](https://doi.org/10.1063/1.1721711)
- [2] R. N. Hall, G. E. Fenner, J. D. Kingsley, T. J. Soltys, and R. O. Carlson, “Coherent Light Emission From GaAs Junctions,” *Phys. Rev. Lett.* **9**, 366 (1962).
doi:[10.1103/PhysRevLett.9.366](https://doi.org/10.1103/PhysRevLett.9.366)
- [3] J. Nick Holonyak and S. F. Bevacqua, “Coherent (Visible) Light Emission from $\text{Ga}(\text{As}_{1-x}\text{P}_x)$ Junctions,” *Appl. Phys. Lett.* **1**, 82 (1962).
doi:[10.1063/1.1753706](https://doi.org/10.1063/1.1753706)
- [4] Z. I. Alferov, “The double heterostructure concept and its applications in physics, electronics, and technology,” *Rev. Mod. Phys.* **73**, 767 (2001).
doi:[10.1103/RevModPhys.73.767](https://doi.org/10.1103/RevModPhys.73.767)
- [5] H. Kroemer, “Quasielectric fields and band offsets: teaching electrons new tricks,” *Rev. Mod. Phys.* **73**, 783 (2001).
doi:[10.1103/RevModPhys.73.783](https://doi.org/10.1103/RevModPhys.73.783)
- [6] L. Esaki and R. Tsu, “Superlattice and Negative Differential Conductivity in Semiconductors,” *IBM J. Res. Dev.* **14**, 61 (1970).
url: <http://www.research.ibm.com/journal/rd/141/ibmrd1401H.pdf>
- [7] R. F. Kazarinov and R. A. Suris, “Possibility of Amplification of Electromagnetic Waves in a Semiconductor with a Superlattice,” *Sov. Phys. Semicond.* **5**, 207 (1971).
- [8] J. Faist, F. Capasso, D. L. Sivco, C. Sirtori, A. L. Hutchinson, and A. Y. Cho, “Quantum Cascade Laser,” *Science* **264**, 553 (1994).
doi:[10.1126/science.264.5158.553](https://doi.org/10.1126/science.264.5158.553)

References

- [9] B. S. Williams, “Terahertz quantum-cascade lasers,” *Nature Photonics* **1**, 517 (2007).
doi:[10.1038/nphoton.2007.166](https://doi.org/10.1038/nphoton.2007.166)
- [10] J. Devenson, O. Cathabard, R. Teissier, and A. N. Baranov, “InAs/AlSb quantum cascade lasers emitting at 2.75–2.97 μm,” *Appl. Phys. Lett.* **91**, 251102 (2007).
doi:[10.1063/1.2825284](https://doi.org/10.1063/1.2825284)
- [11] R. Colombelli, F. Capasso, C. Gmachl, A. L. Hutchinson, D. L. Sivco, A. Tredicucci, M. C. Wanke, A. M. Sergent, and A. Y. Cho, “Far-infrared surface–plasmon quantum–cascade lasers at 21.5 μm and 24 μm wavelengths,” *Appl. Phys. Lett.* **78**, 2620 (2001).
doi:[10.1063/1.1367304](https://doi.org/10.1063/1.1367304)
- [12] Senior Airman Julianne Showalter, *United States Air Force*
- [13] BAE Systems, “BAE SYSTEMS’ ATIRCM/CMWS Successfully Completes Army Live-fire Tests; Key Testing Milestone Accomplished,” *Press Release* (May 15, 2001).
- [14] H. Manor and S. Arnon, “Performance of an Optical Wireless Communication System as a Function of Wavelength,” *Appl. Opt.* **42**, 4285 (2003).
doi:[10.1364/AO.42.004285](https://doi.org/10.1364/AO.42.004285)
- [15] A. A. Kosterev, R. F. Curl, F. K. Tittel, M. Rochat, D. Hofstetter, and J. Faist, “Chemical sensing with pulsed QC–DFB lasers operating at 15.6 μm,” *Appl. Phys. B* **75**, 351 (2002).
doi:[10.1007/s00340-002-0963-z](https://doi.org/10.1007/s00340-002-0963-z)
- [16] M. Beck, D. Hofstetter, T. Aellen, J. Faist, U. Oesterle, M. Illegems, E. Gini, and H. Melchior, “Continuous Wave Operation of a Mid-Infrared Semiconductor Laser at Room Temperature,” *Science* **295**, 301 (2002).
doi:[10.1126/science.1066408](https://doi.org/10.1126/science.1066408)
- [17] G. Scamarcio, F. Capasso, C. Sirtori, J. Faist, A. L. Hutchinson, D. L. Sivco, and A. Y. Cho, “High-Power Infrared (8-Micrometer Wavelength) Superlattice Lasers,”

- Science* **276**, 773 (1997).
doi:[10.1126/science.276.5313.773](https://doi.org/10.1126/science.276.5313.773)
- [18] M. Troccoli, A. Belyanin, F. Capasso, E. Cubukcu, D. L. Sivco, and A. Y. Cho, “Raman injection laser,” *Nature* **433**, 845 (2005).
doi:[10.1038/nature03330](https://doi.org/10.1038/nature03330)
- [19] R. Terazzi, T. Gresch, M. Giovannini, N. Hoyler, N. Sekine, and J. Faist, “Bloch gain in quantum cascade lasers,” *Nature Physics* **3**, 329 (2007).
doi:[10.1038/nphys577](https://doi.org/10.1038/nphys577)
- [20] K.-Y. Cheng, “Molecular beam epitaxy technology of III–V compound semiconductors for optoelectronic applications,” *Proc. IEEE* **85**, 1694 (1997).
doi:[10.1109/5.649646](https://doi.org/10.1109/5.649646)
- [21] J. Coleman, “Metalorganic chemical vapor deposition for optoelectronic devices,” *Proc. IEEE* **85**, 1715 (1997).
doi:[10.1109/5.649647](https://doi.org/10.1109/5.649647)
- [22] Z. Liu, D. Wasserman, S. Howard, A. Hoffman, C. Gmachl, X. Wang, T. Tanbun-Ek, L. Cheng, and F-S. Choa, “Room-temperature continuous-wave quantum cascade lasers grown by MOCVD without lateral regrowth,” **18**, 1347 (2006).
doi:[10.1109/LPT.2006.877006](https://doi.org/10.1109/LPT.2006.877006)
- [23] M. Razeghi, “High-power high-wall plug efficiency mid-infrared quantum cascade lasers based on InP/GaInAs/InAlAs material system,” *Proc. SPIE* **7230**, 723011 (2009).
doi:[10.1117/12.813923](https://doi.org/10.1117/12.813923)
- [24] K. J. Franz, W. O. Charles, A. Shen, A. J. Hoffman, M. C. Tamargo, and C. Gmachl, “ZnCdSe/ZnCdMgSe quantum cascade electroluminescence,” *Appl. Phys. Lett.* **92**, 121105 (2008).
doi:[10.1063/1.2903135](https://doi.org/10.1063/1.2903135)
- [25] K. J. Franz, D. Wasserman, A. J. Hoffman, D. C. Jangraw, K.-T. Shiu, S. R. Forrest, and C. Gmachl, “Evidence of cascaded emission in a dual-wavelength quantum

- cascade laser," *Appl. Phys. Lett.* **90**, 091104 (2007).
doi:[10.1063/1.2709970](https://doi.org/10.1063/1.2709970)
- [26] K. J. Franz, S. Menzel, A. J. Hoffman, D. Wasserman, J. W. Cockburn, and C. Gmachl, "High k -space lasing in a dual-wavelength quantum cascade laser," *Nature Photonics* **3**, 50 (2008).
doi:[10.1038/nphoton.2008.250](https://doi.org/10.1038/nphoton.2008.250)
- [27] C. Sirtori, F. Capasso, J. Faist, and S. Scandolo, "Nonparabolicity and a sum rule associated with bound-to-bound and bound-to-continuum intersubband transitions in quantum wells," *Phys. Rev. B* **50**, 8663 (1994).
doi:[10.1103/PhysRevB.50.8663](https://doi.org/10.1103/PhysRevB.50.8663)
- [28] P. Harrison, *Quantum Wells, Wires and Dots: Theoretical and Computational Physics of Semiconductor Nanostructures* Wiley 2nd edn. (2005).
ISBN **0-470-01080-0**
- [29] I. Vurgaftman, J. R. Meyer, and L. R. Ram-Mohan, "Band parameters for III-V compound semiconductors and their alloys," *J. Appl. Phys.* **89**, 5815 (2001).
doi:[10.1063/1.1368156](https://doi.org/10.1063/1.1368156)
- [30] G. Dehlinger, L. Diehl, U. Gennser, H. Sigg, J. Faist, K. Ensslin, D. Grutzmacher, and E. Muller, "Intersubband Electroluminescence from Silicon-Based Quantum Cascade Structures," *Science* **290**, 2277 (2000).
doi:[10.1126/science.290.5500.2277](https://doi.org/10.1126/science.290.5500.2277)
- [31] O. Malis, L. N. Pfeiffer, K. W. West, A. M. Sergent, and C. Gmachl, "Mid-infrared hole-intersubband electroluminescence in carbon-doped GaAs/AlGaAs quantum cascade structures," *Appl. Phys. Lett.* **88**, 081117 (2006).
doi:[10.1063/1.2179117](https://doi.org/10.1063/1.2179117)
- [32] S. Adachi, *Properties of Group-IV, III-V and II-VI Semiconductors* Wiley (2005).
ISBN **0-470-09032-4**
- [33] Y. P. Varshni, "Temperature dependence of the energy gap in semiconductors," *Physica* **34**, 149 (1967).
doi:[10.1016/0031-8914\(67\)90062-6](https://doi.org/10.1016/0031-8914(67)90062-6)

- [34] J. Faist, F. Capasso, D. L. Sivco, A. L. Hutchinson, S.-N. G. Chu, and A. Y. Cho, "Short wavelength ($\lambda \sim 3.4 \mu\text{m}$) quantum cascade laser based on strained compensated InGaAs/AlInAs," *Appl. Phys. Lett.* **72**, 680 (1998).
doi:[10.1063/1.120843](https://doi.org/10.1063/1.120843)
- [35] S. L. Chuang, *Physics of Optoelectronic Devices* Wiley, New York (1995).
ISBN [0-471-10939-8](https://www.isbn.org/ISBN?i=0-471-10939-8)
- [36] G. L. Bir and G. Pikus, *Symmetry and Strain-Induced Effects in Semiconductors* Wiley, New York (1974).
ISBN [0-470-07321-7](https://www.isbn.org/ISBN?i=0-470-07321-7)
- [37] C. G. Van de Walle, "Band lineups and deformation potentials in the model-solid theory," *Phys. Rev. B* **39**, 1871 (1989).
doi:[10.1103/PhysRevB.39.1871](https://doi.org/10.1103/PhysRevB.39.1871)
- [38] M. Sugawara, N. Okazaki, T. Fujii, and S. Yamazaki, "Conduction-band and valence-band structures in strained $\text{In}_{1-x}\text{Ga}_x\text{As}/\text{InP}$ quantum wells on (001) InP substrates," *Phys. Rev. B* **48**, 8102 (1993).
doi:[10.1103/PhysRevB.48.8102](https://doi.org/10.1103/PhysRevB.48.8102)
- [39] D. F. Nelson, R. C. Miller, and D. A. Kleinman, "Band nonparabolicity effects in semiconductor quantum wells," *Phys. Rev. B* **35**, 7770 (1987).
doi:[10.1103/PhysRevB.35.7770](https://doi.org/10.1103/PhysRevB.35.7770)
- [40] J. H. Davies, *The Physics of Low-Dimensional Semiconductors* Cambridge Univ. Press (1998).
ISBN [0-521-48491-X](https://www.isbn.org/ISBN?i=0-521-48491-X)
- [41] C. Cohen-Tannoudji, B. Diu, and F. Laloë, *Quantum Mechanics* Wiley (1977).
ISBN [0-471-16433-X](https://www.isbn.org/ISBN?i=0-471-16433-X)
- [42] A. Yariv, *Quantum Electronics* Wiley, New York 2nd edn. (1989).
ISBN [0-471-60997-8](https://www.isbn.org/ISBN?i=0-471-60997-8)
- [43] M. A. Parker, *Physics of Optoelectronics* Taylor & Francis (2005).
ISBN [0-8247-5385-2](https://www.isbn.org/ISBN?i=0-8247-5385-2)

- [44] J. H. Smet, C. G. Fonstad, and Q. Hu, "Intrawell and interwell intersubband transitions in multiple quantum wells for far-infrared sources," *J. Appl. Phys.* **79**, 9305 (1996).
doi:[10.1063/1.362607](https://doi.org/10.1063/1.362607)
- [45] B. E. A. Saleh and M. C. Teich, *Fundamentals of Photonics* Wiley (1991).
ISBN [0-471-83965-5](#)
- [46] E. Rosencher and B. Vinter, *Optoelectronics* Cambridge Univ. Press (2002).
ISBN [0-521-77129-3](#)
- [47] G. Bastard, *Wave Mechanics Applied to Semiconductor Heterostructures* Wiley (1991).
ISBN [0-470-21708-1](#)
- [48] R. P. Leavitt, "Empirical two-band model for quantum wells and superlattices in an electric field," *Phys. Rev. B* **44**, 11270 (1991).
doi:[10.1103/PhysRevB.44.11270](https://doi.org/10.1103/PhysRevB.44.11270)
- [49] A. E. Siegman, *Lasers* Univ. Science Books (1986).
ISBN [0935702113](#)
- [50] R. Ferreira and G. Bastard, "Evaluation of some scattering times for electrons in unbiased and biased single- and multiple-quantum-well structures," *Phys. Rev. B* **40**, 1074 (1989).
doi:[10.1103/PhysRevB.40.1074](https://doi.org/10.1103/PhysRevB.40.1074)
- [51] C. Gmachl, D. L. Sivco, R. Colombelli, F. Capasso, and A. Y. Cho, "Ultra-broadband semiconductor laser," *Nature* **415**, 883 (2002).
doi:[10.1038/415883a](https://doi.org/10.1038/415883a)
- [52] A. J. Hoffman, S. Schartner, S. S. Howard, K. J. Franz, F. Towner, and C. Gmachl, "Low voltage-defect quantum cascade laser with heterogeneous injector regions," *Opt. Express* **15**, 15818 (2007).
doi:[10.1364/OE.15.015818](https://doi.org/10.1364/OE.15.015818)

- [53] L. A. Coldren and S. W. Corzine, *Diode Lasers and Photonic Integrated Circuits* Wiley, New York (1995).
ISBN [0-471-11875-3](#)
- [54] T. Gresch, M. Giovannini, N. Hoyer, and J. Faist, “Quantum cascade lasers with large optical waveguides,” **18**, 544 (2006).
doi:[10.1109/LPT.2005.863633](#)
- [55] S. M. Sze, *Physics of Semiconductor Devices* Wiley 2nd edn. (1981).
ISBN [0-471-05661-8](#)
- [56] T. Aellen, M. Beck, N. Hoyler, M. Giovannini, J. Faist, and E. Gini, “Doping in quantum cascade lasers. I. InAlAs–InGaAs/InP midinfrared devices,” *J. Appl. Phys.* **100**, 043101 (2006).
doi:[10.1063/1.2234804](#)
- [57] S. S. Howard, D. P. Howard, K. Franz, A. Hoffman, D. L. Sivco, and C. F. Gmachl, “The effect of injector barrier thickness and doping level on current transport and optical transition width in a $\lambda \sim 8.0 \mu\text{m}$ quantum cascade structure,” *Appl. Phys. Lett.* **93**, 191107 (2008).
doi:[10.1063/1.3028013](#)
- [58] L. Shterengas, G. Belenky, T. Hosoda, G. Kipshidze, and S. Suchalkin, “Continuous wave operation of diode lasers at $3.36 \mu\text{m}$ at 12°C ,” *Appl. Phys. Lett.* **93**, 011103 (2008).
doi:[10.1063/1.2953210](#)
- [59] J. S. Yu, A. Evans, S. Slivken, S. R. Darvish, and M. Razeghi, “Temperature dependent characteristics of $\lambda \sim 3.8 \mu\text{m}$ room-temperature continuous-wave quantum-cascade lasers,” *Appl. Phys. Lett.* **88**, 251118 (2006).
doi:[10.1063/1.2216024](#)
- [60] R. Q. Yang, B. H. Yang, D. Zhang, C.-H. Lin, S. J. Murry, H. Wu, and S. S. Pei, “High power mid-infrared interband cascade lasers based on type-II quantum wells,” *Appl. Phys. Lett.* **71**, 2409 (1997).
doi:[10.1063/1.120076](#)

- [61] M. Kim, C. L. Canedy, W. W. Bewley, C. S. Kim, J. R. Lindle, J. Abell, I. Vurgaftman, and J. R. Meyer, “Interband cascade laser emitting at $\lambda = 3.75 \mu\text{m}$ in continuous wave above room temperature,” *Appl. Phys. Lett.* **92**, 191110 (2008).
doi:[10.1063/1.2930685](https://doi.org/10.1063/1.2930685)
- [62] S. Forouhar and K. Mansour, *private communication* (2008).
- [63] Y. Bai, S. Slivken, S. R. Darvish, and M. Razeghi, “Room temperature continuous wave operation of quantum cascade lasers with 12.5% wall plug efficiency,” *Appl. Phys. Lett.* **93** (2008).
doi:[10.1063/1.2957673](https://doi.org/10.1063/1.2957673)
- [64] L. Wilson, J. Cockburn, D. Carder, M. Steer, M. Hopkinson, C. Chia, R. Airey, and G. Hill, “ $\lambda = 8.3 \mu\text{m}$ GaAs/AlAs quantum cascade lasers incorporating InAs monolayers,” *Electron. Lett.* **37**, 1292 (2001).
doi:[10.1049/el:20010865](https://doi.org/10.1049/el:20010865)
- [65] Q. Yang, C. Mann, F. Fuchs, K. Köhler, and W. Bronner, “High-temperature ($T \geq 400 \text{ K}$) operation of strain-compensated quantum cascade lasers with thin InAs insertion layers and AlAs blocking barriers,” *J. Cryst. Growth* **278**, 714 (2005).
doi:[10.1016/j.jcrysGro.2005.01.001](https://doi.org/10.1016/j.jcrysGro.2005.01.001)
- [66] A. Friedrich, G. Boehm, and M. C. Amann, “Short-wavelength intersubband staircase lasers, with and without AlAs-blocking barriers,” *Semicond. Sci. Technol.* **22**, 218 (2007).
doi:[10.1088/0268-1242/22/3/008](https://doi.org/10.1088/0268-1242/22/3/008)
- [67] D. G. Revin, M. R. Soulby, J. W. Cockburn, Q. Yang, C. Manz, and J. Wagner, “Dispersive gain and loss in midinfrared quantum cascade laser,” *Appl. Phys. Lett.* **92**, 081110 (2008).
doi:[10.1063/1.2884699](https://doi.org/10.1063/1.2884699)
- [68] M. P. Semtsiv, M. Ziegler, S. Dressler, W. T. Masselink, N. Georgiev, T. Dekorsy, and M. Helm, “Above room temperature operation of short wavelength ($\lambda = 3.8 \mu\text{m}$) strain-compensated $\text{In}_{0.73}\text{Ga}_{0.27}\text{As}-\text{AlAs}$ quantum-cascade lasers,” *Applied Physics Letters* **85**, 1478 (2004).
doi:[10.1063/1.1789246](https://doi.org/10.1063/1.1789246)

References

- [69] R. Teissier, J. J. Finley, M. S. Skolnick, J. W. Cockburn, J. L. Pelouard, R. Grey, G. Hill, M. A. Pate, and R. Planel, “Experimental determination of Γ - X intervalley transfer mechanisms in GaAs/AlAs heterostructures,” *Phys. Rev. B* **54**, R8329 (1996).
doi:[10.1103/PhysRevB.54.R8329](https://doi.org/10.1103/PhysRevB.54.R8329)
- [70] M. P. Semtsiv, M. Wienold, S. Dressler, W. T. Masselink, G. Fedorov, and D. Smirnov, “Intervalley carrier transfer in short-wavelength InP-based quantum-cascade laser,” *Appl. Phys. Lett.* **93**, 071109 (2008).
doi:[10.1063/1.2973212](https://doi.org/10.1063/1.2973212)
- [71] C. Gmachl, H. M. Ng, and A. Y. Cho, “Intersubband absorption in GaN/AlGaN multiple quantum wells in the wavelength range of $\lambda \sim 1.75\text{-}4.2 \mu\text{m}$,” *Appl. Phys. Lett.* **77**, 334 (2000).
doi:[10.1063/1.126968](https://doi.org/10.1063/1.126968)
- [72] L. Nevou, M. Tchernycheva, F. H. Julien, F. Guillot, and E. Monroy, “Short wavelength ($\lambda = 2.13 \mu\text{m}$) intersubband luminescence from GaN/AlN quantum wells at room temperature,” *Appl. Phys. Lett.* **90**, 121106 (2007).
doi:[10.1063/1.2715001](https://doi.org/10.1063/1.2715001)
- [73] A. Vardi, G. Bahir, F. Guillot, C. Bougerol, E. Monroy, S. E. Schacham, M. Tchernycheva, and F. H. Julien, “Near infrared quantum cascade detector in GaN/AlGaN/AlN heterostructures,” *Appl. Phys. Lett.* **92**, 011112 (2008).
doi:[10.1063/1.2830704](https://doi.org/10.1063/1.2830704)
- [74] K. Jinen, T. Kikuchi, M. Watanabe, and M. Asada, “Room-temperature electroluminescence from single-period (CdF₂/CaF₂) inter-subband quantum cascade structure on Si substrate,” *Jap. J. Appl. Phys.* **45**, 3656 (2006).
doi:[10.1143/JJAP.45.3656](https://doi.org/10.1143/JJAP.45.3656)
- [75] S. Nakamura, M. Senoh, S. ichi Nagahama, N. Iwasa, T. Yamada, T. Matsushita, H. Kiyoku, and Y. Sugimoto, “InGaN-Based Multi-Quantum-Well-Structure Laser Diodes,” *Jap. J. Appl. Phys.* **35**, L74 (1996).
doi:[10.1143/JJAP.35.L74](https://doi.org/10.1143/JJAP.35.L74)

- [76] S. Guo and M. C. Tamargo, “II–VI Materials for Visible Light Emitters,” in “II–VI Semiconductor Materials and their Applications,” (edited by M. C. Tamargo) vol. 12 of *Optoelectronic Properties of Semiconductors and Superlattices* Taylor & Francis (2002).
ISBN 1560329149
- [77] M. Tamargo, A. Cavus, L. Zeng, N. Dai, N. Bambha, A. Gray, F. Semendy, W. Krystek, and F. Pollak, “MBE growth of lattice–matched ZnCdMgSe quaternaries and ZnCdMgSe/ZnCdSe quantum wells on InP substrates,” *J. Electron. Mater.* **25**, 259 (1996).
doi:[10.1007/BF02666254](https://doi.org/10.1007/BF02666254)
- [78] Y. Guo, G. Aizin, Y. C. Chen, L. Zeng, A. Cavus, and M. C. Tamargo, “Photo-pumped ZnCdSe/ZnCdMgSe blue-green quantum well lasers grown on InP substrates,” *Appl. Phys. Lett.* **70**, 1351 (1997).
doi:[10.1063/1.118576](https://doi.org/10.1063/1.118576)
- [79] DARPA MTO, “Broad Agency Announcement for the DARPA Visible InGaN Injection Lasers (VIGIL) program.”
url: <http://www.darpa.mil/mto/solicitations/baa07-28/pdf/VIGIL.pdf>
- [80] J. R. Chelikowsky and M. L. Cohen, “Nonlocal pseudopotential calculations for the electronic structure of eleven diamond and zinc-blende semiconductors,” *Phys. Rev. B* **14**, 556 (1976).
doi:[10.1103/PhysRevB.14.556](https://doi.org/10.1103/PhysRevB.14.556)
- [81] O. Zakharov, A. Rubio, X. Blase, M. L. Cohen, and S. G. Louie, “Quasiparticle band structures of six II–VI compounds: ZnS, ZnSe, ZnTe, CdS, CdSe, and CdTe,” *Phys. Rev. B* **50**, 10780 (1994).
doi:[10.1103/PhysRevB.50.10780](https://doi.org/10.1103/PhysRevB.50.10780)
- [82] M. Sohel, M. Muñoz, and M. C. Tamargo, “Molecular beam epitaxial growth and characterization of zinc–blende ZnMgSe on InP (001),” *Appl. Phys. Lett.* **85**, 2794 (2004).
doi:[10.1063/1.1804611](https://doi.org/10.1063/1.1804611)

References

- [83] M. J. Kastner, B. Hahn, C. Auchter, M. Deufel, A. Rosenauer, and W. Gebhardt, “Structural characterization and MOVPE growth of ZnCdSe and ZnSSe layers, quantum wells and superlattices,” *J. Cryst. Growth* **159**, 134 (1996).
doi:[10.1016/0022-0248\(95\)00761-X](https://doi.org/10.1016/0022-0248(95)00761-X)
- [84] M. A. Haase, J. Qiu, J. M. DePuydt, and H. Cheng, “Blue–green laser diodes,” *Appl. Phys. Lett.* **59**, 1272 (1991).
doi:[10.1063/1.105472](https://doi.org/10.1063/1.105472)
- [85] N. Dai, A. Cavus, R. Dzakpasu, M. C. Tamargo, F. Semendy, N. Bambha, D. M. Hwang, and C. Y. Chen, “Molecular beam epitaxial growth of high quality $Zn_{1-x}Cd_xSe$ on InP substrates,” *Appl. Phys. Lett.* **66**, 2742 (1995).
doi:[10.1063/1.113694](https://doi.org/10.1063/1.113694)
- [86] M. T. Litz, K. Watanabe, M. Korn, H. Ress, U. Lunz, W. Ossau, A. Waag, G. Landwehr, T. Walter, B. Neubauer, D. Gerthsen, and U. Schüssler, “Epitaxy of $Zn_{1-x}Mg_xSe_yTe_{1-y}$ on (100)InAs,” *J. Cryst. Growth* **159**, 54 (1996).
doi:[10.1016/0022-0248\(95\)00881-0](https://doi.org/10.1016/0022-0248(95)00881-0)
- [87] L. Zeng, B. X. Yang, M. C. Tamargo, E. Snoeks, and L. Zhao, “Quality improvements of $Zn_xCd_yMg_{1-x-y}Se$ layers grown on InP substrates by a thin ZnCdSe interfacial layer,” *Appl. Phys. Lett.* **72**, 1317 (1998).
doi:[10.1063/1.120980](https://doi.org/10.1063/1.120980)
- [88] D. Li and M. D. Pashley, “ZnSe nucleation on the GaAs(001):Se-(2×1) surface observed by scanning tunneling microscopy,” *J. Vac. Sci. Tech. B* **12**, 2547 (1994).
doi:[10.1116/1.587799](https://doi.org/10.1116/1.587799)
- [89] L. Zeng, S. P. Guo, Y. Y. Luo, W. Lin, M. C. Tamargo, H. Xing, and G. S. Cargill, “Defect reduction of $Zn_xCd_yMg_{1-x-y}Se$ based structures grown on InP by using Zn irradiation of the III–V surface,” *J. Vac. Sci. Tech. B* **17**, 1255 (1999).
doi:[10.1116/1.590734](https://doi.org/10.1116/1.590734)
- [90] B. S. Li, A. Shen, W. O. Charles, Q. Zhang, and M. C. Tamargo, “Midinfrared intersubband absorption in wide band gap II–VI $Zn_xCd_{1-x}Se$ multiple quantum wells with metastable zincblende MgSe barriers,” *Appl. Phys. Lett.* **92**, 261104

- (2008).
doi:[10.1063/1.2943660](https://doi.org/10.1063/1.2943660)
- [91] H. Lu, A. Shen, W. Charles, I. Yokomizo, M. C. Tamargo, K. J. Franz, C. Gmachl, and M. Muñoz, “Optical characterization of intersubband transitions in $Zn_xCd_{1-x}Se/Zn_{x'}Cd_{y'}Mg_{1-x'-y'}Se$ multiple quantum well structures by contactless electroreflectance,” *Appl. Phys. Lett.* **89**, 241921 (2006).
doi:[10.1063/1.2405385](https://doi.org/10.1063/1.2405385)
- [92] D. Walsh, K. Mazuruk, and M. Benzaquen, “Raman spectrum of a ZnSe/GaAs heterostructure,” *Phys. Rev. B* **36**, 2883 (1987).
doi:[10.1103/PhysRevB.36.2883](https://doi.org/10.1103/PhysRevB.36.2883)
- [93] P. Y. Yu, “Resonant Raman study of the LO + acoustic phonon modes in CdSe,” *Solid State Comm.* **19**, 1087 (1976).
doi:[10.1016/0038-1098\(76\)90104-6](https://doi.org/10.1016/0038-1098(76)90104-6)
- [94] M. Muñoz, H. Lu, X. Zhou, M. C. Tamargo, and F. H. Pollak, “Band offset determination of $Zn_{0.53}Cd_{0.47}Se/Zn_{0.29}Cd_{0.24}Mg_{0.47}Se$,” *Appl. Phys. Lett.* **83**, 1995 (2003).
doi:[10.1063/1.1606875](https://doi.org/10.1063/1.1606875)
- [95] T. Miyajima, H. Okuyama, and K. Akimoto, “Ti/Pt/Au Ohmic Contacts to n-Type ZnSe,” *Jap. J. Appl. Phys.* **31**, L1743 (1992).
doi:[10.1143/JJAP.31.L1743](https://doi.org/10.1143/JJAP.31.L1743)
- [96] J. Faist, F. Capasso, C. Sirtori, D. L. Sivco, A. L. Hutchinson, and A. Y. Cho, “Vertical transition quantum cascade laser with Bragg confined excited state,” *Appl. Phys. Lett.* **66**, 538 (1995).
doi:[10.1063/1.114005](https://doi.org/10.1063/1.114005)
- [97] V. Moreau, M. Bahriz, R. Colombelli, R. Perahia, O. Painter, L. R. Wilson, and A. B. Krysa, “Demonstration of air-guided quantum cascade lasers without top claddings,” *Opt. Express* **15**, 14861 (2007).
doi:[10.1364/OE.15.014861](https://doi.org/10.1364/OE.15.014861)

References

- [98] V. R. Almeida, Q. Xu, C. A. Barrios, and M. Lipson, “Guiding and confining light in void nanostructure,” *Opt. Lett.* **29**, 1209 (2004).
doi:[10.1364/OL.29.001209](https://doi.org/10.1364/OL.29.001209)
- [99] United States Nuclear Regulatory Comission, “Uranium Enrichment.”
url: <http://www.nrc.gov/materials/fuel-cycle-fac/ur-enrichment.html>
- [100] P. Rabinowitz, A. Kaldor, A. Gnauck, R. L. Woodin, and J. S. Gethner, “Two-color infrared isotopically selective decomposition of UF₆,” *Opt. Lett.* **7**, 212 (1982).
doi:[10.1364/OL.7.000212](https://doi.org/10.1364/OL.7.000212)
- [101] Y. Okada, S. Tanimura, H. Okamura, A. Suda, H. Tashiro, and K. Takeuchi, “Vibrational spectroscopy and predissociation of UF₆ clusters in a supersonic Laval nozzle,” *J. Molec. Struct.* **410-411**, 299 (1997).
doi:[10.1016/S0022-2860\(96\)09567-1](https://doi.org/10.1016/S0022-2860(96)09567-1)
- [102] C. Gmachl, F. Capasso, A. Tredicucci, D. Sivco, A. Hutchinson, and A. Cho, “Long wavelength $\lambda \approx 13 \mu\text{m}$ quantum cascade lasers,” *Electron. Lett.* **34**, 1103 (1998).
url: http://ieeexplore.ieee.org/xpls/abs_all.jsp?arnumber=684577
- [103] A. Tredicucci, C. Gmachl, F. Capasso, D. L. Sivco, A. L. Hutchinson, and A. Y. Cho, “Long wavelength superlattice quantum cascade lasers at $\lambda \approx 17 \mu\text{m}$,” *Appl. Phys. Lett.* **74**, 638 (1999).
doi:[10.1063/1.123026](https://doi.org/10.1063/1.123026)
- [104] A. Tredicucci, C. Gmachl, M. C. Wanke, F. Capasso, A. L. Hutchinson, D. L. Sivco, S. G. Chu, and A. Y. Cho, “Surface plasmon quantum cascade lasers at $\lambda \sim 19 \mu\text{m}$,” *Appl. Phys. Lett.* **77**, 2286 (2000).
doi:[10.1063/1.1316768](https://doi.org/10.1063/1.1316768)
- [105] M. Rochat, D. Hofstetter, M. Beck, and J. Faist, “Long-wavelength ($\lambda \approx 16 \mu\text{m}$), room-temperature, single-frequency quantum-cascade lasers based on a bound-to-continuum transition,” *Appl. Phys. Lett.* **79**, 4271 (2001).
doi:[10.1063/1.1425468](https://doi.org/10.1063/1.1425468)

- [106] S. Tsujino, A. Borak, E. Müller, M. Scheinert, C. V. Falub, H. Sigg, D. Grützmacher, M. Giovannini, and J. Faist, “Interface–roughness–induced broadening of inter-subband electroluminescence in p-SiGe and n-GaInAs/AlInAs quantum-cascade structures,” *Appl. Phys. Lett.* **86**, 062113 (2005).
doi:[10.1063/1.1862344](https://doi.org/10.1063/1.1862344)
- [107] M. O. Scully and M. S. Zubairy, *Quantum Optics* Cambridge Univ. Press, New York (1997).
ISBN [0-521-43595-1](#)
- [108] G. Scalari, C. Walther, J. Faist, H. Beere, and D. Ritchie, “Electrically switchable, two-color quantum cascade laser emitting at 1.39 and 2.3 THz,” *Appl. Phys. Lett.* **88**, 141102 (2006).
doi:[10.1063/1.2191407](https://doi.org/10.1063/1.2191407)
- [109] C. Sirtori, A. Tredicucci, F. Capasso, J. Faist, D. L. Sivco, A. L. Hutchinson, and A. Y. Cho, “Dual-wavelength emission from optically cascaded intersubband transitions,” *Opt. Lett.* **23**, 463 (1998).
doi:[10.1364/OL.23.000463](https://doi.org/10.1364/OL.23.000463)
- [110] S. S. Howard, Z. Liu, and C. F. Gmachl, “Thermal and stark-effect roll-over of quantum-cascade lasers,” *IEEE J. Quantum Electron.* **44**, 319 (2008).
doi:[10.1109/JQE.2007.912477](https://doi.org/10.1109/JQE.2007.912477)
- [111] J. Faist, F. Capasso, C. Sirtori, D. L. Sivco, A. L. Hutchinson, M. S. Hybertsen, and A. Y. Cho, “Quantum Cascade Lasers without Intersubband Population Inversion,” *Phys. Rev. Lett.* **76**, 411 (1996).
doi:[10.1103/PhysRevLett.76.411](https://doi.org/10.1103/PhysRevLett.76.411)
- [112] G. B. Serapiglia, K. L. Vodopyanov, and C. C. Phillips, “Nonequilibrium electron distributions in a three-subband InGaAs/InAlAs quantum well studied via double resonance spectroscopy,” *Appl. Phys. Lett.* **77**, 857 (2000).
doi:[10.1063/1.1306651](https://doi.org/10.1063/1.1306651)
- [113] A. M. Alcalde and G. Weber, “Nonparabolicity effects on electron–optical-phonon scattering rates in quantum wells,” *Phys. Rev. B* **56**, 9619 (1997).
doi:[10.1103/PhysRevB.56.9619](https://doi.org/10.1103/PhysRevB.56.9619)

References

- [114] B. K. Ridley, *Quantum Processes in Semiconductors* Oxford Univ. Press 4th edn. (1999).
ISBN [0-19-850-580-9](#)
- [115] S. Sinning, T. Dekorsy, M. Helm, G. Mussler, L. Däweritz, and K. H. Ploog, “Reduced subpicosecond electron relaxation in $\text{GaN}_x\text{As}_{1-x}$,” *Appl. Phys. Lett.* **86**, 161912 (2005).
doi:[10.1063/1.1904709](#)
- [116] U. Bockelmann and G. Bastard, “Phonon scattering and energy relaxation in two-, one-, and zero-dimensional electron gases,” *Phys. Rev. B* **42**, 8947 (1990).
doi:[10.1103/PhysRevB.42.8947](#)
- [117] V. Gorfinkel, S. Luryi, and B. Gelmont, “Theory of gain spectra for quantum cascade lasers and temperature dependence of their characteristics at low and moderate carrier concentrations,” *IEEE J. Quantum Electron.* **32**, 1995 (1996).
doi:[10.1109/3.541687](#)
- [118] C. Gmachl, F. Capasso, D. L. Sivco, and A. Y. Cho, “Recent progress in quantum cascade lasers and applications,” *Rep. Prog. Phys.* **64**, 1533 (2001).
doi:[10.1088/0034-4885/64/11/204](#)
- [119] J. Faist, “Quantum Cascade Lasers,” in “Intersubband Transitions in Quantum Wells: Physics and Device Applications II,” (edited by H. C. Liu and F. Capasso) vol. 66 of *Semiconductors and Semimetals* Academic Press (2000).
ISBN [0127521755](#)
- [120] Z. Liu, C. Gmachl, L. Cheng, F.-S. Choa, F. Towner, X. Wang, and J. Fan, “Temperature Dependence of Optical Gain and Loss in $\lambda \approx 8.2\text{--}10.2\text{ }\mu\text{m}$ Quantum-Cascade Lasers,” *IEEE J. Quantum Electron.* **44**, 485 (2008).
doi:[10.1109/JQE.2008.917273](#)
- [121] S. Rudin and T. L. Reinecke, “Electron–LO-phonon scattering rates in semiconductor quantum wells,” *Phys. Rev. B* **41**, 7713 (1990).
doi:[10.1103/PhysRevB.41.7713](#)

- [122] L. J. Olafsen, I. Vurgaftman, and J. R. Meyer, “Antimonide Mid-IR Lasers,” in “Long-wavelength Infared Semiconductor Lasers,” (edited by H. K. Choi) Wiley (2004). ISBN [0471392006](#)
- [123] V. Shastin, “Hot hole inter-sub-band transition p-Ge FIR laser,” *Opt. Quantum Electron.* **23**, S111 (1991).
doi:[10.1007/BF00619761](https://doi.org/10.1007/BF00619761)
- [124] E. Bründermann, “Widely Tunable Far-Infared Hot-Hole Semiconductor Lasers,” in “Long-wavelength Infared Semiconductor Lasers,” (edited by H. K. Choi) Wiley (2004). ISBN [0471392006](#)
- [125] W. E. Pinson and R. Bray, “Experimental Determination of the Energy Distribution Functions and Analysis of the Energy-Loss Mechanisms of Hot Carriers in *p*-Type Germanium,” *Phys. Rev.* **136**, A1449 (1964).
doi:[10.1103/PhysRev.136.A1449](https://doi.org/10.1103/PhysRev.136.A1449)
- [126] A. Wittmann, T. Gresch, E. Gini, L. Hvozdara, N. Hoyler, M. Giovannini, and J. Faist, “High-Performance Bound-to-Continuum Quantum-Cascade Lasers for Broad-Gain Applications,” *Quantum Electronics, IEEE Journal of* **44**, 36 (2008).
doi:[10.1109/JQE.2007.909516](https://doi.org/10.1109/JQE.2007.909516)
- [127] Y. Yao, Z. Liu, A. J. Hoffman, K. J. Franz, and C. F. Gmachl, “Voltage Tunability of Quantum Cascade Lasers,” *IEEE J. Quantum Electron.* **45** (2009).
- [128] G. Wysocki, R. Lewicki, R. F. Curl, F. K. Tittel, L. Diehl, F. Capasso, M. Troccoli, G. Hofler, D. Bour, S. Corzine, R. Maulini, M. Giovannini, and J. Faist, “Widely tunable mode-hop free external cavity quantum cascade lasers for high resolution spectroscopy and chemical sensing,” *Appl. Phys. B* **92**, 305 (2008).
doi:[10.1007/s00340-008-3047-x](https://doi.org/10.1007/s00340-008-3047-x)
- [129] B. G. Lee, M. A. Belkin, R. Audet, J. MacArthur, L. Diehl, C. Pflügl, F. Capasso, D. C. Oakley, D. Chapman, A. Napoleone, D. Bour, S. Corzine, G. Höfler, and J. Faist, “Widely tunable single-mode quantum cascade laser source for mid-infrared spectroscopy,” *Appl. Phys. Lett.* **91**, 231101 (2007).
doi:[10.1063/1.2816909](https://doi.org/10.1063/1.2816909)

- [130] M. Yamanishi, K. Fujita, T. Edamura, and H. Kan, “Indirect pump scheme for quantum cascade lasers: dynamics of electron-transport and very high T_0 -values,” *Opt. Express* **16**, 20748 (2008).
doi:[10.1364/OE.16.020748](https://doi.org/10.1364/OE.16.020748)
- [131] J. Faist, F. Capasso, C. Sirtori, D. Sivco, A. Hutchinson, and A. Cho, “Laser action by tuning the oscillator strength,” *Nature* **387**, 777 (1997).
- [132] J. Faist, F. Capasso, C. Sirtori, D. L. Sivco, A. L. Hutchinson, and A. Y. Cho, “Vertical transition quantum cascade laser with Bragg confined excited state,” *Appl. Phys. Lett.* **66**, 538 (1995).
doi:[10.1063/1.114005](https://doi.org/10.1063/1.114005)
- [133] C. Sirtori, J. Faist, F. Capasso, D. L. Sivco, A. L. Hutchinson, S. N. G. Chu, and A. Y. Cho, “Continuous wave operation of midinfrared ($7.4\text{--}8.6\ \mu\text{m}$) quantum cascade lasers up to 110 K temperature,” *Appl. Phys. Lett.* **68**, 1745 (1996).
doi:[10.1063/1.116654](https://doi.org/10.1063/1.116654)
- [134] C. Sirtori, F. Capasso, J. Faist, A. Hutchinson, D. Sivco, and A. Cho, “Resonant tunneling in quantum cascade lasers,” *IEEEJ. Quantum Electron.* **34**, 1722 (1998).
doi:[10.1109/3.709589](https://doi.org/10.1109/3.709589)
- [135] J. Faist, F. Capasso, C. Sirtori, D. L. Sivco, J. N. Baillargeon, A. L. Hutchinson, S. G. Chu, and A. Y. Cho, “High power mid-infrared ($\lambda \sim 5\ \mu\text{m}$) quantum cascade lasers operating above room temperature,” *Appl. Phys. Lett.* **68**, 3680 (1996).
doi:[10.1063/1.115741](https://doi.org/10.1063/1.115741)
- [136] C. Gmachl, A. Tredicucci, F. Capasso, A. L. Hutchinson, D. L. Sivco, J. N. Baillargeon, and A. Y. Cho, “High-power $\lambda \sim 8\ \mu\text{m}$ quantum cascade lasers with near optimum performance,” *Appl. Phys. Lett.* **72**, 3130 (1998).
doi:[10.1063/1.121569](https://doi.org/10.1063/1.121569)
- [137] D. Hofstetter, M. Beck, T. Aellen, and J. Faist, “High-temperature operation of distributed feedback quantum-cascade lasers at $5.3\ \mu\text{m}$,” *Appl. Phys. Lett.* **78**, 396 (2001).
doi:[10.1063/1.1340865](https://doi.org/10.1063/1.1340865)

- [138] A. Lyakh, C. Pflügl, L. Diehl, Q. Wang, F. Capasso, X. Wang, J.-Y. Fan, T. Tanbun-Ek, A. Tsekoun, R. Maulini, R. Go, and C. K. N. Patel, “1.3 W quantum cascade lasers with optimized design for continuous-wave operation at room temperature,” *Proc. Conference on Lasers and Electro-Optics CTuF3* (2008).
- url: http://ieeexplore.ieee.org/xpls/abs_all.jsp?arnumber=4571883
- [139] M. C. Wanke, F. Capasso, C. Gmachl, A. Tredicucci, D. L. Sivco, A. L. Hutchinson, S.-N. G. Chu, and A. Y. Cho, “Injectorless quantum-cascade lasers,” *Appl. Phys. Lett.* **78**, 3950 (2001).
- doi:[10.1063/1.1378805](https://doi.org/10.1063/1.1378805)
- [140] S. Katz, A. Friedrich, G. Boehm, and M.-C. Amann, “Continuous wave operation of injectorless quantum cascade lasers at low temperatures,” *Appl. Phys. Lett.* **92**, 181103 (2008).
- doi:[10.1063/1.2841704](https://doi.org/10.1063/1.2841704)
- [141] H. Luo, S. R. Laframboise, Z. R. Wasilewski, G. C. Aers, H. C. Liu, and J. C. Cao, “Terahertz quantum-cascade lasers based on a three-well active module,” *Appl. Phys. Lett.* **90**, 041112 (2007).
- doi:[10.1063/1.2437071](https://doi.org/10.1063/1.2437071)
- [142] M. A. Belkin, J. A. Fan, S. Hormoz, F. Capasso, S. P. Khanna, M. Lachab, A. G. Davies, and E. H. Linfield, “Terahertz quantum cascade lasers with copper metal-metal waveguides operating up to 178 K,” *Opt. Express* **16**, 3242 (2008).
- doi:[10.1364/OE.16.003242](https://doi.org/10.1364/OE.16.003242)
- [143] R. Köhler, A. Tredicucci, F. Beltram, H. E. Beere, E. H. Linfield, A. G. Davies, D. A. Ritchie, R. C. Iotti, and F. Rossi, “Terahertz semiconductor-heterostructure laser,” *Nature* **417**, 156 (2002).
- [144] A. Evans, J. S. Yu, S. Slivken, and M. Razeghi, “Continuous-wave operation of $\lambda \sim 4.8 \mu\text{m}$ quantum-cascade lasers at room temperature,” *Appl. Phys. Lett.* **85**, 2166 (2004).
- doi:[10.1063/1.1793340](https://doi.org/10.1063/1.1793340)

- [145] A. Lyakh, C. Pflügl, L. Diehl, Q. J. Wang, F. Capasso, X. J. Wang, J. Y. Fan, T. Tanbun-Ek, R. Maulini, A. Tsekoun, R. Go, and C. K. N. Patel, “1.6 W high wall plug efficiency, continuous-wave room temperature quantum cascade laser emitting at 4.6 μm ,” *Appl. Phys. Lett.* **92**, 111110 (2008).
doi:[10.1063/1.2899630](https://doi.org/10.1063/1.2899630)
- [146] K. Leo, *High-Field Transport in Semiconductor Superlattices* Springer, Berlin (2003).
ISBN [3-540-00569-2](#)
- [147] C. Gmachl, F. Capasso, A. Tredicucci, D. L. Sivco, R. Köhler, A. L. Hutchinson, and A. Y. Cho, “Dependence of the device performance on the number of stages in quantum-cascade lasers,” *IEEE J. Sel. Top. Quantum Electron.* **5**, 808 (1999).
doi:[10.1109/2944.788453](https://doi.org/10.1109/2944.788453)
- [148] P. G. Savvidis, B. Kolasa, G. Lee, and S. J. Allen, “Resonant Crossover of Terahertz Loss to the Gain of a Bloch Oscillating InAs/AlSb Superlattice,” *Phys. Rev. Lett.* **92**, 196802 (2004).
doi:[10.1103/PhysRevLett.92.196802](https://doi.org/10.1103/PhysRevLett.92.196802)
- [149] J. B. Khurgin, Y. Dikmelik, P. Q. Liu, A. J. Hoffman, M. D. Escarra, K. J. Franz, and C. F. Gmachl, “Role of interface roughness in the transport and lasing characteristics of quantum-cascade lasers,” *Appl. Phys. Lett.* **94**, 091101 (2009).
doi:[10.1063/1.3093819](https://doi.org/10.1063/1.3093819)
- [150] E. Yablonovitch and E. Kane, “Band structure engineering of semiconductor lasers for optical communications,” *J. Lightwave Technol.* **6**, 1292 (1988).
doi:[10.1109/50.4133](https://doi.org/10.1109/50.4133)
- [151] R. Dingle, W. Wiegmann, and C. H. Henry, “Quantum States of Confined Carriers in Very Thin $\text{Al}_x\text{Ga}_{1-x}\text{As}-\text{GaAs}-\text{Al}_x\text{Ga}_{1-x}\text{As}$ Heterostructures,” *Phys. Rev. Lett.* **33**, 827 (1974).
doi:[10.1103/PhysRevLett.33.827](https://doi.org/10.1103/PhysRevLett.33.827)
- [152] J. P. van der Ziel, R. Dingle, R. C. Miller, W. Wiegmann, and J. W. A. Nordland, “Laser oscillation from quantum states in very thin $\text{GaAs}-\text{Al}_{0.2}\text{Ga}_{0.8}\text{As}$ multilayer

- structures," *Appl. Phys. Lett.* **26**, 463 (1975).
doi:[10.1063/1.88211](https://doi.org/10.1063/1.88211)
- [153] K. Choquette, K. Geib, C. Ashby, R. Twesten, O. Blum, H. Hou, D. Follstaedt, B. Hammons, D. Mathes, and R. Hull, "Advances in selective wet oxidation of AlGaAs alloys," *IEEE J. Sel. Top. Quantum Electron.* **3**, 916 (1997).
doi:[10.1109/2944.640645](https://doi.org/10.1109/2944.640645)
- [154] C. Gmachl, F. Capasso, J. Faist, A. L. Hutchinson, A. Tredicucci, D. L. Sivco, J. N. Baillargeon, S. N. G. Chu, and A. Y. Cho, "Continuous-wave and high-power pulsed operation of index-coupled distributed feedback quantum cascade laser at $\lambda \approx 8.5 \mu\text{m}$," *Appl. Phys. Lett.* **72**, 1430 (1998).
doi:[10.1063/1.120585](https://doi.org/10.1063/1.120585)
- [155] L. Hvozdara, A. Lugstein, N. Finger, S. Gianordoli, W. Schrenk, K. Unterrainer, E. Bertagnolli, G. Strasser, and E. Gornik, "Quantum cascade lasers with monolithic air–semiconductor Bragg reflectors," *Appl. Phys. Lett.* **77**, 1241 (2000).
doi:[10.1063/1.1289910](https://doi.org/10.1063/1.1289910)
- [156] S. Blaser, A. Bachle, S. Jochum, L. Hvozdara, G. Vandeputte, S. Brunner, S. Hansmann, A. Muller, and J. Faist, "Low-consumption (below 2W) continuous-wave singlemode quantum-cascade lasers grown by metal-organic vapour-phase epitaxy," *Electron. Lett.* **43**, 1201 (2007).
doi:[10.1049/el:20072576](https://doi.org/10.1049/el:20072576)
- [157] Z. Liu, C. F. Gmachl, C. G. Caneau, and C. Zah, "Very Small ($\leq 1.2\text{--}1.7 \text{ W}$) Heat Dissipation, Room Temperature, Continuous-Wave Quantum Cascade Lasers at $\lambda \sim 5.3 \mu\text{m}$," *Proc. Conference on Lasers and Electro-Optics CTuF2* (2008).
url: http://ieeexplore.ieee.org/xpls/abs_all.jsp?arnumber=4571882